UNIVERSITY OF SOUTHAMPTON

The Reverberation Signatures of Accretion Disk Winds in Active Galactic Nuclei

by

Samuel W. Mangham

A thesis submitted in partial fulfilment for the degree of Doctor of Philosophy

in the

Faculty of Engineering and Physical Sciences

School of Physics and Astronomy

April 2019

UNIVERSITY OF SOUTHAMPTON

ABSTRACT

FACULTY OF ENGINEERING AND PHYSICAL SCIENCES
SCHOOL OF PHYSICS AND ASTRONOMY

Doctor of Philosophy

by Samuel W. Mangham

Active Galactic Nuclei are the most luminous objects in the universe; objects that can outshine their host galaxies by orders of magnitude, but are incredibly compact. Some models for AGN describe them as super-massive black holes surrounded by accretion disks of inflowing matter and outflowing 'winds' of material. As the central regions of AGN, responsible for the bulk of the emission, are on the scale of light-months whilst AGN are Mly distant, they are unresolvable.

As such, we must turn to other techniques to investigate their properties. Reverberation mapping is commonly used to estimate black hole masses in AGN using the delayed response of broad emission lines in their spectra to fluctuations in the underlying continuum. Velocity-resolved reverberation mapping offers an effective tool for determining the structure and kinematics of the broad-line region (BLR) that emits these lines, including the accretion disk and winds. Much prior work has been performed using simulations of simplified models to generate the response functions associated with a range of basic geometries. However, no model has included both full ionisation and radiative transfer effects, and a complex geometry with rotation and outflow.

In this thesis, the Monte Carlo radiative transfer and ionisation code Python has been modified for use in reverberation mapping of a range of geometries, from simple to potentially more realistic. Building on prior work, we model the BLR response to the central ionising continuum source taking into account detailed radiative transfer effects and self-consistent calculations of the ionisation state of the disk wind. We find the response functions generated display features that can confound existing analysis, including *negative* responses. We then test the ability of existing techniques to recover these more complex response functions from simulated observing campaigns.

In summary, this thesis demonstrates that radiative transfer and ionisation effects are crucial for generating response functions for realistic geometries and kinematics, and highlights the limits of existing techniques to accurately recover physically-motivated response functions.

Contents

List of Figures

List of Tables

Acknowledgements

I am very thankful for Prof. Christian Knigge for being my supervisor, and for the incredible experiences that I have had both working on my research, presenting at conferences, and throughout the PhD. Christian has been an enthusiastic and consistent font of encouragement and fascinating ideas; as well as taking a truly inspirational number of trips to exotic locations!

I am very grateful to have had the opportunity to work with the PYTHON collaboration; Prof. Knox Long, Stuart Sim, Nick Higginbottom, James Matthews, Edward Parkinson and Mandy Hewitt. It has been a privilege to work on an interesting code with such a dedicated and knowledgeable team. Many thanks in particular to James Matthews for all his friendly and enthusiastic help and support with the code and generally getting used to life as one of Christian's PhD students, and for his help in reading and critiquing my thesis. I am also very grateful to Prof. Long, both for originally writing the code and for his active help with my work on it, as well as for reading and critiquing my thesis.

I would like to thank the Institute for Complex Systems Simulation for accepting me onto a PhD in Complex Systems Simulation, and in particular for allowing me to change project early on. I am indebted to DTC Coordinator Nicky Lewin for her patience and infallible organising skills. Thanks also to the original DTC heads Prof. Hans Fangohr and Prof. Seth Bullock, and current head Chris Cave-Ayland.

Many thanks to John Robinson and Simon Hettrick of the Research Software Group and Software Sustainability Institute, for kindly allowing me to work part-time to finish this thesis over the last year.

Finally, I am grateful for those who have made my PhD so enjoyable a time despite the stresses and strains of research. Many thanks to Sadie Jones, John Coxon and everyone else involved in outreach for allowing me to indulge an interest in it that I didn't know I had. Thanks to all the staff and students of the Astronomy & Astrophysics and Space Science groups, for creating a cheerful, supportive, interesting and engaging workplace that I looked forward to going to every day, and thanks to Nicola for being someone I could look forward to going home to at the end of the day too.

This work was supported by the Engineering and Physical Sciences Research Council via a 4 year PhD studentship. I acknowledge the extensive use of the Matplotlib, Numpy and Astropy Python libraries in this work.

Declaration Of Authorship

I, Samuel William Mangham,

declare that this thesis and the work presented in it are my own and has been generated by me as the result of my own original research.

An Investigation into the Reverberation Mapping of Active Galactic Nuclei

I confirm that:

1. This work was done wholly or mainly while in candidature for a research degree at this University;
2. Where any part of this thesis has previously been submitted for a degree or any other qualification at this University or any other institution, this has been clearly stated;
3. Where I have consulted the published work of others, this is always clearly attributed;
4. Where I have quoted from the work of others, the source is always given. With the exception of such quotations, this thesis is entirely my own work;
5. I have acknowledged all main sources of help;
6. Where the thesis is based on work done by myself jointly with others, I have made clear exactly what was done by others and what I have contributed myself;
7. Parts of this work have been published as Mangham et al. (2017).

Signed:
Date:

Definitions

AGN	Active Galactic Nucleus/Nuclei
FWHM	Full Width at Half Maximum
BEL	Broad emission Line (FWHM $> 10^3$ kms$\dot{}^{-1}$)
BLR	Broad Emission Line Region
BAL	Broad Absorption Line (FWHM $> 10^3$ kms$\dot{}^{-1}$)
NEL	Narrow Emission Line (FWHM $< 10^3$ kms$\dot{}^{-1}$)
NLR	Narrow emission Line Region
NAL	Narrow Absorption Line (FWHM $< 10^3$ kms$\dot{}^{-1}$)
UFO	Ultra-Fast Outflow(s) (velocity $> 10^4$ kms$\dot{}^{-1}$)
Type 1	AGN with both broad and narrow emission lines
Type 2	AGN with only narrow emission lines
CO	Compact object, with high density e.g. white dwarfs, neutron stars, black holes, AGN
SMBH	Super-Massive Black Hole
RM	Reverberation mapping
MEM	Maximum Entropy Method, a deconvolution technique
RLI	Regularised Linear Inversion, a deconvolution technique
r_s	Schwarzschild radius
$r_{\rm ISCO}$	Innermost stable circular orbit around a SMBH , $3\times r_s$.
$M_\odot$	Solar mass
$\dot{M}_{\rm acc}$	Mass accretion rate
$\dot{M}_{\rm wind}$	Wind mass outflow rate
$\Psi(t)$	One-dimensional transfer function
$\Psi(v,t)$	Two-dimensional or *velocity-resolved* transfer function (TF)
$\Psi_R(v,t)$	Two-dimensional or *velocity-resolved* response function (RF)
$\Psi_E(v,t)$	Two-dimensional or *velocity-resolved* emissivity-weighted response function (EWRF), equivalent to $\Psi(v,t)$
n_e	Electron number density, unit: cm^{-3}
PYTHON	Monte Carlo radiative transfer and ionisation code, written in c
Python	Programming language

Chapter 1

Introduction

Active Galactic Nuclei (AGN) are a class of objects observed in the cores of many galaxies (Juneau et al., 2013), shining with incredible brightness across a wide range of wavelengths. The first AGN observed were referred to as quasi-stellar objects or *'quasars'*(Page, 1964), almost star-like 'point' sources of light capable of emitting more visible light than their entire host galaxies.

Over the years a whole family of AGN categories and sub-types has been discovered, from *'blazars'* to *'Seyferts'*, *Type 1s* and *Type 2s*, defined by characteristic features in their spectrum. On closer observation these categories have begun to bleed into each other. This has created a 'zoo' of highly luminous super-massive compact objects, with masses ranging from $10^6 - 10^{10}\times$ the mass of the sun, contained within radii on the order of light-days or less.

AGN exhibit a wide range of observational features; order-of-magnitude changes in luminosity, small-scale x-ray emitting cores (Elvis et al., 1994), intense emission line regions (Peterson and Wandel, 1999), high-velocity outflows (Kellermann et al., 1989; Weymann et al., 1991), thick dust clouds (Antonucci, 1984) and highly energetic polar 'jets' of charged particles (Kellermann, 2016). Geometric unification theory posits that the zoo of types can be united into a single class of object; a super-massive black hole with accretion disk of inflowing material, from which a wind is launched, surrounded by a dusty 'torus' (Urry and Padovani, 1995). This theory ascribes the differences in the observed properties of AGN simply to different viewing angles onto the component parts of the system. The specifics of this arrangement, though, are still very much a matter of debate (Baldwin et al., 1995; Elvis, 2000, 2017).

This is a challenging hypothesis to test; even the nearest AGN are Mega-parsecs away (Ferrarese et al., 2007). Whilst some regions can be resolved, on the scale of parsecs or light-months (Prieto et al., 2004; Koshida et al., 2014; Balmaverde et al., 2016), the brightest, most dynamic regions where the outflowing 'winds' are launched and the

brightest emission lines are generated are too small to be spatially resolved with modern telescope technology. Equally, it is important that we do understand the structure and dynamics of the inner environments of AGN. There is a very strong correlation between the stellar mass of a galaxy, and the mass of the AGN residing at its core (Häring and Rix, 2004). This indicates there must be a feedback effect of some kind between an AGN and its host galaxy, regulating star formation (Begelman, 2004). Understanding the process of feedback will require understanding the regions where the outflows from AGN are launched and accelerated.

Previously, the geometries and dynamics of the inner regions of AGN have been explored using *reverberation mapping* (RM). The ultraviolet luminosity of AGN varies on time-scales of hours to months, believed to be due to instabilities in their accretion disks (Kawaguchi et al., 1998). This drives a change in the luminosity in other wavelengths, which lag behind on a time-scale of light-hours to light-months (Mushotzky et al., 1993). From these delays, it is possible to determine the time taken for light to cross the regions responsible for the emission, and from that their scale. Reverberation mapping has frequently been used with the overall line flux for single 'broad' emission lines (BEL), to determine the masses of their host AGN. By determining the orbital velocity of the emitting material using its Doppler shift (Wandel et al., 1999; Denney et al., 2010; Bentz and Katz, 2015), and assuming the time lag corresponds to the time taken for changes in luminosity at the centre of the system to propagate out, we can calculate the central mass from the orbital distance and velocity. With enough observations, a one-dimensional *response function* can be produced for the system, that describes how a change in the driving luminosity produces a change in line luminosity across a range of future times. However, many different geometries can give rise to very similar response functions; we can only make very broad conclusions from the information. With a *two*-dimensional response function, containing information on how the delay varies for different Doppler shifts across an emission line, we can break the degeneracy and determine the specific geometries of AGN.

Recently projects like De Rosa et al. (2015); Bentz et al. (2009b); Du et al. (2014) have launched high-resolution observing campaigns. With frequent observations of an AGN at high wavelength resolution, we can construct empirical versions of the two-dimensional response functions required to understand the inner structure of AGN environments. There is, however, a comparative lack of realistic two-dimensional response functions for self-consistent physical models of AGN to compare these observations against (with notable exceptions e.g. Waters et al. (2016)). Welsh and Horne (1991); Horne et al. (2004) and others have predicted transfer and response functions of some simplified models, like inflowing and outflowing spheres of gas or simple rotating disks, but without including the complicated ionisation structures that would be expected to affect the distribution of emission lines through a real wind. Disk-wind models of AGN would be expected to show a mixture of these signatures, confounded by the complicated

ionisation structure. There is a clear need for predictions of the two-dimensional response functions that would be expected from detailed models of AGN, featuring geometries with complicated ionisation structures and velocity profiles.

1.1 Observational Signatures of AGN

AGN were originally described as 'quasi-stellar objects', point sources with clearly non-stellar spectral features. As more observations were obtained, it became apparent AGN exhibited an incredibly diverse range of spectra, and the objects were also associated with much larger-scale features like jets and outflows.

A current summary of the zoo of AGN classifications is shown in table 1.1, though it has evolved continually over time (Padovani, 1997; Padovani et al., 2017). There are two main axes that define AGN. One is the presence or absence of synchrotron radio emission. The second is the presence or absence and width of emission lines in the optical and UV; the 'broad' and 'narrow' lines. The work in this thesis is applicable to AGN exhibiting clear broad emission lines, and focuses on application to radio-quiet type 1 AGN (Seyfert-Is and QSOs on table 1.1).

TABLE 1.1: Table of AGN classifications

Radio Loudness	Line Category Type 0	Type 1 (Narrow)	Type 2 (Broad & Narrow)
Radio Quiet	Lineless	Seyfert I LINER I [a] QSO	Seyfert II LINER II[a] QSO2
Radio Loud	Blazars { BL-Lac[b]; FSRG (some)[e] }	BLRG[c] { SSRG[d]; FSRG[e] }	NLRG[f] { FR[g]-I; FR[g]-II }

[a] Low Ionisation Nuclear Emission Region Galaxy
[b] BL-Lacertae Objects
[c] Broad-Line Radio Galaxies
[d] Steep-Spectrum Radio Galaxy
[e] Flat-Spectrum Radio Galaxy
[f] Narrow-Line Radio Galaxies
[g] Fanaroff-Riley Galaxy

The following subsections outline various components of the spectra of AGN:

1.1.1 Luminosity

AGN exhibit an incredibly broad range of bolometric luminosity, from $10^{40} - 10^{47}\text{erg}\,s^{-1}$ (Woo and Urry, 2002). This range is broadly divided into two categories, high luminosity 'QSO' proper ($L > 10^{45}\text{erg}\,s^{-1}$) and Active Galactic Nuclei/Seyfert galaxies ($10^{45} > L > 10^{40}\text{erg}\,s^{-1}$, Laor (2007)). This distinction was originally made on the basis of whether or not the host galaxy was visible. QSOs, typically outshining their host galaxy to the point it could not be seen by ground-based telescopes, were believed to be individual quasi-stellar objects.

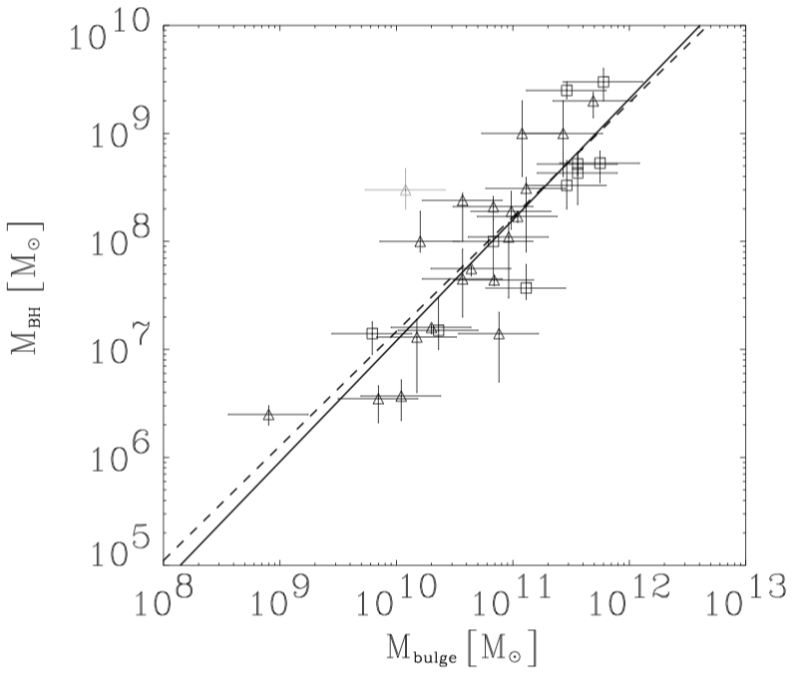

FIGURE 1.1: Plot of the black hole mass M_{BH}-galactic bulge stellar mass M_{bulge} relation from Häring and Rix (2004).

Fusion is incapable of powering an unresolvably small, sub-light-year source with such a high luminosity (Fabian, 1992). Instead, we have to make the assumption that these sources are powered by accretion of material onto a compact, massive source. We can estimate the masses of these objects, originally using the velocity dispersion of stars in the host galaxy bulge (Woo and Urry, 2002), and more recently by using reverberation mapping techniques to analyse the velocity of the orbiting broad emission line gas (see section 1.3.1). Both give central object masses on the order of $10^6 - 10^{10} M_\odot$. When we plot these mass estimates against the total observed stellar mass in the galactic bulge of its host galaxy (M_{bulge}), we see a quite tight correlation as in figure 1.1.

Given these masses and the assumption that AGN are powered by accretion, we can estimate the accretion rate $\dot{M}$ (unit: $M_\odot yr^{-1}$) required to produce this luminosity. This is typically presented in terms of the Eddington Rate. The Eddington rate $\dot{M}_{\rm Edd}$ is the accretion rate at which (for a system approximated as a spherically-symmetric inflow of purely electron-scattering hydrogen) accretion becomes self-limiting as the outward radiation pressure becomes high enough to balance out the gravitational pull of the central source. This results in $\dot{M}/\dot{M}_{\rm Edd}$ typically from $0.01 - 0.1$ but with a small number of super-Eddington sources (Wandel, 1999).

1.1.2 Radio Luminosity

Approximately $\approx 30\%$ of all AGN display radio jets. Unlike the BEL and continuum, jet radio emission is partially resolvable. Whilst there is a large point source associated with the central QSO, radio emission is also distributed across a Mpc scale in either compact 'channels' continuous with the core (FR-I) or extended 'lobes' separated from it (FR-II). This is visibly the consequence of jets heating up the intra- and inter-galactic medium, creating channels and bubbles on Mpc scales. The kinetic energy of the jets can be measured from the X-ray emission of these bubbles, and comes out as approximately $\approx 100\times$ more than the radio emission (Cavagnolo et al., 2010).

1.1.3 UV and Optical Emission Lines

A common feature of AGN spectra are Doppler-broadened emission lines, in two distinct families- broad and narrow lines, attributed to the Broad and Narrow Line Regions respectively (the BLR and NLR).

Spectral emission lines from the light-day scale BLR (known as Broad Emission Lines or BEL) are strongly broadened by Doppler shifts on the order of $10^3 - 10^5 km\ s^{-1}$ (Peterson and Wandel, 1999). The Narrow Emission Lines (NEL) are a distinct population from the broad, with a Doppler broadening of only $10^2 - 10^3 km\ s^{-1}$. The NLR covers a region on the scale of parsecs to kilo-parsecs (Walker, 1968), and has been spatially resolved (Evans et al., 2010; Balmaverde et al., 2016). For both line populations, the Doppler broadening is in many cases attributed to rotational motion as shown in illustrated in figure 1.2 (with a strong outflow component for the NLR).

The strongest BELs are O II, III, IV, C IV, N II and the Balmer and Lyman series (Netzer, 2015) (with C IV and the Balmer series of the most interest for this work). Inspection of the broad spectral lines reveals an absence of forbidden lines with long lives and low critical densities (e.g. $n_e \lessapprox 10^8 cm^{-3}$, Osterbrock (1993)). This indicates that the density and thus collision rate in this region is high enough that such ions, once excited into a state where the transitions required for radiative de-excitation would be forbidden, are collisionally de-excited instead. This stands in contrast to the narrow-line region, where *all* forbidden lines are common. This suggests that NLR densities are lower and thus collision time-scales are longer than the time-scales for forbidden radiative decay. The BLR is shown by simple reverberation mapping studies to lie closer to the AGN centre than the NLR. Within the BLR itself, more strongly ionised species can be found closer to the AGN core. This is shown by higher line widths from Doppler broadening at higher velocities, and shorter time lags to changing central engine luminosities (Peterson et al., 2004).

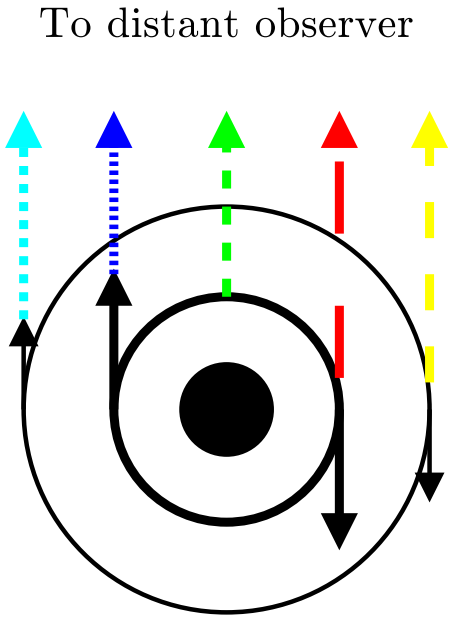

FIGURE 1.2: Top-down diagram of Doppler broadening in BLR and NLR regions ('inner' and 'outer' rings). Solid black lines indicate disk velocity, dashed arrows indicate photons, with colour and dash length indicating frequency.

Broad and narrow lines are not universal. A subset of AGN classified as Type 1 show both broad and narrow lines, but others, classified as Type 2, show only narrow lines. Various subcategories of these exist, denoting differences in strength between the broad and narrow emission lines, and whether a given subset of lines are visible as broad only, narrow only, or a superposition of two distinct lines (e.g. Type 1.8-1.9 are those AGN exhibiting only a few broad Balmer lines superposed over narrow ones (Osterbrock, 1993)). These categories are also not hard and fast, as 'changing-look' AGN have been observed to transition between them on the timescale of $\approx$ 8 years (LaMassa et al., 2015). Further, some AGN that appear to be Type 2 are, in fact, *hidden Type 1*s. By observing scattered photons from a hidden Type 1 in polarised light, AGN that appear to only have NEL reveal a BLR that is not directly visible, but from which photons may be scattered into a non-obscured sight-line (Antonucci and Miller, 1985). In addition, whilst broad lines are generally not visible in blazars, a small fraction of them have visible BEL (Shaw et al., 2012). This suggests some or all of the others may have BEL obscured by the jet emission.

1.1.4 UV and Optical Absorption Lines

Around 43% of AGN exhibit broad or narrow absorption lines (Dai et al., 2008; Misawa et al., 2007). These are the absorption profiles of a single atomic absorption/emission line, spread out over a broad range of velocity space. The broad lines are blue-shifted up to a velocity of a few $10^4 km\ s^{-1}$ (Krongold et al., 2017), whilst the narrow are at speeds on the order of $10^3 km\ s^{-1}$. Both indicate outflows towards the observer, and their line

profiles are spread out in a 'P Cygni profile'. This is associated with a species with a strong resonance line in an accelerating medium; as the material is accelerated, the absorption frequency is gradually shifted to shorter wavelengths. Unlike with emission lines, both broad *and* narrow absorption lines share the same species, suggesting they originate in roughly similar parts of the AGN environment (Krongold et al., 2017). NAL can be harder to categorise as part of the AGN, however, as there can be ambiguity between the intrinsic absorption associated with the AGN environment and absorption from gas between the AGN and observer.

Interestingly, whilst NAL are universal and seen in all QSO, BAL are hardly ever seen in Seyferts, with few exceptions (Leighly et al., 2015; Kaastra et al., 2014).

1.1.5 UV/Optical 'Blue Bump'

The optical & UV spectra of both lower-luminosity Seyferts and high-luminosity QSOs are broadly similar, with a large low-frequency bump, but Type 1 AGN only exhibit a 'big blue bump' (Prieto, 2012). This is a major contribution to the total luminosity; accounting for up to 40% of the bolometric luminosity (Richards et al., 2006).

1.1.6 X-Ray Luminosity

AGN are some of the most luminous X-ray sources in the sky. Up to 40% of their luminosity can be in the form of X-rays (Ward et al., 1987). Comparison of slopes in plots of energy distribution per frequency show there must be different components responsible for the 'big blue bump' UV/Optical emission and the X-ray emission (Elvis et al., 1994).

Type 2 AGN (i.e. Seyfert 2s and Type 2 QSOs) are typically much weaker X-ray sources than Type 1; with a much reduced soft X-ray component, their spectra skew harder (Antonucci, 1993). This suggests a potentially substantial absorption of the soft X-ray component in Type 2 QSOs.

The X-ray spectra of AGN also differ based on the presence or absence of radio emission. AGN with no radio emission/jet tend to exhibit harder spectra, whilst those *with* radio jets tend to emit softer X-ray spectra. This holds independently of the Type classification of the AGN (Maccarone et al., 2003). Radio-loud QSO spectra display two components, one synchrotron emission in the UV & visible, one X-/γ-ray. Both display clear evidence of emission from an unresolvably small location though on the order of parsecs, rather than light-days or months (Lister et al., 2009)) being relativistically beamed towards the observer. The particles in these jets are accelerated up to 99.9% of the speed of light, resulting in apparent speeds far in excess of c.

In addition to X-ray emission, AGN exhibit a range of *absorption* behaviours. For Type 1 Seyferts, over 60% have so-called 'warm absorbers'. They show absorption lines corresponding to multiple high-ionisation species (e.g. Fe L lines), with blueshifts corresponding to outflow in on the order of $10^2 - 10^3 km\,s^{-1}$, distributed across $pc - kpc$ (Tombesi et al., 2013). *Ultra-fast* outflows (UFOs) are also observed, high-ionisation x-ray absorbers (typically detected via Fe K lines) with mildly relativistic outflows of $10^3 - 10^5 km\,s^{-1}$ (Tombesi et al., 2010). Interestingly, these UFOs are determined to be located at substantially sub-pc scale from the central object ($\approx 0.0003 - 0.03pc$, Tombesi et al. (2012)).

1.1.7 Variability

The continuua of AGN vary at a very broad range of timescales, and with dramatic amplitudes, from radio to x-ray (Krolik et al., 1991). The behaviour of this variation differs between bands. The rate of fluctuation shows a power-law dependence on the frequency of the radiation, $\propto f^{-\alpha}$, for $\alpha \approx 1 - 2.5$ (Green et al., 1993; Hayashida et al., 1998). This is to say, shorter wavelengths fluctuate at much faster frequencies, with longer wavelengths changing more slowly. At longer wavelengths, the variations also have a much lower amplitude of variation, as can be seen in Figure 1.3. X-rays can fluctuate by orders of magnitude over the span of hours to days, whilst the optical varies over days to months. Fluctuations in the X-ray can be seen to propagate out to longer wavelengths, and are slowly smoothed out over hours in the X-ray (Ulrich et al., 1997) to weeks or months in the optical (Fausnaugh et al., 2016). Again, the lag is proportional to wavelength; long wavelengths have a longer lag to the X-ray.

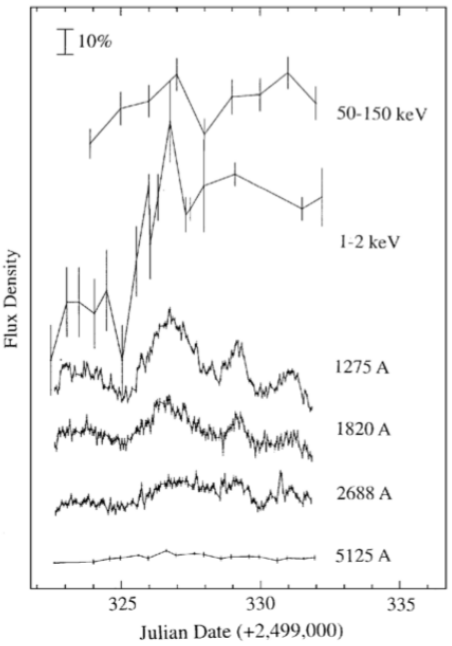

FIGURE 1.3: Continuum light curves of NGC4151 from Ulrich et al. (1997).

1.2 Unification

At first glance, the variety of observations of AGN raise the prospect of an entire zoo of very dissimilar objects existing at the cores of active galaxies; all extremely energetic but too compact to observe. Multiple models have been proposed to unite them into a single class of object, either by evolution (Franceschini et al., 2002), or via orientation (Urry and Padovani, 1995). Both involve (as with most astrophysical compact objects (Cordova and Mason (1982), Lada (1985)) a central object surrounded by a rotating accretion disk of inflowing matter, heated by viscosity, with a high-energy 'corona' around the central object. For AGN, one model is a hot electron corona that up-scatters disk emission into the X-ray (Sunyaev and Truemper (1979)). In the orientation model, an obscuring torus of dust is added to explain the absence of BEL at viewing angles close to the disk (Urry and Padovani, 1995). Some developments of the orientation model add outflowing winds driven off the disk surface (by radiative or magnetic pressure) to explain the presence or absence of emission lines and absorption features (Weymann et al., 1991; Shlosman and Vitello, 1993; Elvis, 2000). An illustration of this can be seen in Figure 1.4, with a diagram in Figure 1.5. Sight-lines to the inner region can be blocked by the torus, resulting in an object with no visible BLR, whilst the NLR high above the disk remains un-obscured (e.g. from angles $70 - 90°$ in the diagram). Meanwhile, sight-lines through the outflowing winds see BAL features. Sight-lines *under* the wind, but above the torus, see NAL features as the observer-projected velocity is much lower. This is particularly the case in models like Elvis (2000) which propose a 'kink' in the wind, where it raises up off the accretion disk vertically before being driven outwards by radiation pressure. This is usually justified by the presence of a 'failed wind' (discussed further in 1.2.2). Even more recent unified models propose the BLR as 'clouds' condensing within a warm outflow and falling back onto the disk (Elvis, 2017). In our work, we have used a modified version of the Shlosman and Vitello (1993) biconical disk wind originally described by Matthews et al. (2016) and outlined in section 2.3. Theories have also been developed to unify radio-quiet and -loud AGN. Models like Yuan et al. (2002) propose that jet emission is a phase triggered by changes in accretion behaviour. They propose the AGN switches from radiatively efficient accretion, where most surplus momentum is transported away via disk emission, to radiatively *inefficient* where the jet fulfils this role (Sbarrato et al., 2014). With these two variables, more or less all the quasar behaviours observed in table 1.1 can be produced (even if the specifics of some factors e.g. the x-ray corona are not nailed down).

1.2.1 Accretion disks

Accretion disks are a common feature amongst astrophysical compact objects like Cataclysmic Variables (Noebauer et al., 2010) and Young Stellar Objects (Sim et al., 2005).

FIGURE 1.4: Artist's impression of a dust-bound AGN. (Pavodani (2004)).

Compact object systems consist of a heavy central object that draws gas and dust towards it gravitationally. As the material is drawn in, conservation of angular momentum forces it to spin in the central object's plane of rotation. As the material descends into the gravitational well it converts potential energy into kinetic energy. For a particularly steep potential well like that of an AGN with a mass on the order of $10^6 - 10^8 M_\odot$, the energy released is on the order of $\approx 10\%$ of the rest mass of the inflow. This is substantially more than the $\approx 0.7\%$ energy-per-rest-mass released from nuclear fusion of even the lightest hydrogen nuclei Peterson (1997). This huge energy release heats the accretion disk (via viscous heating in collisions) to temperatures of up to $10^4 - 10^5 K$ (Bonning et al., 2007), resulting in a huge amount of energy being re-radiated in a black-body spectrum. This results in the accretion disk being the main component responsible for generating the incredible luminosities of AGN.

A major parameter determining disk behaviour is the *Eddington ratio*. The Eddington ratio is defined in terms of the emission luminosity L and the *Eddington luminosity* L_{Edd}. As accretion results in the emission of radiation, eventually the radiation pressure resulting from this emission reaches the point where it drives back any further inflow. The Eddington luminosity L_{Edd} is the luminosity limit where the outward force of radiation pressure balances the inward pull of gravity. This is not a trivial quantity to calculate,

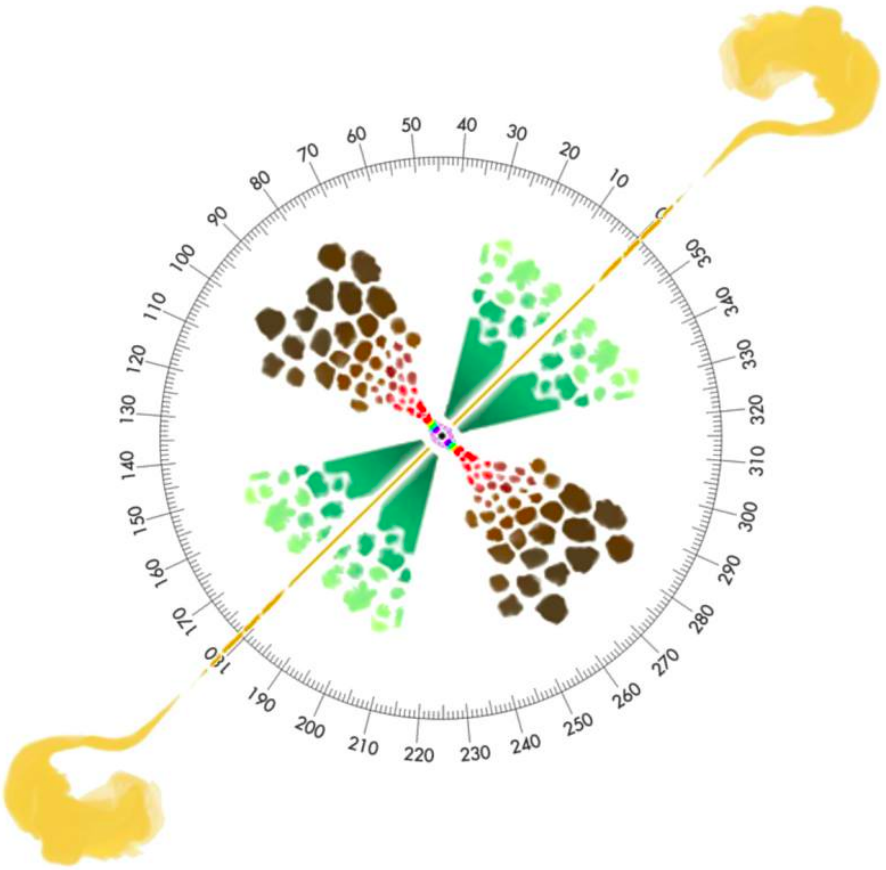

FIGURE 1.5: Diagram of a unified AGN. Axial radio jets in **yellow**, x-ray corona in **purple**, outflowing winds in **green**, accretion disk in **red**, dusty torus in **brown** (Marin (2016)).

as the radiation pressure the inflowing material experiences depends on the absorption and scattering cross-sections of the material, and the spectral energy distribution of the source. We tend to approximate the Eddington limit for a black hole of mass M_{BH} with a spherically-symmetric inflow, accounting purely for electron scattering on hydrogen (with Thompson cross-section σ_e, and proton mass m_p), as equation 1.1:

$$L_{\mathrm{Edd}} = \frac{4\pi G M_{BH} m_p c}{\sigma_e} \tag{1.1}$$

From this, we can derive the Eddington accretion rate $\dot{M}_{Edd}$. Given an energy conversion efficiency of η, the luminosity released by an inflow is $L = \eta \dot{M} c^2$, giving an Eddington accretion rate as equation 1.2.

$$\dot{M}_{Edd} = \frac{L_{Edd}}{\eta c^2} \tag{1.2}$$

The Eddington *ratio* for a given AGN is then $\dot{M}/\dot{M}_{Edd}$. The ratio is thought to be one of the key determiners of whether an AGN emits a radio-loud jet or not (Padovani et al., 2017). There are two main accretion modes proposed; thin-disk or radiatively efficient, and advection-dominated or radiatively inefficient. In a high Eddington ratio system, inflowing material will be shaped into a comparatively thin disk by the radiation pressure- minimising the disk angle and thus the surface area exposed to radiation pressure (Shakura and Sunyaev, 1973). In systems where radiation pressure is not dominant (those with lower Eddington ratios) then we expect to see advection-dominated accretion flow (ADAF) (Narayan et al., 1995, 1998). In these systems, the in-falling material is less dense and unable to effectively cool itself (via collisional excitation and radiative de-excitation), resulting in much lower disk emission. Instead, the faster, more turbulent flow draws most of the released energy into the SMBH itself whilst accelerating a small fraction into a jet via a magnetic shock region.

1.2.2 Disk winds

Within the broad line region of the AGN evidence can be seen for mass outflows from the disk in the form of asymmetrical Doppler broadening (Denney et al., 2009). This effect arises from emission from fast outflowing media being preferentially observed- media flowing away from the observer would be partially obscured by the central engine and the bulk of the wind itself. In addition, the high cross-sections for resonance interactions mean that photons will preferentially escape the wind with or against the gradient of acceleration; where the line has become blue/red-shifted to energies that no longer coincide with the photon, and thus reduce its resonance scattering cross-section.

The most obvious evidence for an outflowing disk wind is seen in broad absorption line QSOs (Begelman et al., 1991), though it is not yet clear whether the broad line region is co-spatial with the wind- some models propose instead a series of orbiting clouds (Gaskell, 2009). These conclusions are drawn from a combination of factors including emission lines and calculated covering factors. They suggesting that rather than all gas being exposed to the same ionising radiation field (and ending up in the same ionisation state), some degree of shielding is in play, softening the radiation spectrum the BLR gas is exposed to. In the cloud-based model, the front of the cloud shields the back of each cloud, softening the spectrum it is exposed to. As a result, emission lines characteristic of a range of ionisation configurations appear.

However, this model does not describe all observed behaviour. It requires much higher covering factors (the proportion of the central source obscured behind the BLR-producing clouds) to produce the observed levels of resonant scatter than were supported by the levels of continuum absorption of central source radiation seen in the spectra. In addition, reverberation mapping studies indicate a strong dependence of ionisation state on distance from the source, as measured by time lag and Doppler broadening effects.

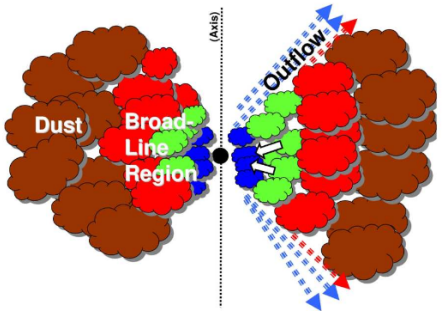

FIGURE 1.6: Diagram of flattened cloudy model of BLR, reproduced from Gaskell (2009)

Alternative models have been developed that describe flatter, denser winds closer to the disk plane with lower covering factors, allowing for the central engine to be observed through the 'hole' in the wind (as in figure 1.6). In these models, the flat, dense wind is self-shielding much like the clouds of older models, as any sight-line to the back of the wind will pass through the front, resulting in a softened spectrum.

These models attribute this behaviour to a 'failed wind', driven off the surface of the disk by radiation pressure from the emitting warm gas and dust. The wind is then slowed at higher inclinations from the central engine by over-ionisation, with radiation pressure from the central engine pushing the wind outwards, or momentum transfer via line scattering. (Proga et al., 2000). Over-ionisation can reduce momentum transfer from the AGN radiation to the wind by destroying species with resonance lines with very high scattering cross-sections. Other models use magneto-hydrodynamic forces to drive the flow of winds into this flattened, conical shape (Fukumura et al., 2010). The internal structures of the wind vary from smooth to clumpy, though computational complexity can limit attempts to model non-continuous wind structures. Large-scale failed winds have recently been observed (Reeves et al., 2017).

1.2.3 Dusty torus

The edges of AGN are believed to be surrounded by a cold, thick low-ionisation dusty torus with an inner edge on a roughly light-year scale (Pozo Nuñez et al., 2015). The torus absorbs and reprocesses higher energy UV and visible photons from emission lines (as well as X-rays from the central engine) into infra-red radiation. Unification schemes like Urry and Padovani (1995) propose the existence of the torus as a way to unify Seyfert-I and Seyfert-IIs into a single object, as well as to unify Quasi-Stellar Objects (QSOs) and the Seyfert-II analogous Quasar-2s. Seyfert-Is and QSOs exhibit both broad and narrow emission lines, whilst Seyfert-IIs and Quasar-2s only exhibit narrow lines. The expectation is that the BLR, closer to the central engine, is more easily obscured by the dusty torus and the NLR-only AGN observations correspond to sight-lines at a low angle to the accretion disk plane as shown in figure 1.5.

1.2.4 Feedback

A crucial reason for understanding the structure and dynamics of AGN environments is the key role they are assumed to play in the evolution of their host galaxies. When the mass of a SMBH (M_{BH}, often determined using 1-d reverberation mapping as detailed in section 1.3.1) is plotted against the total observed stellar mass in the galactic bulge of its host galaxy (M_{bulge}), we see a quite tight correlation as previously discussed in section 1.1.1. A correlation between stellar mass and black hole mass would be expected on some level; a galaxy with little gas would both be be unable to form large numbers of stars, and to grow large central SMBH. The lack of galaxies off of the line suggest, though, that an AGN cannot 'over-eat' and starve the galaxy of gas for star formation, nor can a high rate of star formation use up the galaxy's gas supplies before they reach the central SMBH.

It is unlikely that this feedback mechanism is purely gravitational; the mass of a SMBH is typically on the order of 10^3 lower than the disk bulge, and its gravitational field only dominates over that of the bulge over very short distances- certainly not on the scale of the entire galaxy. Any feedback must therefore arise during the phases when a SMBH is actively accreting gas, and forms an AGN. There are several proposed mechanisms by which an AGN affects star formation in its host galaxy, both promoting and suppressing it (Begelman, 2004). Of particular interest to us are AGN winds (as mentioned in section 1.2.2). Thanks to the high scattering cross sections of the their emission lines, a line-driven wind can efficiently convert radiated energy from the AGN corona and accretion disk into kinetic energy. These high-velocity winds can then potentially 'sweep' out gas supplies from the galaxy (Cielo et al., 2018). The jets of AGN are also hypothesised to be major sources of feedback to their host galaxies. The polar jets of an AGN rapidly heat and transfer a huge amount of outward momentum to any material in their way. This is most obvious in the large 'bubbles' on the scale of 10s of kpc to Mpc, carved out in the intergalactic medium; the 'lobes' of radio galaxies as mentioned in section 1.1.2. The rapid heating process results in sudden pressure changes that generate shock fronts perpendicular to the jet axis. The heating of intra-galactic gas would be expected to reduce star formation rates, as the higher internal kinetic energies of the gas have to be overcome during the process of gravitational collapse. Conversely, jet shocks and outflows are *also* expected to promote star formation, by compressing molecular clouds, enhancing their density and promoting star formation (Silk, 2013), and there is evidence for AGN outflows at the very least failing to *reduce* star formation (Woo et al., 2017).

Current galaxy evolution models require AGN feedback in order to reproduce the features of our observable universe (Bower et al., 2006; Croton et al., 2006). As a result, it is important that we understand the kinematics and structure of these potential outflows.

1.3 Reverberation mapping

In AGN, as the ionising continuum varies, so do the broad emission lines. This variation tracks the driving continuum, but lags behind by a time delay. Different lines respond to changes in the driving continuum with time delays on the order of days to months, as illustrated in figure 1.7 (Kaspi et al., 2005, 2007).

In the context of the accretion disk wind model described in section 1.2, this behaviour is ascribed to radiation from the central engine (i.e. X-rays from the central corona and UV photons from the inner disk) striking the outflow and contributing to the thermal, ionisation and excitation equilibrium at any given point within the outflow. This equilibrium establishes the rates at which radiative, as well as collisional, ionisations, recombinations, excitations and de-excitations occur. Line photons, in particular, are produced when electrons in excited states decay to a lower energy levels. The relevant excited states can be populated by collisional processes, radiative processes, and/or recombination cascades. The specific frequencies at which line photons are produced depend on the populations in each of the ionisation and excitation levels associated with each atomic species.

The time-scale on which ionisation and recombination processes equilibrate the wind ionisation state with the radiation field is fast, $\approx$ 0.5 minutes to 0.5 hours for typical BLR electron number densities of $10^9 - 10^{11} m^{-3}$ (Blandford et al., 2013).

As a result, both resonance line photons arriving at an observer at time t are associated with the ionisation state of the outflow that was set by photons emitted by the central engine at time $t - \tau(\underline{\mathbf{x}})$. Here, $\tau(\underline{\mathbf{x}})$ is the additional time required for photons to travel to the observer via the line-forming region at position $\underline{\mathbf{x}}$ in the wind. In this context, the line-forming region could be the disk, the disk wind or a gas cloud, as discussed in Section 1.2.2. An example of the path differences and thus travel time differences that arise from this can be seen in Figure 1.8. As the scale of accretion disk winds is on the order of light-days to months – orders of magnitude larger than the reprocessing and wind equilibration time-scales – $\tau(\underline{\mathbf{x}})$ can be taken to be *solely* a function of position (Peterson and Horne, 2004). The same is true of collisionally-excited, radiatively de-excited photons; collisionally-excited lines only emit when their de-excitation timescale is lower than the average collisional timescale, suppressing collisional de-excitation. This guarantees that collisionally-excited lines respond *faster* than the timescale for the wind to equilibriate.

In practice, applying these assumptions also requires that the dynamical timescale of the wind ($\tau_{dyn} = \frac{r}{\Delta V}$) is substantially longer than the total observation period, in order to ensure that there are no significant changes in the physical structure of the wind itself.

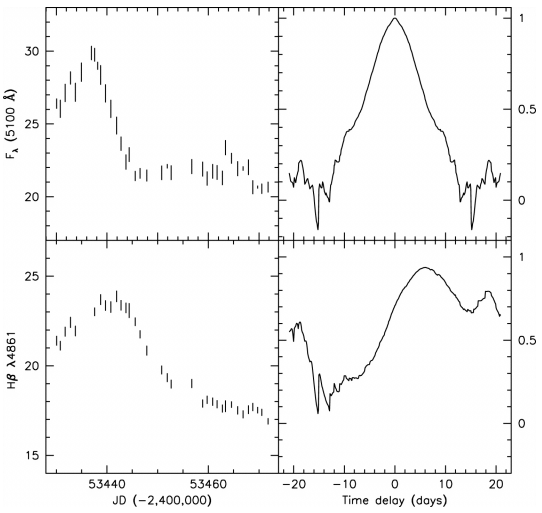

FIGURE 1.7: Light-curves for Hβ emission line (bottom left) and nearby continuum (top left), plus Hβ cross-correlation function (bottom right) and continuum auto-correlation function (top right) reproduced from Bentz et al. (2006). Hβ response peaks $\approx$ 8 days after the continuum peaks.

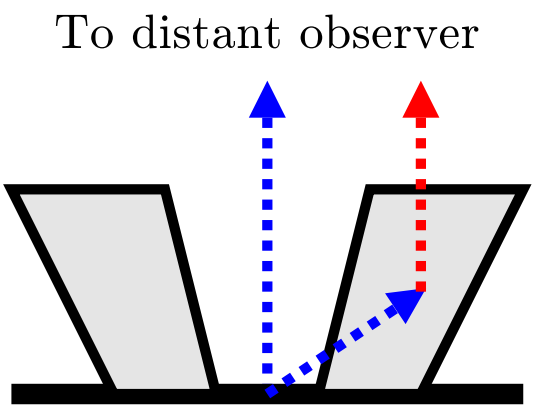

FIGURE 1.8: Diagram of a typical path difference for continuum vs line photons. Black line represents accretion disk, grey regions are the disk wind. **Blue** arrows represent continuum photons from the central source, **red** arrow represents photons emitted, scattered or reprocessed by the disk wind.

The assumption that the recombination timescale is short (relative to the light travel time scale) only hold for attempts to model the broad line region near the central engine. It does not hold for the narrow line region, which has a lower electron density n_e ($10^1 - 10^3 cm^{-3}$, as opposed to $10^{10} cm^{-3}$ in the BLR (Xu et al., 2007)) and thus a much longer recombination time, since $\tau_r \propto n_e^{-1}$.

For an AGN with constant luminosity, there would be no way to determine a time delay. Fortunately, AGN of all types fluctuate in luminosity (Ulrich et al., 1997). The light curves of the ionising luminosity and the emission line luminosity can therefore be compared to estimate a time delay. Note that extremely fast variations in the ionising luminosity, on time-scales shorter than the recombination or reprocessing time-scales in the BLR, cannot be used to estimate delays, since they are smeared out in the emission line light curve. However, most AGN exhibit significant variation in the x-ray range on the order of hours to weeks (Mushotzky et al., 1993), so this is not a major concern. That is, in practice, the BLR is able to adjust its temperature and ionisation state, and reprocess the incoming radiation, more rapidly than the time-scale on which the luminosity changes.

The most important emission lines used in reverberation mapping are recombination lines and collisionally excited resonance lines. The Balmer lines are examples of the former; they are formed as part of the recombination cascade that is associated with the capture of free electrons into excited levels of Hydrogen. Examples of the latter include the classic UV resonance lines, such as N V 1240Å, C IV 1550Å and Si IV 1400Å.

Resonance lines are associated with permitted transitions that connect the ground state of an ion to the next lowest energy level. Such transitions are very strongly radiatively coupled, so any collisional or radiative excitation is followed almost immediately by a radiative de-excitation.

In the context of reverberation mapping, it is generally assumed that the observed resonance emission lines are mainly produced via collisional excitation. *Scattering* – i.e. the absorption and immediate re-emission of a photon in the transition (radiative excitation followed by radiative de-excitation) – can also be important in AGN. For example, the broad absorption features seen in the UV resonance for sight-lines looking into the wind are due to continuum photons from the central engine that happen to be at the right frequency being (approximately) isotropically scattered out of the line of sight. In principle, scattering *into* the line of sight can also produce emission features. However, scattering alone cannot produce any *net* line emission after averaging over all viewing angles. Given that strong, broad emission lines associated with the UV resonance transitions are seen in essentially *all* AGN, these lines are much more likely to be produced thermally, i.e. via collisional excitation. This is fairly natural given physical conditions in the BLR, including in our wind models.

Both resonance and recombination lines are Doppler broadened by the velocity field associated with the accretion disk and the disk wind. Also, both types of lines are driven by the ionising continuum, which sets the thermal and ionisation state of the line-forming region. To first order, the luminosity seen in a given line, $L_{\rm line}$, at a given time, t, can therefore be related to the total continuum luminosity, $L_{\rm cont}$, by allowing for the delay τ, i.e.

$$L_{\rm line}(t) \propto L_{\rm cont}(t-\tau). \tag{1.3}$$

Given a lag of τ_{BLR} between a line and the driving continuum, it is possible to define a characteristic radius of emission for that line as

$$r_{BLR} = \tau_{BLR}/c. \tag{1.4}$$

By using data sets covering a broad wavelength range, time delays can be determined independently for each emission line. These provide insight into the the spatial distribution of the elements (and ionisation states) associated with the relevant transitions. The results show that BLR is stratified, with emission from high-ionisation states occurring preferentially at small radii, while that from low-ionisation states occurs mainly at larger ones (Peterson, 2001; Bentz et al., 2010b).

1.3.1 Mass estimates

Historically, one of the *main* uses of reverberation mapping has been to estimate AGN masses using emission lines (Bentz and Katz, 2015). Assuming the BLR is "virialised" – i.e. that its dynamics are dominated by the gravitational field of the black hole – the velocity width of the Doppler-broadened line profiles, v_{BLR}, can be related to a characteristic distance from the black hole, r_{BLR}, via

$$v_{BLR} = f\sqrt{\frac{GM}{r_{BLR}}}. \tag{1.5}$$

Here, f is a "fudge factor" that accounts for the actual geometry and kinematics of the BLR, as well as our viewing angle. By combining the measured velocity width of an emission line, v_{BLR}, with a lag-based estimate of the radius at which it is produced, $r_{BLR} = \tau_{BLR}/c$, it is therefore possible to determine the mass of the super-massive black hole in an AGN as

$$M_{BH} = f v_{BLR}^2/G. \tag{1.6}$$

As noted above, the constant of proportionality f would be expected to depend on the BLR geometry and kinematics, and also the observer inclination. Empirically, an ensemble average of $\langle f \rangle = 4.47 \pm 1.25$ has been determined for AGN by comparison to other methods of black-hole mass estimation (Grier et al., 2013a). With this range of f values, reverberation-based black hole masses are consistent with those produced by other methods (Wandel et al., 1999; Denney et al., 2010).

1.3.2 One-dimensional reverberation mapping

Reverberation mass estimates are formally based on the assumption that a given lag corresponds uniquely to a given radius of emission. This is not strictly the case, as emission at a single radius will be spread out across a range of times by the geometry of the emitting region and the angle to the observer. Positions of equal distance to the observer form isodelay surfaces (figure 1.9). As a result, for most geometries, emission in given line occurs across a range of delays; the paraboloid isodelay surfaces do not coincide with the distribution of ionisation states within the wind. As can be seen in figure 1.10, two locations with very different radii (and thus very different exposure to the ionising continuum and thus ionisation states and emission levels) occur on a single isodelay surface.

In practice, the reverberation-based mass estimation technique probably works better than might be expected from these considerations. Any given emission line actually

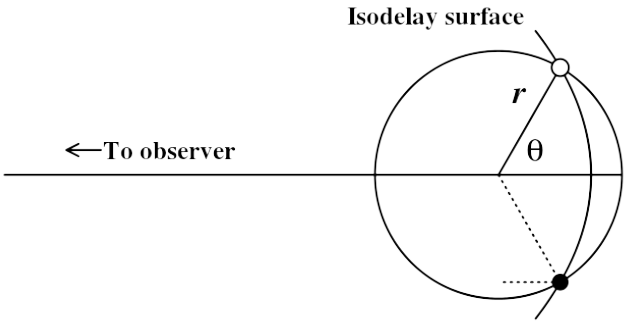

FIGURE 1.9: Diagram of isodelay curve reproduced from Peterson and Horne (2004). Circle represents thin shell, arc indicates points of where locally emitted photons (and scattered continuum photons) arrive at the observer with the same delay to the continuum fluctuations. Small circles indicate where isodelay curve intersects thin shell.

responds with a *range* of lags that reflect the distribution of line-forming material within the BLR. Except for pathological cases, the *mean* lag will be a reasonable measure of the characteristic distance of the line-forming region from the central engine.

A more accurate – but still linear – approximation for the dependence of line luminosity, $L_{\rm line}$, on continuum luminosity, $L_{\rm cont}$, can be obtained by explicitly allowing the line to respond with a range of lags,

$$L_{\rm line}(t) = \int_{-\infty}^{\infty} L_{\rm cont}(t-\tau)\Psi(\tau)d\tau. \tag{1.7}$$

Here, the *transfer function* Ψ describes how, for a given geometry, continuum photons produced at times $t-\tau$ are reprocessed into the line emission observed at time t. This requires the assumption that Ψ does *not* itself depend on $L_{\rm cont}$, which is only likely to be true in the limit of small variations in $L_{\rm cont}$.

The transfer function Ψ depends on the geometry of the emitting region and the angle of the system to the observer. It can therefore be used to probe the geometry of the AGN environment by substituting time resolution for spatial resolution. In theory, given a line luminosity, $L_{\rm line}(t)$, and the driving continuum that produced it, $L_{\rm cont}(t)$, one can attempt to reconstruct the transfer function of the AGN geometry that produced it. In practise, however, $L_{\rm line}$ is not a function *solely* of the observed driving continuum and so equation 1.7 does not accurately describe the relationship. Instead, we can linearise the equation for small changes in the line and continuum around their mean values to get the *response function* Ψ_R as

$$L_{\rm line}(t) = \bar{L}_{\rm line} + \int_{-\infty}^{\infty} (L_{\rm cont}(t-\tau) - \bar{L}_{\rm cont})\Psi_R(\tau)d\tau, \tag{1.8}$$

and therefore

$$\Delta L_{\rm line}(t) = \int_{-\infty}^{\infty} \Delta L_{\rm cont}(t-\tau)\Psi_R(\tau)d\tau. \tag{1.9}$$

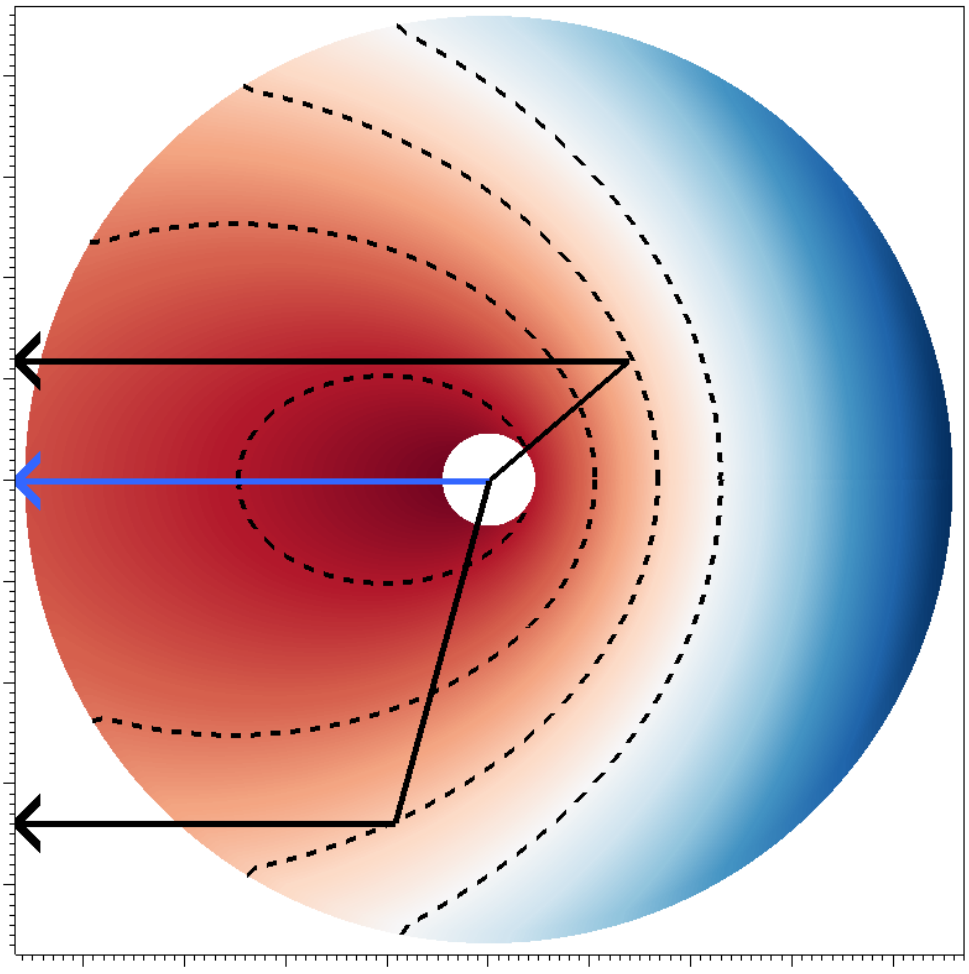

FIGURE 1.10: Expanded version of figure 1.10 for multiple isodelay contours (dotted lines) in spherical wind. Colour indicates delay relative to continuum photons (**red** = short, **blue** = long). Blue arrow shows direct path to observer, black arrows show two photon trajectories resulting in equivalent delay. Produced using Visit (Childs et al. (2012)).

In the limit that $L_{\rm line}(t) \propto L_{\rm cont}(t-\tau)\Psi$, the transfer and response functions are equivalent. Whilst more practical, reconstructing Ψ_R from equation 1.9 is still an inverse problem and can be challenging. In particular, many degenerate solutions may exist for a single set of light curves Reynolds et al. (1999).

1.3.3 Velocity-resolved reverberation mapping

It is possible to distinguish between models giving rise to identical one-dimensional transfer functions by taking into account the varying velocities of the emitting material at different points within the BLR. This gives rise to broadening and frequency shifts

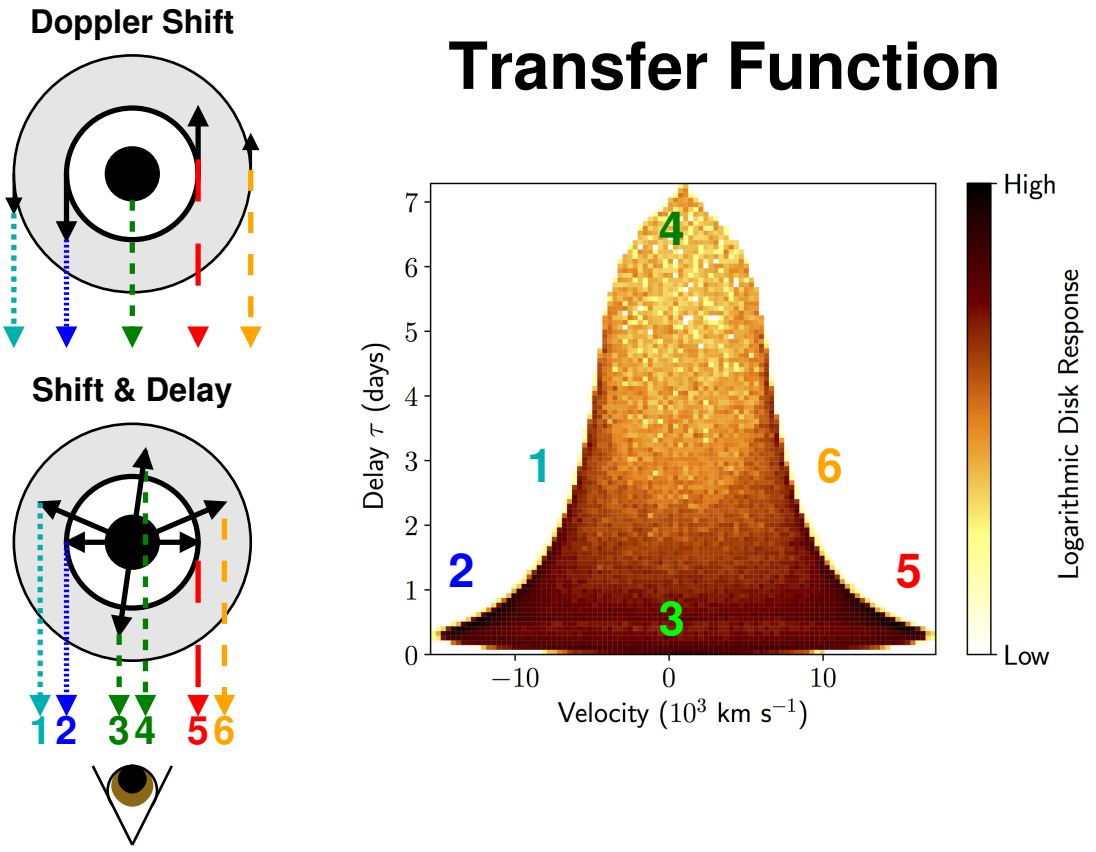

FIGURE 1.11: Velocity-resolved transfer function for rotating disk as Welsh and Horne (1991) viewed at 30°. Includes all photons that have resonantly scattered a single time off the $C-IV$ line, with the luminosity contribution from each photon re-weighted using its last scattering location to match the luminosity contribution per disk annulus to the $r^{-3/2}$ profile from the paper. *Bottom left:* Black lines indicate photons from the central source, dotted lines indicate photons reprocessed by the disk. *Right:* Numbers from reprocessed photons correspond to locations on the transfer function.

in the emitted line, which allows for the construction of a two-dimensional, velocity-resolved response function that converts continuum luminosity $L_{\rm cont}(t)$ into line luminosity $L_{\rm line}(v,t)$ as

$$\Delta L_{\rm line}(v,t) = \int_{-\infty}^{\infty} \Delta L_{\rm cont}(t-\tau)\Psi(v,\tau)d\tau. \tag{1.10}$$

An annotated simulated example for a rotating Keplerian disk can be seen in figure 1.11.

In addition to the symmetrical Doppler broadening resulting from rotation, emission lines can also be asymmetrically broadened by inflow and outflow kinematics. Gas flowing towards the observer blueshifts photons that are emitted or reprocessed there to an extent based on its velocity. Reverberation mapping can distinguish between all three scenarios (Denney et al., 2009), and between different wind structures and angles of incidence.

A clear illustration of the differences between inflow, outflow and Keplerian rotation can be seen in figure 1.12. In an outflowing system, redshifted photons for a given line can only be produced by material outflowing *away* from the observer; therefore, they come from material on the far side of the AGN from the observer, and arrive with long delays. Blueshifted photons can only be produced by material outflowing *towards* the observer; therefore, they come from material on the near side of the AGN, and arrive with short delays. The inverse is true for inflowing systems. This gives characteristic *blue-leads-red* signatures for **outflow**, and *red-leads-blue* signatures for **inflow**. Systems with a rotating Keplerian disk with an inner and outer radius exhibit 'oval' disk edge signatures, with the outer envelope describing the Keplerian velocity profile for the system and thus providing an estimate of the central object mass as in section 1.3.1.

It is worth noting, however, that the previous figures assume that the BLR geometry, kinematics and response are comparatively simple, consisting of single simple components (a disk, a shell) described by simple one-dimensional velocity laws. In addition, the transfer functions describe only the response to the driving continuum at a single time-delay at each point. They neglect intra-BLR interactions, where the continuum at time t sets the ionisation state of the wind at $t + \tau_1$, which then self-irradiates and influences its own ionisation state and emission. These artificially simplified transfer functions make it very easy to distinguish between signatures. Even adding a second velocity component to a simple rotating Keplerian disk model results in a substantial change to the transfer function behaviour as figure 1.13.

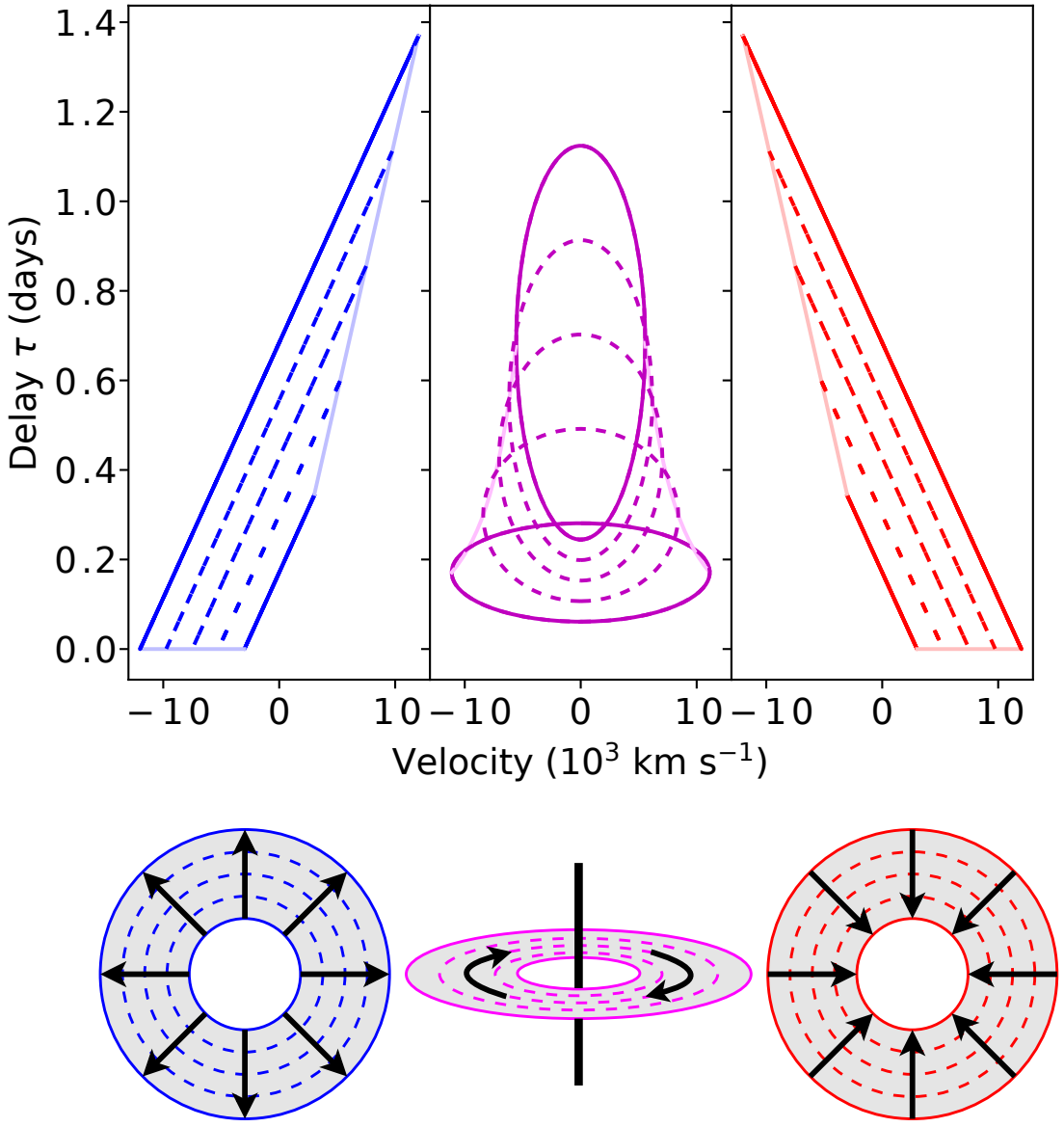

FIGURE 1.12: Outline response functions and schematics for Hubble-type spherical outflow **(left)**, a rotating Keplerian disc viewed at a 20° angle **(centre)**, and Hubble-type spherical inflow **(right)**. Winds extend from $r_{\rm min} = 20r_g$ to $r_{\rm max} = 200r_g$ for an AGN of mass $10^7 M_\odot$. Hubble out/inflows have $V(r_{\rm min}) = \pm 3 \times 10^3$ km s^{-1}. Solid lines denote the response from the inner and outer edges of the winds, dotted lines from evenly-spaced shells within the wind. Pale lines describe the edge of the velocity-delay shape of the response function.

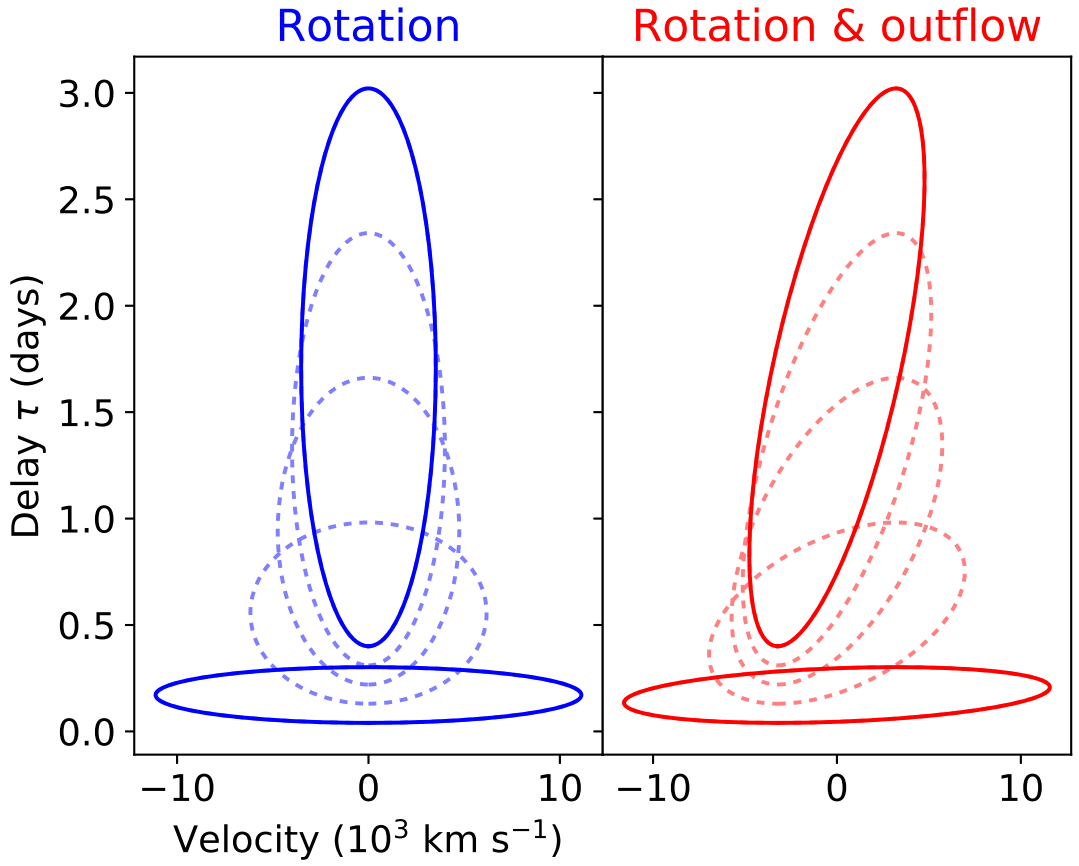

FIGURE 1.13: Simple transfer functions for a rotating Keplerian disk *(left)* and a disk with rotation and outflow *(right.* Solid lines indicate disk inner and outer radii, dotted lines indicate emission from equidistant radii.

1.3.4 Previous models

The transfer function Ψ was first modelled for AGN in Blandford and McKee (1982). As $\Psi(v,t)$ can be expressed as a convolution of the continuum and line light curves, they attempted to recover it via the Fourier transform, $\tilde{L}_{\rm line}$, of the line luminosity light curve, $L_{\rm line}$, i.e.

$$\tilde{L}_{\rm line}(v,\omega) = \int_{-\infty}^{\infty} e^{i\omega t} L_{\rm line}(v,t) dt. \tag{1.11}$$

The multiplication of this by the Fourier transform of the continuum light curve, $\tilde{L}_{\rm cont}$, is equivalent to the Fourier transform of the convolution of $L_{\rm line}$ and $L_{\rm cont}$ (i.e. $\mathcal{F}(L_{\rm line}) \times \mathcal{F}(L_{\rm cont}) = \mathcal{F}(L_{\rm line} \times L_{\rm cont})$). Thus the transfer function can be expressed as

$$\Psi(v,t) = \frac{1}{2\pi} \int_{-\infty}^{\infty} e^{-i\omega t} \frac{\tilde{L}_{\rm line}(v,\omega)}{\tilde{L}_{\rm cont}(\omega)} d\omega. \tag{1.12}$$

As a result, the transfer function of an AGN can be arrived upon directly by Fourier transforming its continuum and line light-curves. In 1982, when Blandford and McKee's paper was published, there were no spectroscopic time series of sufficient quality to warrant an attempt at full 2-D reverberation mapping. Thus, rather than trying to model $\Psi(v,t)$ *proper*, they instead modelled a set of moment functions, defined for integer n as.

$$L^n_{\rm line}(t) = \int_{-\infty}^{\infty} v^n L_{\rm line}(v,t) dv. \tag{1.13}$$

These can then be used to produce corresponding moments of the transfer function as

$$\Psi^n(t) = \frac{1}{2\pi} \int_{-\infty}^{\infty} e^{-i\omega t} \frac{\tilde{L}^n_{\rm line}(w)}{\tilde{L}_{\rm cont}(w)} d\omega \tag{1.14}$$

The two lowest-order moments correspond to the reprocessing fraction (for $n = 0$; i.e. $L_{\rm line}/L_{\rm cont}$), and a measure of the line asymmetry (for $n = 1$).

Having determined how to derive moment functions from observation, they then derived expected moment functions for a range of geometries. To this end, they expressed $L_{\rm line}(v,t)$ in terms of (i) a continuum reprocessing coefficient $\epsilon(\vec{r})$ (cm^{-1}) for a given position $\vec{r}$ and time t, and (ii) a velocity distribution $f(\vec{r},\vec{w})$, for the local velocity vector $\vec{w}$, and a vector $\vec{n}$ defining the direction towards the observer:

$$L_{\rm line}(v,t) = \int dr dw dt' \frac{\epsilon(\vec{r}) L_{\rm cont}(t' - \frac{r}{c})}{4\pi r^2} f(\vec{r},\vec{w}) \delta(v\vec{w}\cdot\vec{n}) \delta(tt' + \frac{\vec{r}}{c}\cdot\vec{n}). \tag{1.15}$$

Blandford and McKee calculated reprocessing coefficients for (i) spherical and disk geometries, and (ii) anisotropic emissivities based on the LOC model, under the assumption that the emitting clouds are optically thick and emit only from the side facing the central continuum source. For the velocity distribution, they considered isotropic, radially anisotropic and Keplerian rotation velocity fields. They could then substitute the resulting expressions for $\epsilon(\vec{r})$ and $f(\vec{r})$ into Equation 1.15 and thus predict the (moments of) the resulting transfer function. Even for these simplified analytic models of the BLR (with no self-irradiation/multiple reprocessing, and basic parameterised r^{α} reprocessing coefficients) directly recovering the properties of the BLR geometry by inverting the analytic form of $\Psi(v,t)$ is intractable, as the equations are too complex. However, generating *example* Ψ (or moment functions of Ψ) for a given geometry and tuning a given model to match observation can nevertheless offer insight.

Whilst their Fourier technique for directly recovering $\Psi(v,t)$ and theur moment function formulation have seen little use, their paper was hugely influential, and their forward-modelling approach has been widely adopted.

1.3.4.1 The BLR as Population of Randomly Distributed Clouds

The work of generating a library of example 2-dimensional transfer functions *proper* for comparison and refinement via the forward-modelling method was first done by Welsh and Horne (1991) and Perez et al. (1992). Here, I will focus on the former. Welsh and Horne (1991) produced transfer functions for 3 separate systems: a constant velocity spherical outflowing wind, a spherical free-fall inflow model, and a thin Keplerian disk. These are all based on the cloud model of the BLR discussed in section 1.2. Their models describe the cloud number densities as a power-law function of radius, and generate a large number of randomly positioned clouds throughout the model. The emissivity of each cloud is then also approximated as a power-law function of radius, with cloud emission lagging behind the central source emission by a delay corresponding to the light travel time from the central source to the cloud. Emission from these clouds then travels directly to the observer. Their code calculates the contribution of each cloud to the transfer function at a Doppler shift corresponding to its observer-projected radial velocity and at a delay corresponding to the total path-length difference of a photon that travels to the observer via the cloud, rather than directly from the central source.

Example transfer functions based on their modelling are shown in figure 1.14. Their code is also capable of producing a trailed spectrogram from a continuum light curve. The method makes several major approximations. Foremost is the the assumption that density and emissivity can be described by a simple power-law approximation. Equally major is the assumption that these profiles are completely static and do not vary with changes in the ionising continuum. The model also includes no radiative transfer physics: no shielding or multiple-scattering effects are considered, and there is

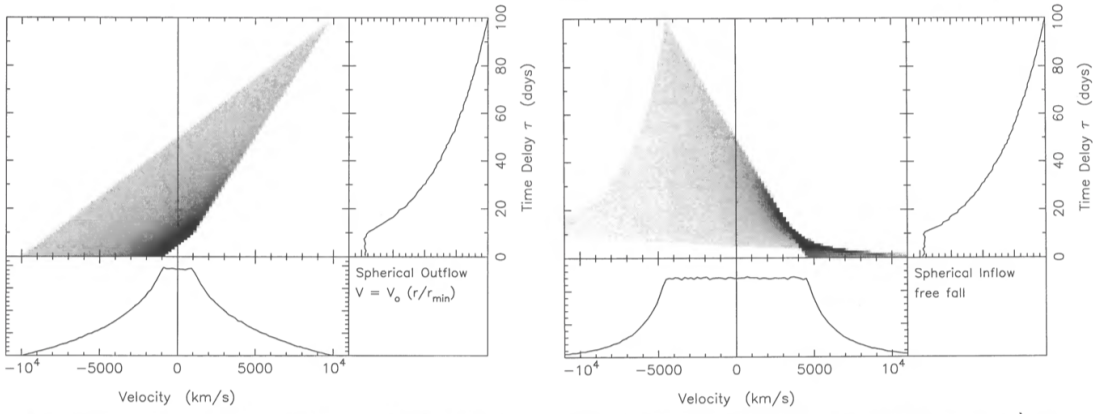

FIGURE 1.14: Transfer functions for spherically-symmetric Hubble-type outflows (left) and free-falling inflows (right) from Welsh and Horne (1991).

no consideration of the spectral energy distribution of the ionising continuum nor the energy-dependent optical depths of the responding lines. Emission is also assumed to be completely isotropic and only dependent on a single continuum source: the clouds are not heated either by radiation from other clouds or by radiation associated with the accretion disk, for example.

Advanced versions of cloud-based BLR models have been developed, implementing anisotropy in both the continuum source (Wanders et al., 1995) and cloud emission (Goad and Wanders, 1996) in an attempt to fit observations; but for a non-biconical wind model (figure 1.15). They implement a distribution of clouds on randomly-inclined Keplerian orbits irradiated by a biconical continuum source. This allows them to obtain a transfer function with biconical features, but without the twin-peaked line profile shape associated with Keplerian rotating biconical winds. They explicitly acknowledge the need for stratified ionisation profile to match observations. The cloud emission anisotropy modelled by Goad and Wanders (1996) is also very specific to the LOC model and based on the optical depth of the cloud, rather than any velocity component. Clouds can be scaled between being fully opaque and functioning as 'reflectors', with only their continuum-source-facing side responding, or being optically thin and responding isotropically. This is similar to the anisotropic emission included in Blandford and McKee (1982).

1.3.4.2 Analytic Descriptions of the BLR

Chiang and Murray (1996) took an alternative approach to the statistical models, instead constructing analytic descriptions of the BLR and solving them to produce a transfer function. The equations for a given geometry are qualitatively similar to the expressions used for $L_{\rm line}$ for a given geometry in Blandford and McKee (1982).

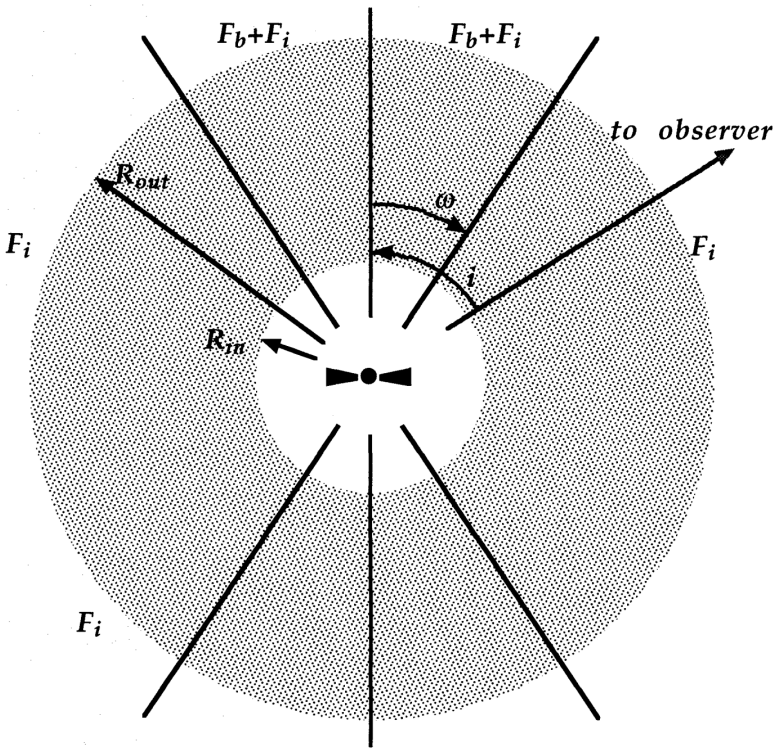

FIGURE 1.15: Geometry for spherical shell BLR (in grey) irradiated by isotropic *and* biconical ionising continuum from Goad and Wanders (1996).

Rather than basic (i.e. purely parametric) disk/inflow/outflow models, they used the physically-motivated disk wind model of Murray et al. (1995), featuring a thin Keplerian disk which launches outflowing winds. In this model clouds are first raised off the surface of the disk by local continuum radiation pressure. They are then driven radially outwards by line driving from the central source. They then produced transfer functions for this model by deriving an analytic solution for the observed luminosity at a given disk position, (r, θ), taking anisotropic emission into account via the local Sobolev optical depth. Notably, however, whilst their model formally describes a disk wind, they assume that all the emission actually comes from the dense 'footprint' where the wind meets the geometrically thin disk.

For this model, $\Psi(v, t)$ is defined for a disk with source term $S(r)$, line opacity $k(r)$ and local escape probability β in the direction of the vector to the observer i as

$$\Psi(v,t) = \int_r k(r)S(r)\beta(r,\theta,i)\delta(\tau - \tilde{\tau}(r,\theta))\delta(v - \tilde{v}(r,\theta))d\theta dr. \tag{1.16}$$

$\tilde{v}$ is the observer-projected velocity taking Doppler shift into account at point on the disk r, θ, and $\tilde{\tau}$ is the delay to an observer from there, also given in terms of r and the disk azimuthal angle θ. Notably, however, when considering observer-projected radial velocities, the outflow component is neglected, as it is small in comparison to the orbital velocity. Whilst the model supports complex emission and ionisation profiles via the k

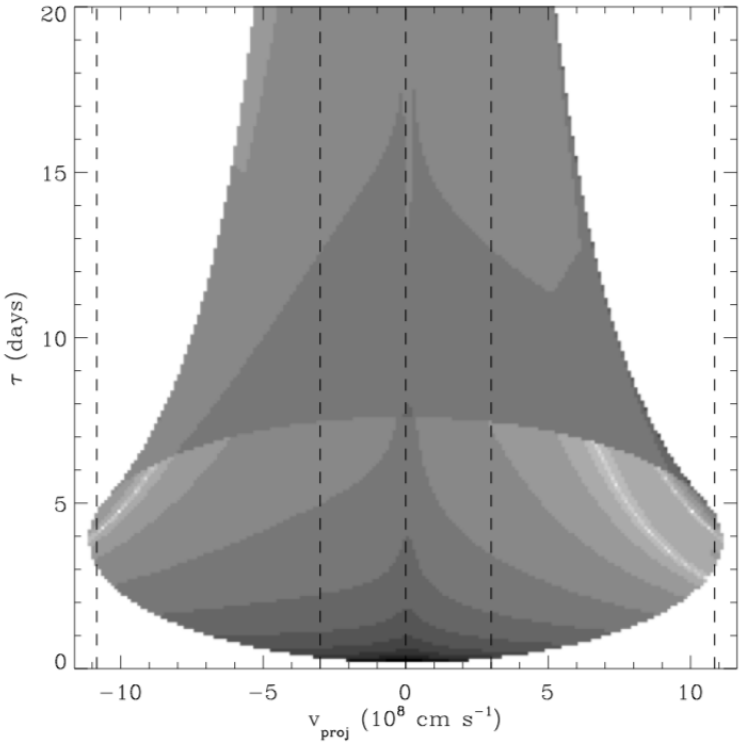

FIGURE 1.16: Transfer function for Murray et al. (1995) disk wind from Chiang and Murray (1996).

and S terms, the analysis is performed only for simple $k \propto r^{-1}$ emissivity profiles. This effectively assumes a consistent ionisation state for the wind between a fixed minimum and maximum radius.

In practical terms, the model is a thin Keplerian disk as in Welsh and Horne (1991), and the outflow component of the model contributes only to the local Sobolev optical depth when considering the component of emission that escapes to an observer at a given angle. This improvement allows it to better capture the behaviour of line photons in optically thick regions with high velocity gradients, but still leaves it lacking in low-velocity-gradient regions. It also still neglects the effects of self-irradiation on a broader scale. Despite this relatively minor deviation from the pure Keplerian disk scenario, their transfer function (Figure 1.16) exhibits some interesting features not seen in the isotropic emission models of Welsh and Horne (1991). The direction-dependence of the Sobolev optical depth leads to a red-leads-blue signature *despite* the lack of inflow kinematics anywhere in the model. A similar signature is found and discussed in Chapter 4.

Waters et al. (2016) improve upon the formulations of Chiang and Murray (1996) with the addition of a *responsivity* term, $\delta j / \delta F_{\rm cont}$. This describes how the emission coefficient j_ν (described further in chapter 2) for a given frequency ν and at a given point in the wind varies with changes in the continuum flux, $F_{\rm cont}$. This formulation allows their code to generate not just transfer functions Ψ but *response functions* Ψ_R. They note,

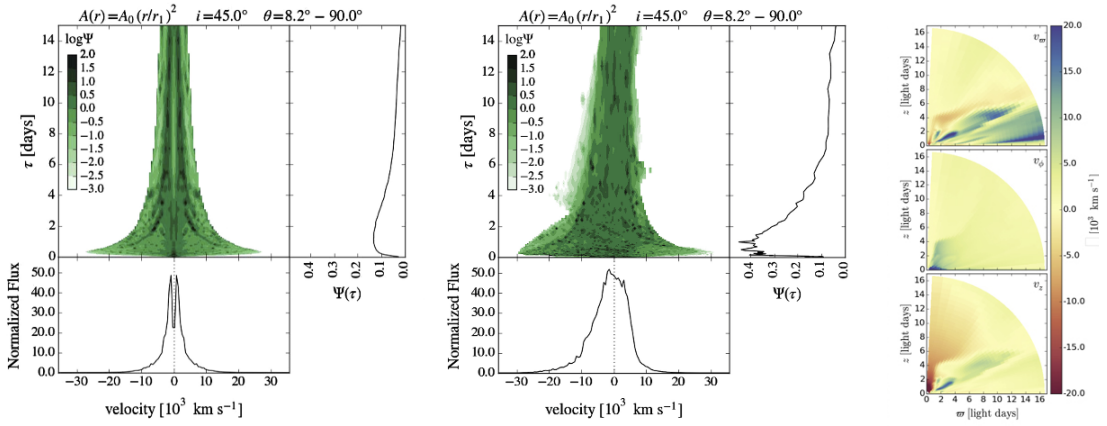

FIGURE 1.17: **Left:** Response function for Proga and Kallman (2004) hydrodynamic outflow from Waters et al. (2016) with purely rotational kinematics, **centre:** with rotation and outflow, **right:** plot of velocity components.

however, that obtaining self-consistent responsivity requires detailed photo-ionisation calculations, which they do not carry out. Instead, they assume a power-law responsivity and describe local line luminosity density $L_{v,\mathrm{line}}$ (units: $ergs^{-1}m^{-3}$) as

$$L_{v,\mathrm{line}}(r) = AF_{\mathrm{cont}}^{\eta(r)}, \tag{1.17}$$

where A is a scaling factor (units: s), and η is a position-dependent responsivity index. Both $A \propto r^2$ and $A \propto constant$ expressions are explored, but in both cases η is set to unity throughout the problem. This factors into j_ν, which depends on the luminosity density and integrated line opacity k as

$$j_\nu \propto k(r)L_{v,\mathrm{line}}(r). \tag{1.18}$$

The line opacity is itself a function of density, which falls off with r^-2. Given the ionising continuum flux F_{cont} also falls off as r^{-2}, this allows Waters et al to expand Chiang et al.'s treatment to explore both the r^{-4} responsivity falloff of Chiang and Murray (1996) and a r^{-2} falloff.

In addition to their improved formulation of the problem, they explore a more detailed hydrodynamic wind model, as calculated by Proga and Kallman (2004). This features a roughly equatorial outflow, with the kinematics illustrated in Figure 1.17. This illustrates how the response function of a system with an equatorial disk wind could appear relatively similar to that of a standard disk. Equally, Waters et al. highlighted how the response function is very sensitive to the responsivity parameter $\eta(r)$, highlighting the need for proper photo-ionisation calculations.

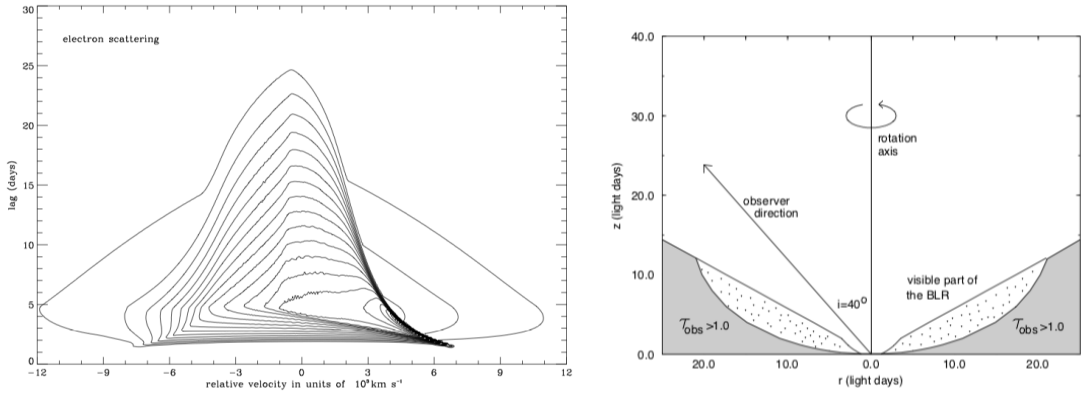

FIGURE 1.18: **Left:** Response function for C IV from Bottorff et al. (1997a) accretion disk wind, **right:** geometry of disk wind.

1.3.4.3 Photo-ionisation Models

Goad et al. (1993) have generated one-dimensional response functions using photo-ionisation models of a LOC BLR. They choose a spherical BLR, composed of isotropically emitting clouds with Keplerian orbital velocities and an outflow velocity component.

Adopting r^{-s} models for the density and cloud pressure, and r^{s-2} models for the ionisation parameter across the BLR (assuming a simple r^{-2} falloff for ionising radiation), they test a range of values of s from $0-2$. From this, they calculate the ionisation profiles and emissivities in each line throughout the BLR. Making the assumption that the lines have a linear dependence on the continuum, this allows them to calculate the transfer function. Further, they then also determine the *response* function Ψ_R, by increasing the continuum luminosity by a small amount, recalculating the ionisation state, and assuming a linear response between the two states. There are crucial differences between the transfer and response functions. The response function is closer to the observable response, as it accounts for shifting ionisation fronts that can open up a response from regions with no previous emission or cut off emission from closer-in regions due to over-ionisation. This results in *negative* responses at some delays, a possibility not supported in most other reverberation mapping models. The method has been employed for a more complex 'bowl-shaped' BLR geometry in Goad and Korista (2014) and Goad and Korista (2015), though still without anisotropic emission or self-irradiation of the BLR.

Bottorff et al. (1997a) have also performed photo-ionisation simulations for 2-dimensional reverberation mapping. They use photo-ionisation modelling to generate the wind emissivity profile of a hydromagnetically-driven outflowing disk wind. Crucially, however, unlike Goad et al. (1993) they only perform a single photo-ionisation calculation, and do not calculate the differential emissivity as a result of changes in the continuum. This means they only produce the *transfer* function for the wind, as shown in figure 1.18. This means that, so far, there are no photo-ionisation models of 2-dimensional *response* functions.

1.3.5 Deconvolution techniques

As discussed in sections 1.3.2 and 1.3.3, given a time-series of line profiles $L_{\rm line}(v,t)$ and a continuum light-curve $L_{\rm cont}(t)$ we can attempt to recover the velocity-resolved response function $\Psi_R(v,t)$. However, this is an ill-posed problem. Accurately inverting data to recover a transfer function requires a high cadence of low-error simultaneous observations of both line and continuum luminosities. When the light-curves are poorly sampled or have high errors, then the problem becomes degenerate. Given a driving continuum and line light curve, many different response functions can give rise to the line within the errors on both.

There have been two main families of approaches to deconvolution. The first is to assume a model form for the response function $\Psi(v,t)$, and in addition to evaluating how well a given candidate $\Psi(v,t)$ fits the observed data, to assign some other optimisation parameter (e.g. Horne et al. (1991); Krolik and Done (1995)). In this context, the degeneracy is broken by assuming that the response function is most likely to take one particular form. This form is usually one that is mathematically simple, but potentially physical considerations can be applied.

The second approach is to assume not a model form for $\Psi(v,t)$, but for the *system* that gives rise to $\Psi(v,t)$. Within this approach, the degeneracy is reduced by the assumption of a specific geometry, kinematics and emissivity/responsivity profile (e.g. Keplerian disk, biconical wind). These models have a range of tuneable physical parameters that can be used to optimise the $\Psi(v,t)$ fit.

1.3.5.1 Discrete Cross-Correlation

The very earliest work makes use of discrete cross-correlation function techniques developed by Edelson and Krolik (1989) to split a time-series of line profiles up into velocity bins and produce one-dimensional cross-correlation functions (CCFs) for each bin. This method places no constraints on the CCFs recovered, and has often only been used on a very coarse velocity grid. These coarse grids give a lag distribution ony the level of only the red- or blue- wings of a line, for example, or for a small number of velocity bins (White and Peterson, 1994; Peterson et al., 2004; Valenti et al., 2015). Whilst this does not produce transfer functions per se (see figure 1.19), the outputs can potentially be Ψ-*like*, and can help differentiate between geometries and kinematics by showing the kind of red-leads-blue or blue-leads-red signatures discussed in section 1.3.3. This method assumes no underlying physical picture; the CCF simply arises from the data, and the technique itself makes no predictions about the type of system that gave rise to the CCF. Some enhanced versions of CCF do not cross-correlate with the observed data, but use Markov-Chain Monte Carlo processes to fit damped random walk models to the discrete observations (instead of interpolating or re-binning when the line and

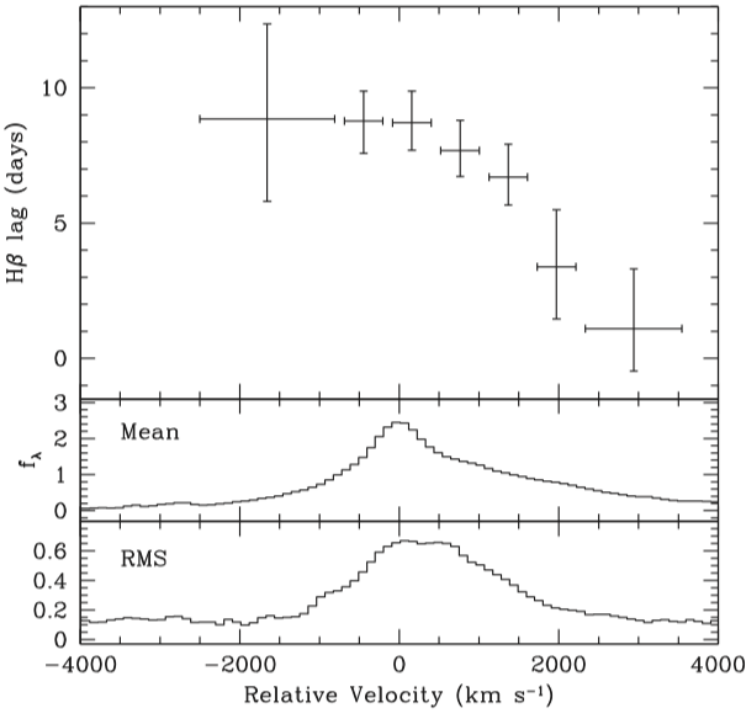

FIGURE 1.19: Velocity-resolved cross-correlation function from Valenti et al. (2015)

continuum observations do not occur at the same times), and then generate a CCF for these two (Zu et al., 2011).

1.3.5.2 Maximum Entropy Method

The *Maximum Entropy Method* (MEM), as implemented in the computer code MEMECHO, was originally developed by Horne et al. (1991) and elaborated upon in Horne (1994). This method determines the response function Ψ_R of the system by solving equation 1.9. The code performs fitting to minimise the χ^2 value for $\Delta L_{\mathrm{line,simulated}}$ compared to $\Delta L_{\mathrm{line,observed}}$. However, Ψ_R is also subject to an additional regularisation constraint. Rather than simply minimising χ^2 the code instead minimises the value Q that combines the goodness-of-fit and the *entropy* of the response function via a weighting parameter γ as

$$Q^2 = \chi^2 - \gamma S. \tag{1.19}$$

The sources of entropy in the code are the continuous models for continuum luminosity L_{cont} and mean line continuum $\bar{L}_{\mathrm{line}}$ it generates from the discrete observations, and the response function Ψ_R. MEMECHO defines the entropy of a system as a measure of its 'smoothness'. Functions with many regions of high rates of change in gradient encode

large amounts of information in these changes, and thus have low entropy. MEMEcho expresses this in terms of weighting factors B, W and A as

$$S = -\int_{t_{\min}}^{t_{\max}} \left(\frac{\delta^2 ln\ L_{\rm cont}(t)}{\delta t^2}\right)^2 dt - B\int_{v_{\min}}^{v_{\max}} \left(\frac{\delta^2 ln\ \bar{L}_{\rm line}(v)}{\delta v^2}\right)^2 dv$$
$$- \frac{W}{1+A}\int_{t_{\min}}^{t_{\max}}\int_{v_{\min}}^{v_{\max}} \left\{\left(\frac{\delta^2 ln\Psi_r(v,\tau)}{\delta\tau^2}\right)^2 + A\left(\frac{\delta^2 ln\Psi_r(v,\tau)}{\delta v^2}\right)^2\right\} dv d\tau. \quad (1.20)$$

This is implemented by discretising Ψ_R, $L_{\rm cont}$ and $L_{\rm line}$ and determining the second derivative numerically. The choices of $\tau_{\min}$ and $\tau_{\max}$ allow the method to limit Ψ_R to a 'plausible' range of times, in a way that simple cross-correlation analysis does not. This does potentially run into issues with the observation that some continuum bands appear to rise *before* the ionising continuum (Fausnaugh et al., 2017).

The code is capable of generating both one- and two-dimensional response functions. As with the CCF method, the MEM is formally blind to the physical nature of the BLR that gave rise to the response function. It "only" recovers the response function - interpreting this in terms of the BLR geometry and kinematics is left to the post-hoc analysis of experts. There still exists the potential for several different geometries to have given rise to the Ψ_R. In addition, MEMEcho applies the constraint that $\Psi_R \geq 0$, which is at odds with existing observations that the line luminosity can be anti-correlated with the continuum (Goad et al., 1993). The maximum entropy method has been extensively used by a wide range of groups (Bentz et al., 2010a; Grier et al., 2013b; Xiao et al., 2018a).

1.3.5.3 Regularised Linear Inversion

A less commonly used technique developed by Krolik and Done (1995), Regularised Linear Inversion (RLI) recovers Ψ_R from observation via χ^2 minimisation. Expressing equation 1.10 in terms of N discrete continuum flux observations $F_{\rm cont}$ and line flux observations $F_{\rm line}$ at times t_i, and the response function in terms of M discrete samples at times τ_j with separation $\Delta\tau_j$, we get for one time

$$\delta F_{\rm line}(t_i) = \sum_{j=1}^{M} \Big[F_{\rm cont}(t_i - \tau_j) - \langle F_{\rm cont}\rangle(\tau_j)\Big]\Psi_R(\tau_j)\Delta\tau_j, \quad (1.21)$$

where the continuum mean is a function of time as AGN continua mean are asserted to 'wander'. This can be expressed as a χ^2 minimisation for a series of N continuum and line observations t_i as

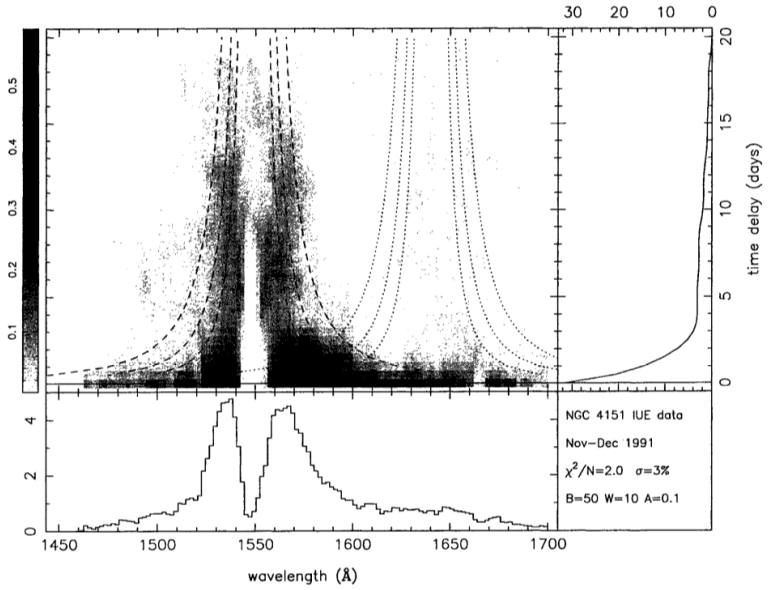

FIGURE 1.20: Velocity-resolved response function generated by MEMECHO from Ulrich and Horne (1996)

$$\chi^2 = \sum_{i=M}^{N} \left(\frac{\delta F_{\rm line}(t_i) - \sum_{j=1}^{M} [F_{\rm cont}(t_j - \tau_j) - \langle F_{\rm cont} \rangle (\tau_j)] \Psi_R(\tau_j) \delta\tau_j}{\sigma_l(t_i)} \right)^2, \tag{1.22}$$

where σ_l is the error on point t_i. This form is still degenerate for many Ψ_R. They regularise it by further minimising the 'smoothness' of Ψ_R via the differencing operator H, resulting in a regularised linear deconvolution equation

$$(C^T C + \lambda H^T H)\Psi_R = C^T L, \tag{1.23}$$

Where C is a matrix based on the continuum flux fluctuations as $C_{ij} = \Delta\tau_j \big[F_{\rm cont}(t - \tau_j) - \langle F_{\rm cont} \rangle (\tau_j)\big]/\sigma_l(t_i)$, and L is a matrix based on the line fluxes $L_i = \delta F_{\rm line}(t_i)/\sigma_l(t_i)$. λ is a scaling factor determining the weight placed on the smoothing factor vs the model fit residuals. Using this model, they fit one-dimensional response functions (similarly to the CCF technique) in each wavelength bin with a range of tuneable fitting parameters. They repeatedly re-sample the line and continuum light-curves applying their measurement errors, perform a fit for each, and arrive at a mean fit value and error from the distribution of fits. The response functions themselves describe a BLR of spherical, isotropically-emitting clouds whose emission falls off with radius. The motions of the clouds is a described by radial inflow with velocity $v_r(r) = v_{r0}(r/r_0)^\alpha$ with a randomly directed Gaussian spread with $\sigma(r) = \sigma_0(r/r_0)^\beta$. Interestingly, despite the lack of an explicit orbital velocity component the Gaussian spread on the inflow velocity serves to provide sufficient line width, allowing the system to be fitted to observation solely by varying the four parameters v_{r0}, α, σ_0 and β.

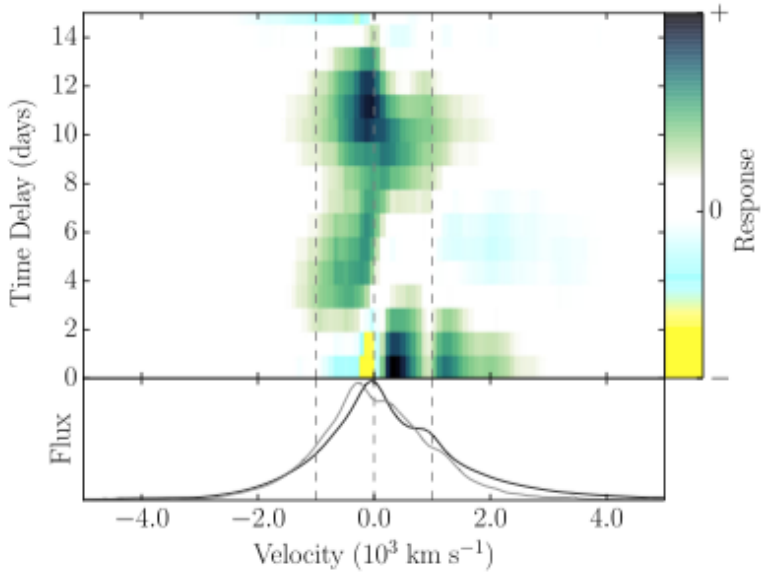

FIGURE 1.21: Velocity-resolved response function generated by RLI from Skielboe et al. (2015)

Recent work by Skielboe et al. (2015) has compiled multiple velocity bins to form a full response function as 1.21. However, a potential drawback is that the velocity-bin-wise generation of Ψ_R does not impose any restrictions on the form of the response function based on adjacent wavelength bins, when we would expect there to be some level of continuity (i.e. the value of v_{r0} should be a property of the entire system, not a function of wavelength). In addition, the form of the predicted response function $\Psi_{R,\mathrm{p}}$ plays a fundamental role in fitting. Without an appropriate model, no response function can be recovered to any level of accuracy.

Despite the advantages of its ability to cope with negative responses, the RLI method has seen only limited use.

1.3.5.4 Markov-chain Monte Carlo Forward Modelling

The Markov-chain Monte Carlo Forward Modelling (MCMCFM) and associated computer code CARAMEL was developed by Pancoast et al. (2011). In contrast to techniques like CCF and MEM that are agnostic about the geometry and kinematics of the BLR, the technique constructs a simple model of a BLR geometry. It produces a LOC-model BLR from a distribution of clouds, each of which is assigned an orbit with a tilt and radius, as well as an inflow or outflow velocity, drawn from a distribution. It then generates a transfer function for the BLR using the same simple method as Welsh and Horne (1991), and uses it to produce a time-series of line profiles from the input continuum. A Markov-chain Monte Carlo iteration process follows, to refine the model parameters and generate a line light-curve that best fits the observations. This generates not only a transfer function, Ψ, as shown in figure 1.22 , but also predicts the

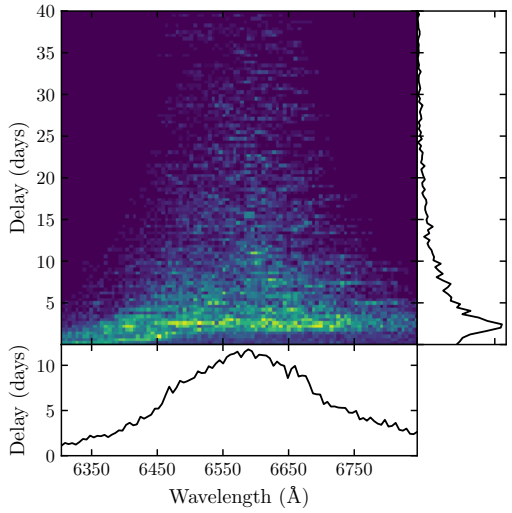

FIGURE 1.22: Velocity-resolved response function generated by CARAMEL for Mangham et al. (2018).

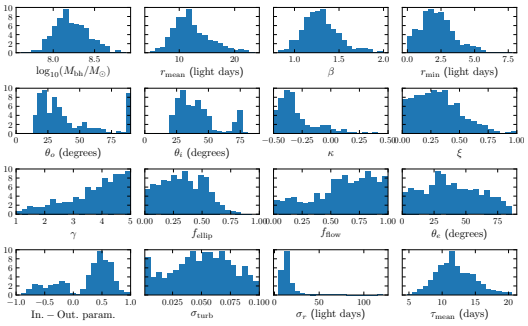

FIGURE 1.23: Table of cloud parameter distributions generated by CARAMEL for Mangham et al. (2018).

full geometry and kinematics of the BLR as figure 1.23. As this method is so strongly dependent upon the model used to generate the BLR, whilst it has great predictive power it can only recover Ψ for a system that falls within the scope of its assumptions. In addition, much like the MEM, this method imposes the constraint that $\Psi \geq 0$. It also allows the continuum between observations to vary as a free parameter, but in a physically-motivated way via a MCMC technique as the refined CCF does. The MCMCFM technique has been widely used for a range of observations (Pancoast et al., 2012, 2014a, 2018).

1.3.6 Recent campaigns

Following Horne et al.'s work on deconvolution using the Maximum Entropy Method, Horne et al. (2004) tested the ability of the MEMECHO code to recover a range of modelled response functions from simulated observing campaigns. This analysis suggests that a campaign with observation time interval Δt can to recover response functions to a resolution $\Delta\tau \approx 2\Delta t$, as long as the observing campaign duration $t_{\rm dur}$ is $> 3r_{\rm BLR}/c$. Their simulated campaigns assumed a resolution of 1.5Å in the far UV, and 3Å in the near UV/optical. The process for this involved creating artificial time-series of line spectra from a template response function and driving continuum, before feeding this output back into MEMECHO to test the fidelity with which it could recover the input response function, with the results shown in Figure 1.24. With 200 days of observations roughly 5 times per day, it was possible to recover even highly detailed response functions to a reasonable level for response functions tuned to match the mean delays of the Seyfert NGC5548 ($\approx$ 10 days for Hβ, Bentz et al. (2013)), a common target of RM campaigns.

Equally, Horne et al. make the point that given lines are localised to different regions of the BLR due to ionisation stratification, any observing campaign hoping to determine the geometry of the BLR will necessarily need to probe a *range* of lines.

The AGN Key Project (Valenti et al., 2015) focused on a single target, ARP-150, acquiring near-daily observations over 200 days. The much larger mean lags ($\approx 7.52^{+1.43}_{-1.06}$ days for Hβ) allow for relatively low sampling rates compared to those required for smaller AGN. Unfortunately, the relatively low spectral resolution ($\approx$ 7Å) makes the campaign unsuitable for determining full, high-resolution response functions though a Ψ-like collection of binned cross-correlation lags can be produced (Figure 1.19).

The LICK AGN Monitoring Project (LAMP, Bentz et al. (2008, 2009a)) included ARP-150, but also expanded to cover 14 other nearby Seyfert galaxies. The campaign was only 64 nights long, with a roughly daily cadence. The Hβ line in this campaign displayed centroid lags of $4.17^{+0.67}_{-0.64}$ days, so the response function resolution resolution would be unfortunately too low to accurately recover the low-delay response signatures. Despite this limitation, the data gathered has been repeatedly used in velocity-resolved reverberation mapping studies, both by the groups involved in the survey (Bentz et al., 2010a) and others (Skielboe et al., 2015; Pancoast et al., 2014a,b)

The AGN Space Telescope and Optical Reverberation Mapping project (AGN-STORM) was focused on a single object; a series of 171 observations over 175-nights of the Seyfert NGC5548 (De Rosa et al., 2015; Edelson et al., 2015; Fausnaugh et al., 2016). The survey covers a wide range of emission lines, from far-UV lines like C IV and Lyα to UV and optical lines like the traditional target of RM campaigns Hβ; allowing it to sample responses throughout the BLR. The campaign was structured explicitly with velocity-resolved reverberation mapping in mind, and the instruments chosen have high spectral resolutions as required ($\approx$ 1Å in the FUV). Interestingly, this campaign noted an unusual anti-correlation of Hβ with the driving continuum towards the end (Pei and AGN STORM Collaboration, 2016).

In terms of future work, the OzDES spectroscopic survey (King et al., 2015) plans to observe a large field for supernovae, hoping to use the observed rates to determine the rate of expansion of the universe. Over 500 AGN lie within this field, and the survey expects to recover mean lags for $\approx 35 - 45\%$ of the quasars observed. Unfortunately, the low cadence (5-7 days) makes it unsuitable for use in velocity-resolved reverberation mapping surveys.

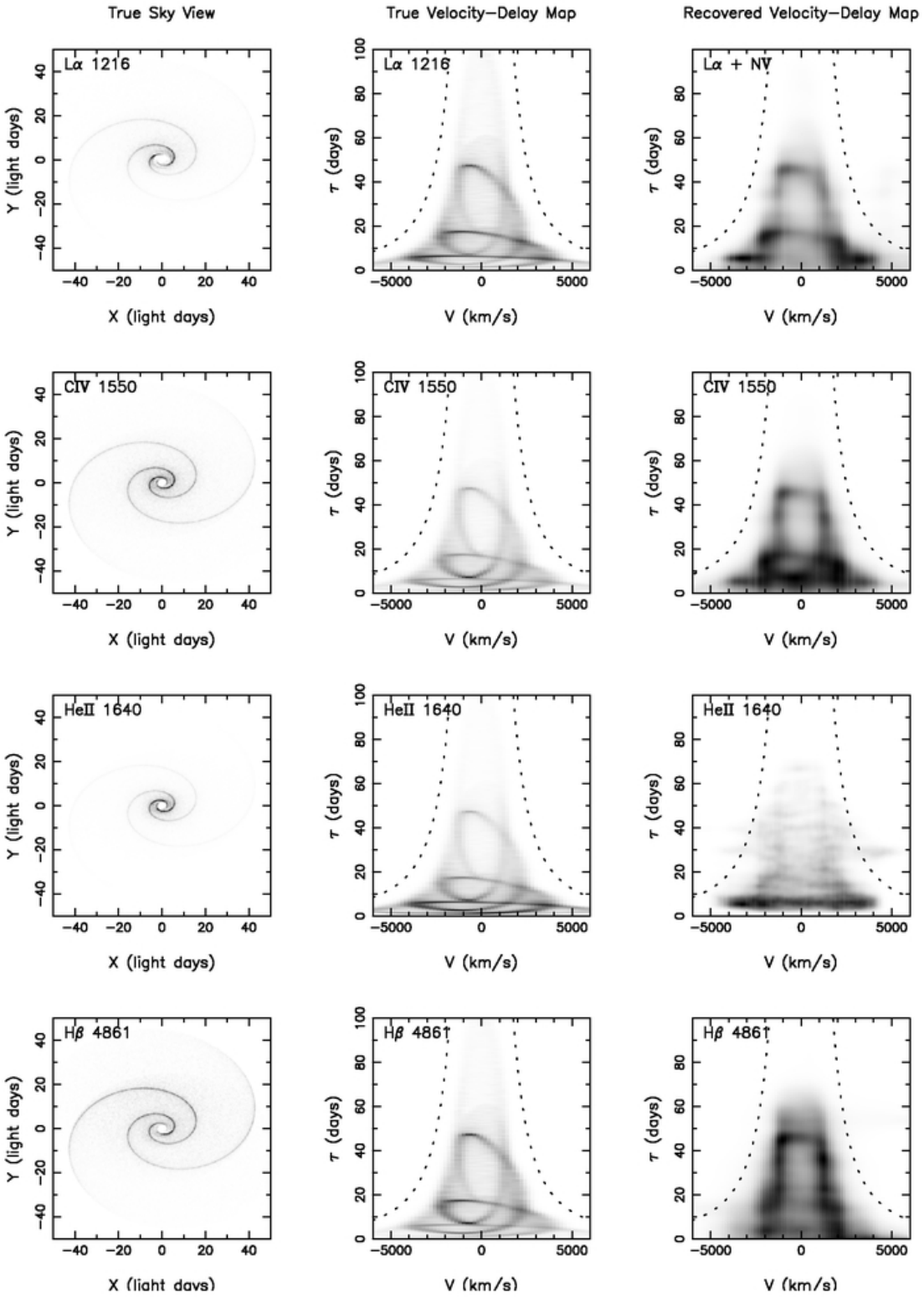

FIGURE 1.24: **Left:** Test geometry of Keplerian disk with two arms. **Centre:**, model response function, **right:** MEMECHO recovered response function, reproduced from Horne et al. (2004).

1.4 Outline

This thesis documents our efforts to modify an existing ionisation and radiative transfer simulation code for the purposes of generating two-dimensional transfer and response functions for AGN, and the insight that has given into their behaviour.

The modelling work done in this thesis was all performed using a modified version of the existing PYTHON Monte Carlo radiative transfer and ionisation code. Long and Knigge (2002) originally developed the code to generate simulated spectra in order to investigate outflow models of a wide range of astrophysical systems. Chapter 2 describes the principles behind Monte Carlo radiative transfer simulations in general, and how the PYTHON code works specifically.

The modifications made to the code are then detailed in chapter 3, along with an explanation of how the modified code's outputs are used to generate two-dimensional transfer functions. We then explore how these transfer functions differ from simple two-dimensional transfer functions produced in previous works that do not feature detailed radiative transfer, or any ionisation modelling (e.g. Welsh and Horne (1991)). The code changes also offer the opportunity to explore *how* photons travel throughout the wind, and to investigate if different regions are affected by different populations of photons. This will also allow us to assess how reasonable other common approximations and assumptions made in reverberation mapping are.

Chapter 4 reproduces a paper published in the Monthly Notices of the Royal Astronomical Society in 2017, along with some additional context. The chapter explores the concept of transfer and response functions in more depth, emphasising the difference between simple *emissivity functions* used in models that apply a single parameterised emissivity profile to the wind for each line, and the more realistic *response functions* that photo-ionisation codes (like our modified PYTHON code) can generate. In particular the paper covers how, unlike emissivity functions, response functions can take *negative* values – and the consequences this has for predicting geometries using them.

Chapter 5 follows up on this work by testing existing techniques used for recovering response functions from series of observations of AGN (Horne et al., 1991; Horne, 1994; Pancoast et al., 2011). It details the development of a technique for generating an artificial series of observations from a real driving continuum (Fausnaugh et al., 2016) and the realistic response functions produced in chapter 4. From there, these artificial observing campaigns are analysed by the Pancoast et al. (2011) and Horne et al. (1991) codes CARAMEL and MEMECHO. We test how accurately these codes can recover our response functions, and to see if there are any limits on what can be recovered. We discover that neither code can accurately recover *negative* response functions, and that the CARAMEL code struggles with geometries that do not match its assumptions.

Finally, chapter 6 describes the conclusions of this work and what consequence the discoveries made have for the field of reverberation mapping of AGN.

Chapter 2

Monte Carlo Radiative Transfer & Ionisation Modelling

The work described in this thesis involved the development and use of a Monte Carlo radiative transfer and ionisation code, PYTHON, to generate two-dimensional transfer and response functions for reverberation mapping. As such, this chapter describes the theory behind Monte Carlo radiative transfer, and outlines why a Monte Carlo code like PYTHON was suitable for this application. It includes a discussion of the technical aspects of the code and outlines the basic structure of the models used in this work.

2.1 Radiative Transfer

Radiative transfer describes how radiation fields travel through and interact with a medium. In one dimension, the basic equation describing radiative transfer of a beam of radiation of frequency ν travelling through a medium can be expressed as

$$\frac{dI_\nu}{ds} = -\alpha_\nu I_\nu + j_\nu, \tag{2.1}$$

where I is the specific intensity of radiation (units: $Wm^2sr^1Hz^1$), and s is distance (units: m). The quantity j_ν is the *emission coefficient* (units: m^{-1}), and describes how much the intensity increases across distance ds, whilst α_ν is the *absorption coefficient* (units: m^{-1}), and describes the fraction of the radiation that is lost by the beam as it travels through the medium. The absorption coefficient is usually defined in terms of interactions with a number density n (units: m^-3) of particles presenting a frequency-dependent *interaction cross-section* to incoming radiation σ_ν (units: m^2) as

$$\alpha_\nu = n\sigma_\nu. \tag{2.2}$$

We can also define α_ν in terms of the density of the medium and the *mass-absorption coefficient* κ_ν (a.k.a. the opacity coefficient, units: $cm^2 g^{-1}$) as equation 2.3:

$$\alpha_\nu = \rho\kappa_\nu \tag{2.3}$$

We can express these equations in a simpler way by defining a new property, optical depth, as $d\tau = \alpha_\nu ds$. When we substitute τ_ν into equation 2.1, we get

$$\frac{dI_\nu}{d\tau_\nu} = -I_\nu + \frac{j_\nu}{\alpha_\nu} \tag{2.4}$$

Considering a purely absorbing medium ($j_\nu = 0$) and integrating along a path from s_0 to s, we find that

$$I_\nu(\tau) = I_\nu(0)e^{-\tau_\nu}, \tag{2.5}$$

where

$$\tau = \int_{s_0}^{s} \alpha(s')ds'. \tag{2.6}$$

Thus for a photon the optical depth, τ, is related to the natural log of the probability of being absorbed along that path. This allows us to describe a system in useful shorthand; if a typical path through a medium has a $\tau_\nu >> 1$, it is said to be *optically thick*. In this limit, an average photon is more likely than not to be absorbed (or scattered, or otherwise reprocessed if we add the cross-sections for other processes) on its path through the medium. By contrast in the limit $\tau_\nu << 1$, the material is *optically thin*, and photons are instead more likely to pass through unaltered.

Now, using optical depth as the independent variable, we can rewrite equation 2.1 as

$$\frac{dI_\nu}{d\tau_\nu} = -I_\nu + S_\nu. \tag{2.7}$$

Here, $S_\nu = j_\nu/\alpha_\nu$ is the so-called frequency-dependent source function for the medium. We can then integrate it up as with equation 2.5 to express the full formal solution to the radiative transfer equation as

$$I_\nu(\tau_\nu) = I_\nu(0)e^{-\tau_\nu} + \int_0^{\tau'_\nu} e^{-(\tau_\nu - \tau'_\nu)} S_\nu(\tau'_\nu)d\tau'_\nu. \tag{2.8}$$

Note that in the optically thin limit $\tau_\nu \to 0$, $I_\nu \to S_\nu$ everywhere.

Historically, most radiative transfer problems in astrophysics, e.g. those for solving stellar atmospheres (e.g. Kurucz (1979); Hubeny and Lanz (2011); Hauschildt and Baron (2008)) have been solved using sophisticated mathematical techniques. These work well for spherical geometries and are designed for situations where high optical depths are involved. They work less well for complex geometries such as those found in AGN, although various attempts have been made to reduce the problem to a sum of 1-d problems.

2.1.1 Monte Carlo Radiative Transfer

Monte Carlo radiative transfer techniques have long been in used in order to avoid the intractable analytic equations of radiative transfer. Originally developed for use in nuclear applications by e.g. Cashwell and Everett (1959), MCRT techniques replace the top-down analytic approach, solving for large-scale system properties, with a bottom-up micro-physics model. These models work by simulating the flight of individual photons, or 'packets' of identical photons, throughout the system. A photon is initialised with a starting position, direction and frequency drawn from the distributions in the system, and their travel through the system is then simulated, including interaction probabilities based on the photon frequency and the cross-section of the material it is travelling through. If a photon scatters, the resulting direction and energy can be generated at random from the known probability distributions for those outcomes. A photon can be followed until it is absorbed or leaves the system, with each of its interactions being recorded as required; then another photon can be generated. For sufficiently large numbers of photons, it is possible to sample the entire possibility space of the system to a low Poisson noise (i.e. for a property X, $\frac{\Delta X}{X} \propto \sqrt{n_{\mathrm{phot}}}/n_{\mathrm{phot}}$).

In terms of advantages and disadvantages, Monte Carlo radiative transfer is well-suited for systems which are not too optically thick and which have complex geometries. The main disadvantages arise when the system is optically thick, or one or more portions of a system (which matter) are optically thick.

Unlike analytic solutions to the radiative transfer equation, Monte Carlo radiative transfer can have difficulties generating solutions for particular sub-sections of a problem. For a system where the properties that affect radiative transfer (e.g. densities, temperatures, ionisation states) vary over a short length scale, it can be challenging to get sufficient sampling throughout the problem. Another major cause of under-sampling is *shielding*; regions with high scattering or absorption cross-sections can prevent photons from passing through them to areas beyond. In addition to the issues this causes with fully sampling a model, this can *also* cause practical issues with the computational requirements of a simulation. If a large fraction of the simulation time is spent processing repeated scatters of a photon in one local region, then attaining higher sample size and lower error in the other regions requires a disproportionately large increase in the number of photons simulated.

2.2 Python

This work involved expanding the pre-existing Monte Carlo radiative transfer modelling code PYTHON. PYTHON was developed for use in modelling accretion disk winds in a variety of astrophysical settings, including AGN and cataclysmic variables (Sim et al., 2005; Higginbottom et al., 2013; Matthews et al., 2015). The code is designed to predict the spectra that would be observed for a disk and wind model with a given set of parameters (e.g. density and velocity as a function of position).

2.2.1 Radiative Transfer

PYTHON simulates the movement of 'photon packets'; each of which is a single particle in simulation terms that represents a large number of identical photons. Each packet has a 'weight' (units: $erg|s^{-1}$), corresponding to the number of photons that bundle represents. Packets are produced in order to obtain a good sampling of the probability space of the simulation; including photon source and starting location (disk/wind/corona), wavelength, and starting direction.

The photon packets are free to move in three dimensions through a system with a central source, disk and wind, over which is superimposed a two-dimensional axisymmetric 'grid' of cells describing the state of the plasma in the wind.

PYTHON's implementation of photon-matter interactions (i.e. line scattering, Compton scattering, photo-ionisation followed by recombination, and collisional excitation) uses a method similar to that outlined in Mazzali and Lucy (1993). The optical depth τ for each cell is calculated from the interaction cross-sections and opacities of all the relevant interactions (electron scattering σ_{es} from electrons of number density n_e, line scattering κ_{bb}, photo-ionisation κ_{bf}, and free-free absorption κ_{ff}) for each species i of density ρ across an in-cell distance s as

$$\tau_\nu(s) = \int_0^s \sigma_{es} n_e + \sum_i^{species} \rho_i(\kappa_{i,bb}(s) + \kappa_{i,bf} + \kappa_{i,ff}) ds.. \tag{2.9}$$

As discussed in section 2.1, the optical depth is related to natural log of the probability that the photon interacts along a given path. Making use of this, the code determines the optical depth at which an interaction happens by drawing a uniform random number P between 0 and 1, and selecting τ_P via

$$\tau_P = -\ln 1 - P. \tag{2.10}$$

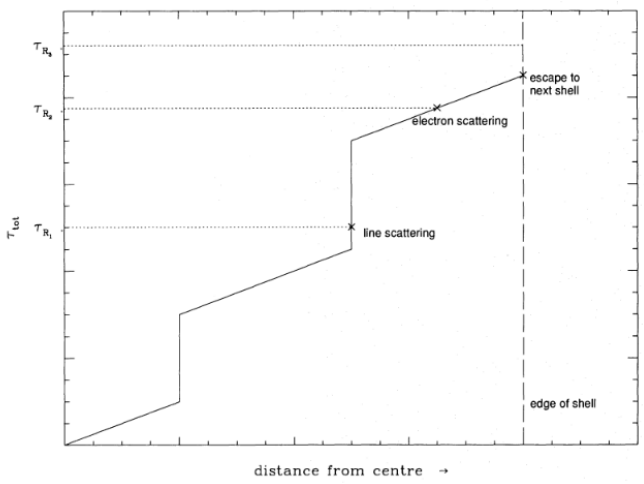

FIGURE 2.1: Plot of combined optical depth in a wind cell reproduced from Mazzali and Lucy (1993), showing how total optical depth is built up from line depth and Compton scattering depth.

If this is lower than the total optical depth in the cell, then the process corresponding to this value of τ is applied at the physical distance through corresponding to the optical depth, as illustrated in figure 2.1. The contribution from line reprocessing interactions like bound-bound scattering is assumed to occur at a single depth into the cell where the packet's frequency is Doppler shifted into the resonance line via the relative movement of the photon and wind. This conveniently serves to simplify the interaction with a given line: instead of having to consider interactions occurring throughout a volume, they are instead on a single surface that the photon path intersects, the basis of the 'Sobolev approximation'.

Once any reprocessing event has occurred and the photon packet has changed direction, or if none has occurred and the packet has left the cell, its packet weight is reduced by an amount appropriate to the attenuation via free-free heating and photo-ionisation within the cell. The photon packet then proceeds to the next wind cell, where the photon interaction properties (temperature, electron density, ionisation structure etc.) differ.

PYTHON also implements an escape probability weighting in areas of high velocity gradient. If a photon is emitted in or scatters off a given emission line in an area with a high optical depth in that line, then it has a high probability of interacting with that line again. Photons in these areas can undergo up to 10^3 interactions before they successfully exit the region. Rybicki and Hummer (1978) show that in this situation, a photon is much more likely to exit that region in the direction of the highest velocity gradient. Along to the velocity gradient, the line will be Doppler shifted out of resonance with the photon wavelength. This allows it to approximate a time-consuming process of multiple-reprocessing as a single direction-biased event.

Radiative bound-bound transitions of most species are treated using a simple 2-level atom approximation (as e.g. Mihalas (1982)), where photons excite an electron which

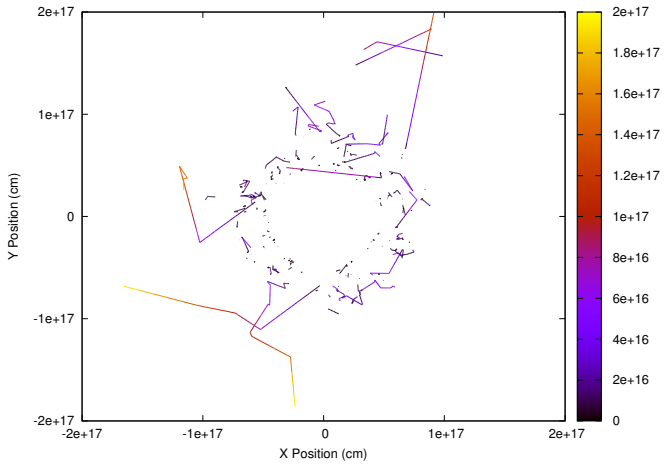

FIGURE 2.2: Plot of the first 2×10^{17}cm of the trajectories of the first 150 photons in a PYTHON simulation of an AGN accretion disk, with colour indicating total travel distance.

immediately radiatively de-excites back down to the lower level, re-emitting a photon at the same frequency. Whilst this is a reasonable assumption in some resonant cases, many lines (e.g. the Balmer series) that are highly important observationally require a more thorough treatment. For those species of high importance with relatively few energy levels, Lucy (2002, 2003) describe a 'macro-atom' method for addressing the full micro-physics of an excited electron's transition between the energy levels of its atom. Sim et al. (2005); Matthews et al. (2016) describe the application of this method to PYTHON and expand upon it. It is discussed further in section 2.2.3.

A collection of example trajectories are shown in figure 2.2.

2.2.2 Simulation Cycles

PYTHON divides its radiative transfer and ionisation simulation into a series of iterative **cycles**. At the start of each cycle, PYTHON generates a fixed number of photons, distributed between the various sources in the model (i.e. X-ray corona, accretion disk, wind). The number of photons $N_{\rm i}$ generated for a source i of luminosity $L_{\rm i}$ depends on the total number of photons run per cycle $N_{\rm total}$ as equation 2.11:

$$N_i = N_{\rm total} \frac{L_i}{\sum_{j}^{\rm sources} L_j} \tag{2.11}$$

$N_{\rm total}$ is typically in the range of $10^7 - 10^8$. Once the photons have been allocated to sources and their starting parameters generated, the cycle continues and their paths through the wind are simulated as shown in figures 2.3 and 2.5.

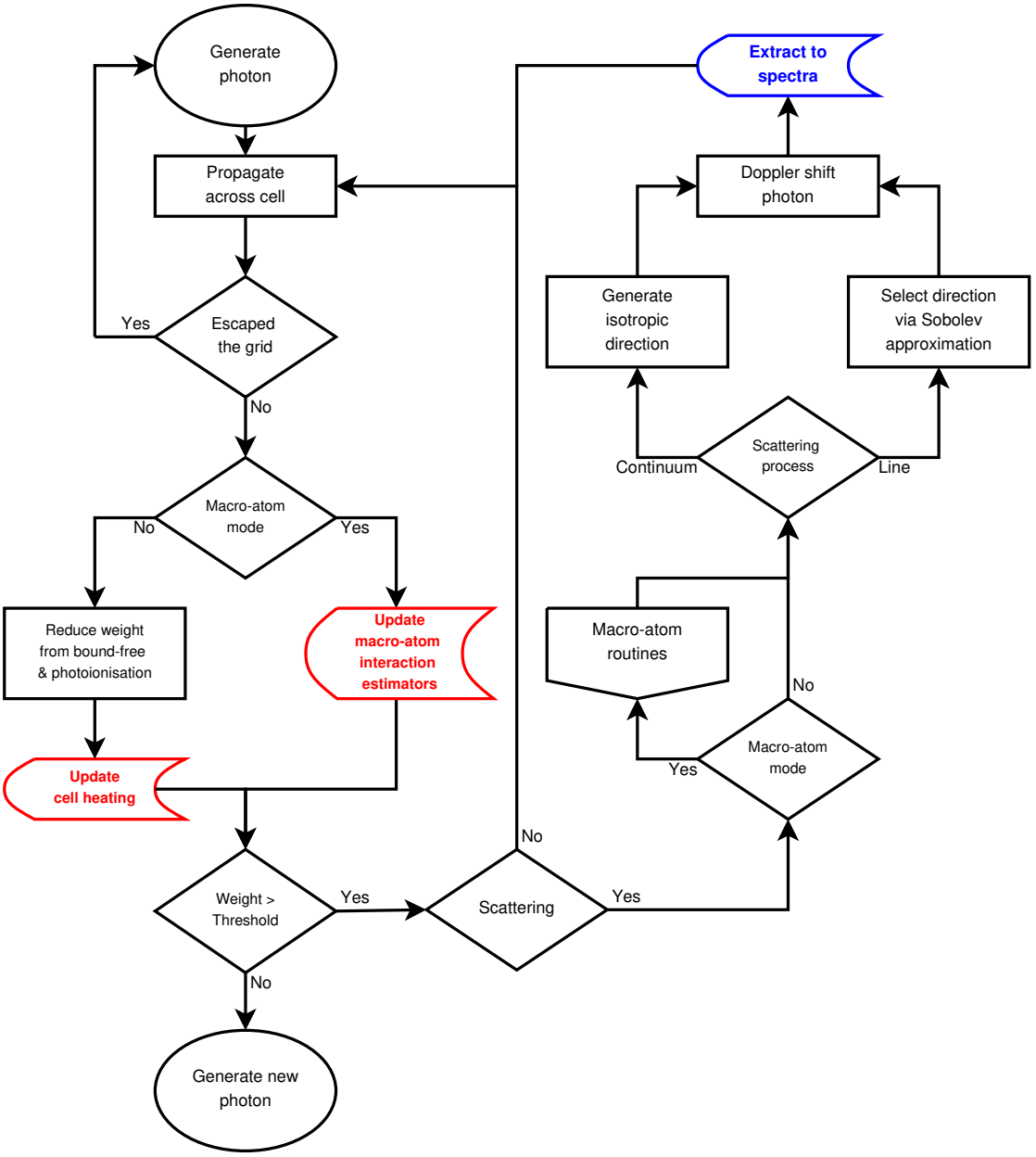

FIGURE 2.3: Diagram of the simulation flow. Processes in **red** are only performed in the ionisation cycles (see section 2.2.2.1), processes in **blue** are only performed in the spectral cycles (see section 2.2.2.2). Macro-atom processes are described in section 2.2.3 and shown in figure 2.5.

Each PYTHON run is split into two different types of cycles; ionisation cycles and spectral cycles. Broadly speaking, the purpose of ionisation cycles is to iteratively determine the ionisation state of the wind, whilst the purpose of the spectral cycles is to iteratively construct the final spectrum (or spectra) as seen by one or multiple observers. In the following subsections, both types are documented.

2.2.2.1 Ionisation cycles

Initially, PYTHON calculates the ionisation state of the wind via an iterative series of ionisation cycles. Before the first cycle, the wind is first initialised with a pre-set wind temperature, and its ionisation state set to the local thermodynamic equilibrium. Then during each cycle, a flight of photon packets is generated and transported through the model. As the photon packets travel through each cell in the wind, the packet luminosities ('weights') are attenuated by free-free absorption and photo-ionisation processes. The cross-sections for these processes are calculated from the densities, ionisation states and temperatures of the wind cell. These are then used to update an 'estimator' for the energy transfer to the cell and reduce the photon packet weight by an appropriate amount, under the assumption that those photons that interact with the cell are representative of the light falling upon it across a broad range of wavelengths. For any given frequency band i between $\nu_{\rm i,min}$ and $\nu_{\rm i,max}$ in a given cell c of volume V_c, the mean spectral intensity is calculated from the path of each photon j of wavelength λ_j in that cell, s_j and its photon weight W_j as

$$J_i = \frac{1}{4\pi V_i} \sum_{\nu_{\rm i,min}<\nu_j<\nu_{\rm i,max}} W_j s_j. \tag{2.12}$$

A photon may only spend some fraction of its total simulation path in a given frequency range, can change frequency mid-cell via reprocessing, and may potentially exit and re-enter a cell. Once a full flight of photons has been run, the code then generates a model for the spectral energy distribution within each frequency band. This is done to allow us to extrapolate the full spectral energy distribution incident upon a given cell from only a small number of photon interactions in each band. Both power law and exponential fits are used as

$$J(\nu)_i = K_{pl}\nu^{\alpha_{pl}} \tag{2.13}$$

and

$$J(\nu)_i = K_{\rm exp}e^{-h\nu/kT_{\rm exp}}, \tag{2.14}$$

where α_{pl} and the constants K_{pl} and K_{exp} are adjusted to ensure the mean spectral intensity within the band fits the total recorded spectral intensity for that band J_i. These band-limited fits can then be integrated to produce ionisation rate estimators, $\gamma_{i,i+1}$, for the ionisation of species in ionisation state i to state $i+1$ as

$$\gamma_{i,i+1} = \sum_{j}^{bands} \int_{\nu_{\rm j,min}}^{\nu_{\rm j,max}} \frac{J(\nu)_i \sigma_K(\nu)}{h\nu} d\nu. \tag{2.15}$$

The code then constructs an ionisation and recombination rate matrix using the number densities for electrons n_e, ionisation state i of species x $n_{\mathrm{x_i}}$, total population of species x n_{x} and recombination probabilities $\alpha_{i,j}$ for each ionisation state. For a simple wind consisting only of H and He, an example rate matrix would be expressed as

$$\begin{bmatrix} 1 & 1 & 0 & 0 & 0 \\ \gamma_{\mathrm{H_I,H_{II}}} & -n_e\alpha_{\mathrm{H_{II},H_I}} & 0 & 0 & 0 \\ 0 & 0 & 1 & 1 & 1 \\ 0 & 0 & \gamma_{\mathrm{He_I,He_{II}}} & -n_e\alpha_{\mathrm{He_{II},He_I}} - \gamma_{\mathrm{He_{II},He_{III}}} & 0 \\ 0 & 0 & 0 & \gamma_{\mathrm{He_{II},He_{III}}} & -n_e\alpha_{\mathrm{He_{III},He_{II}}} \end{bmatrix} \begin{bmatrix} n_{\mathrm{H_I}} \\ n_{\mathrm{H_{II}}} \\ n_{\mathrm{He_I}} \\ n_{\mathrm{He_{II}}} \\ n_{\mathrm{He_{III}}} \end{bmatrix} = \begin{bmatrix} n_{\mathrm{H}} \\ 0 \\ n_{\mathrm{He}} \\ 0 \\ 0 \end{bmatrix}. \tag{2.16}$$

The code then iteratively substitutes in values of n_e and the various species populations into it in order to arrive at a final ionisation state for the wind in that cell.

Once the temperature and ionisation state are set in each cell, the code then runs another flight of photons through the model. The change in ionisation state and temperature in each wind cell will result in both a change to the various interaction cross-sections, and *also* a change to the emission in the wind, plus optionally changes in the disk surface temperature and thus emission. This results in a different radiation field across the model and, as a result, a change in heating and cooling rates. The code iterates for a fixed number of cycles, hoping to attain at least a $\approx 95\%$ convergence rate in the temperature across the wind; which is to say, until $\approx 95\%$ of cells do not substantially change in temperature between iterations. This typically takes 20-30 cycles. Determining whether or not the wind is sufficiently converged is an expert, not automated process. For geometries like the biconical wind outlined in section 1.2.2, some cells in the wind (particularly those on the outer edge of the wind base) can be heavily shielded from the central source. When the rest of the wind is well-sampled, these cells receive few photons. As a result, they have high Poisson noise, which means that the heating and cooling rates calculated can swing wildly from one cycle to the next, preventing the cell from converging. As these heavily-shielded cells are often heavily-shielded from the *observer* as well, their contribution to the final spectrum is quite low, and it is less important if they fail to converge. However, for simulations where observations from underneath the wind cone are important, particularly at low angles, this can be an issue.

2.2.2.2 Spectral cycles

Once the ionisation cycles have concluded and the ionisation state of the wind has been fixed, the *spectral* cycles begin. The aim of these is to generate observed spectra in a

limited frequency range for a set number of observer angles to the disk. Generating multiple spectra in a single run is important considering that many of the observed types of AGN are believed to be the same class of object viewed at a range of angles as discussed in section 1.2. By generating multiple spectra for a single model in a single simulation run, PYTHON can efficiently test how suitable a candidate model is for a unified model.

In this stage, photon packets are generated for the central source and as appropriate for the ionisation state and temperature of the wind. At each photon-matter interaction, the code makes use of the 'viewpoint' technique developed by Woods (1991), and referred to as the *'extract to spectra'* step in figure 2.3. When a photon packet would be reprocessed, the code determines the probability of it being scattered or re-emitted in the direction of each observer specified and increases the amount of radiation seen by that observer by the appropriate amount (attenuated by the thickness of wind material between the reprocessing site and the observer). The photon's path through the wind then continues. This ensures that each photon contributes to the spectrum at each observer position, minimising statistical error. This is particularly important for observer sight-lines through heavily attenuating material like the disk wind (e.g. those corresponding to BAL Quasars or low-angle Type 2s).

As with the ionisation calculations, the spectra are built up in a series of cycles. Even-sized flights of photons are generated, run through the model, and used to update the output spectra. This enables the code to easily 'continue' runs that were originally started with an insufficient number of photons, by working with the saved ionisation states and spectrum files. A typical spectrum may be generated from 20-40$\times$ as many photons as go into each ionisation cycle.

2.2.3 Macro-atoms

For a subset of interactions with species of high importance to the final spectrum, e.g. Hydrogen and Helium, the simple 2-level atom approximation for line interaction is not sufficiently detailed. The Balmer and Lyman series are of particular importance in AGN spectra, and much reverberation mapping is done on the Hβ line, in particular. In order to improve the treatment of lines from certain atomic species, we adopt the macro-atom formulation of Lucy (2002, 2003), which makes several fundamental assumptions of the system:

- The flow of energy through a medium can be described in terms of indivisible packets of either radiant or kinetic energy (*r-packets* or *k-packets*).
- A medium can be discretised into 'macro-atoms', each of which has energy levels that directly correspond to the energy levels of the *true* atomic species they represent.

- A macro-atom can be 'activated' to an internal energy level by absorbing an energy packet.
- An 'activated' macro-atom can change state without emitting or absorbing another energy packet.
- An 'activated' macro-atom can de-activate by emitting an energy packet (either a *k-packet* or *r-packet*).
- An emitted energy packet has the same energy as the original energy packet that 'activated' the macro-atom.

We can define the flow of energy into a level i of a *true* atom in terms of the excitation and ionisation energy of that level ϵ_i (units: eV), and the radiative transition rates into that level from another j as R_{ij} (units: $m^{-3}s^{-1}$). This gives us the rates of radiative absorption to $\dot{A}$ and radiative mission from $\dot{E}$ as

$$\dot{A}_{li}^{R} = R_{li}\epsilon_{li} \text{ and } \dot{E}_{il}^{R} = R_{il}\epsilon_{il}, \tag{2.17}$$

where l is the sum for transitions involving all lower energy levels, and ϵ_{il} is $\epsilon_i - \epsilon_l$. We can equivalently define the rates at which a level absorbs energy from $\dot{A}_i^C$ or loses energy to $\dot{E}_i^C$ the thermal pool in terms of collisional excitation and de-excitation probabilities C_{ij}. This gives us the equation describing the total rate of energy change for a level i as

$$\dot{A}_i^R + \dot{A}_i^C - \dot{E}_i^R - \dot{E}_i^C = (\mathcal{R}_{li} - \mathcal{R}_{il})(\epsilon_i - \epsilon_l) \tag{2.18}$$

Moving from a single atom to an assembly of many, we can state that if the level populations are in statistical equilibrium, then we can describe that the total transition rates to all higher and lower levels u and l from a given level i must be

$$(\mathcal{R}_{li} - \mathcal{R}_{il}) + (\mathcal{R}_{ui} - \mathcal{R}_{iu}) = 0. \tag{2.19}$$

If we multiply by ϵ_i and substitute in equation 2.18 to remove $(\mathcal{R}_{li} - \mathcal{R}_{il})\epsilon_i$, we get a final equation that describes the energy flow into and out of a level i as

$$\dot{E}_i^R + \dot{E}_i^C + \mathcal{R}_{iu}\epsilon_i + \mathcal{R}_{il}\epsilon_l = \dot{A}_i^R + \dot{A}_i^C + \mathcal{R}_{ui}\epsilon_i + \mathcal{R}_{li}\epsilon_l. \tag{2.20}$$

This equation states that in statistical equilibrium, the energy flow *into* a given level i (in terms of energy absorbed from incident radiation and taken from the 'thermal pool' of the system by collision, and from internal transitions from other levels) must be

matched by the energy flow *out* of the level (in terms of radiative losses, energy lost to the thermal pool, and energy lost to transitions to other levels). It describes the bulk behaviour of a volume element consisting of many atoms in terms of the micro-physical processes of a single atom, as long as energy transfer occurs in discrete 'packets'.

If we assume that the system is in radiative equilibrium, i.e. there is no net change in the total energy of the system and all radiation that is absorbed is re-radiated, then we can follow the transitions arising from a given activation indefinitely as energy flows back and forth between the energy levels of one species, the thermal pool, and the energy levels of others until it results in a radiative de-excitation. This process of activation, internal transition and re-emission is shown in figure 2.4.

For most species, PYTHON implements simple 2-level approximation where once excited (by either an *r-* or *k-packet*, the atom either radiatively de-excites or collisionally de-excites, generating a *k-packet*. For Hydrogen and Helium it uses multiple levels (in our work, 10 and 20 respectively), and follows the full macro-atom formulation including internal transitions (Sim et al., 2005; Matthews et al., 2015). During the radiative transfer process, any reprocessing interaction is treated using the method outlined in figure 2.5. One major deviation is the addition of a term for adiabatic cooling; *k-packets* can be lost not just by eventual re-radiation, but also by adiabatic cooling as the wind expands.

In the ionisation cycles, as photon packets pass through the wind, the code updates 'estimators' in each cell. These 'estimators' are Monte Carlo estimations of the *true* mean rate-determining radiation field properties in each cell. They record the contribution a photon packet would make to each process for each ionisation state and energy level of macro-atoms within the cell. This includes continuum processes like Compton scattering and radiative ionisation as in the non-macro-atom mode, but also estimates the contribution of that photon packet to bound-bound interactions when the transition comes into resonance, *even when the photon does not scatter*. This allows for a large number of photon packets to contribute to the estimators for a given line. Given estimators of the rates of each process for each species, we can arrive at the ionisation fractions and level populations by solving a matrix similar to that in equation 2.16.

The full macro-atom method provides much more accurate estimations of level populations than the simple dilute Boltzmann distributions assumed for our two-level atoms. As reverberation mapping makes heavy use of the Hβ line, which is emitted by an internal transition between atomic levels, accurately capturing the populations of these levels is key to accurately simulating the emission process.

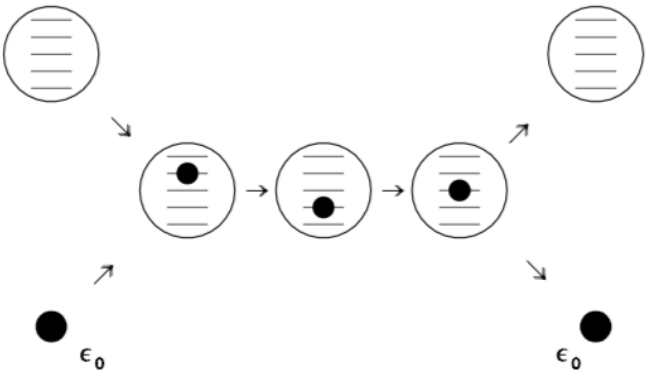

FIGURE 2.4: Plot of combined optical depth in a wind cell reproduced from Lucy (2002), showing a representation of a macro-atom interacting with an incoming packet of energy ϵ_0.

2.2.4 Variance reduction

It can be challenging to obtain sufficient photon sampling in regions of a PYTHON model that are shielded by optically thick regions to get good estimates of the photon fluxes in the cells there. As Monte Carlo estimators have a Poisson error proportional to $\sqrt{n}/n$, for low photon counts the estimators for a given property of the radiation field can be incredibly noisy. This results in dramatic changes in ionisation state between iterations, making it hard to converge on a stable wind state as discussed in 2.2.2.1. Improving the sampling of optically-thick sections of the wind by simply increasing the photon count is highly inefficient and results in large numbers of photons being 'wasted' on already well-sampled regions of the wind. We briefly explored implementing 'variance reduction' by packet splitting/Russian rouletting (Hendricks and Booth, 1985; Harries, 2015). In this modified version of MCRT, photons are 'split' when they enter certain regions into multiple copies each with lower 'weight' when calculating properties (e.g. energy transferred to the region through collisions, presence in a spectrum), allowing one or two photons that penetrate a shielding region to be multiplied up to fully sample the space behind it. An example illustration of a photon in PYTHON splitting is shown in Figure 2.6.

This is typically handled by generating an 'importance map' of the problem. Photons entering an important region from one that is *not* important are split, so they can more fully sample the region. A single inbound photon moving from a region of importance $I_{\rm prev}$ into a region of importance $I_{\rm curr}$ is split into N copies, where $N = I_{\rm curr}/I_{\rm prev}$. Each copy of the photon has a weight equal to N^{-1} that of the original photon. Photons from important regions entering less important ones are instead Russian rouletted. A probability p is drawn from a uniform distribution $0-1$. If $p < N$ the photon survives, and has its weight increased by a factor of N^{-1}. Otherwise, the photon is 'killed', its weight reduced to 0 and it is no longer followed. Over for a large number of photons, this process conserves the total photon weight but reduces the number of photons modelled.

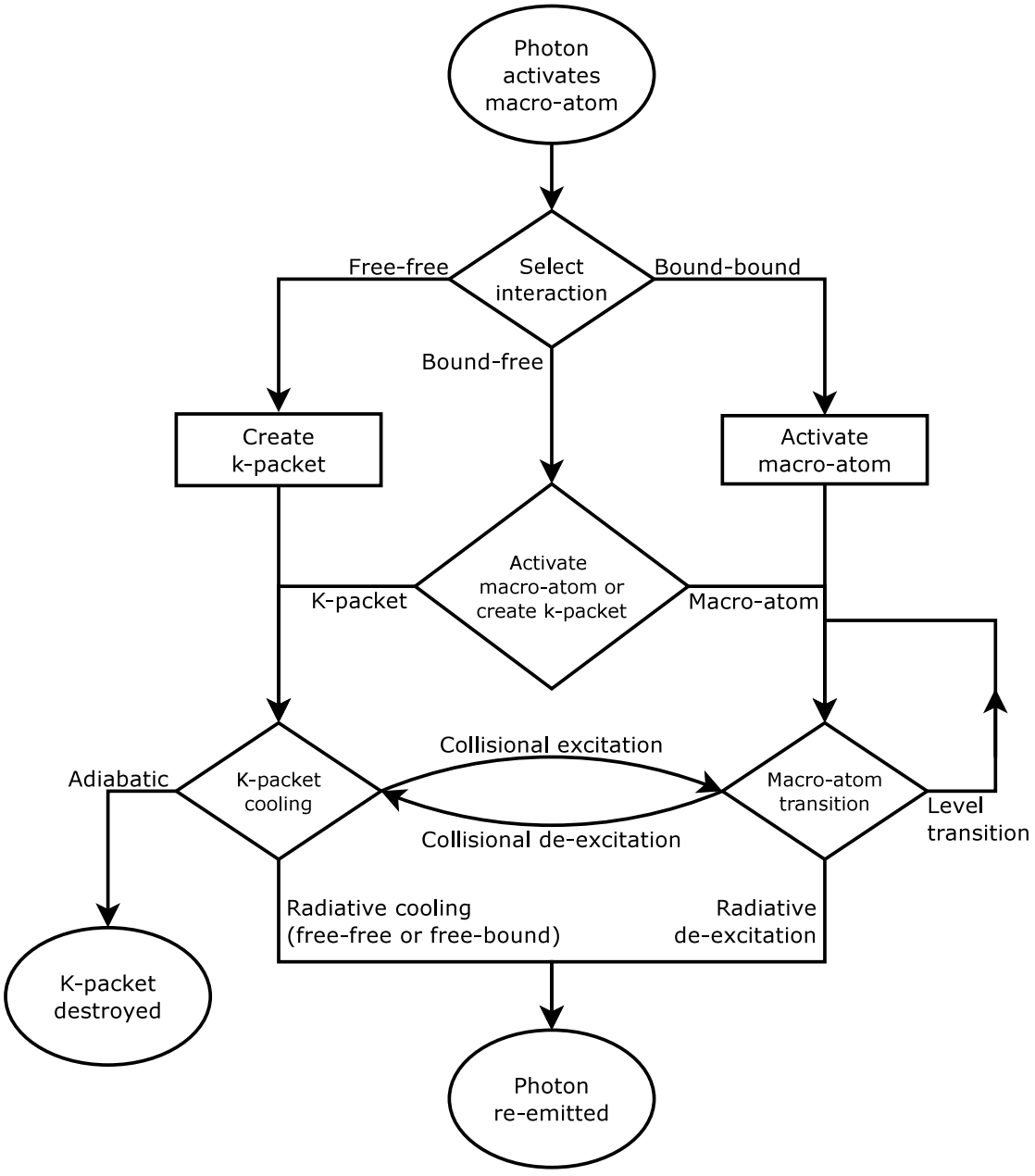

FIGURE 2.5: Diagram of the simulation flow for macro-atom processes. Processes in **red** are only performed in the ionisation cycles (see section 2.2.2.1), processes in **blue** are only performed in the spectral cycles (see section 2.2.2.2).

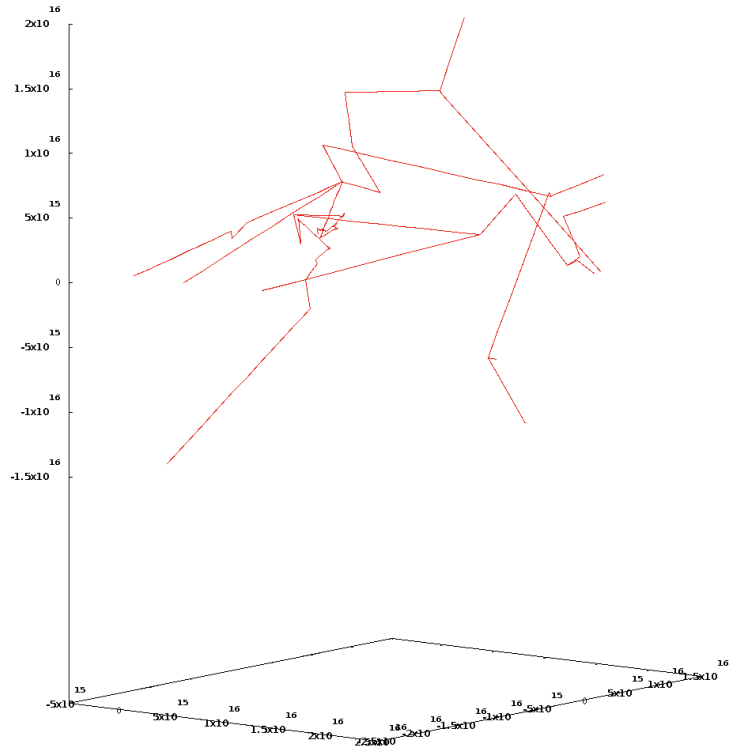

FIGURE 2.6: Example branching photon paths implemented in PYTHON

.

The splitting/rouletting technique has flaws; splitting prematurely can massively increase simulation run-times by oversampling already well-explored regions, and it is possible to end up with spurious precision in regions where a few anomalous photons have been split excessively and failed to spread out. Because of this, creating the importance map is a non-trivial task and the required maps are likely to change with the ionisation state of the wind. We explored implementing the automatic iterative technique developed for nuclear physics applications in Davis and Turner (2011), but had difficulty defining a metric to automatically assign importance based on. The treatment of optically-thick regions in PYTHON is a topic of ongoing work (see section 6.1.4.

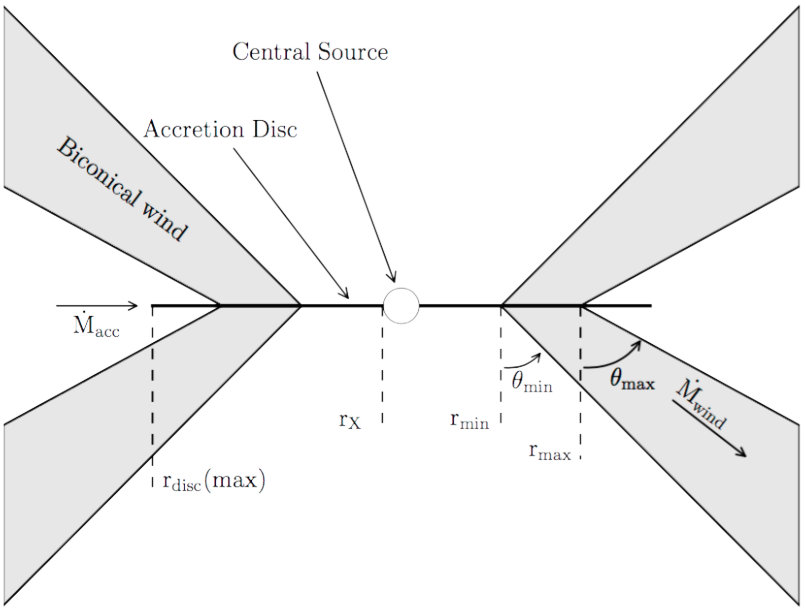

FIGURE 2.7: Diagram of the Shlosman and Vitello (1993)-style biconical disk wind model used in our work, originally defined in Matthews et al. (2016).

2.3 Model

PYTHON implements multiple models of AGN, including one inspired by the model for CVs in Shlosman and Vitello (1993) and the model from Knigge et al. (1995). For this work, we have used the Shlosman and Vitello (1993) model, which is illustrated in figure 2.7, and consists of:

- A central SMBH with a given mass M_{BH}, assumed to have zero spin.
- A spherical X-ray emitting corona surrounding it, with radius r_X. For this work, we take r_X to be innermost stable circular orbit ($r_{\rm ISCO}$ or $3 \times R_s$, the Schwarzchild radius for a non-spinning black hole).
- A Keplerian accretion disk of inflowing matter, extending from a maximum radius $r_{\rm disc,max}$ down to r_X. This accretion disk is computationally modelled as a series of annuli each of which emits as a Shakura-Sunyaev disk modified by the radiation incident upon it. Unlike in other models (e.g. Horne et al. (1991); Murray and Chiang (1996)), this disk is not approximated as infinitesimally thin.
- An outflowing biconical wind launched from the surface of the disk. This wind is launched between an inner radius $r_{\rm min}$ and outer radius $r_{\rm max}$, and has an minimum launching angle $\theta_{\rm min}$ and maximum launching angle $\theta_{\rm max}$. The density of the wind depends on the mass outflow rate $\dot{M}_{\rm wind}$ (units: $M_\odot yr^{-1}$), as well as the terminal velocity v_∞ (units: $cm\ s^{-1}$).

Tables of parameters describing the values for each are included in the science chapters, outlining the specific instances of the model used there. Previous works using PYTHON, including Matthews et al. (2016), have developed 'standard' PYTHON models for a range of systems, and our work is based upon these standard models.

We use the same geometry when simulating both QSOs and Seyferts. According to the unified model of AGN discussed in section 1.2, QSOs and Seyferts are similar objects, distinguished mostly by luminosity and mass of the SMBH. Bentz et al. (2009a) shows that when the mass of the central object is increased by a factor of X, we would also expect r_{ISCO} and the wind launch radius to scale up linearly. As a result, the QSO and Seyfert models used in chapters 3, 4 and 5 are geometrically identical, separated only by this scaling factor.

2.3.1 Smooth and clumpy winds

There are a few key differences between the BLR model used by PYTHON and that of many other codes (e.g. Leighly et al. (2018)). In the common Local Optimally-emitting Cloud model (LOC), the BLR is composed of a large number of individual clouds, typically with clouds of a range of densities existing at any given radius. Each cloud is optically thick and absorbs all radiation that falls upon it. The number and size of the clouds is low enough that each cloud (and the external observer) has a direct view to the central source of ionising radiation. This means that every cloud is exposed to the same spectral energy distribution, with the flux differing with radius. The result is that an ionisation gradient exists *within* each cloud, and as a result virtually all ionisation states exist at all radii. To determine these states, and thus the emission from each cloud, 1-dimensional models can then be run for each using an ionisation code like CLOUDY Ferland et al. (2013). The emission from each cloud can then be combined to synthesise a full spectrum. Figure 2.8 illustrates the SED and ionisation structure at each position within the wind.

Implementing macro-clumping within PYTHON would be impractical, requiring an incredibly high resolution for our plasma grid in order to capture intra-clump ionisation structure (on the order of 100 cells per cloud). This would impose prohibitive memory requirements. For practical reasons, our work instead uses a smooth/micro-clumped wind. In a smooth/micro-clumped wind, instead of being modelled as a large number of individual clouds, the wind is a single continuous medium. It is composed of a large number of tiny clouds, each of which is optically thin, but across large scales (i.e. the size of a grid cell) attenuation and reprocessing by these clouds shape the luminosity and SED of the local radiation field. This results in the ionisation structure becoming stratified *by radius across the wind*, rather than within each individual clump, as shown in figure 2.9. A micro-clumping model differs from a purely smooth model by maintaining the benefits of a smooth model on a large scale, whilst allowing for local

density enhancements to increase the rate of collision-dominated processes. The level of clumping is set by a *clumping factor* f; the proportion of the wind volume that is actually occupied by the clumps. Clumping factors of $10^{-1} - 10^{-3}$ are typical and do not violate the assumption that the clumps themselves are optically thin.

2.3.2 Relativistic Effects

As the BLR is close to the black hole, the effect of gravitational redshift must be considered. Gravitational redshift acts on photons emitted radius r_e from the black hole with wavelength λ_e such that their wavelength measured by a distant observer λ_∞ can be expressed as

$$\frac{\lambda_\infty}{\lambda_e} = (1 - \frac{R_s}{r_e})^{-\frac{1}{2}}. \tag{2.21}$$

In our models, the disk wind is typically launched at a radius of around $150 \times R_s$. At this radius, the ratio λ_∞/λ_e is ≈ 1.0034. Meanwhile, the orbital velocity of the wind is on the order of $10^4\ km\ s^{-1}$. The equivalent ratio of Doppler shifted wavelength λ_{Doppler} to rest line wavelength ratio $\lambda_{\text{Doppler}}/\lambda_0$ is ≈ 1.033, an order of magnitude higher than the effects of gravitational redshift. As such, the model neglects it. The $\approx .1c$ orbital velocities that make gravitational redshift negligible might be expected to require a full treatment of relativistic Doppler shift. At this orbital velocity however, relativistic Doppler shift only results in a 5% departure from classical Doppler shift, making it an important second-order effect, but still one that can be safely neglected for the purposes of generating transfer functions at present.

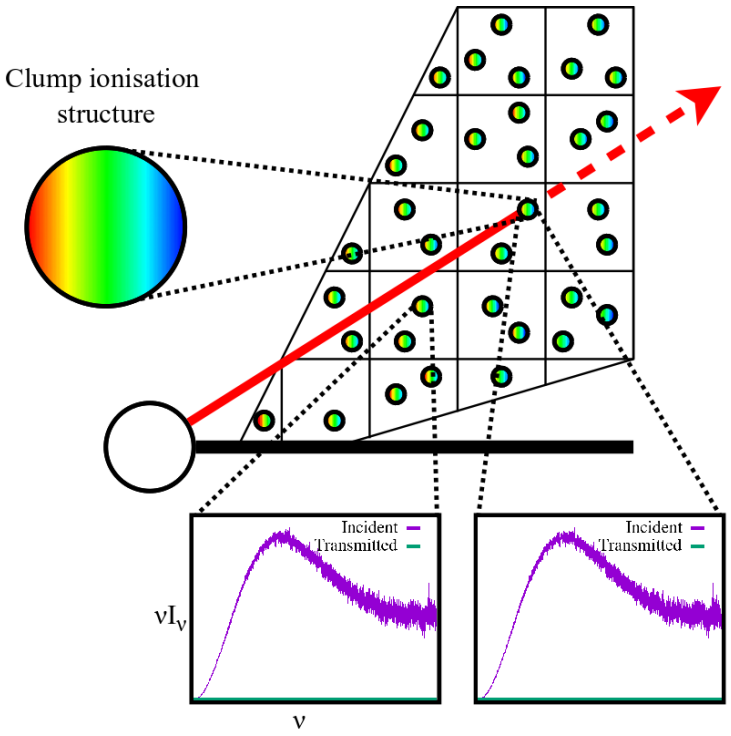

FIGURE 2.8: Diagram of the ionisation structure and spectral energy distribution in the Locally Optimally-emitting Cloud model. Clump size has been exaggerated for visibility; the actual model assumes the clumps are so small that shadowing effects are negligible.

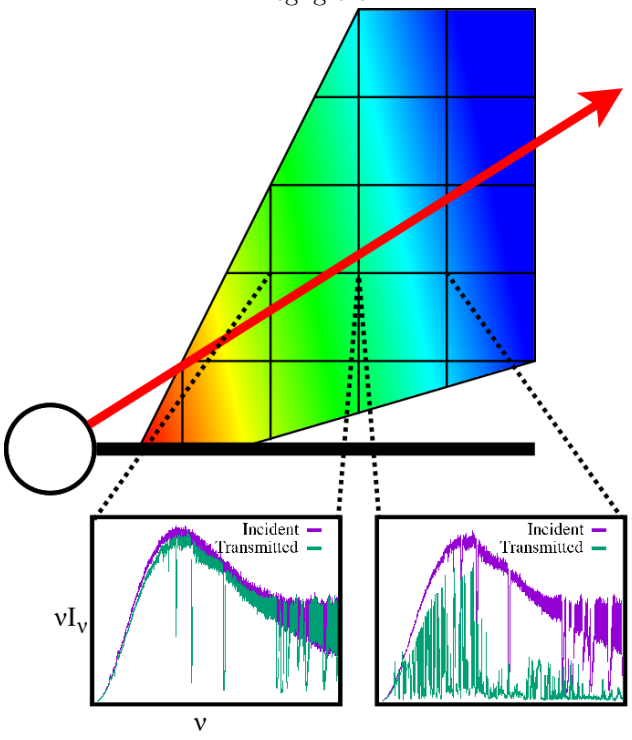

FIGURE 2.9: Diagram of the ionisation structure and spectral energy distributions in the smooth/micro-clumped wind model.

2.4 Software sustainability

The PYTHON code used in this thesis has been under continuous development since 1997, and contains almost 70,000 lines of *c* code. 29 classes define the simulation components, and 648 functions initialise them using custom input files, and define the relationships between them during simulation. The code is mostly written in pre-ANSI-standard *c* format, and as a result is quite challenging for users coming from a modern *c* background, or from languages more modern than *c*, to get used to. As the code has been continuously improved, and applied to a broad range of system types and geometries for each system, it has a huge number of options; 8 different wind types, and 10 separate ionisation schemes, which are selected between using custom input text files. In order to make it easier for new users to join the project, as well as to make the code easier to use for existing users, we set about improving the standard of documentation. Two separate documentation types were set up.

The first was an *end-user* focused set of documentation for the input file format, using the Sphinx open-source Python documentation generator (Sphinx Team, 2018) (where Python refers to the programming language, not the astrophysical simulation code PYTHON that is the subject of this thesis). The documentation was produced, where possible, automatically – by analysing the source code using a Python script to find variables in need of documentation, and listing their types and, where valid, the options they take (e.g. all 8 wind types). This process also acted as an *inventory* of the code's capabilities. Some of the options present in the codebase were no longer maintained, or had been developed for testing purposes and were not suitable for standard use. Parameter naming was also inconsistent and in some cases unintuitive. As part of the documentation effort, many parameters were renamed to follow a standard, consistent format, then for each 'class' of parameter (e.g. the settings for a Shlosman and Vitello (1993)-style wind) a documentation file was created and the options fully described in a way that is as best as possible accessible to a non-developer. The finished documentation was then hosted on the ReadTheDocs documentation hosting website (ReadTheDocs Team, 2018), for easy access.

Secondly, we developed a set of developer-focused documentation to make it easier to contribute to the codebase. This was, again, written partly programmatically. The code has existing comments, but they were inconsistently styled and not every function was commented. A Python script was written to parse the existing comments and generate new ones in a format readable by the Doxygen documentation tool (van Heesch, 2018). Of great use are the function call graphs Doxygen is capable of producing that show how data flows between functions, for example figure 2.10. Our developer documentation was then hosted on the CodeDocs documentation hosting website (CodeDocs Team, 2018).

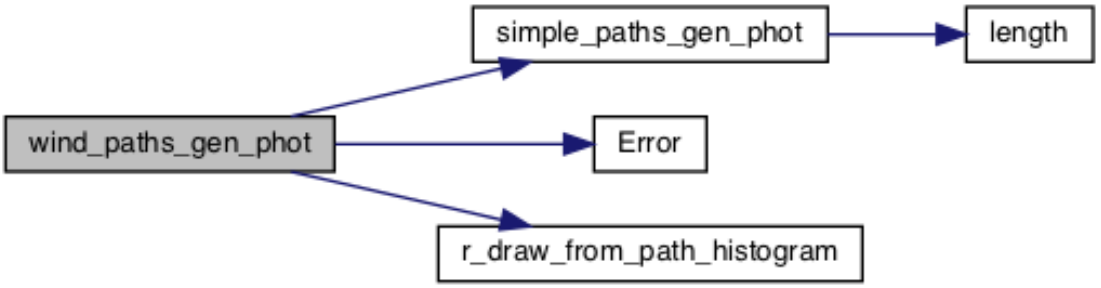

FIGURE 2.10: Example call graph for function generated by Doxygen (van Heesch, 2018)

Chapter 3

Self-Consistent Reverberation Mapping With Python: Implementation, Testing, Interpretation

3.1 Introduction

We attempted to develop a technique for forward modelling transfer functions that would expand on those covered in section 1.3.4.

In summary, the assumptions made in previous models from section 1.3.4 are:

- For models including photo-ionisation e.g. Goad et al. (1993), the entire BLR 'sees' the same spectral energy distribution. The irradiance for a given wavelength at a given point $\vec{r}$ in the BLR I_λ is affected only by geometric dilution, falling off equally for all wavelengths as $I_\lambda(r) \propto L_\lambda r^{-2}$. Absorption does not affect the SED; there are no self-shielding effects (as shown in figures 2.8 and 2.9).
- For simple models e.g. (Welsh and Horne, 1991) the emissivity/responsivity of the BLR is parameterised as a simple function. This is typically dependent on $r^{-\alpha}$ (where α is a constant), within a fixed range $r_{\min} - r_{\max}$. The local atomic physics are not considered.
- The ionisation state and emissivity of a position $\vec{r}$ in the BLR is dependent *solely* on the continuum luminosity L at a time $\tau = r/c$ ago. The contribution to heating and ionisation from wind self-irradiation or photons that have undergone multiple reprocessing interactions (e.g. Compton scattering followed by photo-ionisation

elsewhere in the BLR) is neglected. The transfer function is *also* only dependent upon photons travelling directly from the BLR to the observer without interacting along the way.

- The BLR emits/responds isotropically for all processes. This is relaxed in Murray and Chiang (1996), but the general assumption is that all emission in a given line is isotropic and there is no dependence on the position or local kinematics within the wind.

As Python is a full radiative transfer and ionisation code, it is possible to use it to generate transfer & response functions without these assumptions:

- From the existence of BAL features (in the AGN models where the BELs and BALs arise in the same region outlined in section 1.2) we would expect self-shielding to have an impact on the SED the BLR sees. As a full radiative transfer code using a smooth/micro-clumping wind model, Python allows for the SED and irradiance experienced throughout the BLR to vary with position, taking into account the physics of self-shielding.
- We would expect some photons to undergo multiple reprocessing interactions and contribute to the wind state at a range of times (or rather, that the wind would self-irradiate). This would particularly be expected for those travelling through dense areas of the wind, or those emitted with wavelengths near that of a resonance line with a high interaction cross-section (shown for Fe Kα in (Sim et al., 2010)). As discussed in section 2.2.1, Python uses 'photon bundles' that can undergo multiple reprocessing events. For example, a photon bundle can be emitted at one wavelength, ionise a macro-atom (section 2.2.3), then the energy from the packet can be re-emitted as a new photon bundle at a different wavelength by radiative recombination and go on to be further reprocessed.
- Emission lines within the BLR are observed to be strongly stratified, with different lines occurring at different radii (Kaspi et al., 2007). As such, we would expect the emissivity profile for a given line to be dependent on the atomic physics throughout the wind. This would lead to a more complex emission region than a simple single power-law profile between the hard physical boundaries of the wind model. Python performs full ionisation calculations for the BLR. As a result, the emissivity/responsivity can be determined in a self-consistent way from the atomic physics.
- Photons in emitted in resonance with an atomic line in accelerating outflowing material preferentially escape in a direction either with or against the velocity gradient. Photons travelling normal to it remain in resonance with the line, and are thus likely to be scattered off of it due to the high line opacity (Rybicki and Hummer, 1978). This results in angle-dependent emissivity which would be expected to

affect both the SED experienced up-wind, and the transfer function (from certain viewing angles). This effect is likely to be somewhat suppressed in real winds by the effects of turbulence in the wind, but still merits inclusion. Angle-dependent emissivities are *partially* implemented in Murray and Chiang (1996), but PYTHON supports them fully.

This chapter outlines the changes made to the code in a step-by-step way. We move from a simplified model to a full radiative transfer and ionisation model, illustrating the effect that each change has on the transfer function shape. In addition, we consider the behaviour not just of purely line photons, but also model the interactions of continuum photons that fall into the frequency ranges of interest, as previous works have considered exclusively line photons.

3.2 Methods

Previous models have constructed transfer functions by breaking the geometry down into a grid of elements. For each element, given a fixed delay and emissivity determined solely by their geometry, it is possible to calculate the contribution from that element to a given observer. As each element in the geometry has its own delay and velocity, this produces a transfer function plot of the full velocity-delay space of the system, with the level of precision solely down to how finely the geometry is discretised.

In order to produce a more accurate transfer function, we instead perform self-consistent ionisation calculations to determine the emissivity at each location. We also allow for paths from a given disk location to an observer be informed not just by that location's position relative to the continuum source, but also by the path photons from the continuum take to that location, including multiple scatters. These paths are not constrained to travel on a grid, although the wind ionisation state and temperature affecting their travel *is* discretised on a grid. We then compare the total path travelled to the path direct from the simulation origin, as the X-Ray corona and UV regions contributing most strongly to the wind ionisation state and temperature are small in comparison to the wind scale.

Using Python, we simulate the path of photons through the geometry of interest, in sufficient numbers to ensure that they reach all points in the geometry. This approximates the complete sampling of the simple model, producing a transfer function that exhibits a more realistic broadening of delays in the reprocessing response of the AGN environment. A smoothing would be expected from the contribution to line emission from longer delays arising from multiple scatters, and from the shape of the ionisation profile in the wind.

The precision of each velocity-delay response in the transfer function would be affected both by the discretisation of the geometry in the ionisation cycles of Python, and by the sampling of each region's contribution to the transfer function for a given observer. Sampling is better at regions near the central source. At large distances from the central source, the quality of the transfer function falls off as fewer photons from the central source reach those positions and emission is also substantially lower. The velocity-delay space available to simulations with full radiative transfer is also substantially larger than that of simple models. Photons at any frequency can have almost any delay if they undergo multiple scatters before finally escaping to the observer. However, whilst photons that have undergone multiple scatters are more poorly sampled, they also make a commensurately smaller contribution to the final transfer function.

3.2.1 Simple delays

The delay for a given photon packet is calculated purely as a function of the path travelled, under the assumption that the time spent in interactions like scattering is negligible compared to the travel time. For BLR emission zones on the order of 10s of light days across, this is a reasonable approximation. For those photons that contribute to a spectrum at a given angle of observation, a record is made of their paths and scattering details, including number of scatters and last atomic line interaction. This includes contributions via photon 'peeling off', implemented as Woods (1991) (similarly to Yusef-Zadeh et al. (1984)). In this method, after each interaction the proportion of a photon bundle that would be expected to scatter in the direction of an observer is calculated, and attenuation along the path to the observer is applied. The calculated flux is then recorded by the observer. Each photon bundle has a 'weight', essentially the total number of individual photons it represents. The photon bundle's weight is reduced in proportion to the 'peeled off' flux, and the simulation is then continued.

Not all photons generated in the system begin with 0 delay relative to photons from the central source. As a simple approximation, all photons are started with a delay equivalent to their distance from the origin of the simulation.

This is because we assume that emission from any accretion disk or wind in the model is correlated with the flux from the central source. That would be the case in any system where the surface temperature which determines disk emission is set by the central source. We assume this is the case for a given disk annulus when the local viscous heating is outweighed by the heating due to irradiation from the central source. For accretion disks, equation 5 from King (1997) suggests that for systems with central luminosity L_* and accretion disks of luminosity $L_{\rm acc}$ and albedo β, radiation dominates the surface temperature at *all* radii if equation 3.1 is satisfied:

$$L_* > 2.5 L_{\rm acc}(1-\beta) \tag{3.1}$$

Where $L_{\rm acc} = GM\dot{M}/r_{\rm disc}(min)$, and L_* is set to the central X-ray luminosity L_X. For our model, $r_{\rm disk} = r_g = 6GM/c^2$ and $\dot{M} = 5M_\odot$ yr^{-1}. thus $L_{\rm acc} = M_\odot c^2/(6 * 3.154 \times 10^7)$ ergs^{-1}. BLR disk albedos are calculated in Korista and Ferland (1998). These can vary substantially with wavelength, increasing from ≈ 0 to ≈ 1 for photons in resonance with Doppler-shifted atomic lines at a given location. For our realistic disk models featured in 3.3.2 we expect L_X on the order of L_{acc}. As such, we assume the temperature of the disk near the central source where disk emission is highest will be dominated by the continuum radiation rather than viscous heating. For the much less dense wind, the temperature will be radiation-dominated over a larger distance. It is important to establish this correlation as the inner disk in biconical disk-wind models generates a substantial amount of UV radiation. This flux both contributes to disk

ionisation and is reprocessed into the reverberation mapped lines. If the emission in these inner disk regions was not correlated with the central source flux, we would see a much weaker transfer function response.

We assume that dominant flux component contributing to the ionisation state and thermal pool of energy of the BLR is unscattered, arriving directly from the central source. This is a reasonable assumption, at least for our biconical wind geometries. Multiple-scatter at large scales within the disk is unlikely, and emission up to wavelengths of $\approx$ 6500Åis dominated by those regions of the disk closer than the wind launch radius. As such, the flux setting the ionisation state and temperature of the wind is unlikely to have been multiple-scattered. As emission is strongly dependent on the ion populations and wind temperature, we then assume photons emitted at time t_{emit} at location r are correlated with the central source luminosity at time $T = t_{emit} - (r/c)$. For this to work, we must also assume that the time for the environment to equilibriate to the new radiation field is negligible in comparison to the travel time of the photons (see Peterson and Horne (2004)). It is on the order of 10^2 seconds for expected wind densities, whilst BLR scales are on the order of 10s of light days in diameter.

3.2.2 Emissivity profile effects

The simple method outlined in section 3.2.1 describes the effects of multiple-scattering and simple radiative transfer effects on the delays of photons generated by the central source. However, by assuming that photons from the disk and wind start with a delay equal to $r_{emission}/c$ it treats the wind ionisation state as being wholly dependant on unscattered photons. In order to test whether this is a realistic assumption it is necessary to link the starting delays of recombination line emission from the wind to the distribution of paths of photons that set its ionisation state.

These effects are implemented in the wind ionisation cycles. During the last ionisation cycle, when the wind state has converged, each wind cell can be set to record the weight and path length of all photon bundles passing through it. The photon weights are used to build up a histogram of path lengths within the cell. During the spectral cycles, this histogram is used to generate a probability distribution function for the starting path lengths of photons generated within this cell by wind emission processes (including continuum and line). A path bin is selected proportional to the weight of photons incident within that bin, and a random uniform selection is made of a path within that bin. This is referred to as the 'wind path' method.

3.2.3 Atomic level-based delays

Further modification to the wind path method is necessary to account for the frequency dependence of emission components. Resonant scatter and recombination line emission is

highly dependent on the frequency of incoming photons. As a result, recombination lines are expected to be more dependent on photons that have already been reprocessed into a line (leading to multiple resonant scatter) or Doppler shifted into the correct frequency. In addition, recombination line emission is going to be more dependent on photons with energies high enough to directly ionise the atom. There will also be some dependence on lower-energy photons though heating and collisional ionisation. As accretion disks emit as black bodies, higher energy photons will tend to be emitted near to the central source. Lower-energy lines will therefore depend on photons emitted across a broader region.

A more detailed treatment is possible when using macro-atom models of emission (as discussed in section 2.2.3). It is possible to specify in the program input files a range of line transitions to track. Whenever an incoming photon bundle activates a macro-atom and the end result is emission in a tracked line, the path length of the photon is recorded in the cell in which the interaction took place. A flowchart of the full process is shown in figure 3.1. During the spectral cycles, when photon bundles are emitted in that line their starting path is drawn from the path histogram recorded in the cell of emission. In some cases, no histogram exists in a given cell due to under-sampling. This arises as some cells are impractical to fully sample, perhaps due to self-shielding effects. In this situation, the starting path defaults to using the wind path method. This process is illustrated in the flowchart in figure 3.2.

The escaping photon packets are output to file, including their positions, packet weights and frequencies. Details of their last scattering interaction before they reached the observer (last resonant interaction, and numbers and types of scatters) are also recorded. They are then binned by frequency and path delay, to produce a 2-d velocity-resolved transfer function as per Welsh and Horne (1991). It is possible to select photons by their last line interaction- this allows for an *actual* velocity-resolved transfer function to be plotted.

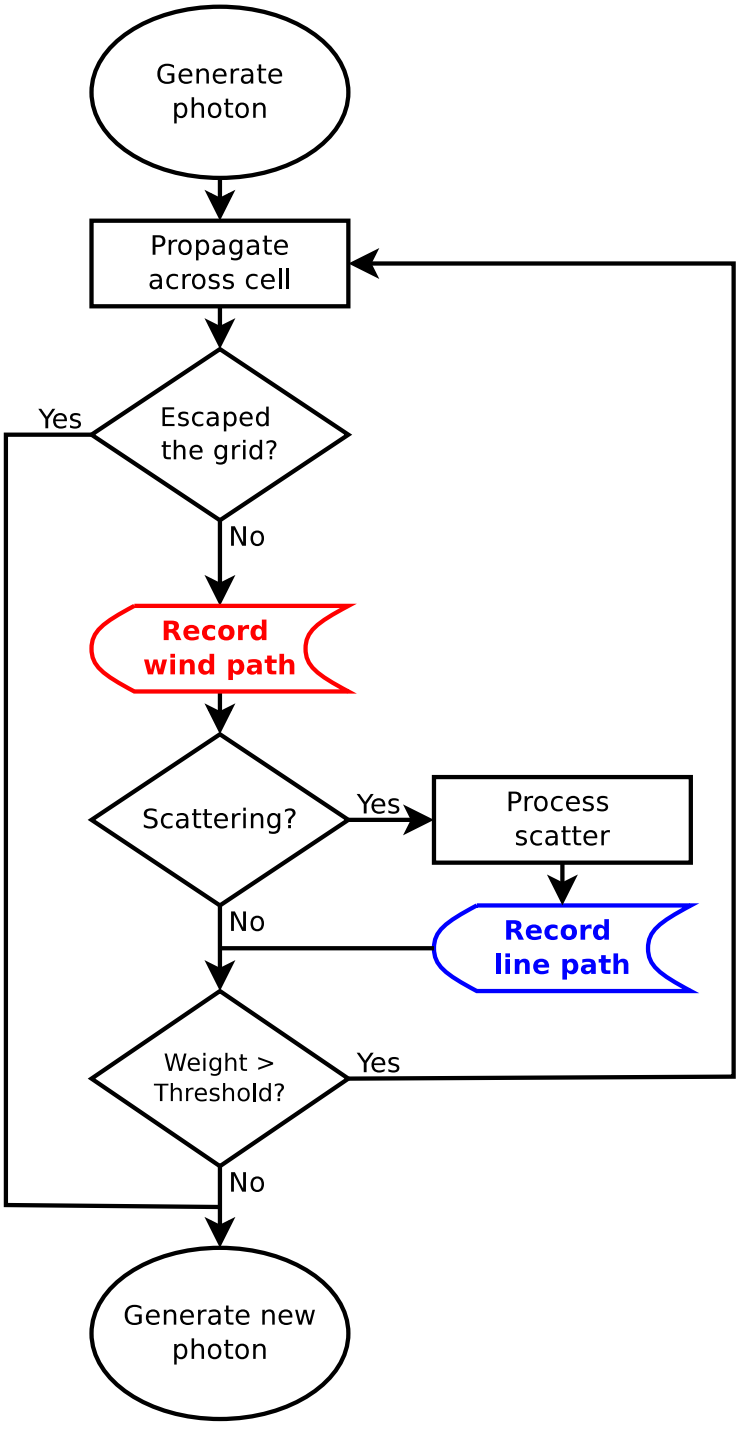

FIGURE 3.1: Photon processing flowchart for ionisation cycles. Processes in **red** occur when the macro-atom line and wind path methods are used, processes in **blue** occur for only for macro-atom line tracking.

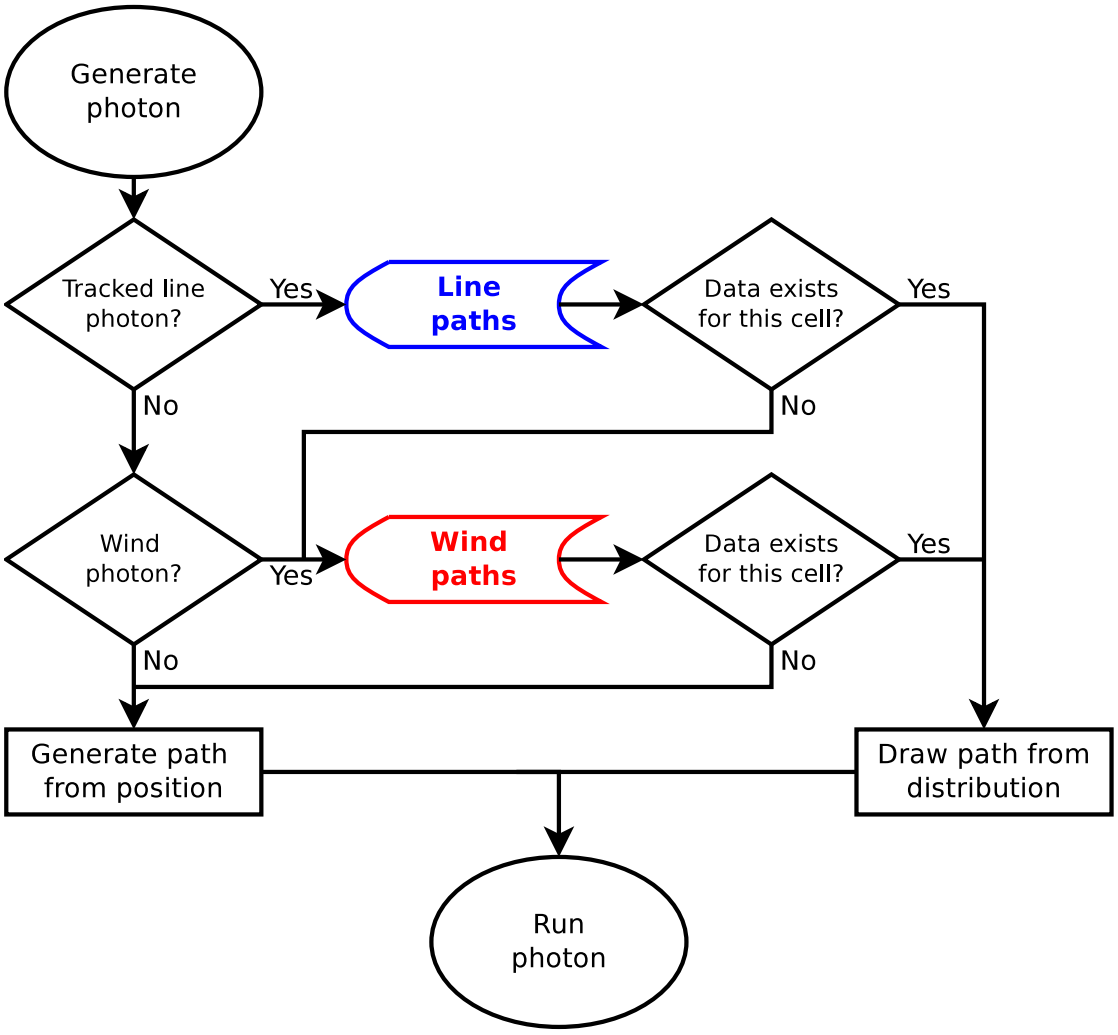

FIGURE 3.2: Photon processing flowchart for ionisation cycles. Processes in **red** occur when both macro-atom line and wind path methods are used, processes in **blue** occur only for macro-atom line tracking.

3.3 Simulations

We performed a range of simulations to compare transfer functions generated by the modified PYTHON code to prior work, and to generate realistic velocity-resolved transfer functions. We focused on rotating and outflowing models; whilst the case has been made for inflow in the BLR (Gaskell and Goosmann, 2016) we aimed to provide validation for other models within the group (Matthews et al., 2016) based on models of outflowing disk winds (observationally supported for AGN by Weymann et al. (1991); Turner and Miller (2009)).

3.3.1 Purely reprocessing models

3.3.1.1 Singly-scattering Keplerian disk

To validate the path tracking features, comparisons were made to transfer functions generated in prior work featuring no radiative transfer effects. Initial comparisons were made for an irradiated purely reprocessing accretion disk, as modelled in Welsh and Horne (1991) (hereafter WH91). The ionisation features of the code were disabled, and the disk modelled with a single-element, fixed-ionisation composition, with the detailed scattering treatment replaced with a single isotropic scatter on collision with the disk. Notable differences still exist between the models despite the simplifications. By moving away from a point source, we see substantial differences in the scattered intensities due to geometric effects. In general, our simulations agree well with those of WH91. In particular, the two elliptical features corresponding to the inner and outer disk edges can be seen. The 'notch' feature present at the long delay/low Doppler shift tip of the transfer function corresponds to the delay added by the finite size of the source in our simulations.

3.3.1.2 Spherical outflow with detailed radiative transfer

Radiative transfer features were enabled for further validation, with emission disabled but transfer effects such as multiple scattering and Sobolev escape probabilities enabled. Transfer functions were generated for a spherical homologous outflow as WH91 (figure 3.4), using the same simplified composition and ionisation as described in section 3.3.1.1. The transfer function for photons last scattered in one of the C IV doublet matches the expected form well. A clear minimum delay at large wavelengths and maximum delay for short wavelengths is visible, arising from the outflow away from/towards the observer. As the fastest points in the outflow are at the furthest radii, the most redshifted photons must have scattered off of the wind edge opposite the observer (with a total path of $3r_{disk}$, with the most blueshifted scattering on the direct line of sight. As a result of the

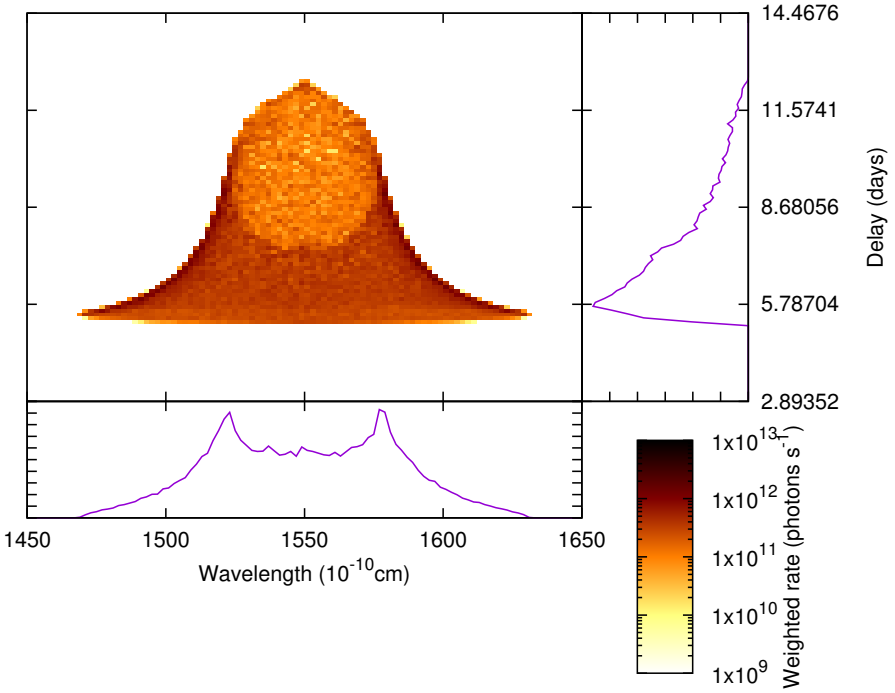

FIGURE 3.3: Velocity-resolved transfer function for rotating disk as Welsh and Horne (1991) viewed at 30°. Includes all photons that have resonantly scattered a single time off the C IV line, with the luminosity contribution from each photon re-weighted using its last scattering location to match the luminosity contribution per disk annulus to the $r^{-3/2}$ profile from the paper.

geometry, no points exist with high redshift at short delay, nor high blueshift at large delay.

3.3.1.3 Spherical outflow with self-consistent ionisation

Having demonstrated basic radiative transfer effects for fixed ionisation states, PYTHON's ionisation routines were used to set the wind conditions, for a quasar-like wind composition. Figure 3.5 illustrates the effects of the resulting inhomogeneous ionisation structure and detailed radiative transfer on the transfer function. The clearest effect is the greatly narrowed line. Whilst the simple model assumes a flat C IV concentration, with ionisation the C IV concentration drops off rapidly, as a result of increasing electron temperatures in the wind and lower density resulting in reduced recombination rates. Combined with the lower scattering at large radii as density falls, this means that we only see substantial C IV resonant scatter at the inner edge of the wind. This constrains the velocity range of the transfer function, as well as the delay range. With no photons scattering at either outer edge of the wind, we do not see the large-scale triangular shape described in section 3.3.1.2. The response is instead constrained to a narrow range of frequencies just around the line centre, with a minimal Doppler shift from the starting

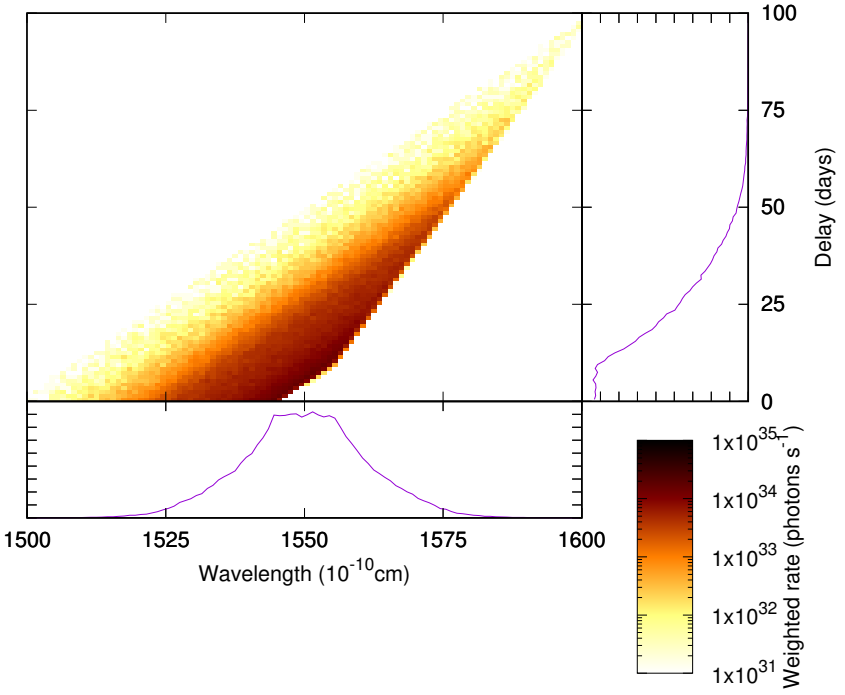

FIGURE 3.4: Velocity-resolved transfer function for Hubble-type spherical outflow as Welsh and Horne (1991). Includes all photons that have resonantly scattered a single time off the C IV line.

velocity of the Hubble outflow. The beginnings of the red and blue 'wings' can be seen, but only briefly; the intensity drops off from the inner-edge scattering 'plateau' much faster than compared to the simple model in figure 3.4.

Radiative transfer adds distinct new features into the wind. The 'stripe' feature at a slight delay from the main, singly-scattered response arises from the C IV doublet. Photons scattering off of the $\lambda = 1548$Å line come into resonance with the $\lambda = 1551$Å line as it is Doppler shifted to shorter wavelengths as the wind accelerates. These doubly-scattered photons have longer delays, offset by the time taken to travel between resonance regions, giving rise to the 'stripe'.

Multiple-scattering effects are highly dependent on the optical depth of the wind. Increasing the density by an order of magnitude resulted in changes to the transfer function as figure 3.6. For the same geometry and central source the profile is smoothed out and extended to longer delays. There is also a broadening of the line. Whilst in the thin outflow C IV density peaks at the innermost edge of the wind, in the denser wind C IV concentration peaks at a longer radius from the central source because shielding by the inner wind alters the intensity and SED it experiences. This results in the C IV response being spread across a more broad region of the wind, and thus giving rise to a longer set of delays. The ionisation profiles differ from the simple $E_{line}(r) \propto r^{-2}$ emissivity profile assumed for a sphere in WH91; as would be expected, each species has a different

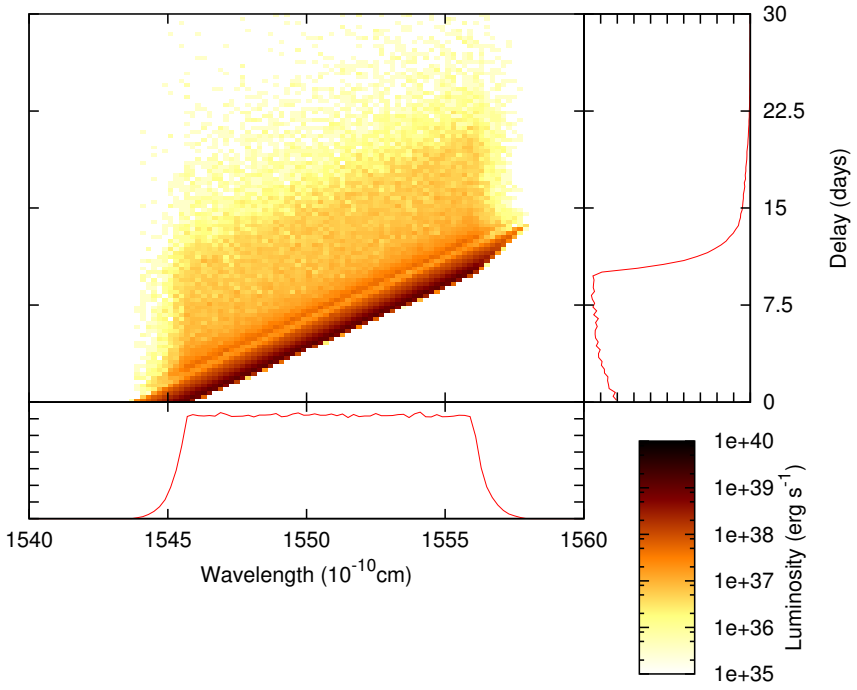

FIGURE 3.5: Velocity-resolved transfer function for Hubble-type spherical outflow as Welsh and Horne (1991). Includes photons that have scattered any number of times, whose last interaction was resonant scatter off the C IV line.

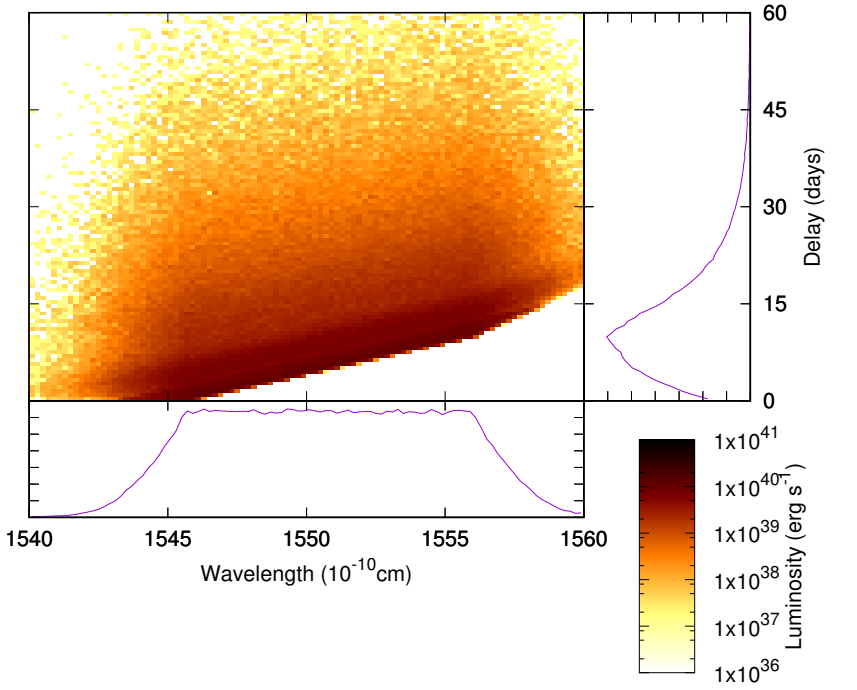

FIGURE 3.6: Sphere as 3.5 with 10× higher density than figure 3.5. Includes all photons whose last interaction was resonant scatter off the C IV line.

ionisation profile. We still see a faint signature of multiple-scatter as figure 3.5 at around 15 days delay for the line centre.

3.3.2 Rotating biconical wind models

Having demonstrated that the modifications to the code were correct, and illustrated possible deviation from prior work arising from radiative transfer and ionisation effects, we proceeded to generate a transfer function for the more complex and realistic model outlined in Matthews et al. (2016) and discussed in section 2.3. This model features an accretion disk and central corona with an equatorial rotating biconical disk wind. The system includes a black hole of radius $r_{ISCO} = 8.86 \times 10^{12} m$, with an accretion disk extending from $1 - 110\ r_{ISCO}$. The biconical wind launches from $50 - 100\ r_{ISCO}$, with opening angles of $\theta_{wind} = 70 - 82°$ to the normal of the accretion disk plane. We build up the delays compared to the photon travel time from the simulation centre, assuming that the ionisation state and temperature of the wind is dependent on the X-Ray corona and UV emitted in the disk at small radii. As a result, the departures from point source behaviour are fairly minimal. This does, however, stand in contrast to observational studies. Most reverberation mapping studies compare to the wavelength at 5100Å as a proxy for the ionising continuum (Wandel et al. (1999), Kaspi et al. (2000)). In our model, the region contributing to the flux at 5100Å actually extends out to $\approx 20\ r_{ISCO}$. This would be expected to lead to a 'smearing' of the transfer function at short timescales in comparison to our models.

The transfer function for this model is presented at two delay timescales in figure 3.7 to illustrate the range of behaviours, for Hα photons. Hα is chosen instead of the C IV line used in previous models as there is a strong Hα response across large regions of the wind. This allows for the contribution of the entire wind model to the transfer function to be sampled well with minimal computational resources.

As shown in the upper panel of figure 3.7, for short delays the transfer function resembles that of a Keplerian disk as figure 3.3. A clear, highly Doppler shifted inner edge to the disk tapering to longer delays with less symmetric rotational Doppler shift. At longer delays as seen in the lower panel, the structure diverges. The response in the blue wing is spread across a broader range of frequencies at a lower intensity, compared to the more clearly-defined, more intense red wing. This arises from the 40° viewing angle falling closer to the side of the wind cone flowing towards the observer. As a result, emission from within this side of the wind has a greater thickness of material to travel through than emission from the far edge of the wind. In addition, the far edge sees a weaker Doppler shift. Scattering off the plane normal to the observer sees no Doppler shift. The angle of the nearer, blue-shifted edge of the outflow to this plane is $\approx 65°$, whilst for the further, red-shifted side of the outflow the angle to this plane is $\approx 25°$. The projected velocities with respect to the observer, and thus the Doppler shifts, vary

accordingly. The outflow also features an 'oval' central structure at long delays. This resembles the oval signatures of the disk edges visible in figure 3.3. There is a rough resemblance to the shape of the spherical outflows, but these disk signatures dominate, suggesting that this feature of the transfer function is likely to correspond to multiple scatter within the disk-velocity dominated region. The low intensity of C IV emission at large radii makes the transfer function noisy and difficult to plot. Switching from Hα to C IV in figure 3.8, we see notably different behaviour. Whilst Hα is prevalent in the dense, heavily-shielded base of the wind C IV occurs mostly at large distances where the thin wind allows for greater ionisation by the central source. The C IV line response is notably narrower as a consequence, showing less rotational Doppler broadening, and has a stronger response at long delays. The oval inner-disk features seen at long delays in figure 3.7 are lost, and a stronger resemblance to the form of the transfer function for spherical outflow as figure 3.4 can be seen. The differing path-wavelength behaviours on the red and blue sides, and lack of low-path, long-wavelength photons for the extended region closely resemble the form of the spherical outflow. The large scale of the wind region, extending to $\approx 1000\ r_{ISCO}$, makes observing the triangular overall shape of the spherical model difficult.

These similarities suggest that for transfer functions generated by observation, it should be possible to derive information on the geometry by breaking them down into component behaviours. Generating a transfer function for all wind and scattered photons in the wavelength range near the line as figure 3.9 indicates that for sufficiently sensitive observations this may be practical. The smooth continuum time response does not completely overwhelm the disk signatures. Whilst when plotting the Hα line at long delays outflow signatures cannot be seen beneath the continuum flux, however the C IV line is visible as shown in figure 3.10.

3.3.2.1 Line emission profiles

Simple treatments of winds have modelled the response of the disk with a simple r^{α} intensity profile. For more complex geometries like the rotating biconical wind, where self-shielding may have a strong effect on the ionisation profile and radiation field experienced across the wind, this is unlikely to be accurate. Figure 3.11 plots r^{α} for $\alpha = -\frac{3}{2}$ & 2 against simulated line emission in the wind. At long distances from the central source a biconical wind's response profile quite closely resembles the $\alpha = -\frac{3}{2}$ model used for Keplerian disks, albeit with substantial spread at each distance arising from absorption by the inner edge of the wind. Close to the central source the simulated line emission profile departs dramatically, plateauing and broadening as the dense wind base strongly shields the outer edge of the wind. We see a two-orders-of-magnitude difference in the intensities at the same radius. Given the strong shielding effects, this would have a dramatic effect on transfer functions generated at sight-lines looking into

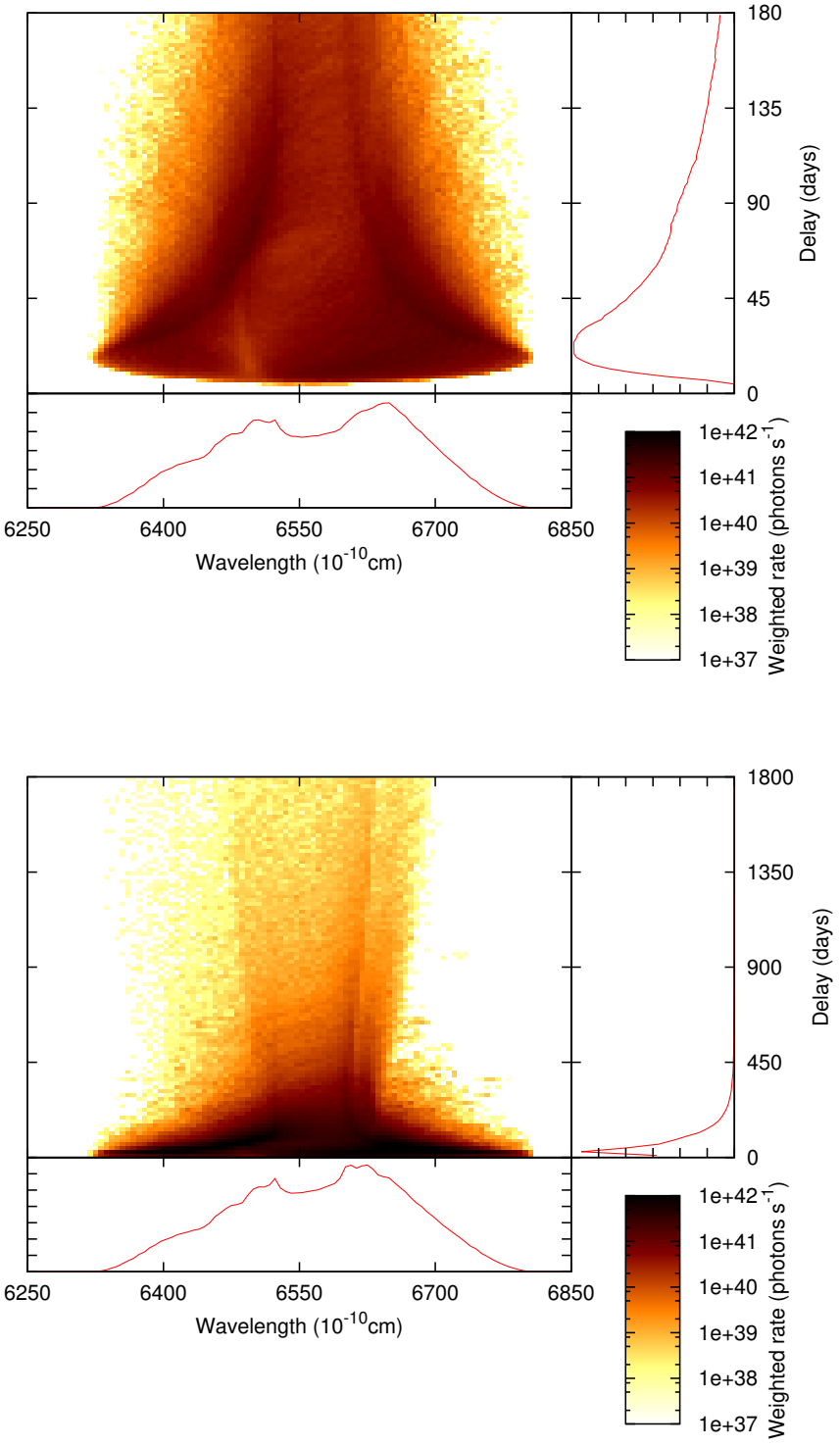

FIGURE 3.7: Velocity-resolved transfer function for $H\alpha$ in biconical disk wind model from Matthews et al. (2016) viewed at 40°. Includes all photons whose last interaction was resonant scatter off the Hα line in the wind, and all photons emitted in the Hα line by the wind.

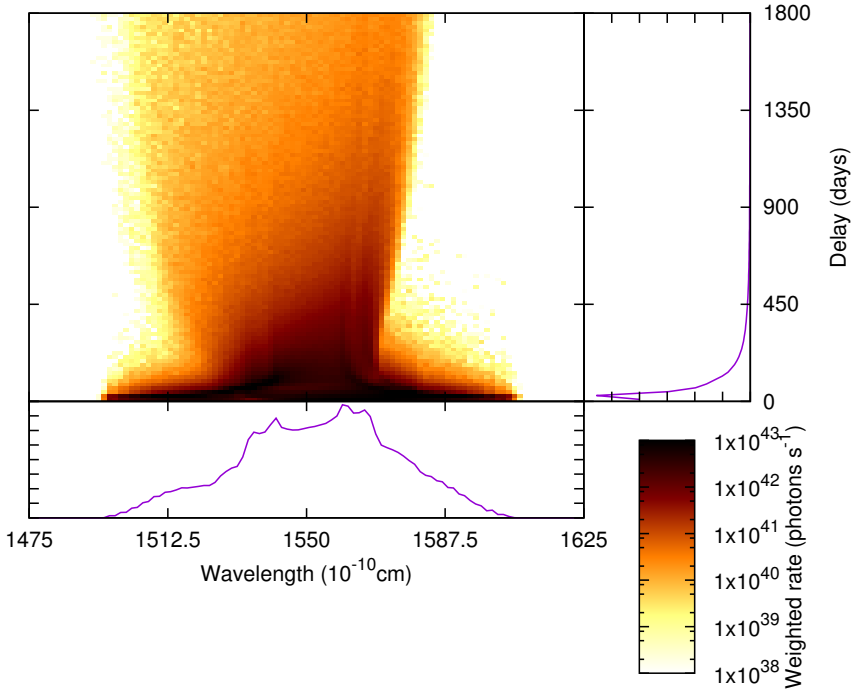

FIGURE 3.8: Velocity-resolved transfer function for C IV in biconical disk wind model from Matthews et al. (2016) viewed at 40°. Includes all whose last interaction was resonant scatter off the C IV line in the wind, and all photons emitted in the C IV line by the wind.

the base of the wind. The transfer function would be dominated by the outflow signatures seen in the lower panel of figure 3.7, with minimal contributions from rotation, and could reduce the intensity of the Keplerian rotation signatures to below continuum scatter levels (as figure 3.9).

3.3.2.2 Cell path distributions

Figure 3.12 illustrates the distribution of photon paths contributing to heating across a cross-section of the wind close to the central source. For cells on the innermost edge of the wind, with an un-obscured path to the central source, the majority of the photons reaching them have paths within the range associated with direct travel from the central source, or for photons travelling directly from nearby regions of the disk. The contribution from multiple-scatter within the wind or from distant disk regions is on or below the 10% level. For cells within the wind, however, the delay distribution profile changes substantially. Photons are more likely to arrive at paths *longer* than the direct path, making these cells dependent mostly on multiply-scattered photons or distant disk photons. In addition to the longer, broader peak path a substantial long tail of paths is recorded. For the mid- and outer-wind locations, a clear point of inflection can be seen where the distribution transitions from being dominated by a sharp, short

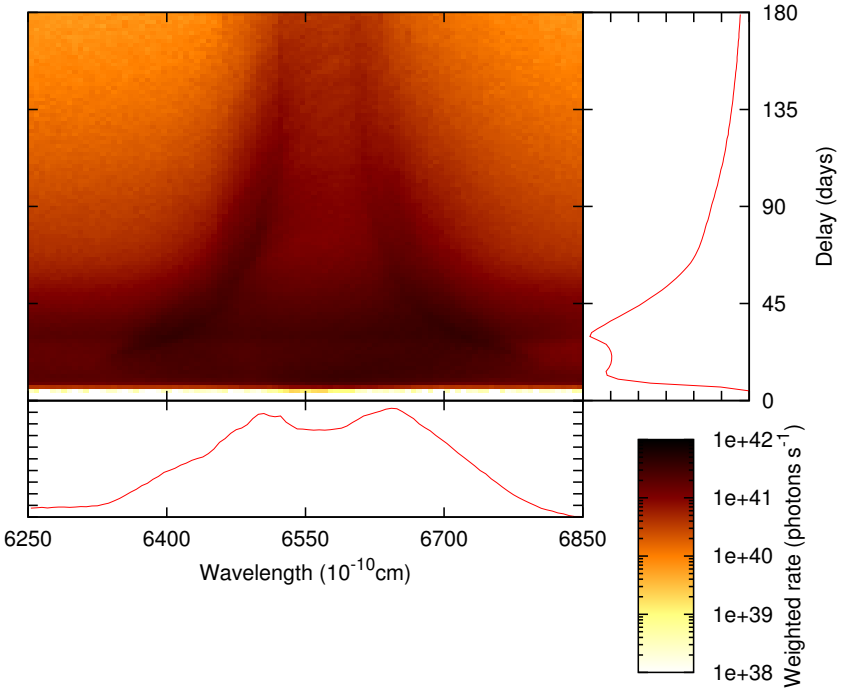

FIGURE 3.9: Velocity-resolved transfer function for Hα in biconical disk wind model from Matthews et al. (2016) viewed at 40°. Includes all photons scattered by resonant or continuum scatter in the wind, and all photons emitted by the wind.

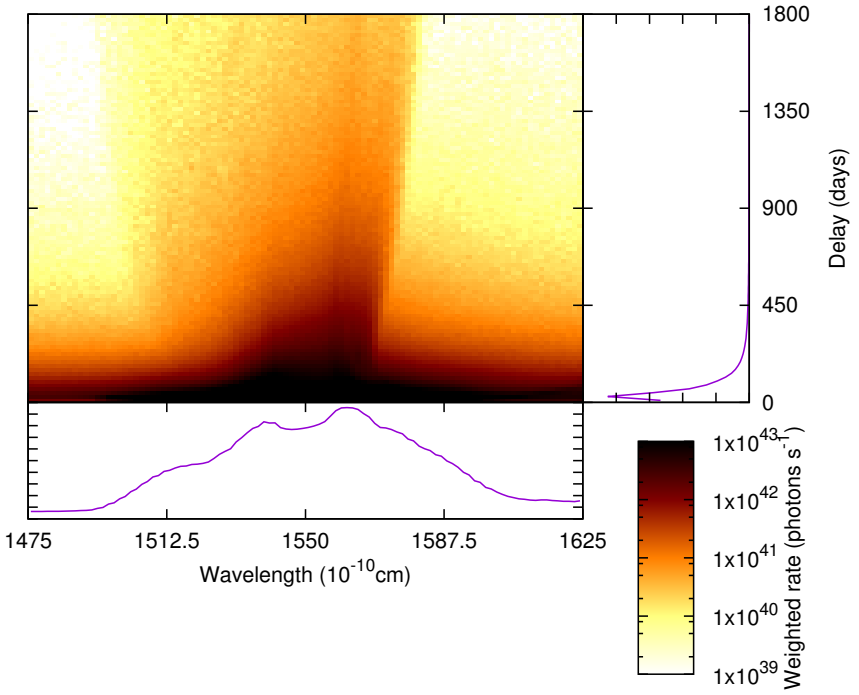

FIGURE 3.10: Velocity-resolved transfer function for C IV in biconical disk wind model from Matthews et al. (2016) viewed at 40°. Includes all photons scattered by resonant or continuum scatter in the wind, and all photons emitted by the wind

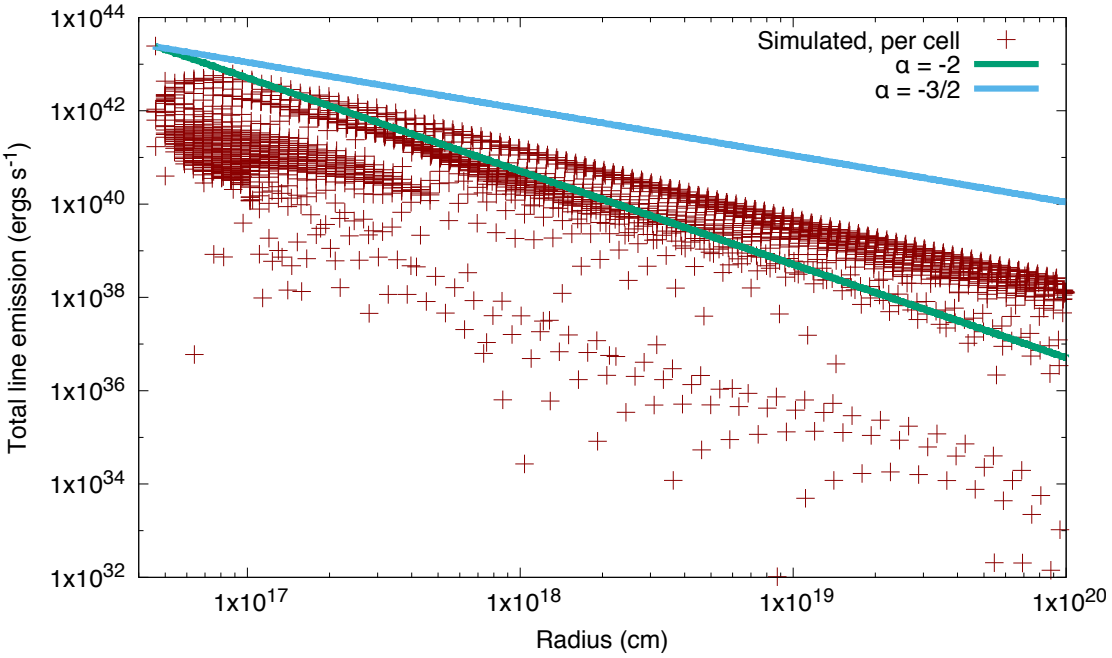

FIGURE 3.11: Total emission in all emission lines for each cell in wind model, against r^{α} models for emission. Each wind cells has a vertical position, not shown on this plot.

distance peak to being dominated by a smooth, gradual fall-off. Tests showed these plots were strongly affected by the assumptions made in section 3.2.1 about disk behaviour. Whilst we assume that emission from the disk surface is effectively correlated with the emission from the central source at $t = t_{curr} - \frac{c}{r}$, if this assumption is removed and disk photons are generated without a starting delay proportional to the central source these delay distributions alter substantially (figure 3.13). For cells on the inner edge of the wind, photons directly from the central source still dominate, and the peak of the delay distribution shifts to a *shorter* path, as photons from nearby on the disk do not arrive with the same path distance as direct photons. For cells in the mid- and outer-wind, however, the removal of disk photons from the distribution results in the removal of the approximately-Gaussian distribution of paths at short distances they add. The delay distribution is then dominated by photons multiply-scattered within the wind. This shift suggests that disk photons have a lower chance of multiple-scattering within the wind. There is no clear 'third distribution' corresponding to photons emitted within the wind, suggesting that they share the behaviour of central source photons. This implies disk photons are less likely to multiple-scatter than coronal or wind photons, most likely due to having lower energies than coronal photons and not being emitted at frequencies in-resonance with resonant lines in the wind. The end result is for regions deeper into the wind, the bulk of the photons from the central source are multiple-scattered, and peaks of the delay distributions are shifted to $\approx 10\%$ longer delays. When plotting the transfer functions with uncorrelated disk photons, this comparatively small change does not notably alter the shape of the function. This does, however, imply that attempts to use reverberation delays to determine detailed geometry information (like

the specific location of a given emission line region) will change depending on the central source luminosity. For coronal luminosities failing to satisfy equation 3.1, reverberation mapping campaigns would be expected to produce longer distance estimates for a given line, and thus higher black hole masses. This is unlikely to be one of the larger sources of error on these estimates though.

We expected reverberation from lower energy lines to be more dependent on high delay photons. As the disk emits as a black-body and the temperature falls off with radius, high energy photons will tend to be produced closer in to the centre, whilst lower energy photons will be produced across a broader range of the disk. Checking this relationship in our models is challenging due to the low photon numbers in the Hβ and Hγ lines, but the behaviours are compared in figure 3.14. We see a small, but noticeable effect. The peak path for photons contributing to heating in the cell lies within the range of direct photon travel (with a substantial long path tail). Photons that activate the Balmer series, however, tend to have slightly longer paths, and the distribution of paths is substantially different. Heating photons see a rapid drop-off at longer paths, whilst Balmer series photons show a sustained dependence on longer paths. Equally, as figures 3.12 and 3.13 show, disk photons tend to contribute a roughly Gaussian peak to a path distribution at a path slightly larger than the direct path to the cell. This implies that Balmer series photons are mostly dependent upon multiple-scatter. As Balmer photons are emitted in-resonance with the local line, we would expect a high scattering cross-section for these photons. This implies that we would definitely expect a longer delay for the Hα lines used in reverberation mapping studies than those actually used.

These trends are illustrated for cells in the middle of the wind both closer to and further from the central source in figure 3.15. Cells near the central source still show a clear disk response peak in the delay distribution, arguably even showing a small peak in the Hα distribution. The path distributions both show the same falloff profile too, suggesting Hα emission near the central source is affected much more strongly by un-scattered central source and disk photons. However, Hα emission was of comparable luminosity in each cell, and path-integrated luminosities appear greater at large distances from the central source. This suggests that even though the innermost cells are dominated by the disk/central continuum, the line is still likely to be dominated by multiple-scattered photons.

3.3.3 Comparison to AGN Key Project

We modified our post-processing software to allow us to compare our results with those of the AGN Key Project's robotic reverberation mapping (Valenti et al. (2015), hereafter Valenti et al.). In Valenti et al., they outline an observation that closely resembles the velocity transfer function for a spherical inflow. Whilst our models do not reproduce this, our post-processing code produces point-wise transfer functions like figure 3.16.

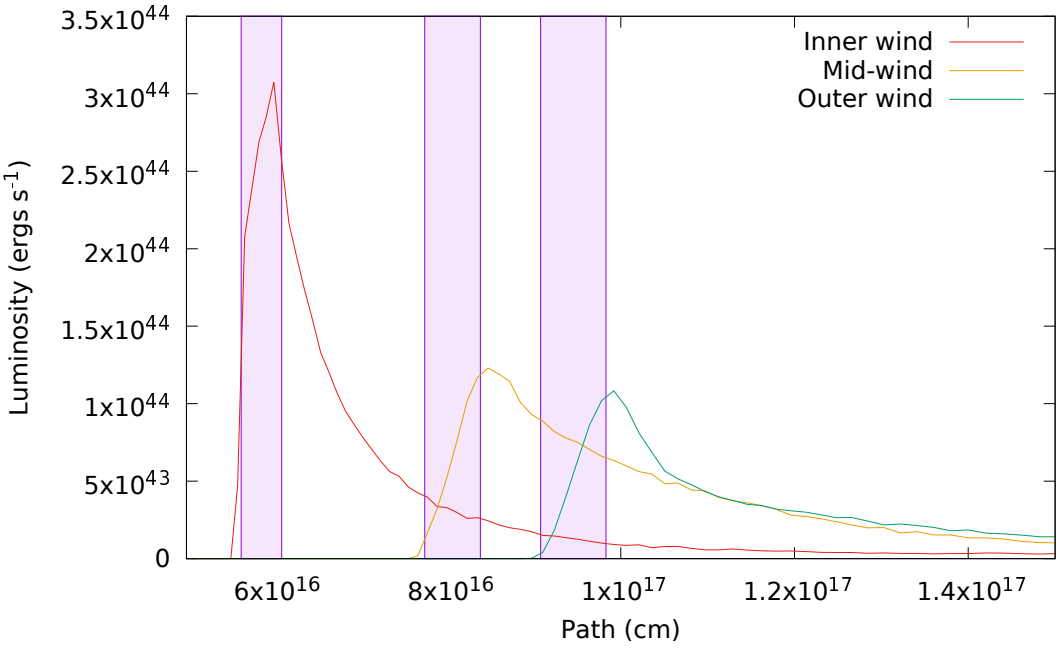

FIGURE 3.12: Path distributions for all photons undergoing continuum absorption (and thus contributing to cell heating) in the biconical disk-wind model, from cells on the inner to outer edge of the wind, assuming disk emission *is* correlated with the central source. Purple regions describe range of direct paths to the cells.

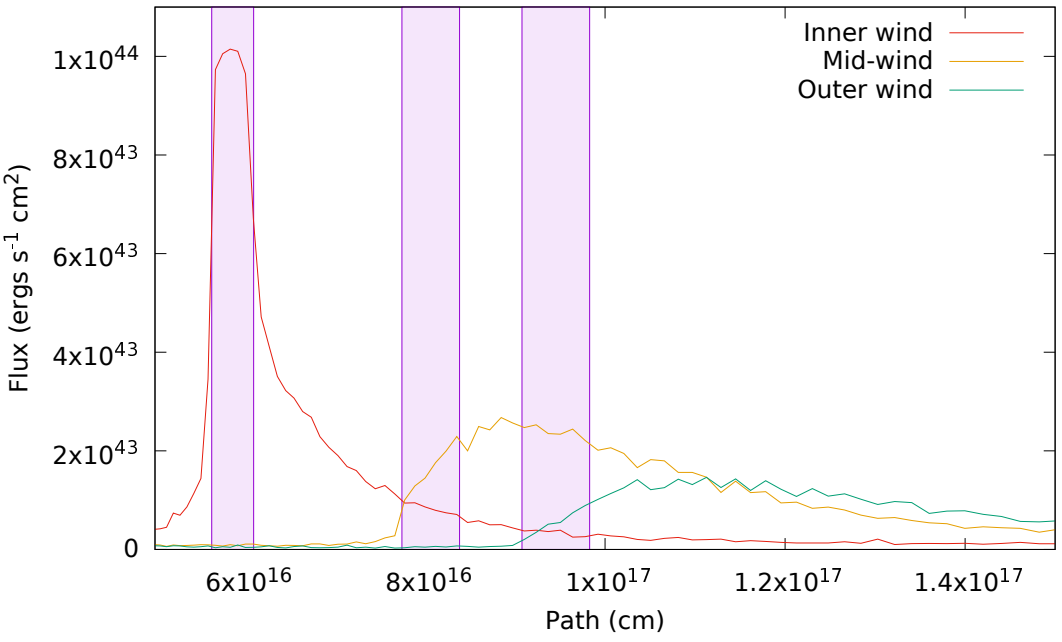

FIGURE 3.13: Path distributions for all photons undergoing continuum absorption (and thus contributing to cell heating) in the biconical disk-wind model, from cells on the inner to outer edge of the wind, assuming disk emission is *not* correlated with the central source. Purple regions describe range of direct paths to the cells.

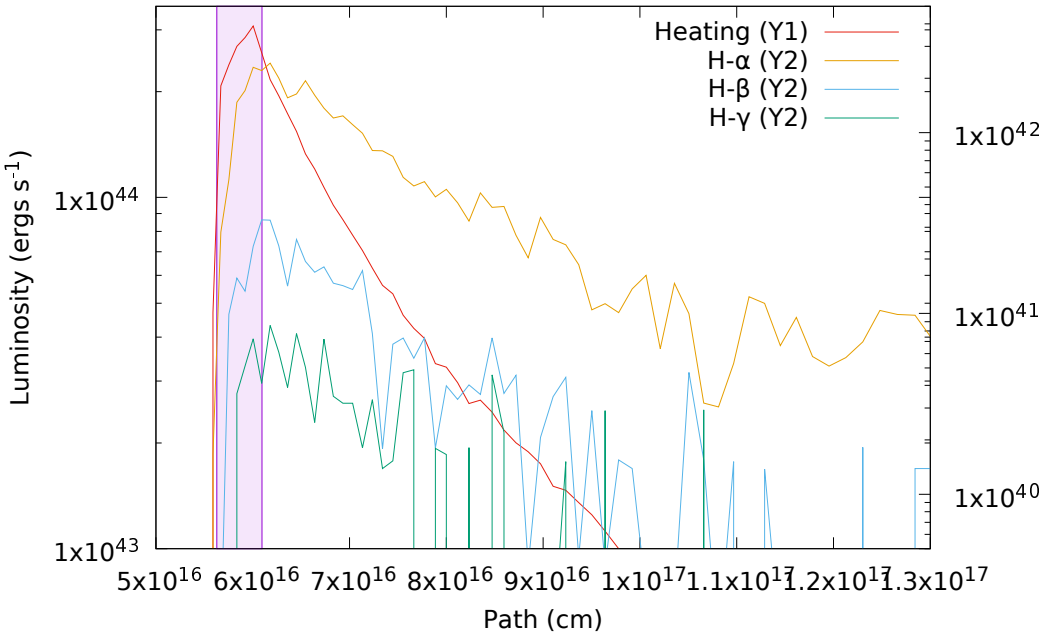

FIGURE 3.14: Path distributions for photons interacting via multiple processes in one cell of the biconical disk-wind model. Chosen cell is the 'inner wind' cell from figure 3.12. 'Heating' photons are as figure 3.12, H($\alpha/\beta/\gamma$) refers to the paths of all photons that activate a macro-atom within this cell causing it to de-excite via a H($\alpha/\beta/\gamma$) process. Purple regions describe range of direct paths to the cell.

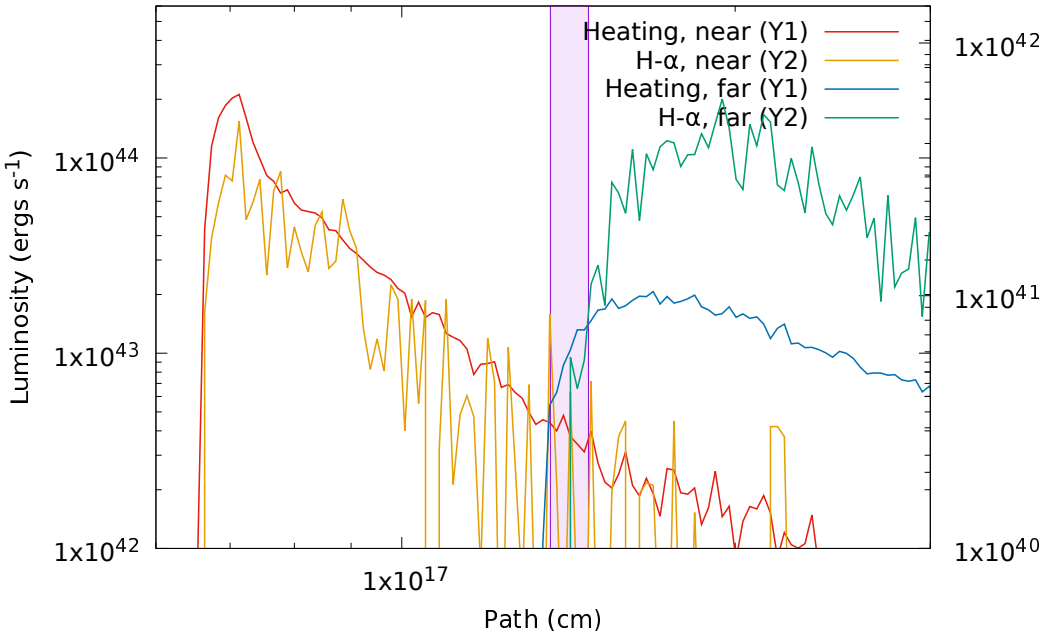

FIGURE 3.15: Cell path distributions for two different cells in biconical disk-wind model, located in the middle of the wind at two different distances. 'Heating' photons as described in figure 3.12, Hα as described in figure 3.14. Purple regions describe range of direct paths to the cells.

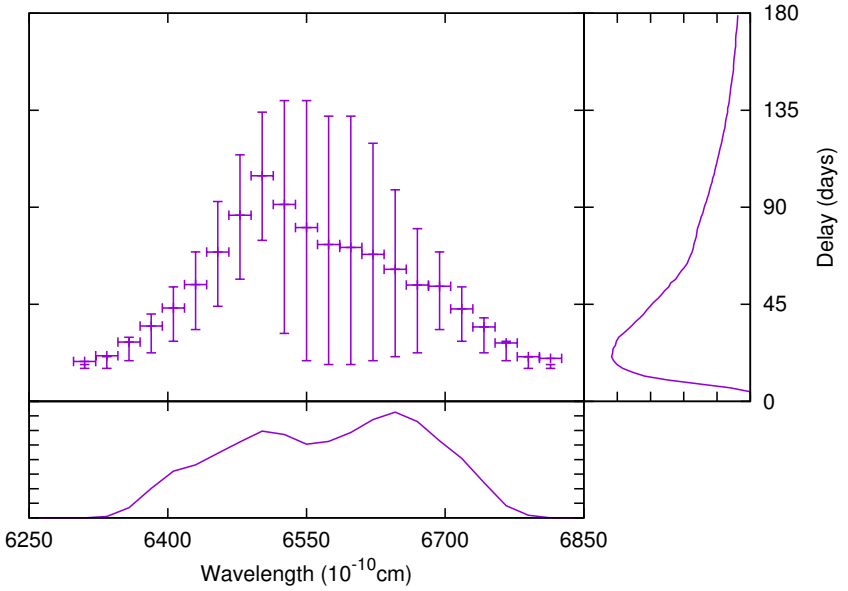

FIGURE 3.16: Centroids of transfer function for biconical disk wind model from section 3.3.2, viewed at 40°. Includes all photons whose last interaction was resonant scatter off the Hα line in the wind, and all photons emitted in the Hα line by the wind. X error bars indicate bin widths, Y error bars indicate 1σ range as described in Valenti et al. (2015).

The plot for an outflowing sphere displays the same relationship to the full transfer function for an outflowing sphere as Valenti et al.'s displays to that of the inflowing sphere from Welsh and Horne (1991). When continuum scattered photons are included, we see a much less clear translation of the transfer function structures to these plots than is shown in Valenti et al. (2015). This raises the possibility that as multiple scattering processes tends to give rise to a very broad range of paths at long delays (as shown in figure 3.15) that multiply-scattered photons may have such low correlation with central source fluctuations that they behave like background noise and are excluded from the cross-correlation analysis used to generate observational transfer functions. As a result, our generated transfer functions like figure 3.8 may under-estimate the clarity with which we can observe.

3.4 Discussion

We have demonstrated that radiative transfer effects have a substantial impact on observed transfer functions. Whilst generally matching the shape of simple models, the inclusion of multiple scattering effects adds clearly identifiable features to our transfer functions. In the spherical outflow model in figure 3.5, scattering of line photons into resonance with nearby lines produces a 'stripe' feature. In addition, multiple scatter results in substantial extensions of transfer functions. This can be seen in the differences between figures 3.4 and 3.6, where scattering from a shell of C IV at 5-10 light-days from the central source results in a transfer function extending up to and beyond 60 days of delay. These delays extend far beyond those seen in the simple sphere model where scattering occurs out to a radius of 50 light-days. For more complex geometries, figure 3.12 illustrates that the degree of extension is likely to change for differing positions within the wind, as well as showing that multiple scattering can substantially change the peak response. This is particularly the case for lines of interest in reverberation mapping (figure 3.14). This suggests that for lines generated in optically thick regions of the BLR, attempts to use them to measure black hole mass may over-estimate the average orbital radius of the material scattering or reprocessing into the line simply due to the multiple scattering effect. This would result in a slight but consistent over-estimation of black hole masses via this method.

Implementing self-consistent ionisation for a wind model also substantially changes its transfer function (dramatically visible in figures 3.4 and 3.5). As ionisation states become much more localised within the wind, emission from the corresponding lines is also localised. As a result, a single line cannot be used to probe the geometry of the whole wind. This effect can be seen in figures 3.7 and 3.9 as compared to figure 3.8. The mutually exclusive range of wind positions where C IV and Hα dominate result in substantial differences in the features visible at long delay times. This suggests that for AGN reverberation mapping campaigns a range of lines should be chosen to ensure the full velocity-delay space available to the system can be well-sampled. Modelling campaigns can have a role before surveys by identifying those lines most likely to provide good coverage.

Whilst radiative transfer and ionisation work to complicate and obscure transfer functions in unrealistic trial geometries, we see from figures 3.7 and 3.8 that these effects do not necessarily overwhelm the signatures of the underlying geometry. We can clearly distinguish the component signatures of rotation and outflow in a rotating biconical wind. The actual form of the outflow signature in the transfer function differs from spherical, and is dependent on the acceleration in the wind, but can still be seen quite clearly. However, given the orders-of-magnitude difference in response at long timescales determining the large-scale velocity profiles of winds via reverberation mapping is probably impractical. We expect our single line models to produce unrealistically well-defined

transfer functions, as they neglect scattering from continuum processes (or Doppler-shifted adjacent lines) into the frequency range of interest. The transfer function would be expected to include these processes as continuum scattering of flux from the central source would still correlate with fluctuations in the central source intensity. However, the fact that continuum scattering into a given wavelength can occur at any position and velocity has the potential to obscure the line scattering features in the transfer function. Figure 3.9 makes it clear that for our realistic test geometry, line emission is strong enough to produce distinguishable features at short delays when these effects are considered. In addition, whilst the transfer function response drops off by orders of magnitude with increasing delays, by selecting appropriate lines as figure 3.10 we can still observe these features against the continuum scatter background. Comparison with the existing results from the AGN key project suggests that if anything our full scattering models may underestimate the clarity of the observational transfer functions.

3.5 Conclusions

We have advanced simple reverberation mapping simulations with the addition of radiative transfer effects and ionisation modelling. We show the resulting differences in the predicted transfer functions, which are substantial. In particular, multiple-scattering produces both smearing of the delay at long timescales and distinct signatures for inner edges. Taking into account self-consistent ionisation processes can also dramatically alter the transfer function for a given geometry by constraining scatter to only a subset of it. Despite these effects, it is still possible to produce transfer functions for resonant line scatter from a realistic rotating biconical winds that can be interpreted in terms of its component parts, even when continuum photons are taken into account. Once detailed observational transfer functions are available, forward modelling of geometries to match them should be possible.

Chapter 4

The reverberation signatures of rotating disc winds in active galactic nuclei

4.1 Introduction

Chapter 3 features only the transfer functions of our disk wind model. We submitted a paper containing the biconical wind transfer function analysis from chapter 3 to the Monthly Notices of the Royal Astronomical Society. Our reviewers noted that one of the truly unique capabilities of the code was the ability to consider ionisation effects. By including i.e. differential changes in ionisation and thus emissivity as a result of changes in ionising continuum, we could generate proper *response functions*, rather than simply transfer functions. This led to a substantial rewrite of the paper, and a result, we developed techniques for determining the response function Ψ_R detailed in this paper. Whilst previous works have considered the *possibility* of negative responses (Krolik and Done, 1995), this paper demonstrated that for a physically-motivated disk wind model it is possible to generate response functions dominated by negative responses.

A second major difference between the work in this chapter and chapter 3 is that continuum-scattered photons are no longer included in the response functions; only those emitted in, or scattering off, an emission line. This was motivated by a change of assumptions. Whilst continuum emission is a major component of a spectrum within a given wavelength range, it typically has a less dynamic delay distribution than that of line emission, arriving mostly directly. The continuum photons that *are* likely to 'contaminate' the delay distributions are those from the wind, which would also share a more complex response function. Figure 3.14 from chapter 3 suggests that, for most lines, the distribution of paths for photons governing both continuum and line emission are essentially equivalent. In addition, for our lines of interest, the line luminosities

are on the order of 5× the continuum luminosities emitted by the wind. As a result, we chose to focus on pure line photons when generating response functions as it was computationally easier and unlikely to produce dramatically different results to observationally-recoverable response functions. Future work could involve accounting for both the range of continuum lags observed (e.g. Homayouni et al. (2018)), and the effect of wind continuum photons; though this would require substantial improvements in the data capture and processing abilities of the code.

4.2 Journal paper

The journal paper reproduced below was originally published in the Monthly Notices of the Royal Astronomical Society in 2017 as Mangham et al. (2017). The models used in the study were the biconical AGN disk wind models originally created by Dr James Matthews for Matthews et al. (2016), as discussed in section 2.3.

The reverberation signatures of rotating disc winds in active galactic nuclei

S. W. Mangham,[1] C. Knigge,[1] J. H. Matthews,[2] K. S. Long,[3,4] S. A. Sim,[5] and N. Higginbottom[1]
[1] Department of Physics and Astronomy, University of Southampton, Southampton, SO17 1BJ, UK
[2] University of Oxford, Astrophysics, Keble Road, Oxford, OX1 3RH, UK
[3] Space Telescope Science Institute, 3700 San Martin Drive, Baltimore, MD 21218, USA
[4] Eureka Scientific, Inc., 2452 Delmer St., Suite 100, Oakland, CA 94602-3017, USA

[5] School of Mathematics and Physics, Queen's University Belfast, University Road, Belfast, BT7 1NN, UK

The broad emission lines (BELs) in active galactic nuclei (AGN) respond to ionizing continuum variations. The time and velocity dependence of their response depends on the structure of the broad-line region: its geometry, kinematics and ionization state. Here, we predict the reverberation signatures of BELs formed in rotating accretion disc winds. We use a Monte Carlo radiative transfer and ionization code to predict velocity-delay maps for representative high- (C IV) and low-ionization (Hα) emission lines in both high- and moderate-luminosity AGN. Self-shielding, multiple scattering and the ionization structure of the outflows are all self-consistently taken into account, while small-scale structure in the outflow is modelled in the micro-clumping approximation. Our main findings are: (1) The velocity-delay maps of smooth/micro-clumped outflows often contain significant *negative* responses. (2) The reverberation signatures of disc wind models tend to be rotation dominated and can even resemble the classic "red-leads-blue" *inflow* signature. (3) Traditional "blue-leads-red" outflow signatures can usually only be observed in the long-delay limit. (4) Our models predict lag-luminosity relationships similar to those inferred from observations, but systematically underpredict the observed centroid delays. (5) The ratio between "virial product" and black hole mass predicted by our models depends on viewing angle. Our results imply that considerable care needs to be taken in interpreting data obtained by observational reverberation mapping campaigns. In particular, basic signatures such as "red-leads-blue", "blue-leads-red" and "blue and red vary jointly" are not always reliable indicators of inflow, outflow or rotation. This may help to explain the perplexing diversity of such signatures seen in observational campaigns to date.

Accepted by MNRAS 2017 July 20. Received 2017 June 22; in original form 2016 December 6

4.2.1 Introduction

Reverberation mapping (RM) has become a powerful tool in the study of active galactic nuclei (AGN; Peterson 1993). Its primary application to date has been in efforts to estimate central black hole (BH) masses. The broad emission lines (BELs) in AGN respond to variations in the underlying continuum with a characteristic time delay, τ. This delay is due to the light travel time from the central engine to the broad line region (BLR) and therefore depends on the size of the BLR, $R_{BLR} \simeq c\tau$. If the dynamics of the

BLR are dominated by the gravitational potential of the BH, the width of the Doppler-broadened emission lines must be $\Delta v_{BLR} \simeq (GM_{BH}/R_{BLR})^{1/2}$. Thus the combination of line width and lag immediately provides an estimate of the BH mass, the so-called *virial product* $M_{BH} \simeq c\tau_{BLR} v_{BLR}^2/G$.

Lag-based BH mass estimates have been successfully calibrated against both the $M_{BH}-\sigma$ (Gebhardt et al., 2000; Ferrarese et al., 2001; Onken et al., 2004; Woo et al., 2010) and the $M_{BH} - M_{bulge}$ relations (Wandel, 2002; McLure and Dunlop, 2002). However, even though the BLR sizes obtained via RM seem to yield reliable BH masses, the nature of the BLR itself has remained controversial. This uncertainty regarding the geometry and kinematics of the BLR also limits the accuracy of RM-based BH mass estimates (Park et al., 2012; Shen and Ho, 2014; Yong et al., 2016).

RM itself offers one of the most promising ways to overcome this problem, since the physical properties, geometry and kinematics of the BLR are encoded in the time- and velocity-resolved responses of BELs to continuum variations. Decoding this information places strong demands on observational data sets (Horne et al., 2004), but recent campaigns have begun to meet these requirements (e.g. LAMP [Bentz et al. (2011); Pancoast et al. (2012, 2014a); Skielboe et al. (2015)], SEAMBH [Du et al. (2014, 2016)]; AGN Storm [De Rosa (2015)]). Most previous velocity-resolved RM studies found signatures that were interpreted as evidence for inflow and/or rotation (Ulrich and Horne, 1996; Grier, 2013; Bentz et al., 2008, 2010a; Gaskell, 1988; Koratkar and Gaskell, 1989), although apparent outflow signatures have also been reported (Denney et al., 2009; Du et al., 2016).

On the theoretical side, considerable effort has been spent over the years on modelling and predicting BLR reverberation signatures (e.g. Blandford and McKee, 1982; Welsh and Horne, 1991; Wanders et al., 1995; Pancoast et al., 2011, 2012, 2014a). However, most modelling efforts to date have treated the line formation process by adopting parameterized emissivity profiles, rather than calculating the actual ionization balance and radiative transfer within the BLR self-consistently. Also, one of the most promising models for the BLR – rotating accretion disc winds (Young et al., 2007) – has received surprisingly little attention in these modelling efforts.

Evidence for powerful outflows from luminous AGN is unambiguous: approximately 10% - 15% of quasars display strong, blue-shifted broad absorption lines (BALs) in UV resonance transitions such as C IV 1550 Å (e.g. Weymann et al., 1991; Tolea et al., 2002). The *intrinsic* BAL fraction must be even higher – probably 20% - 40% – since there are significant selection biases against these so-called BALQSOs (Hewett and Foltz, 2003; Reichard et al., 2003; Knigge et al., 2008; Dai et al., 2008; Allen et al., 2011). These outflows matter. First, they provide a natural mechanism for "feedback", i.e. they allow a supermassive BH to affect its host galaxy on scales far beyond its gravitational sphere of influence (Fabian, 2012). Second, they can produce most of the characteristic

signatures of AGN, from BELs (Emmering et al., 1992; Murray et al., 1995) to BALs to X-ray warm absorbers (Krolik and Kriss, 1995). Third, they may be the key to unifying the diverse classes of AGN/QSOs (Elvis, 2000).

Despite the importance of these outflows, there have been few attempts to study the reverberation signature of rotating disc winds. Chiang and Murray (1996) - hereafter CM96 - calculated the time- and velocity-resolved response of the C IV 1550 Å line based on the line-driven disc wind model described by Murray et al. (1995). Taking the outflow to be smooth, CM96 treated velocity-dependent line transfer effects self-consistently, but adopted a power-law radial emissivity/responsivity profile instead of carrying out photoionization calculations. They also assumed that only the densest parts of the wind (near the disc plane) produce significant line emission. More recently, Waters et al. (2016) used a similar formalism to predict the emission line response according to their hydrodynamic numerical model of a line-driven AGN disc wind.

Similarly, Bottorff et al. (1997b) predicted time- and velocity-dependent response functions for C IV, based on the centrifugally-driven hydromagnetic disc wind model of Emmering et al. (1992). In this model, the BLR is composed of distinct, magnetically confined clouds, each of which is assumed to be optically thick to both the Lyman continuum and C IV and to possess no significant internal velocity shear. Moreover, Bottorff et al. (1997b) adopted the "locally optimally emitting cloud" (LOC) picture of the BLR (Baldwin et al., 1995), according to which a population of clouds spanning a huge range of particle density is assumed to exist at any given distance from the central engine. These assumptions dramatically reduce the complexity of the necessary photoionization and line transfer calculations.

Against this background, our goal here is to use a fully self-consistent treatment of ionization and radiative transfer to predict Hα and C IV reverberation signatures for a generic model of rotating accretion disc winds in both high- and moderate-luminosity AGN. Our starting point is the disc wind model developed by Matthews et al. (2016) for luminous QSOs. This model was explicitly designed with disc-wind-based geometric unification in mind: it predicts strong BALs for observer orientations that look into the outflow, produces strong emission lines for other orientations and is broadly consistent with the observed X-ray properties of both QSOs and BALQSOs. We use a scaled-down version of this model to represent lower-luminosity AGN, such as Seyfert galaxies. For both types of model AGN, we calculate the time- and velocity-resolved emission line responses and compare the predicted reverberation signatures to observations.

The remainder of this paper is organized as follows. In subsection 4.2.2, we outline the theory behind RM and describe the code we have employed to model it. In subsection 4.2.3, we use the code to calculate model response functions for both Seyfert galaxies and QSOs. In subsection 4.2.4, we test the lag-luminosity relationships predicted by our models against observations. We also present the viewing angle dependence of the virial

product for these models and compare it to the results of recent observational modelling efforts. Finally, in subsection 4.2.5, we summarize our conclusions.

4.2.2 Methods

4.2.2.1 Fundamentals

The premise of RM is that the BLR reprocesses the ionizing continuum generated by the central engine. This immediately implies that the emission lines produced in the BLR should respond to variations in the continuum. The response of a small parcel of BLR gas to a change in the continuum flux it receives is effectively instantaneous. As seen by a distant observer, parts of the BLR that lie directly along the line of sight to the central engine will therefore respond to a continuum pulse with no delay. However, the response from any other part of the BLR will be delayed with respect to the continuum. For each location in the BLR, the delay is just the extra time it takes photons to travel from the central engine to the observer, via this location. As illustrated in Figure 4.1, the isodelay surfaces relative to a point-like continuum source are paraboloids centered on the line of sight from the source towards the observer.

The response of a line will usually involve a range of delays. The relationship between continuum variations, $\Delta C(t)$, and variations in the flux of an emission line, $\Delta L(t)$, can be expressed in terms of a *response function*, $\Psi_R(\tau)$,

$$\Delta L(t) = \int_{-\infty}^{\infty} \Delta C(t-\tau)\Psi_R(\tau)d\tau. \tag{4.1}$$

The response function describes how the emission line flux responds to a sharp continuum pulse as a function of the time delay, τ.

Since each parcel of gas has a different line of sight velocity v with respect to the observer the line profile will also change with time. line of sight. We can therefore define a 2-dimensional response function, $\Psi_R(v,\tau)$, that specifies the response of the BLR as a function of both time delay and radial velocity,

$$\Delta L(v,t) = \int_{-\infty}^{\infty} \Delta C(t-\tau)\Psi_R(v,\tau)d\tau. \tag{4.2}$$

While the 1-dimensional response function depends only on the geometry of the BLR, the 2-dimensional response function – also known as the "velocity-delay map" – encodes information about both geometry and kinematics.

Turning this argument around, we can *predict* the response of an emission line to continuum variations for any physical model of the BLR. We can test such models by comparing the response functions they predict to those inferred from observations. Our goal here

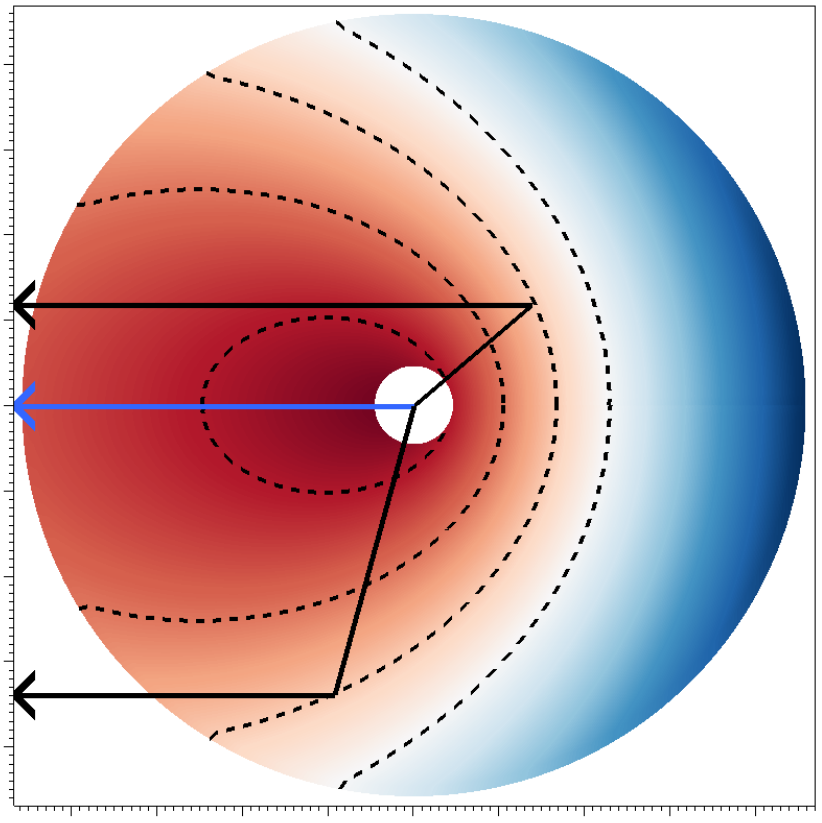

FIGURE 4.1: A cut through the isodelay surfaces surrounding a point source. Colour indicates total path to observer for photons scattering off that point; contours indicate isodelay curves on the 2-d plot. The blue arrow shows the direct path to observer; the two black arrows show the paths taken by two photons that scatter on different points of the same isodelay surface. Figure produced using Visit (Childs et al. (2012)).

is to predict these observational reverberation signatures for a rotating disc wind model of the BLR. A sketch of the outflow geometry we adopt is shown in Figure 4.2, and is described in more detail in subsection 4.2.3.

Our model includes both Keplerian rotation and outflow and may therefore be expected to show a mix of both rotation and outflow signatures. The conversion of spherical inflow, spherical outflow and rotating disc kinematics into velocity-delay space is illustrated in Figure 4.3 (for more details, see, e. g. Welsh and Horne (1991)). Whilst a Keplerian disc has a symmetric signature, with the line wings leading the low-velocity core, outflow and inflow signatures are strongly asymmetric, with the blue wing leading the red for outflows, and the red wing leading the blue for inflows. As noted in subsection 4.2.1, all of these basic signatures have been seen observationally, although symmetric and red-leads-blue signatures are more common.

Sketches like those shown in Figure 4.3 represent a purely geometric projection of BLR gas from 6-D position and velocity space onto our 2-D line-of-sight velocity and time delay space. The actual appearance of a velocity-delay map within the boundaries imposed by this projection depends on the *strength* of the line response across the map.

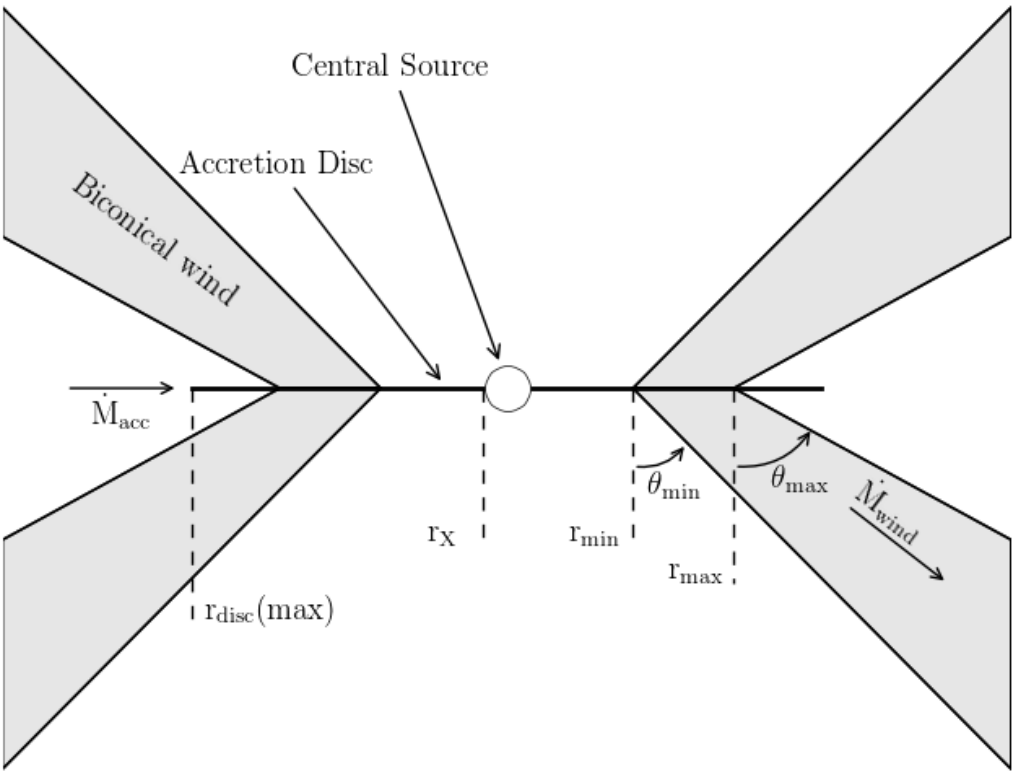

FIGURE 4.2: Sketch of the biconical disc wind geometry from Matthews et al. (2016).

As we shall see, this is a crucial effect that can make it difficult to identify even basic reverberation signatures with particular kinematics.

4.2.2.2 Predicting reverberation signatures with self-consistent ionization and radiative transfer

The ionization state of the BLR depends primarily on its density structure, as well as on the luminosity and spectral shape of the ionizing continuum. In an outflowing biconical disc wind, the ionization structure is naturally stratified, which is in line with observations (Onken et al., 2004; Kollatschny and Zetzl, 2013; Kollatschny et al., 2014).

For a given BLR ionization state, the emission line formation process involves the generation of line photons within the BLR and their radiative transfer through it. In order to reliably predict the strengths, shapes and reverberation signatures of BELs, it is necessary to deal correctly with radiative transfer effects and solve self-consistently for the ionization state of the BLR.

In our work, we accomplish this by using a modified version of our Monte Carlo radiative transfer and ionization code PYTHON (Long and Knigge, 2002), which was developed specifically for modelling the spectra of accretion disc winds. PYTHON is a useful tool

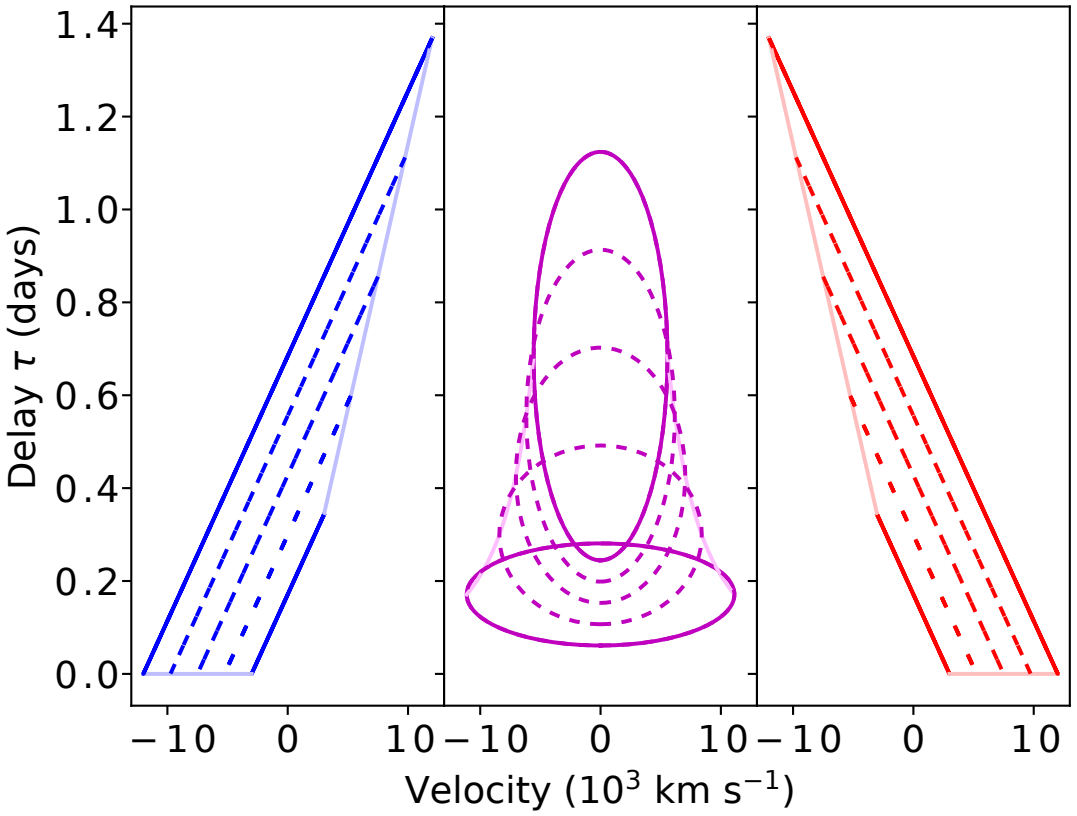

FIGURE 4.3: Outline response functions for Hubble-type spherical outflow **(left)**, a rotating Keplerian disc viewed at a 20° angle **(centre)**, and Hubble-type spherical inflow **(right)**. Winds extend from $r_{min} = 20r_g$ to $r_{max} = 200r_g$ for an AGN of mass $10^7 M_\odot$. Hubble out/inflows have $V(r_{min}) = \pm 3 \times 10^3$ km s^{-1}. Solid lines denote the response from the inner and outer edges of the winds, dotted lines from evenly-spaced shells within the wind. Pale lines describe the edge of the velocity-delay shape of the response function.

for reverberation modelling, since a given outflow geometry can be tested not just against the response function of a single line, but also against the full predicted spectrum. The code has already been described several times in the literature (Long and Knigge, 2002; Sim et al., 2005; Noebauer et al., 2010; Higginbottom et al., 2013, 2014; Matthews et al., 2015, 2016), so we only provide a brief overview here, focusing on the modifications we have made in order to predict reverberation signatures. A full description of the method, including tests against existing reverberation modelling, and an exploration of radiative transfer effects in RM will be presented elsewhere.

PYTHON generates synthetic spectra for astrophysical systems in which an outflow with given geometry, kinematics and density structure reprocesses the radiation generated by one or more continuum sources. Our AGN wind models are based on a kinematic (i.e. parameterized) description of a rotating biconical outflow emanating from the surface of the accretion disc (Shlosman and Vitello, 1993, Figure 4.2). The same description was used by Higginbottom et al. (2013) and Matthews et al. (2016, hereafter M16) to predict the spectroscopic signatures of disc winds in QSOs. The geometry and kinematics of

the wind are determined by a set of parameters (fully detailed in Table 4.1). Our high-luminosity ("QSO") model is identical to that developed in M16, while our lower-luminosity ("Seyfert") model is a simple scaled-down version of this. These models are described further in subsection 4.2.3. All of our radiative transfer and ionization calculations are performed on a cylindrically symmetric grid imposed on the wind. The relevant continuum sources are taken to be a geometrically thin, optically thick accretion disc (which dominates the UV and optical light) and a compact, optically thin corona (which dominates the X-ray emission).

The calculation of synthetic spectra with PYTHON proceeds in two steps. In the first step, the code generates 'bundles' of continuum photons across the full frequency range, tracks their interactions and iterates towards thermal and ionization equilibrium throughout the wind. In the second step, the converged state of the wind is kept fixed, photons are generated only across a limited frequency range, and emergent spectra are predicted for a set of user-defined observer orientations.

In our models, reverberation delays are associated solely with photon light travel times. This is in line with other RM studies (Welsh and Horne, 1991; Waters et al., 2016) and can be justified on the basis that the recombination time scales at typical BLR densities (minutes to hours) are much shorter than light-travel times across the BLR (days to weeks).

For the purpose of this study, we have modified PYTHON to track the distances travelled by photons that contribute to the observed line emission. This is relatively straightforward, since PYTHON is a Monte Carlo code that already explicitly follows photons as they make their way through the outflow.

The use of a full ionization and radiative transfer code offers two significant advantages in predicting reverberation signatures. First, the dependence of line emissivity on position within the BLR is calculated self-consistently, based on the density, ionization and thermal structure of the outflow. Second, radiative transfer effects are self-consistently taken into account. For example, a continuum (e.g. disc) photon that scatters many times before reaching a particular location in the BLR will have travelled a significantly longer distance than one that reaches the same location without undergoing any scatter. BLR locations that "see" primarily scattered/reprocessed continuum photons will therefore respond to continuum variations with a longer delay than expected solely based on geometry. A benefit of this approach is that we can isolate the contributions of singly- or multiply-scattered photons to the overall reverberation signature.

4.2.2.3 Initializing and updating photon path lengths

In line with essentially all RM models to date, we assume that all of the correlated line and continuum variability we observe has its origin in the immediate vicinity of

the central BH. The time-dependent signal produced there is then reprocessed by other components in the system, such as the accretion disc and the BLR.

For the continuum photons produced by the accretion disc, we implement this picture by assigning to each an initial path length equal to its starting distance from the origin of the model, i.e. $r_{\rm disc}(\rm min)$ from Table 4.1 for photons emitted at the inner edge of the disc. For our QSO model, the UV emission of the accretion disc is concentrated within a radius several times smaller than the wind launch radius, whilst optical emission is concentrated within the radius of the wind base. Both of these lie within the radius within which the accretion disc temperature profile would be expected to be dominated by the central source luminosity (King, 1997) and therefore would lag behind changes in the central source continuum. Photons produced by the X-ray emitting corona are assigned initial path lengths equal to $r_X = r_{\rm disc}(\rm min)$, i.e. we assume that the corona varies coherently. As the corona is compact in comparison to the wind (at least a factor of 50 smaller), this is a reasonable approximation. The light travel time across the corona $2Rr_X/c$ is $\simeq 10$ min for the Seyfert model and $\simeq 16$ hrs for the QSO model.

PYTHON enforces thermal equilibrium throughout the outflow, i.e. the heating and cooling rates are always in balance (in a converged model). Except for cooling due to adiabatic expansion, the wind is also assumed to be in radiative equilibrium, i.e. photon absorption and emission provide the only channels for net energy flows into and out of a given grid cell. The effective initial path lengths of photons representing thermal wind emission must therefore reflect the path length distribution of the absorbed photons that were responsible for heating the wind. In order to ensure this, PYTHON keeps track of the path length distribution of photons depositing energy into each cell. When a 'bundle' of photons with a given wavelength passes through a cell, its total energy is reduced in proportion to the optical depth it encounters along its path. We record its path, and the bundle's total energy, in the cell. When a line photon is thermally emitted within a given grid cell, it is then assigned an initial path length drawn from the distribution of paths contributing to heating weighted by the energy contribution at each path. We refer to this as the thermal approach to path length initialization.

Most of the strong metal lines seen in AGN – e.g. N V 1240 Å, Si IV 1440 Å, C IV 1550 Å– are collisionally excited. In PYTHON, the formation of these lines is treated via a simple two-level atom approach (Long and Knigge, 2002; Higginbottom et al., 2013). This works particularly well for resonance lines (such as all those listed above), in which the lower level is the ground state of the ion. Since collisional excitation is a thermal process, we use the thermal approach to path length initialization for all photons emitted in this way. Observations of these lines will also include a smaller contribution from continuum photons scattered into the line. These photons' path lengths are calculated purely on the basis of their origin and their travel through the winds.

The two-level atom approximation is not appropriate for lines in which the upper level either does not couple strongly to the ground state, or is primarily populated from above. The most important example of such lines are the Hydrogen and Helium recombination lines that are prominent in the UV and optical spectra of AGN. To model such features more accurately, one or both of these elements can be treated via Lucy's (Lucy, 2002, 2003) *macro-atom* approach within PYTHON (Sim et al., 2005; Matthews et al., 2015, 2016). In this approach, a H or He macro-atom can be "activated" by a photon packet travelling through a wind cell, then undergoes a number of internal energy level "jumps", and finally "de-activates" via the emission of a line or continuum photon. In order to predict the reverberation signature of a given H or He recombination line, the code keeps track of all macro-atom de-activations associated with this line in a given cell. After each de-activation, the path length travelled by the photon that activated the macro-atom is stored, gradually building up a distribution. When the same cell emits a photon associated with this recombination line, the initial path length is then drawn from this distribution. This approach is appropriate if photoionizations are quickly followed by radiative recombinations in the BLR. We therefore refer to this as the prompt recombination approach to path length initialization.

Our simulations allow for clumpiness in the wind within the "micro-clumping" approximation (e.g. Hillier, 1991; Hamann and Koesterke, 1998; Matthews et al., 2016). Thus we assume that the outflow, though smooth on a bulk scale, comprises very many small, optically thin clumps. These clumps enhance physical processes with a density-squared dependence. However, there is no effect on the photon paths due to micro-clumping compared to a fully smooth wind flow. Since each clump is optically thin at all wavelengths in this approximation, it is characterized by a unique set of physical conditions (ionization state, temperature, electron density...). Thus, like fully smooth flows, micro-clumped flows are stratified only on large scales. This is a fundamental difference to BLR models based on optically thick clouds, such as "locally optimally-emitting cloud" (LOC) models (Baldwin et al., 1995; Ferguson et al., 1997).

4.2.2.4 Generating Response Functions

The response function, $\Psi_R(v, \tau)$, describes the time- and velocity-dependent response of an emission line to a continuum pulse. The contribution of a particular parcel of BLR gas to the overall response depends primarily on three factors: (i) its distance from the continuum source (which sets the characteristic delay with which it responds); (ii) its line-of-sight velocity (which sets the velocity at which we observe its response); (iii) its *responsivity* (which sets the strength of its response).

The responsivity is the hardest of these factors to calculate. It is a measure of the number of *extra* line photons that are created when a given *extra* number of continuum photons are produced. Note that this is different from the *emissivity* of the parcel,

which describes the efficiency with which it reprocesses continuum into line photons in a steady state. To see this more clearly, consider a parcel with line-of-sight velocity v and characteristic delay τ, which produces a line flux $L(v,\tau)$ when subjected to a steady continuum flux C. The reprocessing efficiency of this parcel can be defined simply as $\epsilon(v,\tau) = L(v,\tau)/C$. However, its responsivity measures how the line flux *changes* when the continuum does.

In the limit of small continuum variations, the overall response of the parcel is fully characterized by the partial derivative of the line flux it produces, $L(v,\tau)$, with respect to the continuum flux, C. If we adopt a power-law approximation for the dependence of $L(v,\tau)$ on C,

$$L(v,\tau) = L_0(v,\tau)\left(\frac{C}{C_0}\right)^{\eta}, \tag{4.3}$$

we can evaluate this partial derivative and write the response function at $C = C_0$ in the form

$$\Psi_R(v,\tau) = \left.\frac{\partial L(v,\tau)}{\partial C}\right|_{C=C_0} = \eta\frac{L_0(v,\tau)}{C_0} = \eta\epsilon_0(v,\tau). \tag{4.4}$$

The response function is therefore the product of reprocessing efficiency, $\epsilon_0(v,\tau)$, and a dimensionless responsivity, η.

In the limit that η is constant throughout the BLR, the response function is just a scaled version of $\epsilon_0(v,\tau)$. We will refer to a response function calculated under the assumption that $\eta \equiv 1$ as an *emissivity-weighted response function* (*EWRF*, originally defined as such in Goad et al. (1993)), $\Psi_E(v,\tau)$, i.e.

$$\Psi_E(v,\tau) = \epsilon(v,\tau) = \frac{L(v,\tau)}{C}. \tag{4.5}$$

However, in general, the assumption that $\eta =$ constant across the BLR is poor (e.g. Goad et al., 1993; O'Brien et al., 1995; Korista and Goad, 2004; Goad and Korista, 2014), i.e. $\eta = \eta(v,\tau)$. For example, a parcel of gas might be very efficient at reprocessing continuum into line photons, but may respond to a pulse of additional continuum photons by producing *fewer* line photons, either in relative or perhaps even in absolute terms. This is possible, for example, because its ionization state may have changed as a result of the pulse. Such a parcel will have a high emissivity (high reprocessing efficiency), but low (or even negative) responsivity.

Despite this, the emissivity-weighted response function provides a useful approximation for, and stepping stone towards, the response function proper. In our case, an EWRF can be calculated from a single run of PYTHON, simply by keeping track of the delay associated with each photon arriving at the observer. For example, given a simulation for continuum luminosity C_0, we bin all photons from the simulation that are associated with a given line in time-delay- and velocity-space, yielding the 2-D EWRF for the line in that system.

In order to estimate the *true* (responsivity-weighted) response function, we then calculate two more EWRFs, for continuum luminosities $C_{\rm low} < C_0 < C_{\rm high}$, where $\Delta C = C_{\rm high} - C_{\rm low} \ll C_0$. In this limit, the line response is approximately linear, i.e. η does not depend on C. This allows us to estimate the response function from the high-and low-state EWRFs as

$$\Psi_R(v,\tau) = \left.\frac{\partial L(v,\tau)}{\partial C}\right|_{C=C_0} \simeq \frac{\Delta L(v,\tau)}{\Delta C} \tag{4.6}$$

$$\simeq \frac{L_{\rm high} - L_{\rm low}}{C_{\rm high} - C_{\rm low}} \tag{4.7}$$

$$\simeq \frac{C_{\rm high}\Psi_{E,{\rm high}}(v,\tau) - C_{\rm low}\Psi_{E,{\rm low}}(v,\tau)}{C_{\rm high} - C_{\rm low}}. \tag{4.8}$$

For the response function calculations in this work, we use $\Delta C/C_0 = 0.1$. This is large enough to be astrophysically interesting, but small enough to ensure our models have an approximately linear response to changes in the continuum level.

4.2.3 Results: the reverberation signatures of rotating accretion disc winds

We are now ready to study the predicted reverberation signatures of our simple disc wind scenario for the BLR. The basic geometry of our model is shown in Figure 4.2 and describes a biconical outflow emerging from the surface of the accretion disc around the supermassive black hole (SMBH). The outflow gradually accelerates away from the disc plane, with each streamline reaching a terminal velocity on the order of the local escape speed at the streamline's footpoint on the disc surface. Similarly, material in the outflow initially shares the (assumed Keplerian) rotational velocity in the accretion disc, and then conserves its specific angular momentum as it rises above the disc and moves away from the rotation axis. Much more detailed descriptions of this basic disc wind model, including the importance of clumping within the wind, can be found in Shlosman and Vitello (1993), Long and Knigge (2002), Higginbottom et al. (2013), and Matthews et al. (2015, 2016).

To systematically study the reverberation signatures predicted by this model for the BLR, we need to distinguish between at least two types of AGN and two types of emission lines. First, the highest luminosity AGN – i.e. quasars/QSOs – are known to have significantly longer characteristic reverberation lags than lower luminosity AGN – i.e. Seyfert galaxies (Grier et al., 2012a; Kaspi et al., 2005). Second, low-ionization and high-ionization lines are also known to display significantly different reverberation lags (e.g. Kaspi and Netzer, 1999; Grier et al., 2012b). Both of these effects are qualitatively consistent with the idea that the physical conditions within the BLR are set by photoionization physics (Bentz et al., 2009a). As discussed in the previous subsection, strictly

TABLE 4.1: Model parameters

Parameter	Symbol, units	Seyfert	QSO
SMBH mass	$M_{\rm BH}$, $M_\odot$	10^7	10^9
Accretion rate	$\dot{M}_{\rm acc}$, $M_\odot\ yr^{-1}$	0.02	5
	$\dot{m}_{\rm acc}$, $\dot{M}_{\rm Edd}$	≈ 0.1	≈ 0.2
X-ray power-law index	α_X	-0.9	-0.9
X-ray luminosity	L_X, $erg\ s^{-1}$	10^{43}	10^{45}
X-ray source radius	r_X, r_g	6	6
	r_X, cm	8.8×10^{12}	8.8×10^{14}
Accretion disc radii	$r_{\rm disc}$(min)	r_X	r_X
	$r_{\rm disc}$(max), r_g	3400	3400
	$r_{\rm disc}$(max), cm	5×10^{15}	5×10^{17}
Wind outflow rate	$\dot{M}_w$, $M_\odot\ yr^{-1}$	0.02	5
Wind launch radii	$r_{\rm min}$, r_g	300	300
	$r_{\rm max}$, cm	4.4×10^{14}	4.4×10^{16}
	$r_{\rm min}$, r_g	600	600
	$r_{\rm max}$, cm	8.8×10^{14}	8.8×10^{16}
Wind launch angles	θ_{min}	70°	70°
	θ_{max}	82°	82°
Terminal velocity	$v_\infty(r_0)$	$v_{esc}(r_0)$	$v_{esc}(r_0)$
Acceleration length	R_v, cm	10^{16}	10^{19}
Acceleration index	α	1.0	0.5
Filling factor	f_V	0.01	0.01
Viewing angle	i	20°	20°
Number of photons		2×10^9	3×10^9

speaking we should also distinguish between collisionally excited and recombination lines in this context.

To cover this parameter space, we explicitly consider two distinct AGN models: one representative of high-luminosity QSOs, the other representative of lower-luminosity Seyferts. The physical characteristics we adopt for these models are listed in Table 4.1. Moreover, for each model, we present results for two types of lines: one high-ionization, collisionally excited metal line (C IV 1550 Å) and one low-ionization recombination line (Hα). Hα was chosen due to the strong Hα response in our model allowing for clearer response function plots than Hβ, though both lines are commonly used in RM studies.

4.2.3.1 A high-luminosity QSO

The key parameters of our representative QSO disc wind model are summarized in Table 4.1. It is essentially identical to the model described in Matthews et al. (2016), which was in turn based on the model described by Higginbottom et al. (2013). The Matthews et al. (2016) model is an attempt to test disc-wind based geometric unification for BALQSOs and "normal" (non-BAL) QSOs. It produces BALs for sightlines that

look directly into the wind cone and BELs for sightlines that do not. It is also broadly consistent with the observed X-ray properties of both QSOs and BALQSOs.

Figure 4.4 shows the UV and optical spectra predicted by this model for two representative sightlines. The first corresponds to an inclination of $i = 75°$, where $i = 90$ corresponds to an edge-on view of the system. An observer at this orientation necessarily views the central engine through the accretion disc wind and therefore sees a BALQSO. The second sight line corresponds to $i = 20°$ and allows a direct view of the inner accretion disc. An observer at this orientation should therefore see the system as an ordinary Type I QSO. The spectra in Figure 4.4 are consistent with this. The predicted UV spectrum for $i = 75°$ exhibits strong blue-shifted BALs and P Cygni features, whereas the spectra for $i = 20°$ only show BELs superposed on a blue continuum. Since absorption features are necessarily formed along the line of sight to the continuum source, BAL troughs respond to continuum variations without any light travel time delays. Our focus here is therefore on the BEL reverberation signatures in our $i = 20°$ Type I QSO model.

Figures 4.5 and 4.6 show the 2-D EWRFs and response functions we predict for the C IV and Hα lines in the $i = 20°$ QSO model. Figures 4.7 and 4.8 show the distribution of the C IV and H I ionization fractions and line luminosities within the outflow.

As shown in the upper panels of Figures 4.5 and 4.6, the EWRFs at short delays generally lie within the $v \propto \tau^{-1/2}$ envelope expected for a virialized flow dominated by Keplerian rotation, $v \propto R^{-1/2} \propto (c\tau)^{-1/2}$. The outflow kinematics of our models are only marginally apparent and only at the longest delays. In this regime the EWRFs, particular that for C IV, show a weak diagonal "blue-leads-red" structure. However, the strongest overall feature is found at the shortest delays ($\tau \lesssim 50$ days) and positive velocities ($v \simeq 2000$ km s^{-1}). Partly because of this, the EWRF in the observationally relevant regime $\tau \lesssim 200$ days appears to have a diagonal slant towards short delays and positive velocities, which could easily be (mis-)interpreted as an *inflow* signature.

In addition, whilst the two EWRFs are broadly similar, the C IV function is clearly narrower in velocity space. This reflects the difference in the respective line forming regions, as shown in Figure 4.8: Hα is concentrated in the Keplerian-dominated wind base, whilst C IV has a substantial contribution from the extended outflow (as well as a contribution from a thin layer near the inner edge of the wind).

Broadly speaking, the *response* functions look similar to the EWRFs, but there are some important differences. For example, the response functions for the two lines differ more than their EWRF counterparts, with the long delay component being far stronger in C IV than in $H\alpha$. Thus even though the C IV *emission* is quite concentrated towards short delays, the *response* of the line is more evenly spread across a range of delays. Conversely, we see a weak *negative* response at long delays in Hα. This happens because

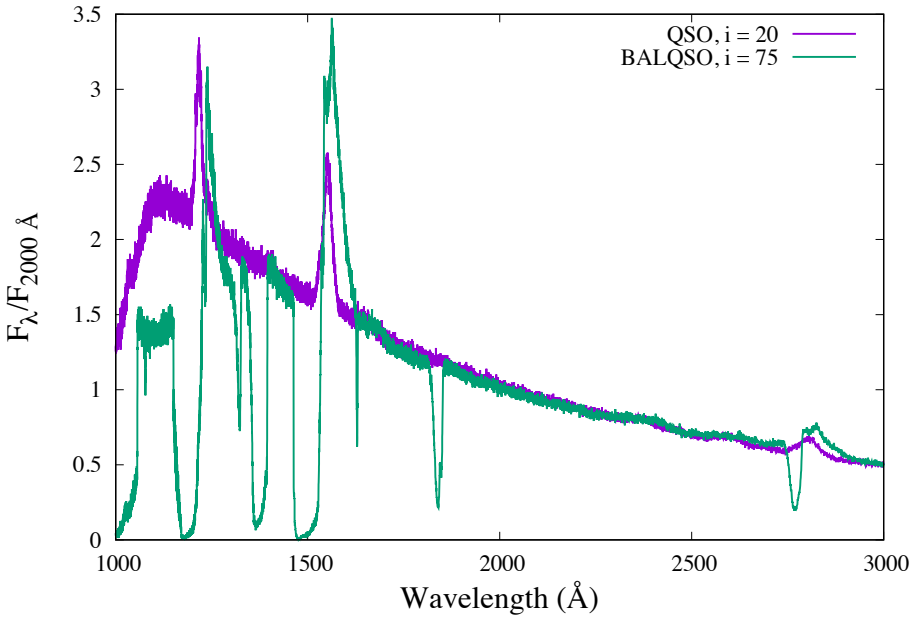

FIGURE 4.4: Spectra produced for the disc wind model of Matthews et al. (2016), viewed along QSO ($i = 20°$) and BALQSO ($i = 75°$) sightlines. Both spectra have been normalised to unity at 2000 Å.

an increase in continuum luminosity over-ionizes the extended wind and pushes the line-forming region (seen in figure 4.8) down towards the denser wind base. The potential to generate negative responses is an important feature of smooth/micro-clumped disc wind models. As we shall see in subsection 4.2.3.2, it can have a very significant effect on the overall reverberation signature.

4.2.3.2 A moderate luminosity Seyfert galaxy

Since the most extensive RM campaigns to date have been carried out on nearby Seyfert galaxies, rather than on QSOs, it is important to ask what the reverberation signature of a rotating disc wind BLR would be in this setting. We can attempt to answer this question by down-scaling down the QSO model developed by Matthews et al. (2016). In principle, there are many ways to carry out such a scaling, since essentially all system and outflow parameters may be mass- and luminosity-dependent. As a first step in this direction, here we take the simplest possible approach and scale the wind launching radii, wind acceleration length and X-ray luminosity in the model in proportion with the adopted BH mass ($10^7\ M_\odot$), as suggested by Sim et al. (2010).

In order to make our Seyfert model at least somewhat specific, we also adopt $\dot{M}_{\rm acc} = 0.02\ M_\odot\ {\rm yr}^{-1}$, based on the inferred accretion rate of NGC 5548 (Woo and Urry, 2002;

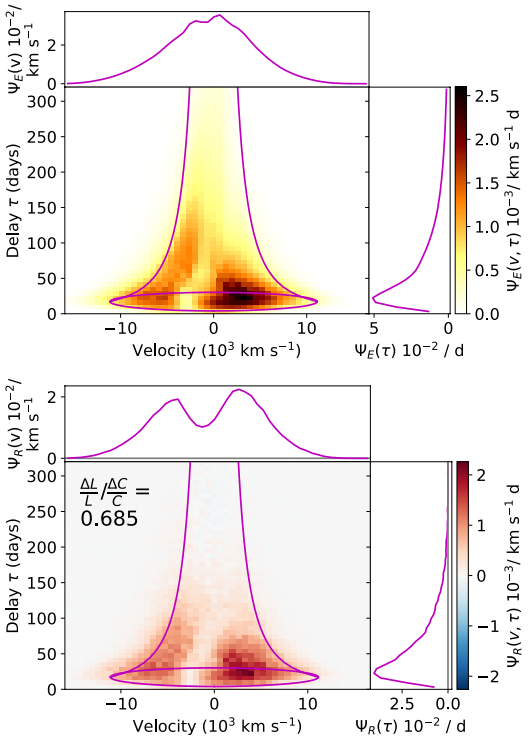

FIGURE 4.5: The velocity-resolved EWRF (upper) and response function (lower) for Hα in the QSO model, shown for time delays up to 320 days. The violet lines illustrate the function edges for a Keplerian disc at the wind launching radius, and the $\nu \propto \tau^{-1/2}$ "virial flow" envelope. Note that the velocity-integrated line response is weakly *negative* at low velocities beyond $\tau \gtrsim$ 220 days.

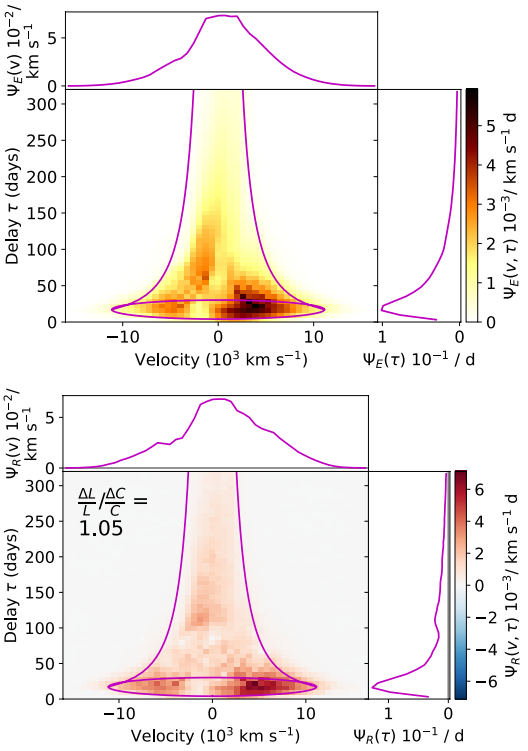

FIGURE 4.6: The velocity-resolved EWRF (upper) and response function (lower) for C IV in the QSO model, shown for time delays up to 320 days. The violet lines illustrate the function edges for a Keplerian disc at the wind launching radius, and the $\nu \propto \tau^{-1/2}$ "virial flow" envelope.

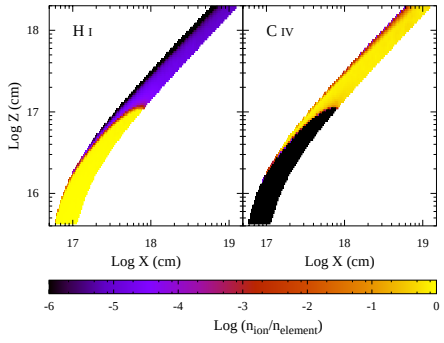

FIGURE 4.7: The H I and C IV ionization fractions within the wind in the QSO model.

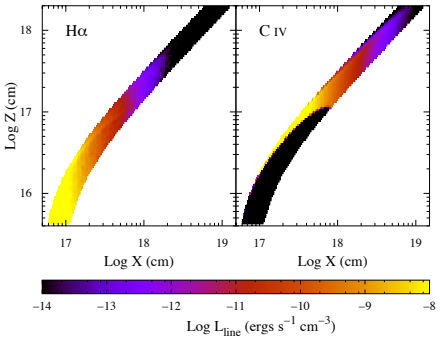

FIGURE 4.8: The line emissivity distribution for the Hα and C IV lines in the QSO model.

Chiang and Blaes, 2003). We then set $\dot{M}_w = \dot{M}_{\rm acc}$, as in the QSO model, and the basic geometry and kinematics of the outflow are also kept exactly the same as for the QSO case. The overall set of parameters describing our Seyfert model are listed in Table 4.1. Even though this model should not be construed as an attempt to *fit* observations of NGC 5548, it is instructive as a point of comparison for RM campaigns on this systems, such as that recently carried out by the AGNStorm collaboration (De Rosa et al., 2015; Kriss and Agn Storm Team, 2015; Edelson et al., 2015).

Figure 4.9 shows the UV and optical spectra predicted by our NGC 5548-like Seyfert I model for the same two sightlines as for our QSO model. In this case, even the sightline looking directly into the outflow does *not* produce a strong BAL signature in the UV resonance lines. This is interesting: to the best of our knowledge, there are no Type I Seyfert galaxies that exhibit permanent BALs, and only two that have shown bona-fide transient BAL features. One of these is, in fact, NGC 5548 (Kaastra et al., 2014), the other being WVPS 007 (Leighly, 2009). Additionally, in both of those cases the BALs appeared superposed on the overall BEL features without dipping significantly below the local continuum level. Thus, empirically, BALs are rare in Seyfert galaxies compared to QSOs. Intriguingly, our result here suggests that the BLR in Seyferts may nevertheless be an outflow, even one with the same overall geometry as those responsible for the BALs in QSOs.

Physically, the reason for the weakness of BAL features in the Seyfert model is related to the ionization structure of the outflow. In this type of model, the more distant parts of the outflow that are responsible for producing BALs in the QSO model are overionized (relative to the ionization stages associated with BAL transitions). The optical depth can therefore be insufficient for the production of strong, broad absorption features in these transitions, even for sightlines that look directly into the outflow cone. This overionization arises because Seyferts preferentially harbour black holes at the lower end of the mass range for AGN. As a result, their accretion discs extend to much smaller radii and reach much higher maximum temperatures. This leads to the spectral energy distribution being noticeably harder in comparison to QSOs, as seen in Figure 4.10. The tendency of AGN with lower mass BHs to produce more ionized winds has also been seen in hydrodynamic models of line-driven winds and reduces the efficiency of this driving mechanism (Proga and Kallman, 2004; Proga, 2005). This effect might explain the relative dearth of UV BAL features in Seyferts, as well as the occurrence of highly blue-shifted and highly ionized X-ray lines (Pounds, 2014; Reeves et al., 2016; Tombesi et al., 2010).

Figures 4.11 and 4.12 show the predicted 2-D EWRFs and response functions for Hα and C IV for our NGC 5548-like model Seyfert I model. To aid interpretation, we also once again show the distribution of the H I and C IV ionization fractions and line luminosities within the outflow (Figures 4.13 and 4.14).

The EWRFs in Figures 4.11 and 4.12 show reverberation signatures roughly similar to those of QSO models. However, the characteristic delay timescales are much shorter, as would be expected from the much smaller wind launch radius ($1/100^{\text{th}}$ that of the QSO model). This trend is also observed empirically (Bentz et al. 2013; also see subsection 4.2.4.1 below). There are also other differences from the QSO EWRFs. Perhaps most notably, the velocity ranges in which C IV and Hα are preferentially found have switched: Hα now appears at lower characteristic velocities than C IV. The reason for this is clear from Figure 4.13. The inner edge of the disc wind in these models is more strongly ionized in the Seyfert model compared to the QSOs one. This pushes the Hα emission back into the dense, heavily-shielded back of the wind. Meanwhile, C IV emission is concentrated in a thin ionization front near the inner edge of the flow and along the transition region between the dense, quasi-Keplerian base and the fast wind. The outflow-dominated distant regions of the flow are strongly over-ionized, so there are no obvious diagonal outflow signatures in Figures 4.5 and 4.6, even at long delays.

The *response* functions for the Seyfert model are even more interesting. Most importantly, both Hα and C IV exhibit strong *negative* responses in the low-velocity regime ($|v| \lesssim 5000$ km s^{-1}). In the case of Hα, this negative response contribution is strong enough to render even the integrated line response negative. Unlike in LOC-type models, negative responsivities can arise naturally in smooth/micro-clumped models. A simplistic explanation for this behaviour is that, as the continuum luminosity increases or decreases, any given line-forming region tend to move outwards or inwards. Parts of the wind that shift *out of* the line-forming region when the continuum increases will exhibit negative responsivities. In practice, the line-forming region is, of course, not always so sharply delineated.

To illustrate this, Figure 4.15 shows the local responsivities in the wind. The C IV line provides a particularly simple example, since here the emission is concentrated near a thin ionization front that shifts backwards through the wind with increasing luminosity. In this case, the regions of peak emission all exhibit positive responsivities of order $\eta \simeq 1$. By contrast, there is no clear ionization front for Hα, which is instead mostly produced near the outer edge of the wind. Near the disc plane, in the dense base of the wind, the responsivity remains positive, corresponding to the positive response seen at high velocities in Figure 4.11. However, the responsivity is mostly negative everywhere else. In these regions, the increased continuum luminosity has changed the thermal and ionization state in such a way as to *reduce* the number of photons that are produced.

Seyfert galaxies have long been attractive targets for RM campaigns, thanks to their short characteristic delays. Our results suggest that such campaigns may be able to test models such as ours, but considerable care needs to be taken in interpreting the observational data. Most importantly, attempts to reconstruct the response function from such data sets need to allow for the possibility of *negative* emission line responses in parts of the velocity-delay plane. Moreover, it is *not* safe to assume that all rotating disc

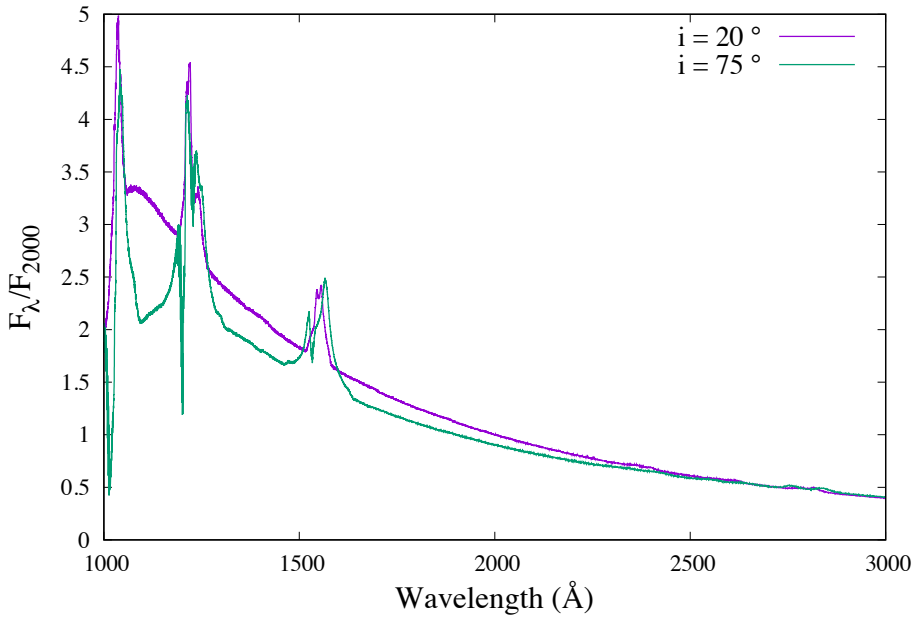

FIGURE 4.9: Spectra for Seyfert model along above wind $i = 20°$ and through-wind (BAL-equivalent in QSO model) $i = 75°$ sightlines, for comparison to Figure 4.4, normalised to flux at 2000 Å. Only very faint BAL features are apparent for BALQSO-like sightlines.

winds will produce response functions with a diagonal structure running from negative velocities and short delays to positive velocities and long delays. Such a structure is commonly thought of as the smoking-gun of an outflow (Denney et al., 2009), but our disc wind models do not produce this.

4.2.4 Discussion

In the previous subsection, we have presented the reverberation signatures predicted by smooth/micro-clumped rotating disc winds for representative QSO and Seyfert galaxy models. The resulting response functions are complex and differ substantially from those predicted by simple models for rotating accretion discs and quasi-spherical outflows (Welsh and Horne, 1991).

Perhaps most importantly, at the short lags that dominate the overall response, our response functions do *not* usually show the "blue-leads-red" diagonal structure that is often considered to be a characteristic outflow signature (cf. Figure 4.3). Such a signature is really only visible in our QSO model for C IV, on timescales of $\gtrsim 100$ days. Given the limitations of current reverberation mapping campaigns, this is unlikely to be detectable in practice. Instead, the response functions for our Seyfert models are roughly

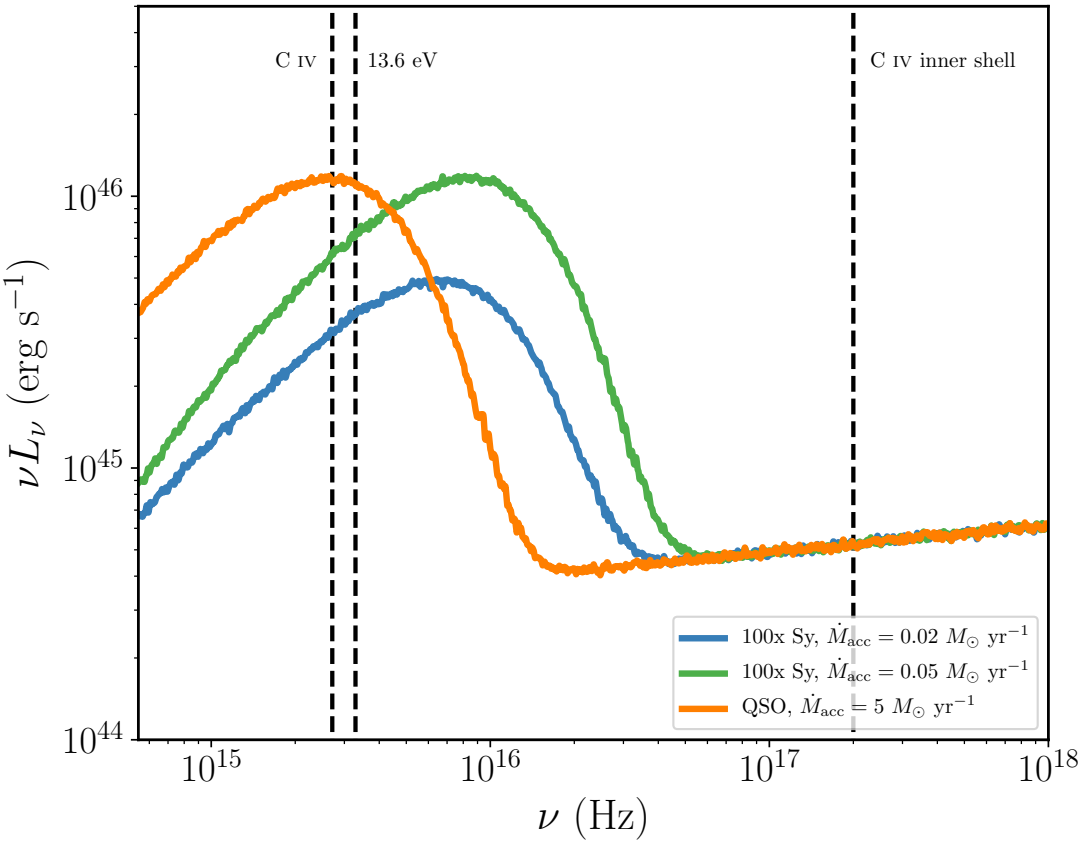

FIGURE 4.10: The spectral energy distributions (SEDs) for Seyfert and QSO models, including the contributions of both disc and corona. Our standard Seyfert model has an Eddington-normalized accretion rate of $\dot{m}_{acc} \simeq 0.1$, but we also show here an additional Seyfert model in which the Eddington fraction is identical to the QSO model, $\dot{m}_{acc} \simeq 0.2$. The SEDs for both Seyfert models are multiplied by a factor of 100, so they can be shown on the same scale as that for the QSO model. The locations of the H I (13.6eV), C IV and C IV inner shell ionization edges are marked.

symmetric, indicating that rotational kinematics dominate in the line-forming regions. This finding is in line with earlier disc-wind modelling efforts Chiang and Murray (1996); Kashi et al. (2013); Waters et al. (2016).

In our QSO models, the strongest response actually occurs at short lags and positive velocities. Indeed, the overall response functions for this model could easily be (mis-)interpreted as the "red-leads-blue" signature of an *inflow* (see Figures 5 and 6). "Red-leads-blue" reverberation signatures have, in fact, already been observed in several AGN and interpreted as evidence for inflows (Grier et al., 2012a; Bentz et al., 2010a; Gaskell, 1988; Koratkar and Gaskell, 1989). Based on our results, we urge caution in taking such interpretations at face value, at least in the absence of detailed kinematic and radiative transfer modelling of the data.

Another key feature of our disc-wind reverberation modelling is the prevalence for *negative* responses, particularly at low velocities and long delays. Negative responsivities are a common occurrence in smooth/micro-clumped flows, as an increase in the ionizing

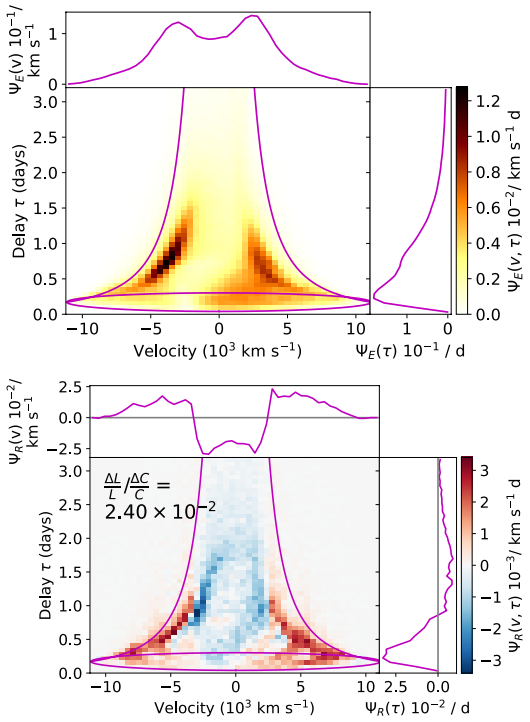

FIGURE 4.11: The velocity-resolved EWRF (upper) and response function (lower) for Hα in the Seyfert model, shown for time delays up to 3.2 days. The violet lines illustrate the function edges for a Keplerian disc at the wind launching radius, and the $\nu \propto \tau^{-1/2}$ "virial flow" envelope.

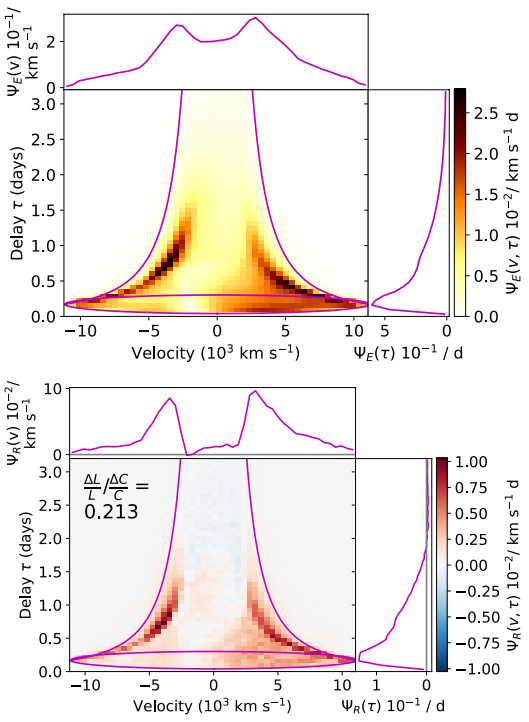

FIGURE 4.12: The velocity-resolved EWRF (upper) and response function (lower) for C IV in the Seyfert model, shown for time delays up to 3.2 days. The violet lines illustrate the function edges for a Keplerian disc at the wind launching radius, and the $\nu \propto \tau^{-1/2}$ "virial flow" envelope.

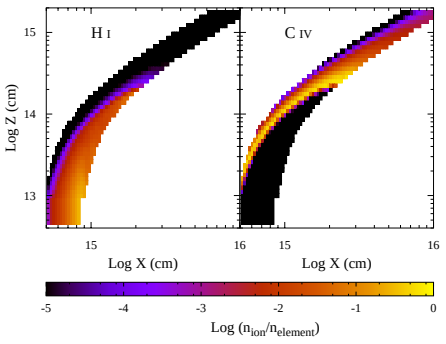

FIGURE 4.13: The H I and C IV ionization fractions within the wind in the Seyfert model. This graph shows a smaller region of the wind than figure 4.7 as the outflow is overionized in the Seyfert model and does not show emission in common RM lines.

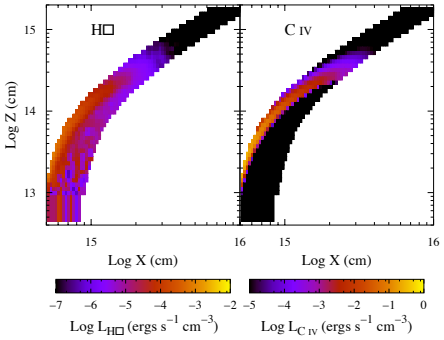

FIGURE 4.14: The line emissivity distribution for the Hα and C IV lines in the Seyfert model. This graph shows a smaller region of the wind than figure 4.8 as the outflow is overionized in the Seyfert model and does not show emission in common RM lines.

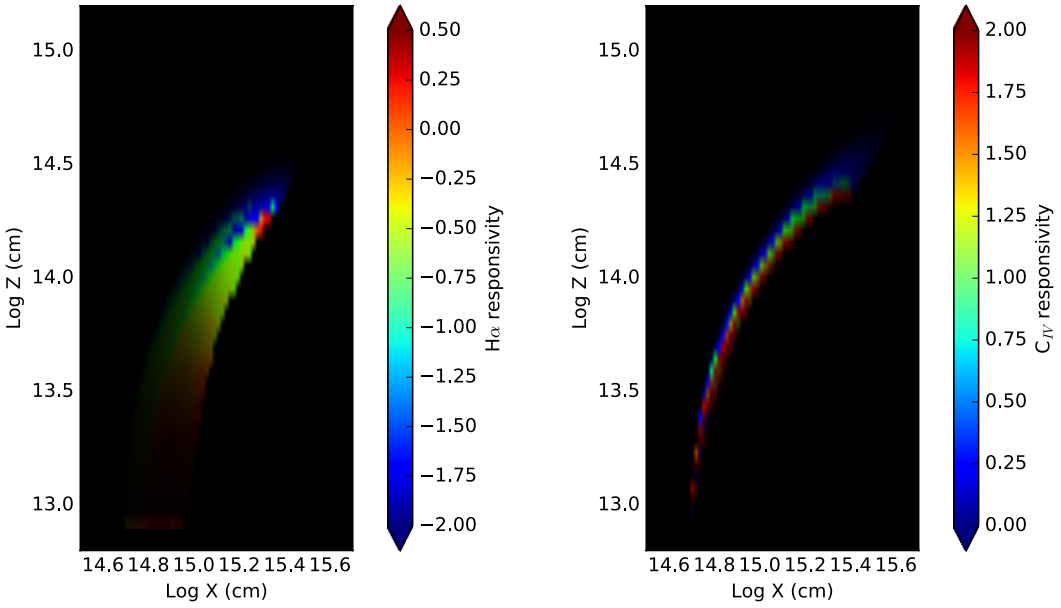

FIGURE 4.15: The local responsivity η for Hα (left) and C IV (right). Colour indicates responsivity, brightness indicates local emissivity. The brightest cells on the figure are in the upper 99.9% of cells for line emission; other cell brightnesses are scaled linearly to this value.

continuum shifts the line-forming region through the flow, enhancing the emissivity in some regions, but reducing it in others. This is similar to the way in which negative responsivities can arise in "pressure-law" models containing a significant portion of optically thin clouds Goad et al. (1993). As such, we predict that negative responses will arise in a wide range of systems, not just our specific model.

The process of inferring response functions from observational data is sensitive to negative responsivities in parts of the velocity-delay plane. At least one technique that allows for this possibility is available (Regularized Linear Inversion: Krolik and Done (1995); Skielboe et al. (2015)). However, both of the two most widely used methods – maximum entropy inversion (Krolik et al., 1991; Horne et al., 1991; Horne, 1994; Ulrich and Horne, 1996; Bentz et al., 2010a; Grier, 2013) and forward dynamical modelling (Pancoast et al., 2011; Waters et al., 2016) – explicitly assume that the responsivity is positive-definite. Given that negative responsivities are quite common in smooth/micro-clumped BLR models, this may not be a safe assumption.

We have also pointed out the weakness of BAL features in the spectra we have calculated for our Seyfert model, even for sightlines that look directly into the wind cone. This same sightline does produce strong BAL features in our QSO model. This behaviour is consistent with the observational dearth of BAL features in Seyfert galaxies. In our models, the absence of strong BALs in Seyferts is associated with the higher ionization state of their outflows. This is interesting, since it implies that disc winds might be ubiquitous in Seyfert galaxies – and even dominate the BLR emission – even though

hardly any of them show the BAL features that are the smoking gun for such outflows in QSOs.

4.2.4.1 Comparison to empirical lag-luminosity relations

A detailed comparison of our predicted response functions to observations is beyond the scope of the present study. However, it is instructive to ask whether the characteristic delays we predict for the C IV and Hβ lines are broadly consistent with the trends that have been established empirically (Peterson et al., 2005, 2006; Bentz et al., 2013).

An important consideration here is how to calculate the appropriate characteristic delay. In observational analyses, lags are usually estimated from the cross-correlation function (CCF) of the line and continuum light curves. More specifically, a typical procedure is to quote the centroid of the CCF, calculated within some fixed distance from the peak of the CCF. As discussed in detail by Welsh (1999), the CCF is equal to the velocity-integrated 1-D EWRF/response function convolved with the auto-correlation function of the continuum. Thus the CCF is simply a blurred version of the 1-D EWRF/response function. Consequently, we estimate characteristic delays for our models by calculating the centroid of the EWRF/response function within 80% of its peak (cf De Rosa (2015)). [1]

Figure 4.16 shows the empirical lag-luminosity relations for both transitions, over a luminosity range that includes both Seyferts and QSOs. The luminosities and mean lags predicted by our models are also shown. The luminosities are those that would be inferred from the spectrum observed for this particularly sightline (i.e. $\lambda L_\lambda = 4\pi d^2 \lambda F_\lambda$). For comparison, we show delays estimated from both EWRFs and response functions for our standard Seyfert and QSO models.

Figure 4.16 shows that the lags predicted by our standard Seyfert and QSO models are too small to match observations, by about an order of magnitude. The *slope* of the line connecting low- and high-luminosity models matches the data very well, however. Thus our models reproduce the observed power-law index of the lag-luminosity relation, but not its normalization. In principle, the simplest way to reconcile models and observations would be to move the wind-launching region radially outwards in the accretion disc. In practice, this will also require other parameter changes in order to roughly preserve the ionization state and spectral signatures of the outflow.

[1] It is worth noting that centroid delays calculated across the *entire* EWRF can be significantly longer, by as much as $\times 3$ or more. Moreover, the overall response of the Hα line in our Seyfert model – integrated over both velocity and delay – is negative, so it is hard to justify any estimate of a a global centroid delay for this line.

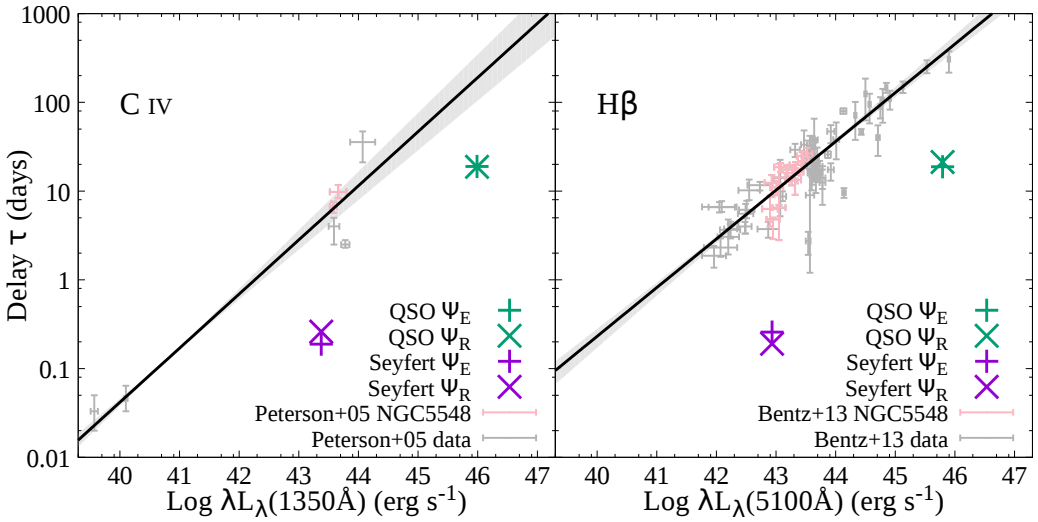

FIGURE 4.16: Luminosity-delay relationship for $H\beta$ and C IV compared to that determined observationally by Bentz et al. (2013) and Peterson et al. (2004). The line and shaded area around it are the fit and error on the fit. The points are the values from Bentz et al. (2013) and Peterson et al. (2004) with errors, with those corresponding to NGC5548 highlighted.

4.2.4.2 The inclination dependence of the virial product

As mentioned in subsection 4.2.1, RM-based SMBH mass estimates rely on the determination of the so-called *virial product*, $c\tau_{BLR}v^2_{BLR}/G$. Even if the velocity field in the BLR is dominated by the gravitational field of the SMBH, the virial product is, strictly speaking, not an estimate of M_{BH}, but is only proportional to it,

$$M_{BH} = fc\tau_{BLR}v^2_{BLR}/G, \tag{4.9}$$

where f is the constant of proportionality (the so-called "virial factor"). The need to introduce f arises primarily because the BLR is unlikely to be spherically symmetric. As a result, the measured lags and velocities are both expected to depend on the observer orientation with respect to the system. In such situations, f will then also depend on the emission line that is being used, due to the ionization stratification of the BLR.

There have been several attempts to estimate a "typical" or mean value for f. The derived values typically lie in the range $3 \lesssim f \lesssim 6$ (e.g. Onken et al., 2004; Woo et al., 2010; Park et al., 2012; Grier, 2013; Ho and Kim, 2014). More recently, Pancoast et al. (2014a) carried out an inverse RM analysis for several AGN in order to constraint the geometry and kinematics of the BLR. The inclination-dependence of the virial product – i.e. $f(i)$ – is a byproduct of their analysis and is shown in Figure 4.17. We also show there the values of f predicted by Yong et al. (2016) from two types of disc wind models in the literature (Murray et al., 1995; Elvis, 2004), for two specific inclinations. All of these results are for the Hβ line.

TABLE 4.2: Table of f factors against observation angles.

	Log f	
Angle	Hβ Ψ_R	Hβ Ψ_E
20°	0.9102	0.8738
30°	0.3011	0.3330
40°	0.1410	0.1239
50°	0.0509	0.0293
60°	-0.0508	0.0965
75°	0.2478	0.3573

For our own models, M_{BH} is an input parameter, and we can measure v_{BLR} from our predicted spectra and τ_{BLR} from our reverberation modelling. We can therefore easily calculate $f(i)$ for the models. The results for our $M_{BH} = 10^9$ $M_\odot$ QSO model are given in Table 4.2, where we provide our estimates of the virial factor associated with the Hβ line for five viewing angles. In Figure 4.17, we compare these calculations to the results of Pancoast et al. (2014a) and Yong et al. (2016). Pancoast et al. (2014a) model observations of AGN with $10^6 \lesssim M_{BH} \lesssim 10^7 M_\odot$, whilst Yong et al. (2016) adopt $M_{BH} = 10^8 M_\odot$ for their models. Despite these differences in M_{BH}, we find reasonable agreement between all of these estimates, as well as with the results of Storchi-Bergmann et al. (2017).

We do see one feature in our calculations of the virial factor that is not present in the simulations of Yong et al. (2016). At angles approaching the edge of the wind cone, f increases markedly in our models. This increases arises as sightlines close to the disc wind see their blue wing suppressed significantly, narrowing the line and reducing the estimated v_{BLR}. Sightlines through the disc wind experience an even greater suppression of their blue wing, but this is counterbalanced by an increase in the associated delay. Real AGN disc winds are unlikely to have sharp edges, of course. In any case, there is currently no observational data at high inclinations that could be used to look for such a feature.

4.2.5 Summary

Reverberation mapping has become an important tool for studying the structure of the broad line region of AGN. Here, we have used a Monte Carlo radiative transfer code to calculate the reverberation signatures for rotating disc wind models of the BLR. The QSO model presented by Matthews et al. (2016) is used to describe high-luminosity AGN, while a scaled-down version of this model (with parameters similar to NGC 5548) is used to describe moderate-luminosity Seyferts. We present spectra, velocity-delay maps and lag-luminosity relationships for the Hα and C IV emission lines for these models. Our main conclusions are as follows:

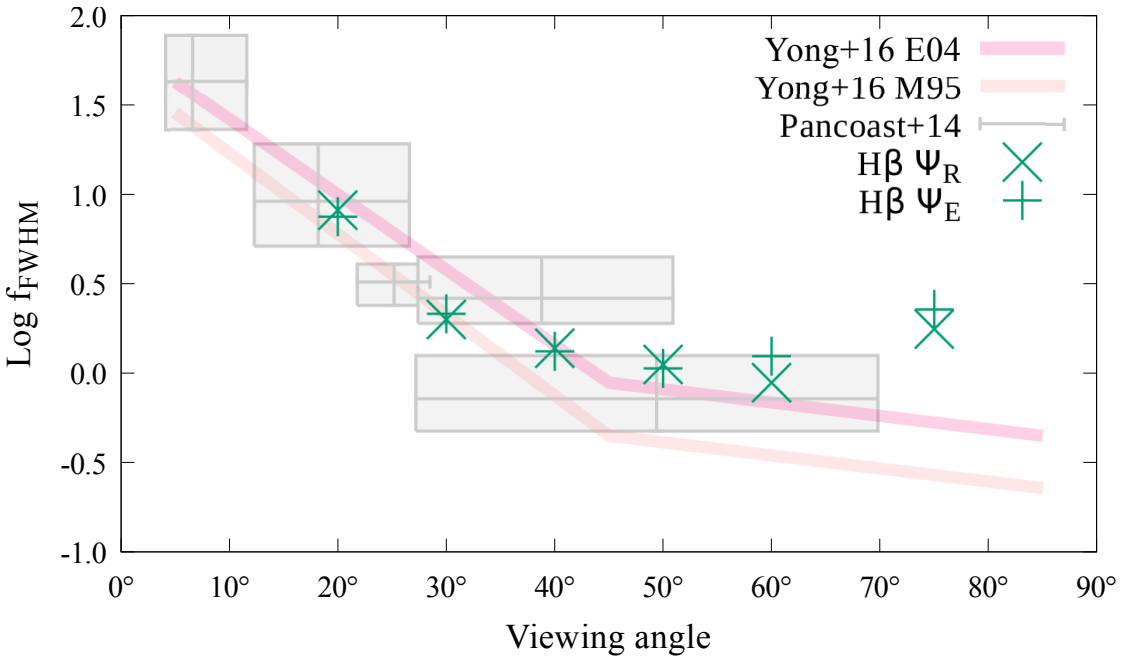

FIGURE 4.17: The virial factor (Equation 4.9) for our QSO disc wind model. The values listed here have been estimated from the velocity widths (FWHM) and centroid delays of the emission lines for mean emission. Observational data for 4 AGN from Pancoast et al. (2014a) are plotted with their error bars. Two sets of models from Yong et al. (2016) are also shown (see text for details).

- Smooth/micro-clumped disc-wind models of the BLR can produce *negative* responses in parts of the velocity-delay plane. This possibility needs to be taken into account when reconstructing response functions from observational data.
- The kinematics of the line-forming region tend to be rotation-, rather than outflow-dominated. In some lines, and at short delays, the red wing can even lead the blue wing, a signature usually thought of as characteristic of *inflow*.
- The classic "blue-leads-red" outflow signature can usually only be observed in the long-delay limit.
- The slope of the lag-luminosity relations predicted by the models is consistent with observations, but the centroid delays are too short, by about an order of magnitude.
- The dependence of the "virial product" on viewing angle in our models is consistent with the relationship suggested by recent observational modelling efforts.

Whilst our conclusions have been derived for a specific disc wind model, many of them can be applied more generally.

Acknowledgements

We are grateful to the anonymous referee for an excellent and constructive report that led to significant improvements to the paper. We acknowledge the University of Southampton's Institute for Complex Systems Simulation and the EPSRC for funding this research. CK acknowledges support from the Leverhulme Foundation in the form of a Research Fellowship and from STFC via a Consolidated Grant to the Astronomy Group at the University of Southampton. Part of his contribution to the project was carried out at the Aspen Centre for Physics, which is supported by National Science Foundation grant PHYS-1066293. JHM is supported by STFC grant ST/N000919/1. KSL acknowledges the support of NASA for this work through grant NNG15PP48P to serve as a science adviser to the Astro-H project.

4.3 Further Comments

In response to comments during my corrections, some further work was performed on the models used in this chapter.

4.3.1 Alternative Lines

It was requested that I comment on the Mg II and C III] line response times. In order to maintain consistency with the other simulations performed as part of this thesis, these were run in the same relatively old version of the code and input data. In this context it appears that there is no substantial C III] emission. In the intervening time, progress has been made on modelling carbon lines using the macro-atom techniques discussed in Section 2.2.3. Using the macro-atom model for carbon would allow for a more thorough treatment of the line, particularly collisional activation of it, and result in higher C III] emission. Alternatively, tweaks to the model geometry that enhance the line-to-continuum ratio (discussed in Section 6.1.1) could also produce enough C III] to allow for a response to be determined.

Mg II is produced in sufficient quantities to be used for reverberation mapping studies. We reproduced Figure 4.16 including the Mg II data from Shen et al. (2016) as Figure 4.18, using only the emissivity-weighted centroid delays (as they were equivalent to the full responsivity-weighted centroid delays to within a factor of 2). Interestingly, where they find that the Mg II and Hβ lines have approximately equal delays for a given luminosity, in our models the line emitting regions differ by almost an order of magnitude in delay. The actual Mg II delay for the QSO model is off the Hβ delay-luminosity trend; a plausible trend-line could be fit through our prediction and the existing Mg II observations, but there are insufficient data points to make a reasonable conclusion, and given the substantial underestimation of Hβ delays this suggests more serendipity than that the model accurately reflects where in the wind Mg II is produced.

As part of the initial work performed for Chapter 3, we calculated f-factors for a range of lines and compared to predictions and calculations from prior work as Figure 4.19. In this work, we determined that for this purpose, Mg II was likely to be as reliable as any other line. It lacked the 'jump' in f-factor seen in Hα for viewing angles close to the wind opening angle (where Hα serves, in this figure, as a proxy for Hβ; insufficient Hβ photons could be produced in this iteration of the code). At the time, we concluded that this suggested Mg II was generated further up in the wind, away from the dense wind base where the influence of a sight-line near the wind would have a greater effect. This appears to be backed up by the approximate order-of-magnitude difference in delay shown in Figure 4.18.

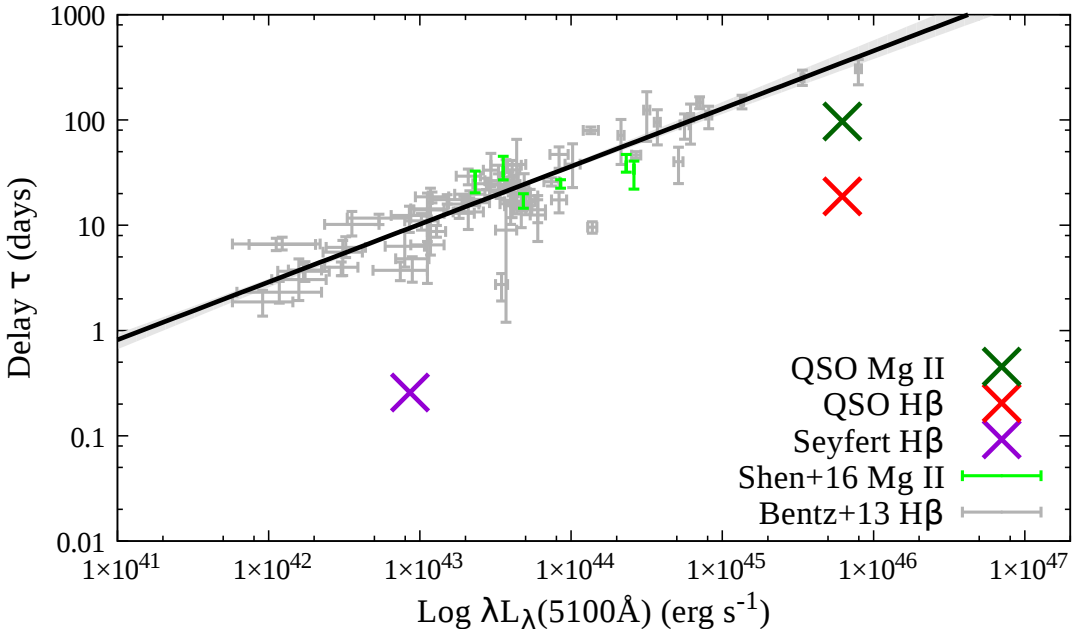

FIGURE 4.18: Luminosity-delay relationship for Hβ and Mg II using Hβ data from Bentz et al. (2013) and Mg II data from Shen et al. (2016). Trend-line is for Hβ as Figure 4.16.

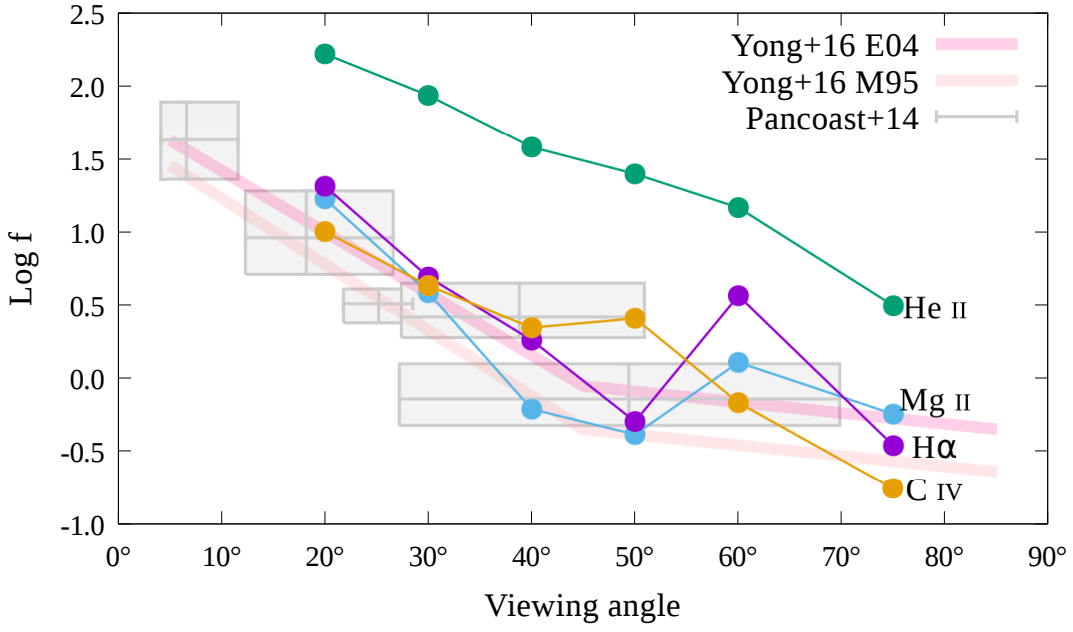

FIGURE 4.19: f-Factor calculated from various lines versus previous observations and models.

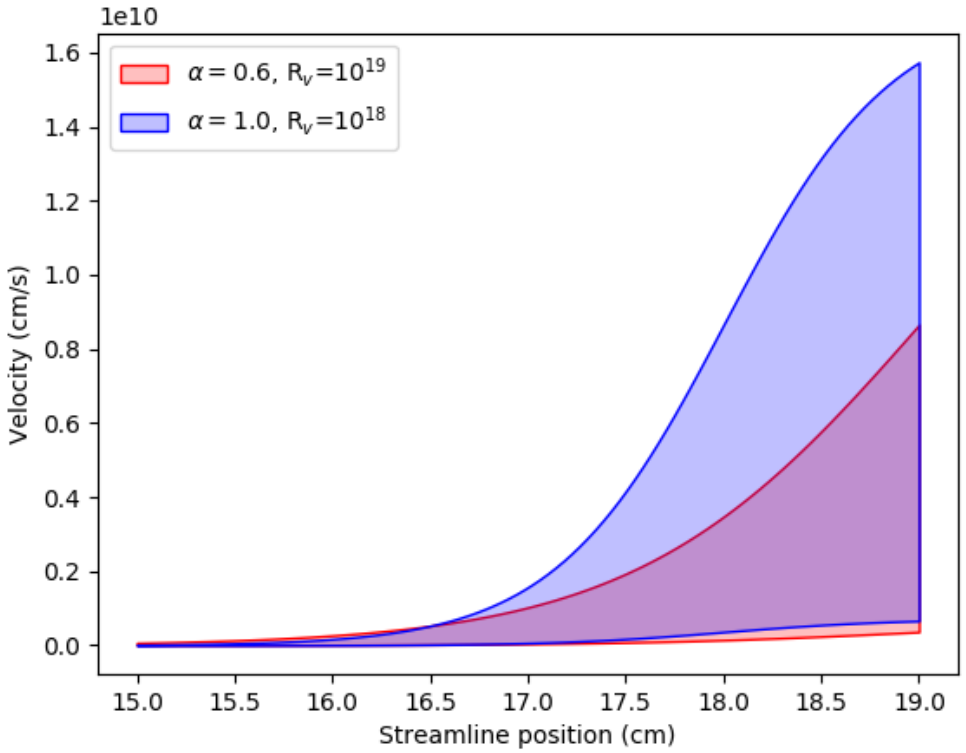

FIGURE 4.20: Wind outflow components along streamlines for the QSO model for varying wind velocity laws. Envelopes describe range of outflow velocities in wind at given position along streamline.

4.3.2 Matched Wind Parameters

In the paper, we used two broadly similar wind models, each of which had individually been tweaked to attempt to match the observed spectra of the class of system they represent. We did not comment on those differences beyond the 1:100 scaling in radius and luminosity. The actual *kinematics* of the outflow, however, exhibit reasonable differences between the two models. The QSO model has a much longer acceleration length R_v, and lower acceleration index α. These describe the wind density as per equation 2 of (Schlosman and Vitello, 1993) as

$$v_l = v_0 + (v_\infty - v_0) \times (\frac{(l/R_v)^\alpha}{(l/R_v)^\alpha + 1}). \tag{4.10}$$

With a relative order of magnitude reduction in acceleration length, the Seyfert model arrives at its maximum wind velocity sooner. However, when applying a scaled version of the Seyfert velocity law parameters to the QSO model as Figure 4.20 we see that the velocity profiles are broadly similar across the first 10^{17} cm of a streamline along the wind, where the majority of the line emission occurs.

Chapter 5

Testing Reverberation Mapping Inversion Methods

5.1 Introduction

Recent observational campaigns like AGN-STORM (De Rosa et al., 2015), the LICK AGN Monitoring Project (Bentz et al., 2009b) and others (Du et al., 2014; King et al., 2015; Shen et al., 2015) have focused on obtaining data with both high wavelength and time resolution. This enables velocity-resolved reverberation mapping of a large number of systems, allowing us to gain an insight into the kinematics of the AGN population. Studies have already shown a very mixed set of results, with AGN exhibiting response functions dominated by an assortment of Keplerian rotation, inflows (Ulrich and Horne, 1996; Grier, 2013; Bentz et al., 2008, 2010a; Gaskell, 1988; Koratkar and Gaskell, 1989) and outflows (Denney et al., 2009; Du et al., 2016). Given the broad range of signatures observed, it is necessary to understand whether these varied results are a genuine reflection of the variety of AGN geometries and kinematics. There exists the potential that they instead arise from the limitations of the deconvolution techniques used to recover the response functions, as to date they have only been tested against more simple model response functions. To investigate this, we set up collaborations with two of the main groups working on velocity-resolved reverberation mapping of AGN; Prof. Keith Horne and his MEMEcho code (Horne, 1994; Horne et al., 2004) and Prof. Anna Pancoast and her CARAMEL code (Pancoast et al., 2011, 2014a). We performed a blinded test of the codes, providing both groups with a time-series of synthetic line profiles from an artificial observing campaign without informing them of the response function used to generate them. We then tested their ability to recover the response maps from these datasets; both comparatively simple ones, and more complex features like negative responses. Our collaborators were not made aware of the specific

response functions being used until *after* they had performed their de-convolution and written their analysis of their recovered response functions.

5.2 Journal paper

The journal paper reproduced below is in preparation to submit to the Monthly Notices of the Royal Astronomical Society in 2018. Thanks to unanticipated delays on our collaborators' end, it has not been possible to provide a final, submitted version of the paper. We anticipate the draft to be altered due to the last-minute submission of a fit to the Seyfert model by Prof. Keith Horne 3 days before the thesis submission deadline. The authors of each code were responsible for writing both the method section describing the code's operation, and for the blinded analysis of the results of each code.

Testing Reverberation Mapping Inversion Methods

S. W. Mangham,[1] C. Knigge,[1] P. Williams, [3] K. Horne,[2] A. Pancoast, [3] J. H. Matthews,[4] K. S. Long,[5,6] S. A. Sim,[7] and N. Higginbottom[1]

[1] Department of Physics and Astronomy, University of Southampton, Southampton, SO17 1BJ, UK
[2] School of Physics and Astronomy, University of St. Andrews, North Haugh, St. Andrews KY16 9SS, UK
[3] Harvard-Smithsonian Center for Astrophysics, Garden Street, Cambridge, MA 02138, USA
[4] University of Oxford, Astrophysics, Keble Road, Oxford, OX1 3RH, UK
[5] Space Telescope Science Institute, 3700 San Martin Drive, Baltimore, MD 21218, USA
[6] Eureka Scientific, Inc., 2452 Delmer St., Suite 100, Oakland, CA 94602-3017, USA

[7] School of Mathematics and Physics, Queen's University Belfast, University Road, Belfast, BT7 1NN, UK

Reverberation mapping (RM) is a powerful approach for determining the nature of the broad-line region (BLR) in active galactic nuclei. However, inferring physical BLR properties from an observed spectroscopic time series is a difficult inverse problem. Here, we present a blind test of two widely used RM methods: MEMEcho (developed by Horne) and CARAMEL (developed by Pancoast and collaborators). The test data are simulated spectroscopic time series that track the Hα emission line response to an empirical continuum light curve. The underlying BLR model is a rotating, biconical accretion disc wind, and the synthetic spectra are generated via self-consistent ionization and radiative transfer simulations. We generate two mock data sets, with parameters designed to represent Seyfert galaxies and QSOs. The Seyfert model produces a largely *negative* response, which neither MEMEcho nor CARAMEL are able to recover. However, both methods fail "gracefully", with neither generating spurious results. For the QSO model, the MEMEcho velocity-delay map is a good match to the input response function. Expert interpretation of the map as pointing to an annular, rotation-dominated line-forming region is also broadly correct, although its size is overestimated by 50%. CARAMEL similarly captures the overall geometry of the QSO line-forming region, describing it as a flared, inclined disc with the correct size and orientation. The importance of rotation to the BLR kinematics is also correctly recovered, but CARAMEL is unable to distinguish between additional inflow and outflow components. Surprisingly, the CARAMEL velocity-delay maps and RMS line profiles are strongly inconsistent with the input data. This is difficult to understand, since the individual spectra are well fit. Finally, since the Hα line-forming region is rotation dominated, neither method recovers the disc wind nature of the underlying BLR model. Thus considerable care is required when interpreting the results of RM analyses in terms of physical models.

5.3 Introduction

Reverberation mapping (RM) has become a powerful tool for determining the physical properties of active galactic nuclei (AGN; Peterson 1993). As the continuum of an AGN

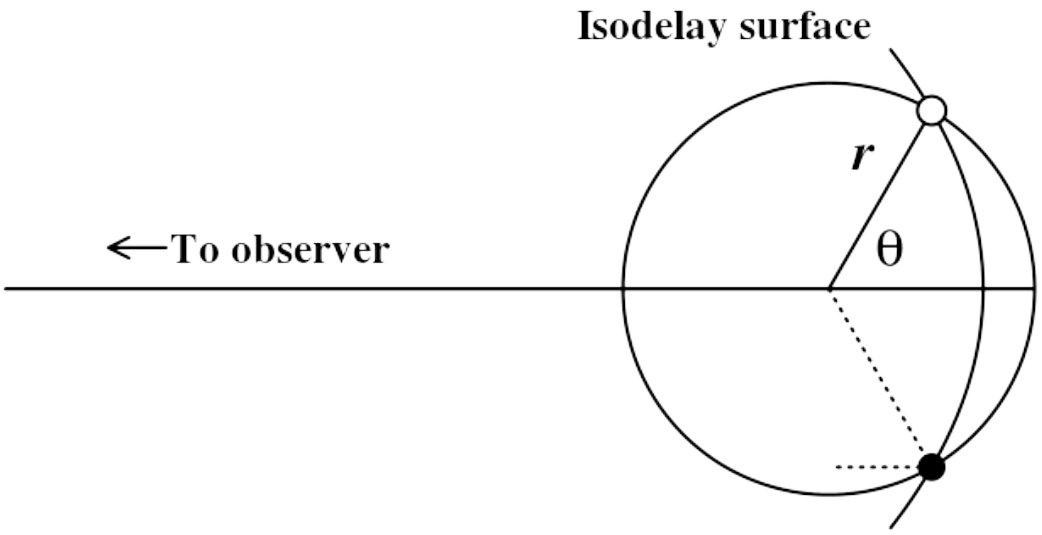

FIGURE 5.1: Isodelay contour from Peterson et al. (2004).

varies, each broad emission line (BEL) in its spectrum usually responds with a mean lag, τ, on the order of hours to months, depending on the luminosity of the system and the specific transition involved (Onken et al., 2004; Kaspi and Netzer, 1999; Kaspi et al., 2005). By associating this lag with the light travel time from the central engine to the line-forming region, one obtains an estimate for the size of the broad line region (BLR), $R_{\rm BLR} \simeq c\tau$. Moreover, BELs in Type I AGN are substantially Doppler-broadened, so the width of a line is a measure of the velocity field in the BLR. If this is assumed to be roughly virialized – $v_{\rm BLR} \simeq \sqrt{GM_{\rm BH}/R_{\rm BLR}}$ – a black hole mass estimate can also be found immediately as $M_{\rm BH} \simeq c\tau_{\rm BLR} v_{\rm BLR}^2/G$.

In reality, line-emitting material at any given distance from the central engine can produce a wide range of observed lags. Equivalently, any given lag can in principle be produced by line-emitting material across a wide range of distances. More specifically, isodelay surfaces around a point source form a set of concentric paraboloids of revolution centred on the line connecting the observer and the source (Figure 5.3; Peterson et al. (2004)). Which parts of an isodelay surface *actually* produce the observed line emission at a given lag – and which isodelay surfaces actually contribute to a given line – depends on the geometry, density and ionization state of the BLR, as well as on the inclination of the observer with respect to the system. In addition, different *parts* of a given line – e.g. red and blue line wings – will exhibit different responses, depending on the kinematics of the BLR. For example, if the BLR is dominated by outflow kinematics, material moving towards the observer is also physically closest to the observer. The response of the blue wing is then expected to lead that of the red wing (see Figure 5.2).

The true response of a given line to continuum variations is therefore a distribution

function over (at least[1]) time delay and radial velocity. Moreover, the shape of this function encodes information about the structure of the BLR – its geometry, kinematics and ionization state – on otherwise unresolvably small physical scales (Welsh and Horne, 1991). Thus, provided we can decode them, time- and velocity-resolved response functions (aka "velocity-delay maps") provide us with a powerful tool for determining the physical nature of the BLR.

Several recent observational campaigns have obtained time-resolved spectroscopic data sets designed to allow the recovery of such 2-D response functions (De Rosa et al., 2015; Du et al., 2014). These efforts have produced a wide range of apparent kinematic signatures, from simple rotation to both inflows (Ulrich and Horne, 1996; Grier, 2013; Bentz et al., 2008, 2010a; Gaskell, 1988; Koratkar and Gaskell, 1989) and outflows (Denney et al., 2009; Du et al., 2016). This variety of recovered response functions suggests that either the BLR is a much more heterogeneous entity than envisaged by current unification models, or that we are not correctly recovering and/or interpreting response functions from observational data. The aim of this paper is to test the latter possibility.

It is reasonable to worry about our ability to infer the physical structure of the BLR from the available observational data. Fundamentally, the issue is that this type of inference represents an ill-posed inverse problem. In particular, even though any time-resolved spectroscopic data set of finite quality contains *some* information about the BLR geometry and kinematics, this provides no guarantee of uniqueness. Thus, in principle, many physically different BLR structures might all produce very similar observational signatures. In practice, external constraints (aka "regularization") are usually used to select a unique solution from the set of models that are consistent with the data. The challenge is establishing that the selected solution is the physically correct one.

An excellent way to validate the inversion methods used in RM is to test them in a controlled manner against a *known* response function. We can do this by calculating the response function for a physically-motivated BLR model and using this to generate a simulated spectroscopic time series that is comparable in quality to those provided by current observing campaigns (e.g. De Rosa et al., 2015). We can then apply the RM methods to this mock data set and check the results against "ground truth" (which is known in this case).

Here, we implement this idea by building on the results of Mangham et al. (2017). There, we used a radiative transfer and ionisation code (Long and Knigge, 2002) to produce physically-motivated response functions for one candidate BLR geometry, a rotating biconical disc wind (Shlosman and Vitello, 1993). We now use these response functions, together with a driving continuum derived from an actual UV data set (Fausnaugh et al., 2016), to generate mock spectroscopic observing campaigns.

[1]In principle, the line response also depends on the (possibly variable) source spectral energy distribution (SED), on the amplitude and shape of the continuum variations and on any physical changes in the BLR structure over the course of the observing campaign.

The two specific model response functions we use in our tests are based on a high-luminosity QSO and low-luminosity AGN disc wind model, respectively. One of these satisfies standard assumptions about response function behaviour (i.e. linear positive response with increasing luminosity), the other one does not. Taken as a pair, they provide a sensitive test of RM methods in very different regimes.

The remainder of this paper is organised as follows. In Section 5.4, we outline the theory behind RM. In Section 5.5, we describe the radiative transfer and ionisation code we use to generate our simulated response functions and explain how these response functions are then used to generate the synthetic spectroscopic time series for our mock observing campaigns. The authors of the two specific RM methods we test – MEMEcho and CARAMEL – then describe their respective analysis techniques. In Section 5.6, we present, assess and discuss the results obtained by each method. Finally, in Section 5.7, we summarise our main conclusions.

5.4 Background

5.4.1 Reverberation Mapping: Basic Principles

Reverberation mapping is based on the premise that the BLR reprocesses the ionising continuum from the central source into line emission. Fluctuations in the continuum propagate outwards at the speed of light, causing changes in the line emission when they interact with material in the BLR at later times. The time-scale on which this material responds – i.e. the time-scale on which ionization equilibrium is established in the BLR – is thought to be short compared to both the continuum variability and light-travel time-scales. The contribution of BLR material at position $\underline{\mathbf{r}}$ to the total line luminosity observed at time t then depends only on the continuum luminosity at the earlier time $t - \tau$. Here, τ is the additional time required for light emitted by the central engine to reach the observer via a path that includes $\underline{\mathbf{r}}$.

5.4.2 1-D Response Functions: Delay Distributions

If the line response is perfectly linear – i.e. if each location in the BLR always produces a fixed number of line photons per continuum photon – the total line luminosity L at time t is a function of the continuum C as

$$L(t) = \int_0^\infty C(t-\tau)\,\Psi_R(\tau)\,d\tau, \tag{5.1}$$

where $\Psi_R(\tau)$ is the so-called *1-D response function* or *delay distribution*. More specifically, $\Psi_R(\tau)$ is the weighted average reprocessing efficiency of all parts of the BLR that contribute to the response observed at delay τ.

In reality, line responses are *not* perfectly linear. A better approximation is to linearise the response around reference (e.g. long-term average) continuum and line luminosities C_0 and L_0 (e.g. Horne 1994):

$$C(t) \simeq C_0 + \Delta C(t), \tag{5.2}$$

and

$$L(t) \simeq L_0 + \Delta L(t). \tag{5.3}$$

We can then define the response function to refer to only the variable parts of the luminosities,

$$\Delta L(t) = \int_0^\infty \Delta C(t-\tau)\, \Psi_R(\tau)\, d\tau. \tag{5.4}$$

This model can deal with *globally* non-linear responses, so long as the continuum variations are small enough to ensure that the *local* response remains approximately linear.

Conceptually, the 1-D response function, $\Psi_R(\tau)$ describes how the line emission produced by a sharp continuum pulse is spread across a range of time delays, τ. Mathematically, the response function is just the partial derivative

$$\Psi_R(\tau) = \frac{\partial L(\tau)}{\partial C(t-\tau)}. \tag{5.5}$$

We can make the dependence of the response function on the local conditions within the BLR more explicit by writing it in terms of the line luminosity *per unit volume*,

$$\Psi_R(\tau) = \int_{V_{\rm BLR}} \frac{\partial l(\underline{\mathbf{r}})}{\partial C(t-\tau)}\, \delta(\tau(\underline{\mathbf{r}}))\, dV. \tag{5.6}$$

Here, the integral on the right-hand-side is over the entire volume of the BLR, $\partial l(\underline{\mathbf{r}})/\partial C(t-\tau)$ is the line response *per unit volume* at location $\underline{\mathbf{r}}$, and the delta function ensures that only locations that produce the correct delay contribute to the total response at τ.

5.4.3 2-D Response Functions: Velocity-Delay Maps

The 1-D response function can be calculated straightforwardly from Equation 5.6 for any given BLR geometry and emissivity distribution. However, many different physical models of the BLR could, in principle, produce the same delay distribution.

One way to partially break this degeneracy is to add kinematic, i.e. velocity, information. We can do this by splitting our emission line light curve into distinct radial velocity bins and constructing the delay distribution separately for each bin. This immediately leads to velocity-resolved versions of Equations 5.4-5.6:

$$\Delta L(v,t) = \int_0^\infty \Delta C(t-\tau)\, \Psi_R(v,\tau)\, d\tau, \tag{5.7}$$

$$\Psi_R(v,\tau) = \frac{\partial L(v,\tau)}{\partial C(t-\tau)}, \tag{5.8}$$

$$\Psi_R(v,\tau) = \int_{V_{\rm BLR}} \frac{\partial l(\underline{\mathbf{r}})}{\partial C(t-\tau)}\, \delta(\tau(\underline{\mathbf{r}}))\, \delta(v(\underline{\mathbf{r}}))\, dV. \tag{5.9}$$

Here, $v(\underline{\mathbf{r}})$ is the radial velocity at position $\underline{\mathbf{r}}$ in the BLR. The 2-D response function, $\Psi_R(v,\tau)$, is also often referred to as the *velocity-delay map* of the BLR.

5.4.4 Reverberation Mapping in Practice: Constructing a Data-Driven BLR Model

The addition of kinematic information lifts some of the degeneracy associated with $\Psi_R(\tau)$. For example, inflows and outflows that differ only in the sign of their velocity vector will produce identical 1-D response functions, but very different velocity-delay maps. As illustrated in Figure 5.2 (c.f. Horne 1994), inflow [outflow] kinematics are generally expected to produce a "red-leads-blue" ["blue-leads-red"] signature in $\Psi_R(v,\tau)$. Similarly, pure rotation tends to produce symmetric velocity-delay maps, whose envelope is defined by the dependence of the rotation speed on distance from the central object.

However, in physically motivated models, such as the rotating disc wind model of Matthews et al. (2016), we may expect to see a mix of these signatures. Moreover, the geometry of the line-emitting region will also depend strongly on the ionisation structure of the BLR. In fact, the line response may even be *negative* in parts of the velocity-delay space, as the associated sections of the wind become over-ionised and stop emitting. These effects can significantly complicate the interpretation of $\Psi_R(v,\tau)$ (Mangham et al., 2017).

Fundamentally, the issue is that even 2-D reverberation mapping is non-unique: a given data set, $C(t)$ and $L(v,t)$, may be consistent with many different physical BLR models. This is easy to understand. A full physical picture of the BLR requires us to specify at least the density and velocity at each position. Suppose we were to discretize the BLR spatially and kinematically into just 10 bins in each of these 7 parameters (position vector, velocity vector, density). The resulting model space then contains 10^7 distinct parameter combinations, which vastly exceeds the number of data points in any realistic set of observations. In order to find a unique solution for this type of ill-posed inverse problem, additional "regularization" constraints have to be provided (e.g. based on physics, geometry, kinematics, smoothness, etc).

Two different approaches have so far been used to develop a data-driven physical picture of the BLR from time- and velocity-resolved observational reverberation mapping campaigns. In the first approach, the primary aim is the construction of $\Psi_R(v,\tau)$ from the data. Even this is an inverse problem, but determining a 2-D response function is a much more constrained problem than inferring an at least 7-D physical description of

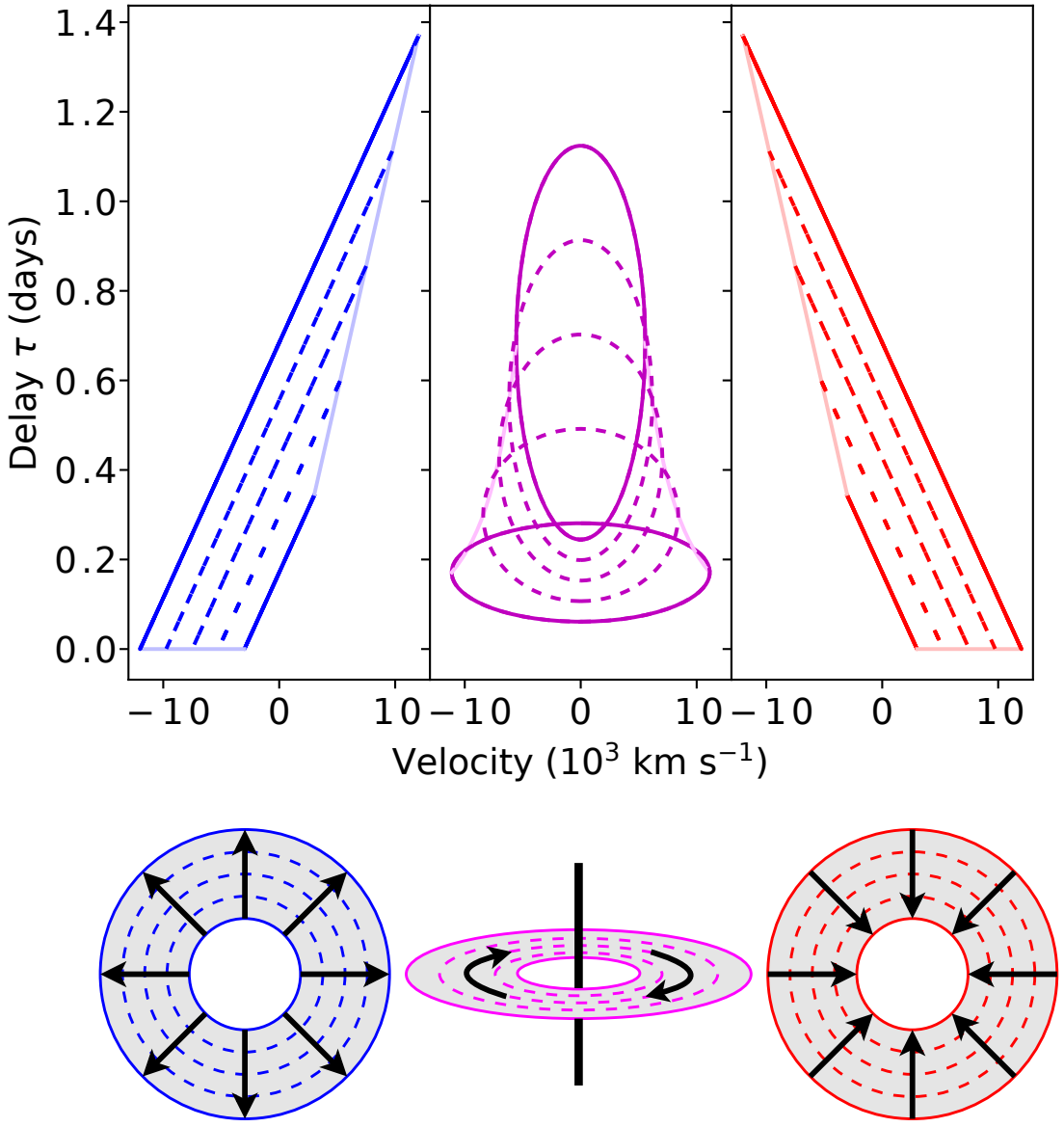

FIGURE 5.2: Outline response functions and schematics for Hubble-type spherical outflow **(left)**, a rotating Keplerian disc viewed at a 20° angle **(centre)**, and Hubble-type spherical inflow **(right)**. Winds extend from $r_{\rm min} = 20r_g$ to $r_{\rm max} = 200r_g$ for an AGN of mass $10^7 M_\odot$. Hubble out/inflows have $V(r_{\rm min}) = \pm 3 \times 10^3$ km s^{-1}. Solid lines denote the response from the inner and outer edges of the winds, dotted lines from evenly-spaced shells within the wind. Pale lines describe the edge of the velocity-delay shape of the response function.

the BLR. The interpretation of the velocity-delay map in terms of an underlying physical picture is up to the user in this approach. Typically, this is based on a qualitative comparison of the recovered $\Psi_R(v, \tau)$ to the response functions produced by simple toy models, such as those in Figure 5.2. We will refer to this as the "inverse approach". In our tests, this approach is represented by MEMEcho (Horne, 1994), which is described more fully in Section 5.5.5. The SOLA method (Pijpers and Wanders, 1994), regularized linear inversion (Krolik and Done, 1995; Skielboe et al., 2015) and the Sum-of-Gaussians method (Li et al., 2016) all belong to this class as well.

The second approach is to build a highly flexible physical model of the BLR, whose parameters can be adjusted to fit the observed $L(v, t)$, using the observed $C(t)$. In principle, this approach does not require $\Psi_R(v, \tau)$ to be calculated explicitly for either the model or the data. In practice, the response function of the best-fitting model still provides a useful visualization tool and is easy to calculate from Equation 5.9. The advantage of this approach is that the optimal fit parameters immediately provide a basic physical picture of the BLR. A key risk is that the parametrization of the model is incapable of describing the true BLR. This method also requires the implementation of all the physics needed to predict $L(v, t)$ from $C(t)$ for any given set of model parameters. We will refer to this as the "forward-modelling approach". It is represented in our test by CARAMEL (Pancoast et al., 2011, 2014a,b), which models the BLR as a population of reflecting, non-interacting clouds. CARAMEL is described more fully in Section 5.5.6.

5.5 Methods

5.5.1 Simulating an Observational Campaign

5.5.1.1 Line Formation in a Rotating disc Wind

We use the radiative transfer and ionisation code Python to simulate the formation of the Hα emission line in a rotating, biconical accretion disc wind model of the BLR. Python has already been described several times in the literature (Long and Knigge, 2002; Sim et al., 2005; Noebauer et al., 2010; Higginbottom et al., 2013, 2014; Matthews et al., 2015, 2016), so we provide only a brief description of it here. Given a specification of the radiation sources, as well as of the disc wind geometry and kinematics, the code performs an iterative Monte Carlo ionization and radiative transfer simulation. It follows the paths of photons generated by a central X-ray source, an accretion disc and the wind itself through the system, records their interactions with the wind, and calculates their effect on the local temperature and ionization state. Once all photons in a given iteration have traversed the grid, the temperature and ionisation state of each wind cell is updated. This changes the emission profile and opacity of the wind, so the radiation transfer process is repeated. The ionisation state is then recalculated, and this process

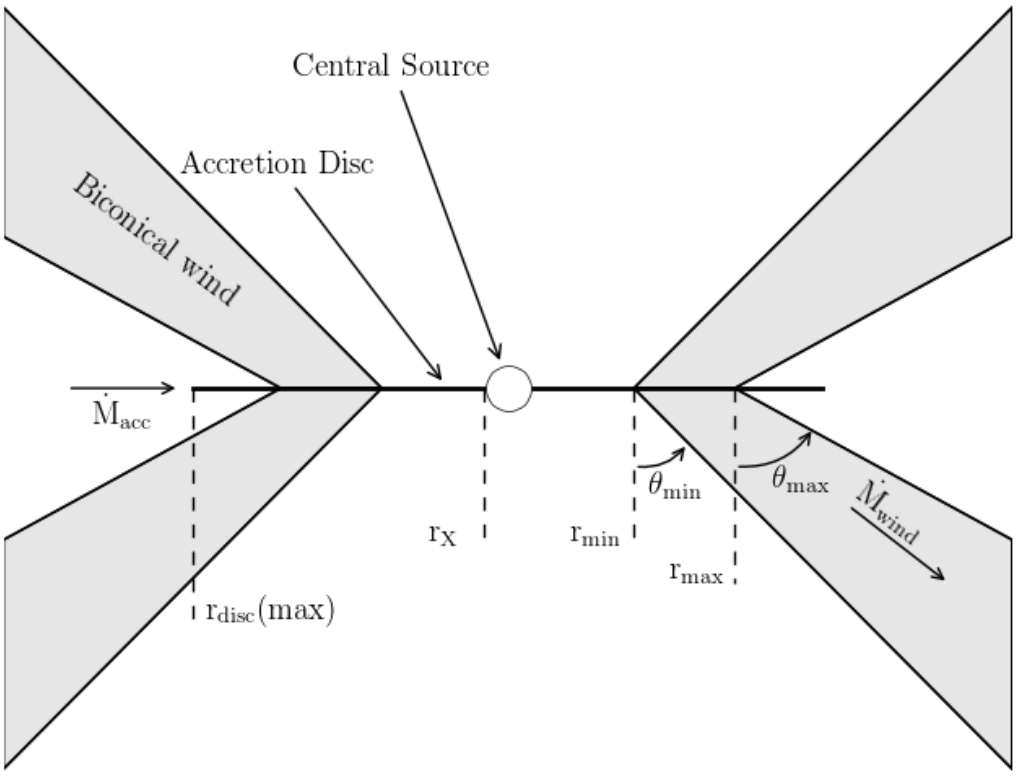

FIGURE 5.3: Sketch of the biconical disc wind geometry from Matthews et al. (2016).

is iterated until the temperature and ionisation state of the wind have converged. The converged wind model is then used to generate detailed spectra for a range of user-specified observation angles.

The basic disc wind geometry we adopt for the BLR is illustrated in Figure 5.3. For the purpose of testing RM inversion methods, we consider two specific parameter sets: the Seyfert and QSO models from Mangham et al. (2017). These were chosen because they represent plausible, physically-motivated response function signatures and display a range of behaviours that allow us to investigate the capabilities of inversion tools to cope with both straightforward and unusual response functions (see Section 5.5.1.2). All relevant parameters of these models – along with brief explanations of what they encode – are provided in Table 5.1. The corresponding mean line profiles are shown in Figure 5.4.

5.5.1.2 Creating Response Functions

We use PYTHON to generate 2-D response functions using the methodology described in Mangham et al. (2017). Briefly, the response function, $\Psi_R(v, \tau)$, describes how a change in line emission at time t depends upon changes in the continuum across a range of

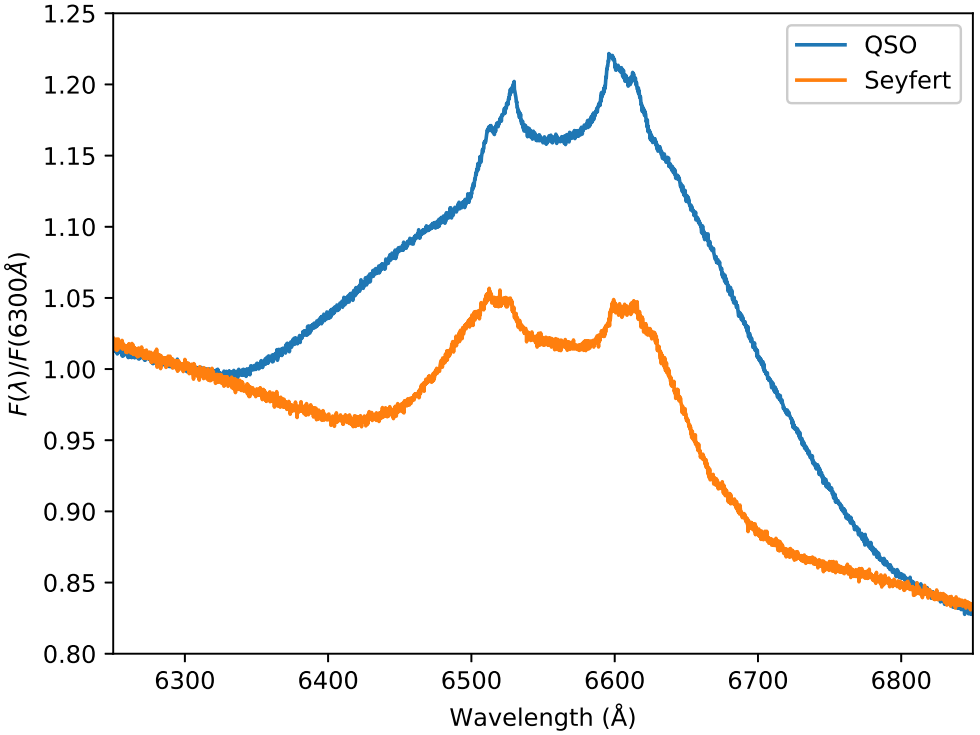

FIGURE 5.4: Mean line profiles for our the Hα line in our QSO and Seyfert models.

previous times $t - \tau$. This requires making the assumption that the response function itself is *not* dependent on the incident continuum luminosity. If this is the case, then the response function can also be mirrored in time: it describes not only how the line emission observed at time t depends on the continuum at time $t - \tau$, but *also* how the continuum at time t propagates out to change the line emission at time $t+\tau$. As a result of this, we can derive the response function Ψ_R by forward-modelling. An instantaneous change in continuum luminosity at time t drives changes in line emission at a range of times $t+\tau$. These changes can be calculated by tracking the photons in our Monte Carlo simulation and calculating their arrival time delay, τ, from their path. These photons are then binned by velocity and delay to produce a response function $\Psi_R(v, \tau)$.

In order to match the average ≈ 3 day delays seen in Hβ for NGC 5548 (Bentz et al., 2013), we re-scale the time axis in our response functions so that the peak delay occurs at ≈ 3 days (the exact peak delays in our rescaled models are 2.25 days for the Seyfert model and 4.05 days for the QSO model). The resulting rescaled response functions no longer correspond directly to a fully self-consistent BLR model, but this is not a concern for the purpose of testing RM inversion methods. Here, our main requirement is simply to have known response functions that (a) are characterised by an empirically-motivated mean delay, and (b) account for the complexities associated with physically motivated BLR models (e.g. mixed kinematics, complex emissivity distributions, negative responses).

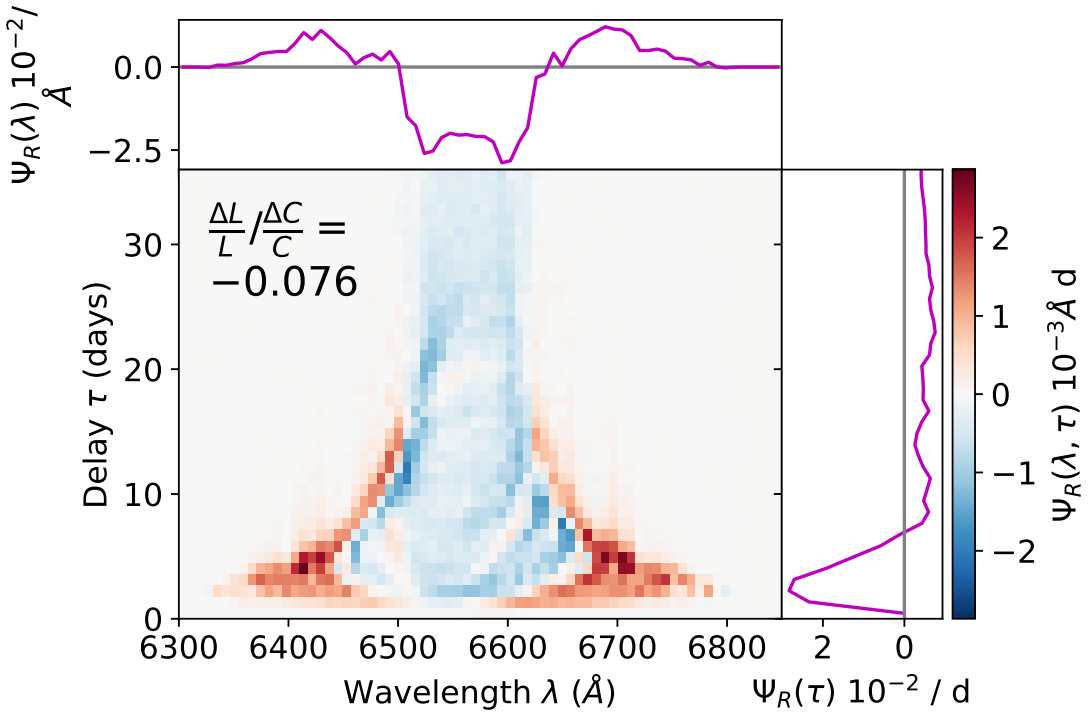

FIGURE 5.5: The 'true' velocity-resolved response function (lower) for Hα in the Seyfert model, rescaled to a peak delay of ≈ 3 days.

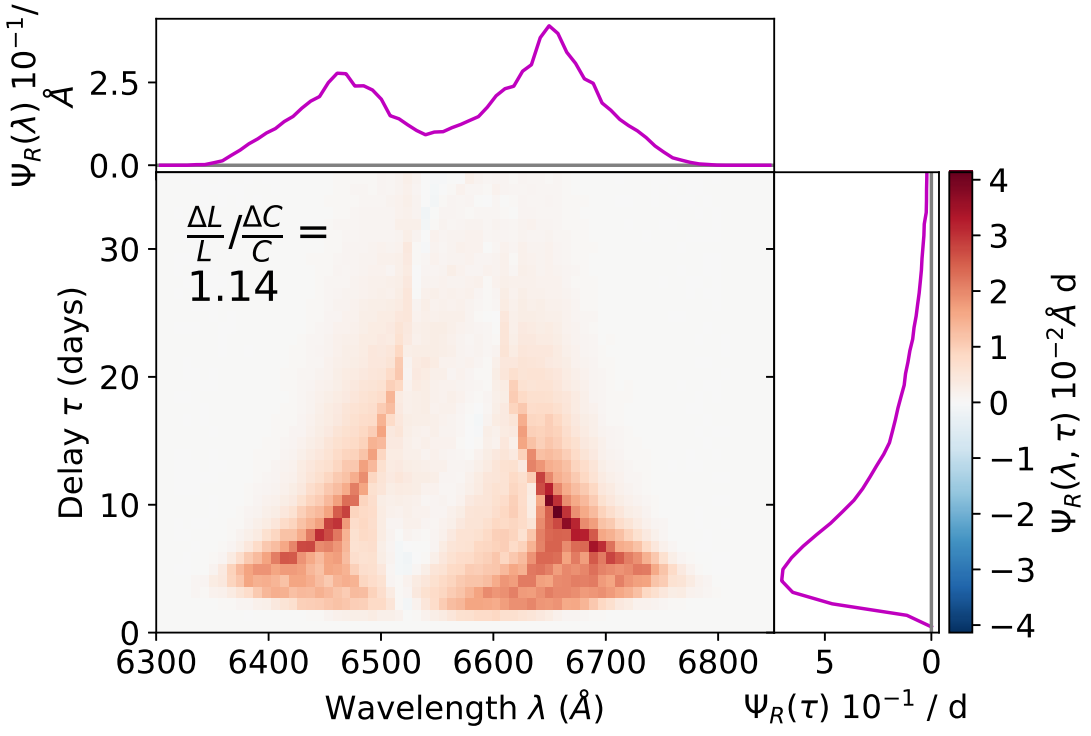

FIGURE 5.6: The 'true' velocity-resolved response function (lower) for Hα in the QSO model, rescaled to a peak delay of ≈ 3 days.

TABLE 5.1: Model parameters

Parameter	Symbol, units	Seyfert	Seyfert, rescaled	QSO	QSO, rescaled
Original SMBH mass	$M_{\rm BH}$, $M_\odot$	10^7	1.33×10^8	10^9	1.94×10^8
Accretion rate	$\dot{M}_{\rm acc}$, $M_\odot$ yr^{-1}	0.02		5	
	$\dot{m}_{\rm acc}$, $\dot{M}_{\rm Edd}$	≈ 0.1		≈ 0.2	
X-ray power-law index	α_X	-0.9		-0.9	
X-ray luminosity	L_X, erg s^{-1}	10^{43}		10^{45}	
X-ray source radius	r_X, r_g	6		6	
	r_X, cm	8.8×10^{12}	1.17×10^{14}	8.8×10^{14}	1.71×10^{14}
Accretion disc radii	$r_{\rm disc}$(min)	r_X		r_X	
	$r_{\rm disc}$(max), r_g	3400		3400	
	$r_{\rm disc}$(max), cm	5×10^{15}	6.63×10^{16}	5×10^{17}	9.69×10^{16}
	$r_{\rm disc}$(max), ld	1.93	25.6	193	37.41
Wind outflow rate	$\dot{M}_w$, $M_\odot$ yr^{-1}	0.02		5	
Wind launch radii	$r_{\rm min}$, r_g	300		300	
	$r_{\rm min}$, cm	4.4×10^{14}	5.83×10^{15}	4.4×10^{16}	8.53×10^{15}
	$r_{\rm min}$, ld	0.1699	2.251	16.99	3.293
	$r_{\rm max}$, r_g	600		600	
	$r_{\rm max}$, cm	8.8×10^{14}	1.17×10^{16}	8.8×10^{16}	1.71×10^{16}
	$r_{\rm max}$, ld	0.3397	4.517	33.97	6.602
Wind launch angles	$\theta_{\rm min}$	70°		70°	
	$\theta_{\rm max}$	82°		82°	
Terminal velocity	$v_\infty(r_0)$	$v_{\rm esc}(r_0)$		$v_{\rm esc}(r_0)$	
Acceleration length	$R_{\rm v}$, cm	10^{16}	1.33×10^{17}	10^{19}	1.94×10^{18}
Acceleration index	α	1.0		0.5	
Filling factor	f_V	0.01		0.01	
Viewing angle	i	40°		40°	
Number of photons		6×10^9		1×10^{10}	

The response functions calculated for our two models in this way are shown in Figures 5.5 and 5.6. A full discussion of these velocity-delay maps has already been provided by Mangham et al. (2017), so here we only highlight some salient features. In both Seyfert and QSO models, the line emission and response is dominated by the dense, rotation-dominated base of the disc wind (c.f. Figures 5.10 and 5.11 below). Correspondingly, the mean wavelength-dependent response is double-peaked in both cases. Both response functions also clearly show the virial envelope associated with this part of the outflow.

A key difference between the models is that the Hα response is always positive in the QSO model, but not in the Seyfert model. In fact, at low Doppler shifts and long delays, the velocity-delay map for the Seyfert model is so dominated by *negative* responsivities that the *net* line response is also negative. As discussed in Mangham et al. (2017), the Seyfert model includes substantial emission from the extended, low-density parts of the wind. As the ionising continuum luminosity increases, these regions become over-ionised, which reduces the Hα emission produced at large radii. By contrast, the denser wind base is not over-ionised and responds positively to the increased continuum luminosity.

The combination of a net negative response and a change in the characteristic emission radius with ionising continuum is physically plausible. It has been observed in

NGC 5548, for example, Cackett and Horne (2006), although there the BLR radius appears to *increase* with increasing ionising luminosity. A possible negative correlation of the Hα response with ionising continuum may also be present in the AGN STORM dataset of Pei et al. (2017) (see epoch T2 in their Figure 7).

5.5.2 Generating Spectroscopic Time Series

Actual RM campaigns do not observe response functions; they observe spectroscopic time series. In order to test RM methods, we therefore have to generate such time series from our models. Equation 5.7 shows how the response function can be used to translate changes in the ionising continuum into corresponding emission line changes. In the limit of small variations in the ionising continuum luminosity, the response function Ψ_R is constant. In this case, the time-dependent emission line, $L(v,t)$, can be expressed straightforwardly as

$$L(v,t) = L_0(v) + \int_0^\infty \Psi_R(v,\tau)\,\Delta C(t-\tau)\,d\tau, \tag{5.10}$$

where $L_0(v)$ is the base-line reference spectrum (c.f. Equation 5.3). We use Equation 5.10 to generate the spectroscopic time series for our simulated observing campaigns.

The code for producing these synthetic spectroscopic time-series is written in *Python* using the *Numpy* (Oliphant, 2015) and *Astropy* (The Astropy Collaboration et al., 2018) modules. We initialise each spectrum in the time series to a base spectrum taken from an assumed mean luminosity model. Then, we create a grid in time between the initial and last continuum measurement, with spacing Δt equivalent to the smallest bin in our discretised response function, $\Psi_{RD}(v,t)$. For each step in this grid, $t_i = t_0 + i\,\Delta t$, we perform simple linear interpolation to arrive at the value of the driving continuum, C, and thus the deviation from the mean luminosity, $\Delta C(t_i)$. Then, starting at the initial time-step, we apply the contribution from the change in luminosity, ΔC, to the spectrum at each later time-step, $t_i + \tau$, as $\Psi_{RD}(v,\tau)\,\Delta C(t_i)$. Continuing this process for every time-step yields the emission line at time t as

$$L(v,t) = L_0(v) + \sum_{t_i} \Psi_{RD}(v, t-t_i)\,\Delta C(t_i)\,\Delta t, \tag{5.11}$$

which is the mirrored, discrete equivalent to Equation 5.11. A diagram of this process for a toy transfer function is shown in Figure 5.7. The physically-motivated design behind this implementation (seeking to mimic the actual process giving rise to the response function) makes it relatively intuitive and offers the scope for further development. In particular, it is straightforward to allow for *continuum-dependent response functions* in this framework, though that is not within the scope of the present work.

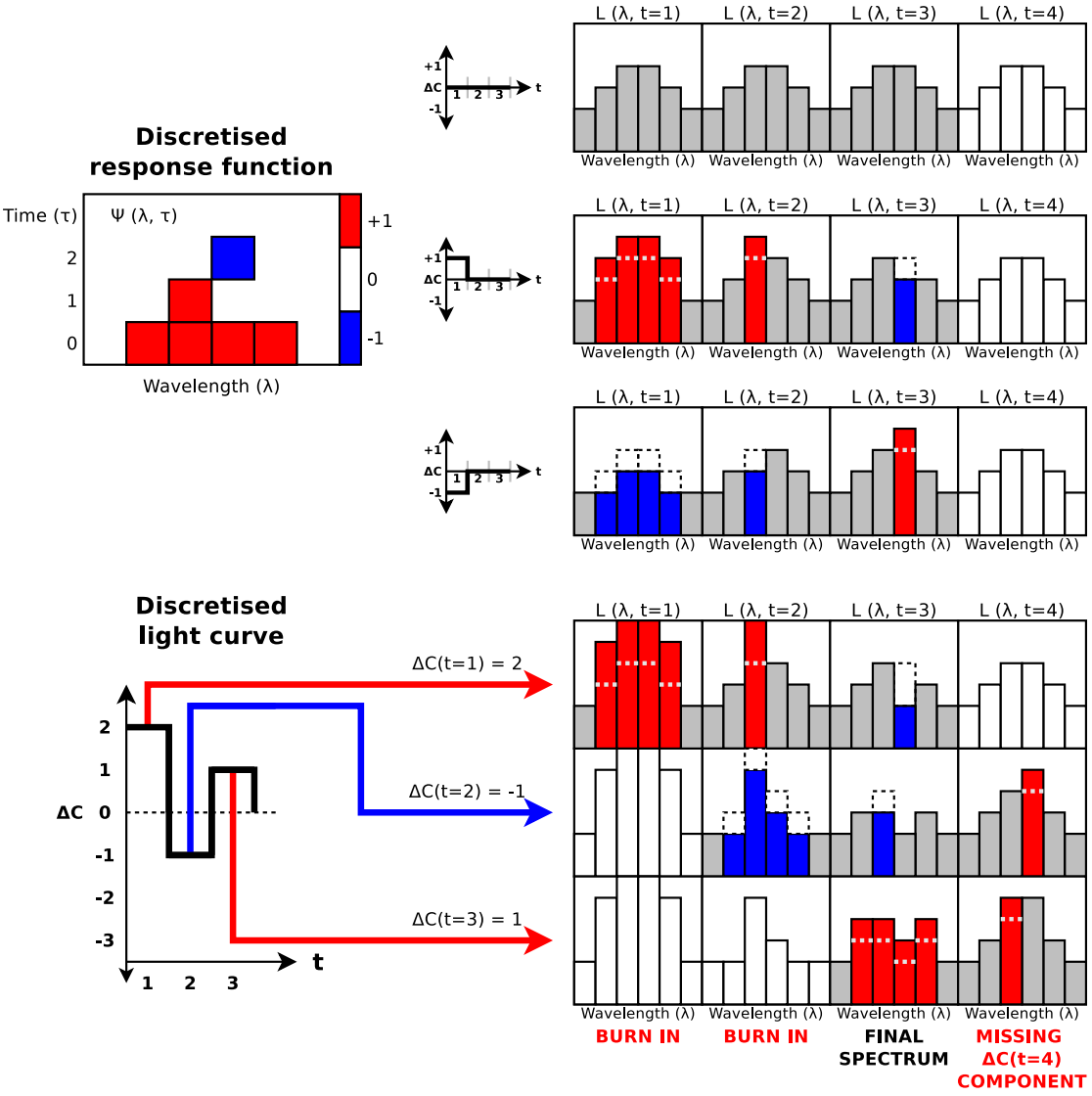

FIGURE 5.7: Diagram showing how a discretised toy response function $\Psi_R(\lambda, \tau)$ (top left) applies changes in continuum luminosity ΔC to a base spectrum to form a series of spectra at later. Top right 3 panels illustrate how a change in luminosity in a single time step t propagates out over a range of times $t + \tau$. Within a spectrum, columns in **blue** indicate a wavelength bin whose flux has been *decreased* by a negative response at this τ and λ, columns in **red** a wavelength bin whose flux has been *increased*, and columns in grey a wavelength bin whose flux is unchanged. Columns in **white** are those outside of the $t + \tau$ range that the response function applies to, and so that were *ineligible* to be changed this time-step. The lower panels illustrate how a discretised light curve (bottom left) can be used to produce a final spectrum (bottom right). Only spectra for time-steps $t > t_0 + \tau_{\max}$ and $t < t_{S,\max}$ are *fully-constructed* spectra.

CARAMEL works on continuum-subtracted spectra. When generating time-series for CARAMEL, we therefore set L_0 to the continuum-subtracted base spectrum from the mean luminosity model. A simple linear fit is used to subtract the continuum under the line. By contrast, MEMEcho is designed to work on a sequence of spectra that include the (variable) local continuum. Denoting line plus continuum spectra as $\mathcal{L} = C + L$, the input we provide to MEMEcho can be written as

$$\mathcal{L}(v,t) = \mathcal{L}_0(v) + \Delta C(t) + \sum_{t_i} \Psi_{RD}(v, t - t_i)\, \Delta C(t_i)\, \Delta t. \tag{5.12}$$

Here, $\mathcal{L}_0(v) = C_0 + L_0(v)$, is just the base spectrum provided by Python for our mean luminosity model.

Our variable driving continuum is based on the empirical 1158 Å light-curve of NGC 5548 from De Rosa et al. (2015). The light-curve is rescaled to match the mean luminosity for each model, and the range of variation is reduced to $\pm 50\%$ about this mean value. This data set contains 171 observations spread over $\simeq$ 175 days. Given a BLR extending out to $R_{\max}$, the line profile at time t will depend on continuum levels as far back as $t - 2R_{\max}/c$. It is therefore not possible to calculate self-consistent line profiles for times earlier than $2R_{\max}/c$ in the time series, since these depend on unknown continuum values. This affects not only our ability to simulate spectra, but any attempt to invert observational spectroscopic time-series.

Here, we deal with this by means of a "burn-in period", as illustrated in Figure 5.7. Thus, we discard $L(v,t)$ calculated at early times, when the line profiles still depend on unobserved continuum fluxes. We do, however, retain the continuum values observed during these early times. We thus provide both MEMEcho and CARAMEL with 171 continuum measurements across 175 days, but only 101 simultaneous line plus continuum spectra over 100 days. This is comparable to the best existing observation campaigns (Du et al., 2014; De Rosa, 2015).

We finally add simulated observational errors to the spectra for each time series. We adopt a constant absolute error in each spectral bin of each spectrum in the simulated time series. For the QSO model, the actual level of added noise is set so that the error on the integrated line flux measured from a single spectrum is, on average, 2% of the peak-to-peak variation in the integrated line flux. Since this peak-to-peak variation is much smaller for our Seyfert model – as a consequence of its globally small and negative response (c.f. Figure 5.5), this method would produce unrealistically small errors in this case. We therefore instead set the noise in our Seyfert time series such that, on average, the signal-to-noise near the peak of the line in a single spectrum for the Seyfert model is the same as for the QSO model. We also assume that the noise is drawn from a Gaussian distribution and that all of the uncertainties are uncorrelated. Representative MCMC samples of the line profiles from one of our simulated data sets are shown shown

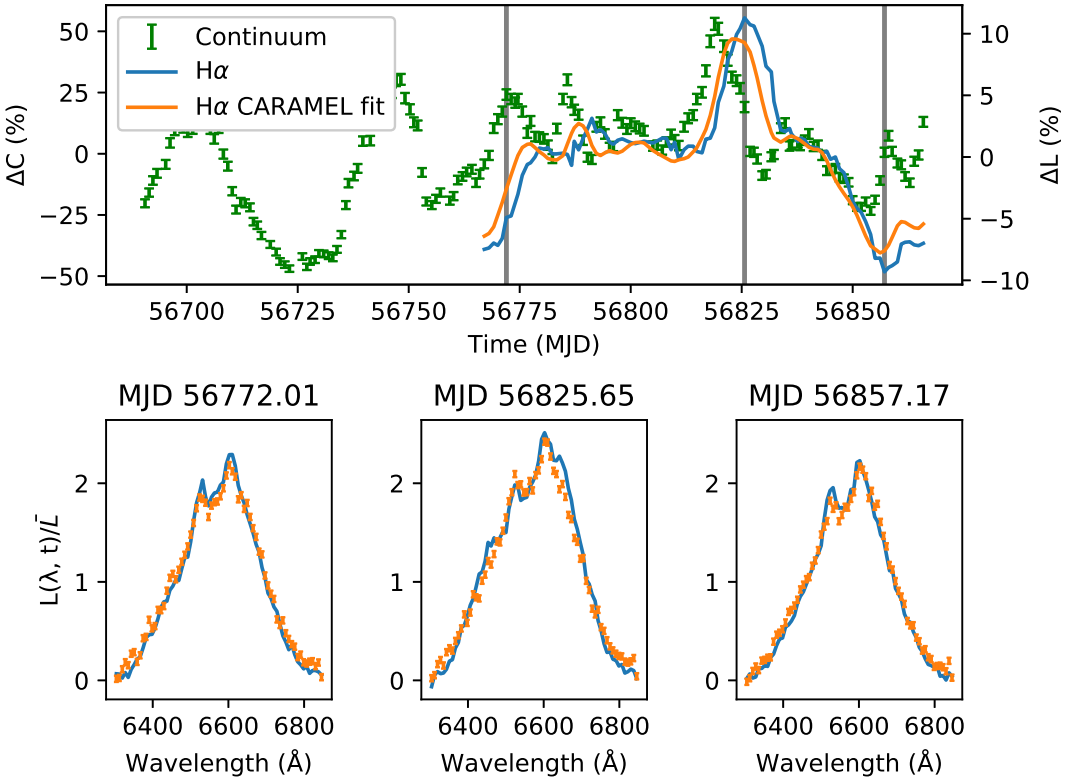

FIGURE 5.8: Driving continuum and line light-curves for our model and the CARAMEL fit (upper). Spectra associated with three 'observational' times, and their CARAMEL fit (lower).

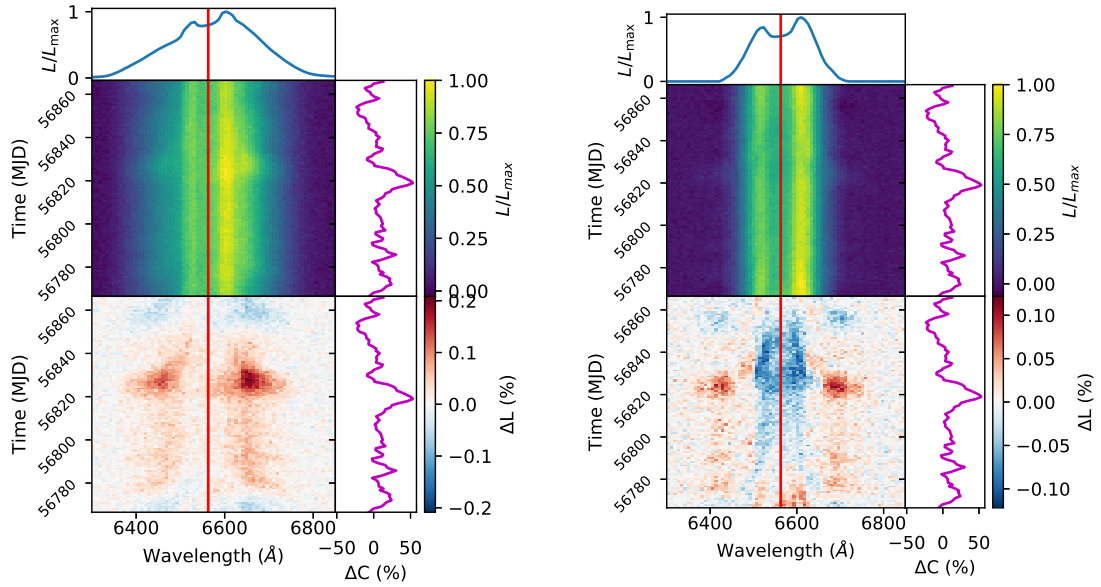

FIGURE 5.9: Trailed spectrograms generated for the continuum-subtracted Hα lines of our QSO (left) and Seyfert (right) models over a simulated observing campaign of 98.9 days.

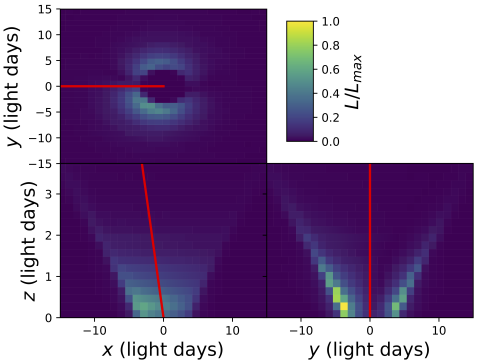

FIGURE 5.10: The emissivity distribution in the QSO model. Distances have been rescaled to correspond to the rescaled delays (see 5.5.1.2). The red lines indicate the projection of the direction vector towards the observer in each plot. Note the different (smaller) dynamic range used for the z-axis.

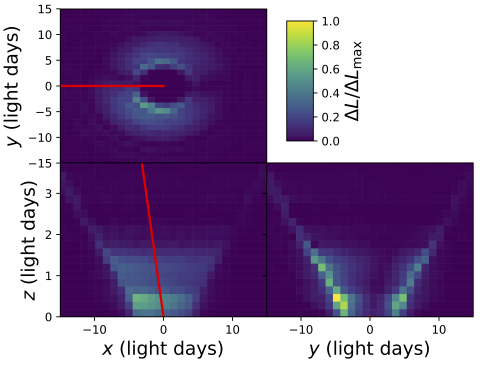

FIGURE 5.11: The responsivity-weighted emissivity distribution in the QSO model. Distances have been rescaled to correspond to the rescaled delays (see 5.5.1.2). The red lines indicate the projection of the direction vector towards the observer in each plot. Note the different (smaller) dynamic range used for the z-axis.

in Figure 5.8. The full time-series are shown in the form of trailed spectrograms in Figure 5.9.

5.5.3 Benchmarks: Defining Success

To assess the results produced by the RM techniques we are testing, we need to define what constitutes success. At the most basic level, any successful RM analysis must be consistent with the input data. Thus quantities like the mean line profiles, response functions and full spectroscopic time-series should be well reproduced by whatever inversion method is being used. Unless this minimal requirement is met, it is impossible to have confidence in the results obtained or their interpretation. The relevant benchmarks for our input models have already been shown and discussed in Sections 5.5.1.1 (mean line profiles: Figure 5.4), 5.5.1.2 (response functions: Figures 5.5 and 5.6), and 5.5.2 (spectroscopic time series: Figure 5.9).

Of course, the real goal of RM is to gain insight into the physical nature of the BLR. Success in this context means correctly inferring physical properties such as the characteristic size of the line-forming region, its geometry, and the dominant kinematics. As additional benchmarks for assessing performance in this area, we provide in Figures 5.10 and 5.11 the spatially resolved "raw" and responsivity-weighted emissivity distributions for our QSO model. [2] Both of these matter. The former controls the shape of the *mean*

[2]The corresponding emissivity distributions for the Seyfert model have been omitted here, since neither of the RM methods we tested was able to reproduce the negative response of this model (see Section 5.6.1).

line profile, while the latter controls the velocity-dependent line response and the RMS line profile.

The raw and responsivity-weighted emissivity distributions illustrate where in our biconical disc wind model the simulated Hα line is primarily formed, and which parts of the line-emitting region are most sensitive to changes in the continuum. Note that there is no significant line emission from $z < 0$, since the optically thick accretion disc blocks the observer's view of this region. In addition, even though the line-forming region is vertically extended, its aspect ratio is small, $H/R \sim 0.1$ (note the different scales on the axes of Figures 5.10 and 5.11). Thus, geometrically, the Hα line in this model could be reasonably described as being formed in a moderately thin disc or annulus, extending over 3 to 6 light days.

5.5.4 Blinding

In order to ensure that our RM tests are realistic, we carried them out as blinded trials. Thus neither P.W. and A.P. (the CARAMEL team), nor K.H. (the one-man MEMEcho team) were given prior access to the response functions used to generate the time-series. They were also not given the disc wind model parameters we adopted. Instead, both were provided only with the time-series for the QSO and Seyfert models in their preferred input format, as well as the rescaled continuum light curves used to generate them. Neither were informed that the Seyfert model would exhibit a negative response.

The following methods sections for each technique were written by their respective teams, after they had access to the time-series, but before they were shown the actual Python-generated response functions that were used to produce the data.

5.5.5 Inversion Methods: MEMEcho

Echo mapping assumes that a compact source of ionising radiation is located at or near the centre of the accretion flow. Photons emitted here shine out into the surrounding region, causing local heating and ionisation of gas which then emits a spectrum characterised by emission lines as it cools and recombines. Reprocessing times are assumed to be short compared with relevant light travel times. As distant observers, we see the response from each reprocessing site with a time delay τ from the light travel time and a Doppler shift v from the line-of-sight velocity. Thus the reverberating emission-line spectrum encodes information about the geometry, kinematics, and ionisation structure of the accretion flow.

To decode that information, we interpret the observed spectral variations as time-delayed responses to a driving light-curve. By fitting a model to the reverberating spectrum

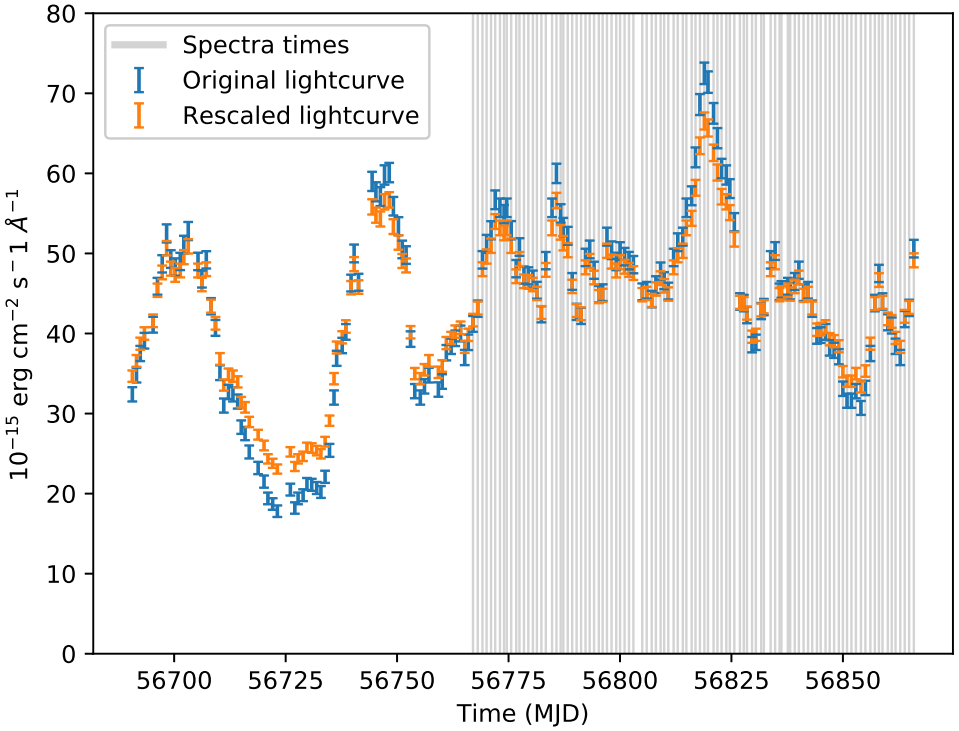

FIGURE 5.12: Original and rescaled driving light-curves used in generating time series of spectra, taken from NGC 5548 (Fausnaugh et al., 2016).

$F(\lambda, t)$, we reconstruct a 2-dimensional wavelength-delay map $\Psi_R(\lambda, \tau)$. This effectively "slices up" the accretion flow on isodelay surfaces, which are paraboloids co-axial with the line of sight with a focus at the compact source. Each delay slice gives the spectrum of the response, revealing the fluxes and Doppler profiles of emission lines from gas located on the corresponding isodelay paraboloid. The resulting velocity-delay maps $\Psi_R(v, \tau)$ provide 2-dimensional images of the accretion flow, one for each emission line, resolved on isodelay and iso-velocity surfaces.

5.5.5.1 Linearised Echo Model

The full spectrum of ionising radiation is not observable, and so an observed continuum light-curve, $C(t)$, is adopted as a proxy. At each time delay τ, the responding emission-line light-curve $L(t)$ is then some non-linear function of the continuum light-curve $C(t-\tau)$ shifted to the earlier time $t-\tau$. In addition, the observed line and continuum fluxes include constant or slowly-varying background contributions from other light sources, such as narrow-line emission and starlight from the host galaxy. To model these backgrounds and account for the non-linear BLR responses, MEMECHO employs a *linearised* echo model, with reference levels C_0 for the continuum and L_0 for the line flux, and a tangent-curve approximation to variations around these reference levels. Thus the

continuum light-curve $C(t)$ is decomposed as

$$C(t) = C_0 + \Delta C(t) \ , \tag{5.13}$$

and the emission-line light-curve,

$$L(t) = L_0 + \int \Psi_R(\tau)\, \Delta C(t-\tau), \mathrm{d}\tau \ , \tag{5.14}$$

is a convolution of the continuum variations with a delay map $\Psi_R(\tau)$, giving the 1-dimensional delay distribution of the emission-line response.

To model reverberations in the emission-line profile, with many wavelength channels, we generalise the echo map from 1 to 2 dimensions, $\Psi_R(\lambda, \tau)$, and the line reference level becomes a reference spectrum $L_0(\lambda)$.

5.5.5.2 MEMEcho fits to the synthetic data

In our blind analysis, we treat the synthetic spectra in exactly the same way as in the analysis of time-resolved spectroscopy of real AGN. Thus a linear continuum model fit to each of the synthetic spectra provides the continuum light-curve data, and the continuum-subtracted spectra isolate Hα light-curve data in many wavelength channels. Note that MEMEcho did not use the full 171 continuum measurements including the preceding times; only those corresponding to the times for which spectra were available.

Using the MEMEcho code (Horne, 1994) we then perform regularised fits of the linearised echo model, with parameters p_k, to the synthetic data $D_i \pm \sigma_i$. The data D comprise measurements at specific times of the continuum light-curve and of the emission-line flux in each wavelength channel. For 1-D echo mapping, the parameters p include 3 parts: the continuum light-curve $C(t)$, the echo map $\Psi_R(\tau)$, and the line reference level L_0. $C(t)$ and $\Psi_R(\tau)$ are evaluated on suitable time and delay grids, with equal spacing $\Delta t = 1$ day, interpolating as needed to match the observation times. We set the continuum reference level C_0 to the median of the continuum data, and the fit adjusts L_0 accordingly. For 2-D velocity-delay mapping, the data D comprise the continuum light-curve plus Hα light-curves in many wavelength channels, and the model parameters include $\Psi_R(\lambda, \tau)$ and $L_0(\lambda)$ in the same wavelength channels.

Our MEMEcho fit is achieved by varying the model parameters p to minimise

$$Q(p, D) = \chi^2(p, D) - 2\,\alpha\, S(p) \ . \tag{5.15}$$

Here the "badness-of-fit" statistic

$$\chi^2 = \sum_{i=1}^{N} \left(\frac{D_i - \mu_i(p)}{\sigma_i} \right)^2 \tag{5.16}$$

quantifies consistency between the linearised echo model predictions $\mu_i(p)$ and the data values $D_i \pm \sigma_i$. The fit employs a Bayesian prior $\propto \exp\{\alpha\, S(p)\}$, where the entropy is

$$S(p) = \sum_k w_k \, \{\, p_k - q_k - p_k \, \ln\left(p_k/q_k\right) \,\} \ , \tag{5.17}$$

where w_k is the weight and q_k is the default value of parameter p_k. Note that $S(p)$ requires $p_k > 0$ and that

$$\frac{\partial Q}{\partial p_k} = 2 \sum_{i=1}^{N} \frac{D_i - \mu_i(p)}{\sigma_i^2} \frac{\partial \mu_i}{\partial p_k} + 2\,\alpha\, w_k \, \ln\left(p_k/q_k\right) \ , \tag{5.18}$$

so that as χ^2 pulls the model prediction $\mu_i(p)$ toward the data D_i, $\alpha\, S$ pulls each parameter p_k toward its default value q_k. The default values are set to weighted averages of "nearby" parameters, e.g. $q(t) = \sqrt{p(t-\Delta t)\, p(t+\Delta t)}$, so that the entropy favours smoothly-varying functions $C(t)$ and $\Psi_R(\tau)$. We also "pull down" on $\Psi_R(\tau)$ at the maximum delay $\tau_{\rm max} = 30$ d. The weights w_k depend on control parameters. Increasing the control parameter W "stiffens" structure in $\Psi_R(\tau)$ relative to that in $C(t)$. Similarly, in 2-D velocity-delay mapping, a second parameter A controls the trade-off in $\Psi_R(\lambda, \tau)$ between structure in the delay vs wavelength direction, and parameter B controls "stiffness" of $L_0(\lambda)$.

In practice we use MEMEcho to follow a maximum entropy trajectory from an initial large value of α and corresponding large χ^2, decreasing α and thus χ^2 gradually until an "acceptable" χ^2 is reached. A measure of the angle between the gradients of S and χ^2 provides evidence that the fit at each chosen χ^2 level is converged to machine precision. A value near $\chi^2/N = 1$ is expected for N data values with reliable error bars when the linearised echo model can achieve an acceptable fit. Attempts to lower χ^2 too far result in a dramatic increase in S as the parameters become noisy due to over-fitting noise in the data. From the resulting series of MEMEcho fits we choose the control parameters W and A and the χ^2 level so as to achieve plausible fits that reproduce the data well while keeping relatively smooth the continuum light-curve $C(t)$ and response maps $\Psi_R(\lambda, \tau)$.

5.5.6 Inversion Methods: CARAMEL

CARAMEL produces transfer functions from data by directly modelling the broad emission line region as a distribution of many massless point particles surrounding an ionizing continuum source. The particles instantaneously and linearly reprocess the AGN continuum emission and re-emit the light towards the observer in the form of emission lines. Each particle re-emits at a wavelength determined by its line-of-sight velocity and with a time-lag determined by its position. Using the particles' positions and velocities, CARAMEL can then calculate the transfer function resulting from a given BLR model.

The model consists of a geometric component describing the positions of the point particles and a dynamical component describing the particle velocities. In addition, CARAMEL models the continuum light curve using Gaussian processes as a flexible interpolator to produce simulated spectra at arbitrary times. By feeding the continuum light curve through the BLR model, the code produces a time-series of spectra that can be directly compared to data. We use a Gaussian likelihood function to compare the model to the data, and use the diffusive nested sampling code DNest3 (Brewer et al., 2011) to explore the parameter space of the BLR and continuum models. The full details of CARAMEL and the BLR model are discussed by Pancoast et al. (2014a), but the main components are described in the rest of this section.

The particles in the BLR model are first assigned radial positions drawn from a Gamma distribution,

$$p(x|\alpha,\theta) \propto x^{\alpha-1} \exp\left(-\frac{x}{\theta}\right) \tag{5.19}$$

which allows for Gaussian-like, exponential, and heavy-tailed distributions. The distribution is then offset from the origin by the Schwarzschild radius plus a minimum BLR radius, $r_{\rm min}$, and a change of variables between (α, θ, $r_{\rm min}$) and (μ, β, F) is applied:

$$\mu = r_{\rm min} + \alpha\,\theta \tag{5.20}$$

$$\beta = \frac{1}{\sqrt{\alpha}} \tag{5.21}$$

$$F = \frac{r_{\rm min}}{r_{\rm min} + \alpha\,\theta}, \tag{5.22}$$

where μ is the mean radius, β is the shape parameter, and F is the minimum radius in units of μ. In this formalism, the standard deviation of the Gamma distribution is $\sigma_r = \mu\beta(1-F)$. The particles are then rotated out of the plane of the disc by a random angle uniformly distributed over the range $\pm\theta_o$, and the distribution is inclined by an angle θ_i relative to the observer, where $\theta_i \to 0^\circ$ is face-on. The opening angle prior θ_0 is uniform between 0° and 90°, and the inclination angle prior is uniform in $\cos\theta_i$ between 0° and 90°

The emission from each particle is assigned a weight between 0 and 1, determined by

$$W(\phi) = \frac{1}{2} + \kappa\,\cos\phi, \tag{5.23}$$

where ϕ is the angle from the observer's line of sight to the origin to the particle position, and κ is a free parameter with uniform prior between -0.5 and 0.5. In this set-up, $\kappa = 0$, -0.5, and 0.5 correspond to particles that emit isotropically, back towards the ionizing source, and away from the ionizing source, respectively. A parameter γ, with uniform prior between 1 and 5, allows the particles to be distributed uniformly throughout the BLR ($\gamma \to 1$) or clustered near the faces of the disc ($\gamma \to 5$). This is achieved by setting

the angle between a point particle and the disc to be

$$\theta = \arccos\left[\cos\theta_o + (1 - \cos\theta_o)\, U^\gamma\right], \tag{5.24}$$

where U is drawn randomly from a uniform distribution between 0 and 1. Finally, an additional free parameter, ξ (uniform prior between 0 and 1), allows the disc mid-plane to be opaque ($\xi \to 0$) or transparent ($\xi \to 1$).

The wavelength of light emitted by each particle is determined by its velocity, which is in turn determined by the black hole mass, a free parameter with uniform prior in the log of $M_{\rm BH}$ between 2.78×10^4 and 1.67×10^9 $M_\odot$, and the parameters $f_{\rm ellip}$, $f_{\rm flow}$, and θ_e. First, the particles are assigned to be on near-circular elliptical orbits or on either inflowing or outflowing orbits. The fraction of particles on near-circular orbits is determined by the free parameter $f_{\rm ellip}$ which has a uniform prior between 0 and 1. Those with near-circular elliptical orbits have their radial and tangential velocities drawn from a Gaussian distribution centred on the circular velocity in the $v_\phi - v_r$ plane. The remaining particles are drawn from Gaussian distributions centred on the radial inflowing or outflowing escape velocities, where the direction of flow is determined by the parameter $f_{\rm flow}$. $f_{\rm flow}$ has a uniform prior between 0 and 1, where $f_{\rm flow} < 0.5$ (> 0.5) indicates inflow (outflow). We also allow the centres of the inflowing and outflowing distributions to be rotated by an angle θ_e towards the circular velocity in the $v_\phi - v_r$ plane, where θ_e has a uniform prior between 0° and 90°.

5.6 Results and Discussion

In the following sections, we will present the blinded analysis and interpretation of the simulated QSO data, as obtained by the two methods and written by their respective teams (MEMEcho Section 5.6.2; CARAMEL: 5.6.3). We will then unblind the analysis and compare the blind results to "ground-truth", i.e. to the known response function and the underlying QSO BLR model (5.6.4).

First, however, in Section 5.6.1, we briefly consider the results obtained for the Seyfert data set. Perhaps unsurprisingly, both methods struggled to deal with the negative line response exhibited by this model. Since neither method obtained acceptable fits to this data set, it does not make sense to force a detailed analysis and interpretation of the "best" models. If similarly poor fits were obtained for actual data, we would expect this to be interpreted (correctly) as evidence of a mis-specified model. We will therefore simply summarize the difficulties encountered by both deconvolution methods when faced with this model.

5.6.1 MEMEcho and CARAMEL Results for the Seyfert model

Neither MEMEcho nor CARAMEL were able to successfully fit our simulated Seyfert data set. In both cases, the underlying problem is the negative line response presented by this model. On the one hand, it is reassuring that neither method was "fooled" by this data set – i.e. both methods failed, rather than producing misleading results. On the other hand, the inability of both methods to deal with negative emission line responses is a significant limitation. In particular, it is unclear whether this could cause serious systematics in cases where the *net* response is clearly positive, but where specific *parts* of the BLR exhibit negative responsivity. Answering this question is beyond the scope of the present paper, but must be the focus of future work. It is also worth noting that there *are* deconvolution methods that explicitly allow for negative responsivities, such as regularized linear inversion (Krolik and Done, 1995; Skielboe et al., 2015) and even an extension to MEMEcho discussed by Horne (1994).

MEMEcho was able to produce a response function for the Seyfert model (Figure 5.15). As the MEMEcho code is not designed to model negative responses the response function can only display the region of negative response as simply zero response, but surprisingly the regions of *positive* response are captured reasonably well. The comparatively fine features corresponding to the positive response from the far side of the inner disk are even reflected, albeit smoothed out by regularization. The response is also shifted to a lower delay- with the peak moved from ≈ 2 days to ≈ 0. Despite this, the response function recovered still matches the Keplerian envelope of a $10^8 M_\odot$ central mass well, very close to the $1.33^1 08 M_\odot$ rescaled mass for this model.

In order to provide some insight into how and why our benchmark methods struggle with the negative-response Seyfert model, we show in Figures 5.13 and 5.14 a summary of the fits to this data set achieved by CARAMEL end MEMEcho, respectively. Taking the CARAMEL results first (Figure 5.13), we see that the overall *shape* of the Hα line profile is reproduced very well, but that none of the models drawn from the posterior parameter distribution succeed in reproducing the integrated emission line light curve. In their interpretation of these results, the CARAMEL team correctly highlighted that this failure may be due to a non-linear response. Turning to MEMEcho (Figures 5.14 and 5.15), we first note that a high target $\chi^2/101 = 3$ had to be adopted in order to fit this data set. The resulting model reproduces well the light curve features in the wings of the emission line, but fails to reproduce the variations in the core of the Hα line. Here, the model light curve is too low at the start and too high after the main peak at $t \approx 6820$. This difficulty in matching the line center behaviour makes sense, since this is where the true response is most strongly negative. Both the CARAMEL and MEMEcho teams correctly interpreted the difficulties their methods encountered in fitting the Seyfert data set as pointing towards the presence of a significant negative response in the Seyfert model.

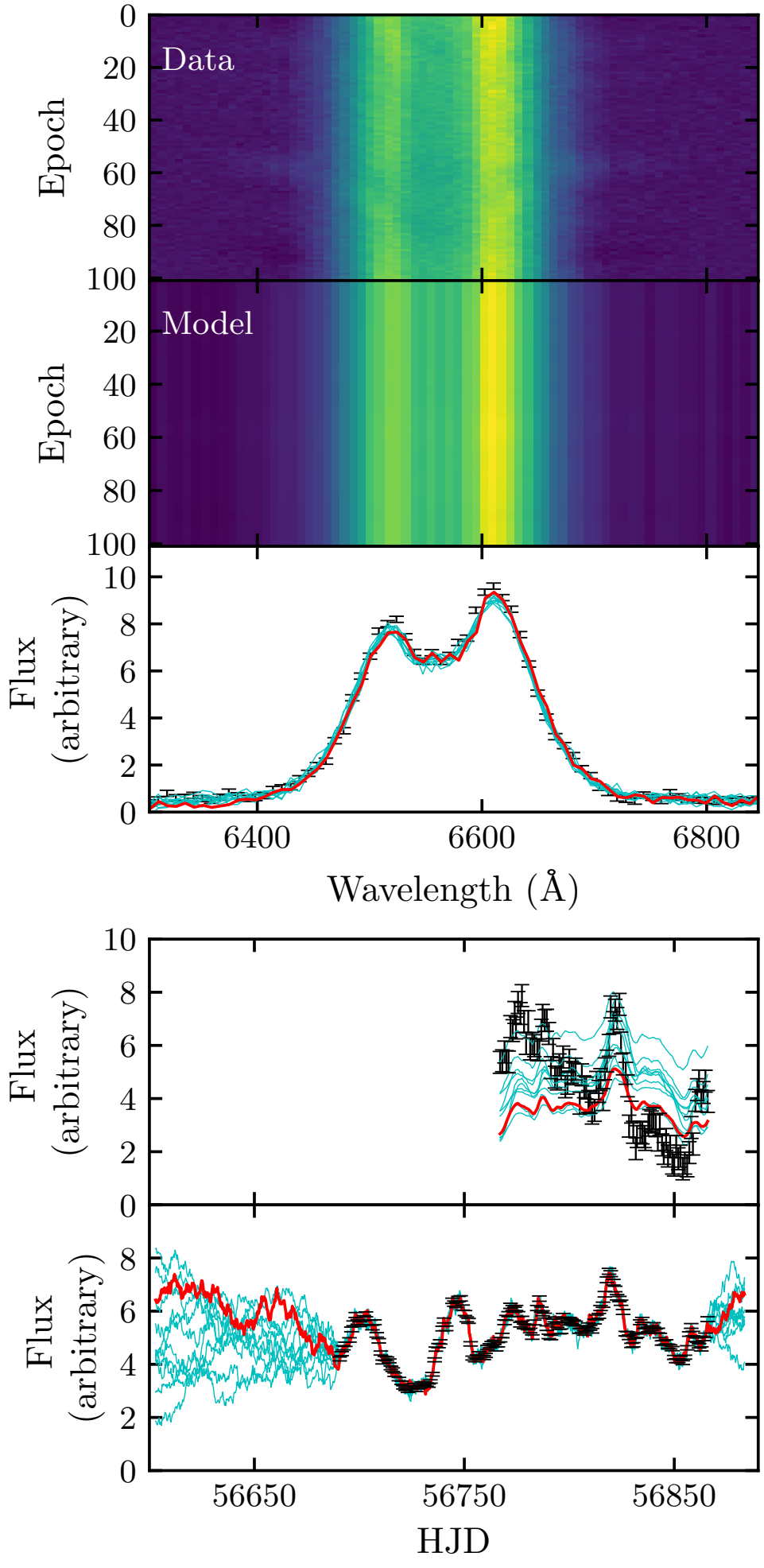
Data
Model
Epoch
Epoch
0
20
40
60
80
100
Flux
(arbitrary)
10
8
6
4
2
0
6400
6600
6800
Wavelength (Å)
Flux
(arbitrary)
Flux
(arbitrary)
56650
56750
56850
HJD

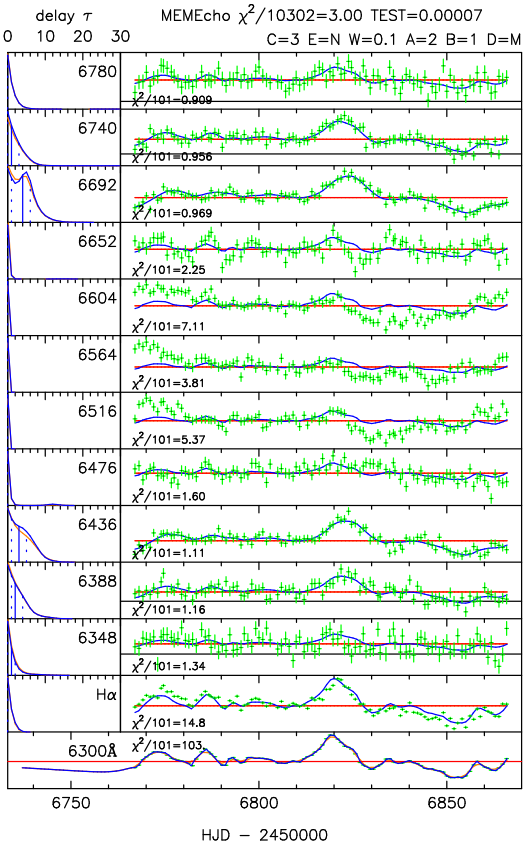

FIGURE 5.14: MEMECHO fit to the synthetic Seyfert data. Bottom panel is the driving light-curve, above which are the 1-D echo maps (left) and echo light-curves (right) at selected wavelengths. Note the high target $\chi^2/101 = 3$ and the poor fits achieved near line center.

5.6.2 Blind Analysis and Interpretation: MEMECHO Results for the QSO model

5.6.2.1 1-D delay maps $\Psi_R(\tau)$ for the QSO simulation

In Figure 5.16 we show the results of a successful MEMECHO fit to the synthetic QSO data. The lower panel shows the continuum light-curve data, with error bars too small to see, and in blue the fitted model driving light-curve $C(t)$. The upper right panel shows the integrated line profile data points with error bars (green) and the fitted line light-curve $L(t)$ (blue). The reference levels, C_0 for the continuum and L_0 for the line, are indicated by horizontal red lines. The line variations $L(t) - L_0$ are obtained by convolving the continuum variations $C(t) - C_0$ with the delay distribution $\Psi_R(\tau)$ shown in the upper left panel. This fit was successful, achieving $\chi^2/N = 1$ for the $N = 101$ data points in the continuum light-curve and the same for the line light-curve.

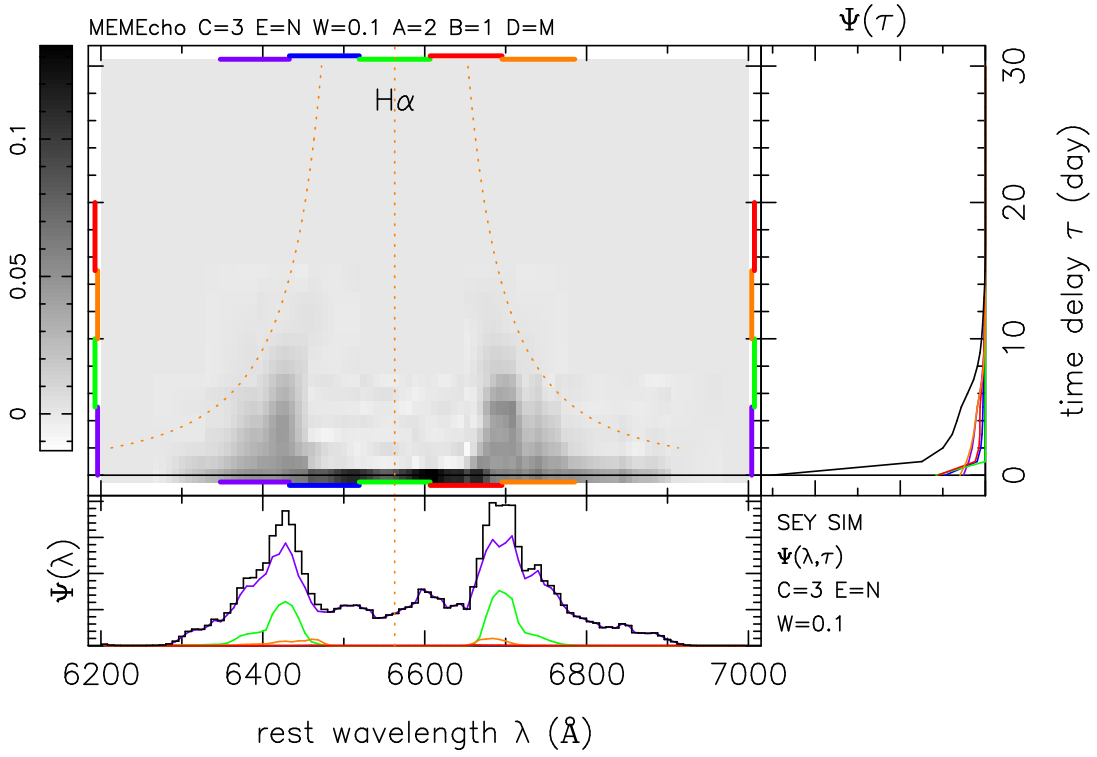

FIGURE 5.15: Two-dimensional wavelength-delay map $\Psi_R(\lambda,\tau)$ reconstructed from the MEMECHO fit to the synthetic Seyfert data. Given below the greyscale map are projections of $\Psi_R(\lambda,\tau)$ giving delay-integrated responses $\Psi_R(\lambda)$ for the full delay range (black), and for restricted delay slices 0-5 d (purple), 5-10 d (green), 10-15 d (orange), and 15-20 d (red). To the right of the greyscale map are wavelength-integrated responses $\Psi_R(\tau)$ for the full line (black), and for 4000 km/s wide velocity bins centred at $V = 0$ (green), at ± 4000 km s^{-1} (red and blue), and at ± 8000 km s^{-1} (orange and purple). For a black hole mass of $M_{BH} = 10^8\,M_\odot$, the orange dotted curves show the virial envelope for edge-on circular Keplerian orbits.

The continuum light-curve has a large peak near $t = 6820$ MJD, and shows numerous smaller peaks and troughs that are well detected at a high signal-to-noise ratio. The strongest peak in the line light-curve crests at $t = 6828$ MJD, ~ 8 days later than the corresponding peak in the continuum light-curve. The line light-curve data is low near the start, then rises to a plateau that has 3 or perhaps 4 local maxima before the main peak, and drops to a low level again near the end. Given the quality of the MEMECHO fit, these features can evidently be interpreted in terms of the linear echo model.

The 1-D delay map $\Psi_R(\tau)$ is well determined from the synthetic QSO data. The prompt response at $\tau = 0$ is small. The response rises rapidly to a ledge near 4 days, a peak

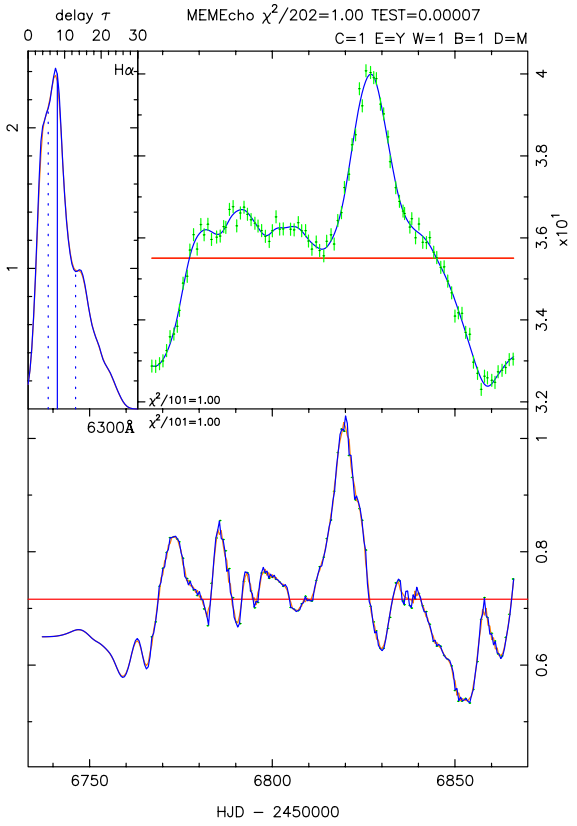

FIGURE 5.16: MEMECHO fit to the continuum and integrated Hα light-curve from the synthetic QSO dataset. The fit achieves $\chi^2/N = 1$ both for the continuum variations (lower panel) and the line variations (upper right panel). Blue curves show the fitted model, including the continuum light-curve $C(t)$ (bottom panel), the delay map $\Psi_R(\tau)$ (upper left panel) and the line light-curve $L(t)$ (upper right panel). Horizontal red lines indicate the reference levels C_0 for the continuum and L_0 for the line.

near 8 days, then declines to a ledge at 17 days, and declines to near 0 at 30 days. The data quality is high enough to warrant interpretation of these features.

5.6.2.2 2-D Velocity-Delay Maps $\Psi_R(v, \tau)$

We now present the more detailed results of a 2-D MEMECHO fit to the synthetic QSO data including variations not just in the continuum and integrated line flux, but also in the emission-line velocity profile.

The quality of this MEMECHO fit may be judged from Figure 5.17. This shows the continuum light-curve and the integrated Hα line light-curve in the lower two panels. Above these are delay maps on the left and echo light-curves on the right for selected

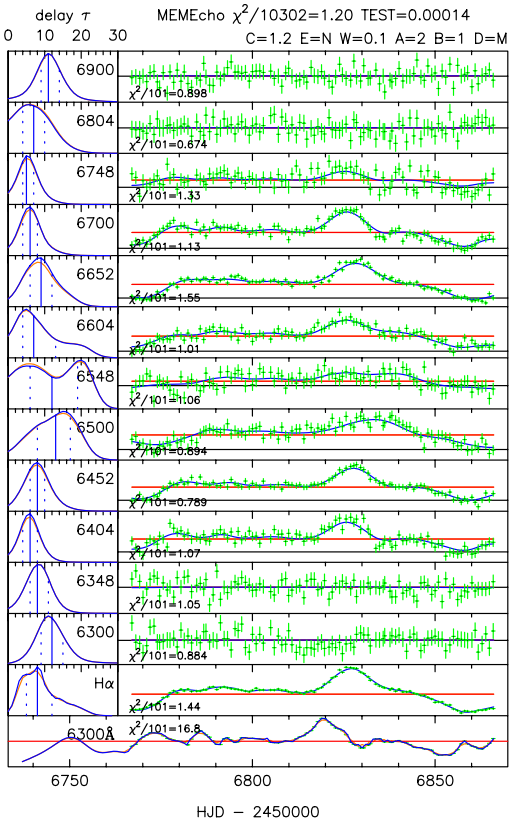

FIGURE 5.17: MEMECHO fit to the synthetic QSO data. Bottom panel is the driving light-curve, above which are the 1-D echo maps (left) and echo light-curves (right) at selected wavelengths.

wavelengths as indicated. The echo light-curve data, with green error bars, is shown along with the fitted model $L(\lambda, t)$ (blue curve) and background level $L_0(\lambda)$ (red line).

The 2-D velocity-delay map $\Psi_R(\lambda, \tau)$ resulting from the MEMECHO fit is shown as a grey-scale image in Figure 5.18. To the right are projections of $\Psi_R(\lambda, \tau)$ to form the velocity-integrated delay map $\Psi_R(\tau)$ (black) and $\Psi_R(\tau|\lambda)$ for selected 4000 km s^{-1} wide velocity bins centred at $V = 0$ (green), $\pm$4000 km s^{-1} (orange and blue), and $\pm$8000 km s^{-1} (red and purple). Below the grey-scale map are projections of $\Psi_R(\lambda, \tau)$ to form the velocity profiles $\Psi_R(V)$ for the delay-integrated response (black), and $\Psi_R(V|\tau)$, in colour, for 4 delay bins, 0-5 d (purple), 5-10 d (green), 10-15 d (orange) and 15-20 d (red).

This MEMECHO fit achieved an overall $\chi^2/N = 1.2$ for $N = 10302$ data values. A lower χ^2 could also be achieved but not without introducing small-scale structure in the map, suggestive of over-fitting to noise in the data. Maps with higher χ^2 were also constructed, and give poorer fits to the data while smearing out the structure seen in

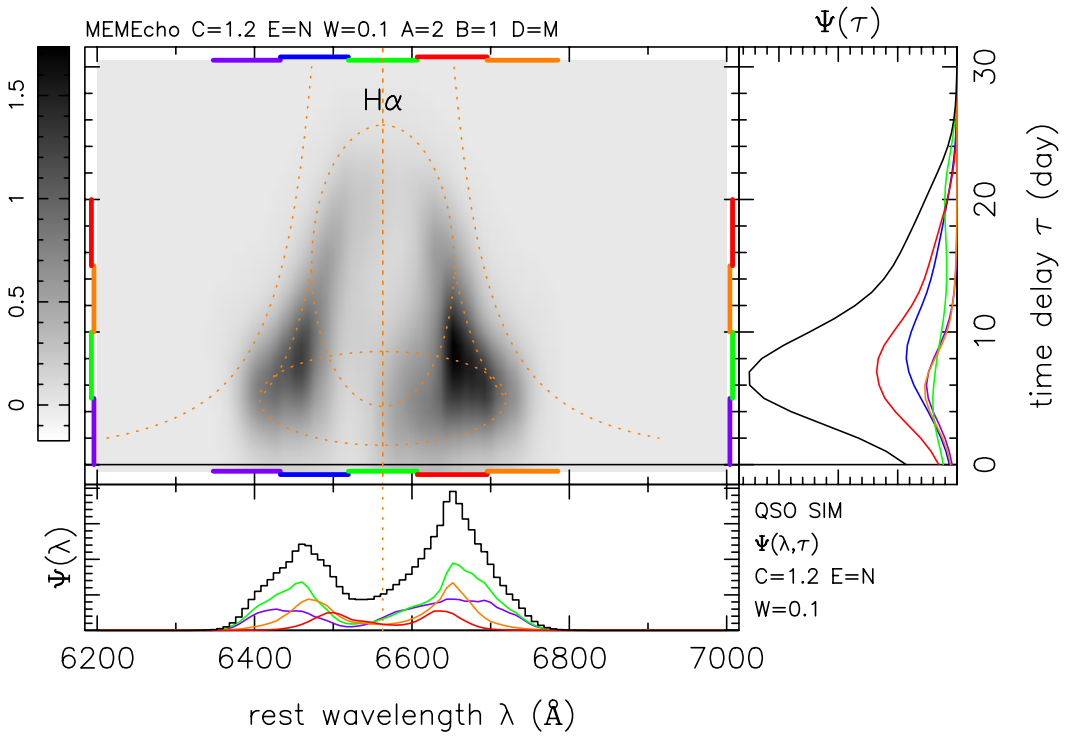

FIGURE 5.18: Two-dimensional wavelength-delay map $\Psi_R(\lambda, \tau)$ reconstructed from the MEMECHO fit to the synthetic QSO data. Given below the grey-scale map are projections of $\Psi_R(\lambda, \tau)$ giving delay-integrated responses $\Psi_R(\lambda)$ for the full delay range (black), and for restricted delay slices 0-5 d (purple), 5-10 d (green), 10-15 d (orange), and 15-20 d (red). To the right of the grey-scale map are wavelength-integrated responses $\Psi_R(\tau)$ for the full line (black), and for 4000 km/s wide velocity bins centred at $V = 0$ (green), at ± 4000 km s^{-1} (red and blue), and at ± 8000 km s^{-1} (orange and purple). For a black hole mass of $M_{BH} = 10^8\,M_\odot$, the orange dotted curves show the virial envelope for edge-on circular Keplerian orbits, and for a Keplerian disc inclined by $i = 45°$ and extending from 5 to 15 light days.

the map for $\chi^2/N = 1.2$. The map shown is thus a good compromise between noise and resolution.

The MEMECHO map exhibits interesting velocity-delay structure. To first order, the Hα response has a double-peaked velocity structure with a delay structure that is symmetric on the red and blue sides of the line profile. In more detail, the response is stronger on the red side than on the blue side.

In the lower panel of Figure 5.18, the delay-integrated response $\Psi_R(V)$ (black) extends to ± 10000 km s^{-1} with two roughly triangular peaks cresting at $V \approx \pm 4000$ km s^{-1}. The red peak is stronger and sharper than the blue one, and the central minimum is at

-1500 km s^{-1}. The velocity profiles in different delay bins are also double-peaked. The sharpness, velocity separation and red/blue asymmetry in strength of the peaks, and the velocity at the minimum between the peaks, all change with the time delay. In the 0-5 day bin (purple), the response extends to ± 10000 km s^{-1} with two smooth dome-shaped peaks, stronger and broader on the red than the blue side, and with a minimum near -2000 km s^{-1}. In the $5-10$ d bin (green), the response still covers ± 10000 km s^{-1} but the triangular peaks have now appeared near ± 4000 km s^{-1}, and the central minimum moves redward to perhaps -1600 km s^{-1}. In the $10-15$ d bin (orange), the response declines in the far wings, the sharp peaks remain but move inward somewhat, and the central minimum moves redward to $+400$ km s^{-1}. In the $15-20$ d bin (red), the wings decline further, the two peaks move together to ± 3000 km s^{-1} and the central minimum is near $+1200$ km s^{-1}.

The two velocity peaks are separated by ± 4000 km s^{-1} at $\tau \sim 15$ d delays, moving closer together at longer delays, perhaps toward a merger at a maximum delay of 25 d. This structure suggests the top half of an elliptical ring feature, such as might arise from an annulus of orbiting gas with $R \approx 15$ light days and $V \sin i \approx 4000$ km s^{-1}. For an inclined circular Keplerian orbit, with $\tau = (R/c)\ (1 + \sin i \cos\theta)$ and $V = V_{\rm Kep} \sin i \sin\theta$, the implied black hole mass is $M_{\rm BH} \sin^2 i \sim 5 \times 10^7\,{\rm M}_\odot$. For an ellipse with maximum delay 25 d and mean delay 15 d, $1 + \cos i \approx 1.67$ and thus $i \approx 45°$. For $i = 45°$, then $M_{\rm BH} \approx 10^8\,{\rm M}_\odot$.

For a $10^8\,{\rm M}_\odot$ black hole, the orange dotted curves on Figure 5.18 show the virial envelope for edge-on circular Keplerian orbits, and for 45° inclined orbits extending from 5 to 15 light days. This framework captures much of the structure evident in the velocity-delay map, and provides a reference against which to consider evidence for departures from that simple model. Note that the outer disc ring becomes indistinct at maximum delay of ~ 25 d, and its lower edge is also missing or obscured. There appears to be low or negative response at $-3000 < V < -1000$ km s^{-1} and $\tau < 10$ d. Such response gaps may arise from azimuthal structure on the ring, suppressing the line response at the corresponding azimuth.

5.6.3 Blind Analysis and Interpretation: CARAMEL Results for the QSO model

The CARAMEL BLR model is able to reproduce both the Hα line profile shape as well as the integrated Hα flux light curve for the QSO model (Figure 5.19). Below, we discuss the modelling results, giving median values and 68% confidence intervals for the key model parameters. In cases where the posterior PDF is one-sided, upper and lower 68% confidence limits are given instead. The full posterior PDFs are provided in Figure 5.20.

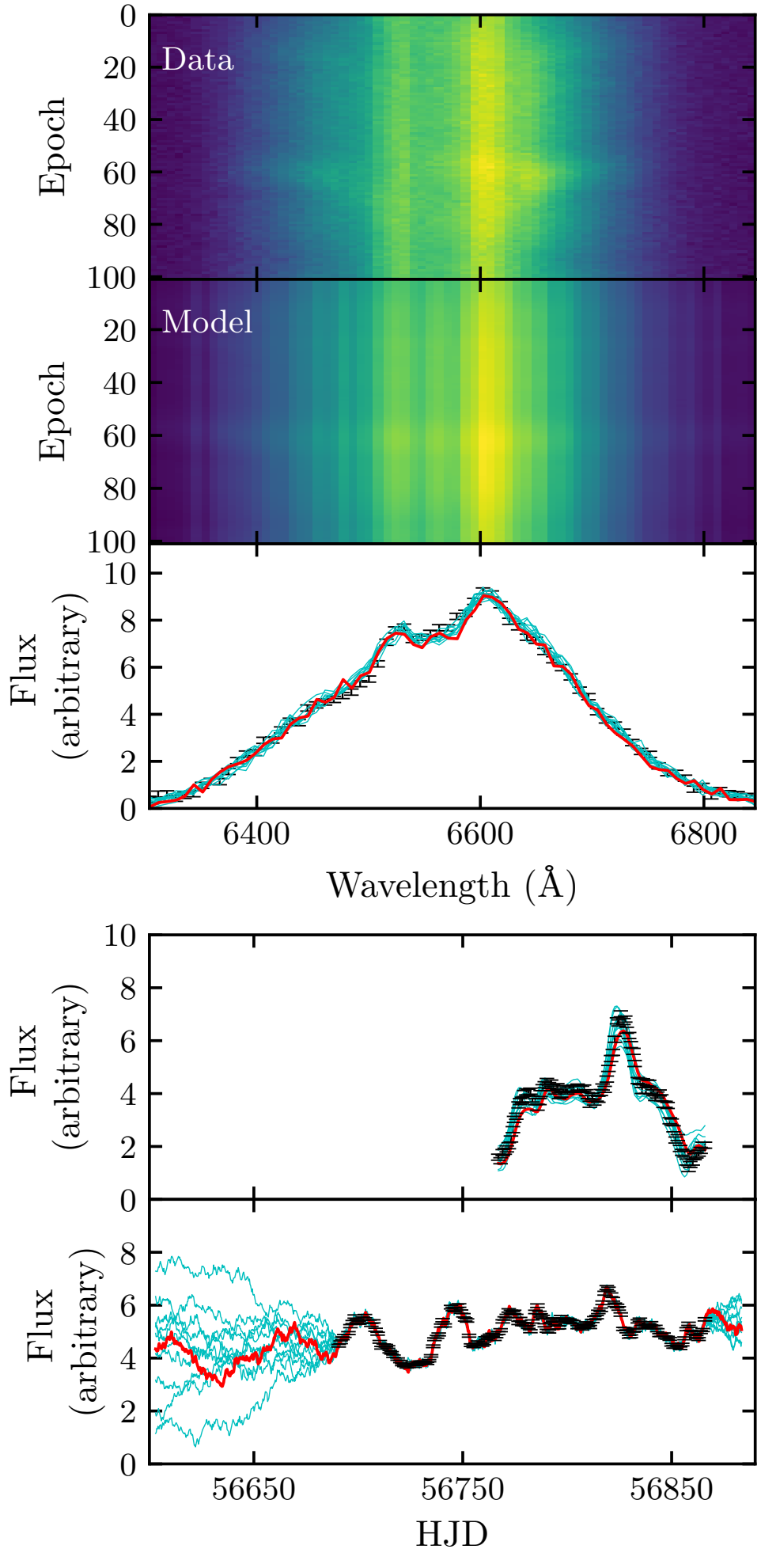
Data
Model
Epoch
Epoch
Flux (arbitrary)
Wavelength (Å)
Flux (arbitrary)
Flux (arbitrary)
HJD

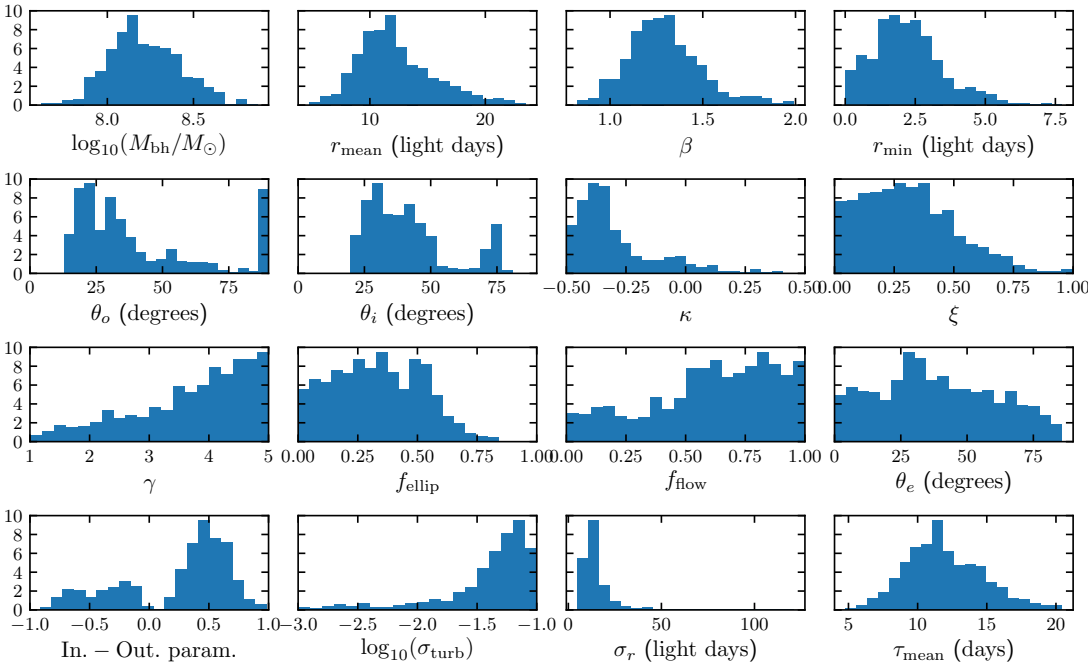

FIGURE 5.20: Posterior distributions of select model parameters for the QSO model.

The CARAMEL modelling results for the QSO model show an Hα-emitting BLR that is steeper than exponential with a shape parameter $\beta = 1.28^{+0.20}_{-0.16}$ for the Gamma distribution. The distribution is shifted from the origin by $r_{\rm min} = 2.1^{+1.2}_{-1.1}$ light days. The mean and median radii are $r_{\rm mean} = 11.7^{+4.0}_{-2.5}$ and $r_{\rm median} = 7.5^{+2.4}_{-1.7}$ light days, and the radial thickness of the distribution is $\sigma_r = 12.3^{+6.9}_{-2.7}$ light days. The mean and median lags are $\tau_{\rm mean} = 11.6^{+3.1}_{-2.3}$ and $\tau_{\rm median} = 6.6^{+1.9}_{-1.5}$ days. The full posterior PDFs show multiple solutions for the opening angle and inclination angle, so a spherical BLR is not completely ruled out. Taking the median value and 68% confidence intervals, we find an Hα-emitting BLR that is a thick disc, with $\theta_o = 32^{+36}_{-12}$ degrees. The disc is inclined relative to the observer's line of sight by an inclination angle $\theta_i = 38^{+18}_{-11}$ degrees. The 2d posterior PDF for θ_i vs. θ_o shows that the models in which $\theta_i \approx 75$ degrees are the same models for which $\theta_o \rightarrow 90$ degrees.

The emission comes preferentially from the far side of the BLR ($\kappa = -0.35^{+0.24}_{-0.08}$), which is what one would expect if the BLR clouds emit preferentially back towards the ionizing source. Models with an opaque disc mid-plane are slightly preferred over those with a transparent mid-plane ($\xi = 0.29^{+0.21}_{-0.19}$). Finally, the results show that the emission comes preferentially from the faces of the disc ($\gamma \geq 3.4$), making the geometry closer to a cone than a uniformly distributed thick disc.

Dynamically, models are preferred in which there is a mixture of gas on near-circular elliptical orbits and gas in inflowing or outflowing trajectories ($f_{\rm ellip} = 0.33^{+0.21}_{-0.21}$). There is a slight preference for outflowing gas over inflowing gas ($f_{\rm flow} = 0.64^{+0.24}_{-0.34}$) for the gas that is not on near-circular elliptical orbits. We note that since $\theta_e = 36^{+28}_{-23}$ degrees, the

radial and tangential velocities are drawn from a distribution that may be rotated a non-negligible angle towards the circular velocity, resulting in fewer of the BLR particles with truly unbound trajectories. To summarize the total amount of inflowing or outflowing gas, we calculate an additional parameter:

$$\text{In.} - \text{Out.} = \text{sgn}(f_{\text{flow}} - 0.5) \times (1 - f_{\text{ellip}}) \times \cos\theta_e, \tag{5.25}$$

where sgn is the sign function. This parameter is constructed such that a BLR with pure radial outflow (inflow) will have In. − Out. = 1 (−1), and a BLR with no preference for either solution will have In. − Out. = 0. The posterior distribution for this parameter shows solutions for both inflow and outflow, although those with outflowing gas are preferred. Finally, we find that macro-turbulence may be important to the dynamics, with $\sigma_{\text{turb}} = 0.052^{+0.025}_{-0.031} * v_{\text{circ}}$. The black hole mass inferred for this model is $\log_{10}(M_{\text{BH}}/M_\odot) = 8.20^{+0.23}_{-0.17}$.

5.6.4 Unblinding: Comparison to Ground Truth

5.6.4.1 MEMEcho vs ground truth

The primary output of the MEMEcho analysis is the recovered 2-D response function, shown in Figure 5.18. This can be directly compared to the true (input) response function in Figure 5.6.

In our view, the performance of MEMEcho in recovering the input velocity-delay map is quite impressive. To a good approximation, the recovered map is a smoothed version of the input map, exactly as one might hope and expect. However, the true peak in the overall delay distribution lies at $\simeq$ 4 days, whereas the peak in the recovered distribution is estimated to be $\simeq$ 6 days. This is almost certainly associated with the inevitable smoothing associated with regularization and exacerbated by the skewness of the delay distribution. The MEMEcho velocity-delay map correctly reproduces the shape of the virial envelope in the input map, as well as the weakness of the response near line centre. The difference in the responses of the two line wings – with the red wing exhibiting a stronger response than the blue wing – is also captured correctly in the MEMEcho map.

Turning to the physical interpretation of the MEMEcho results provided by K.H., he notes that the dominant structure in the recovered velocity-delay map can be explained by a BLR that consists mainly of gas extending from 5 to 15 light days in Keplerian rotation around a $M_{\text{BH}} \simeq 10^8$ $M_\odot$ black hole, viewed from an inclination of $i \simeq 45°$. Comparing this to Figures 5.10 and 5.11, as well as to the numbers in Table 5.1, we see that this interpretation does capture the basic shape and kinematics of the line-forming region. More specifically, in our model, the emission line (and its response) are formed

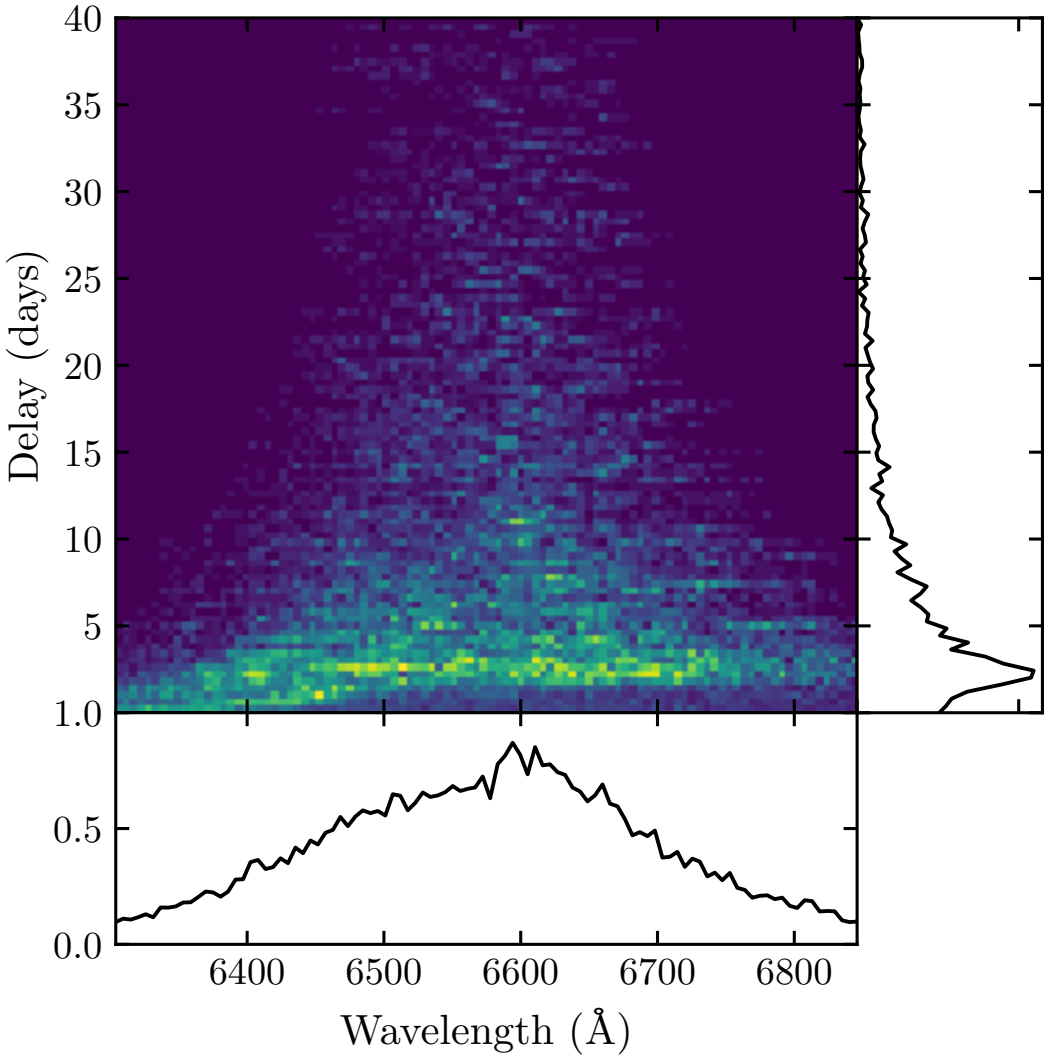

FIGURE 5.21: Velocity-resolved transfer function for the QSO model, chosen to be representative of the full posterior sample. The right-hand panel shows the velocity-integrated transfer function and the bottom panel shows the time-averaged line profile.

primarily in the dense, rotation-dominated base of the outflow. The geometry of and kinematics in this region are indeed similar to those of an annulus in Keplerian rotation between $r_{\rm min}$ and $r_{\rm max}$, and our adopted viewing angle is $i = 40°$, similar to that inferred from the MEMECHOresults.

The main discrepancy between the physical interpretation of the MEMECHO results and the input model concerns the physical scale of the line-forming region. Figures 5.10 and 5.11 show that – in line with $r_{\rm min}$ and $r_{\rm max}$ in Table 5.1 (3.29-6.602 light days)– the actual radius of the line-forming "annulus" in our model is roughly 2/3 of that inferred from the MEMECHO reconstruction (i.e. $\simeq$ 7 light-days $= 1.8 \times 10^{16}$ cm). This is exactly in line with the factor of $\simeq 50\%$ difference between the true and inferred mean delays, and is therefore also presumably caused by the effective smoothing of the response function during the maximum entropy inversion.

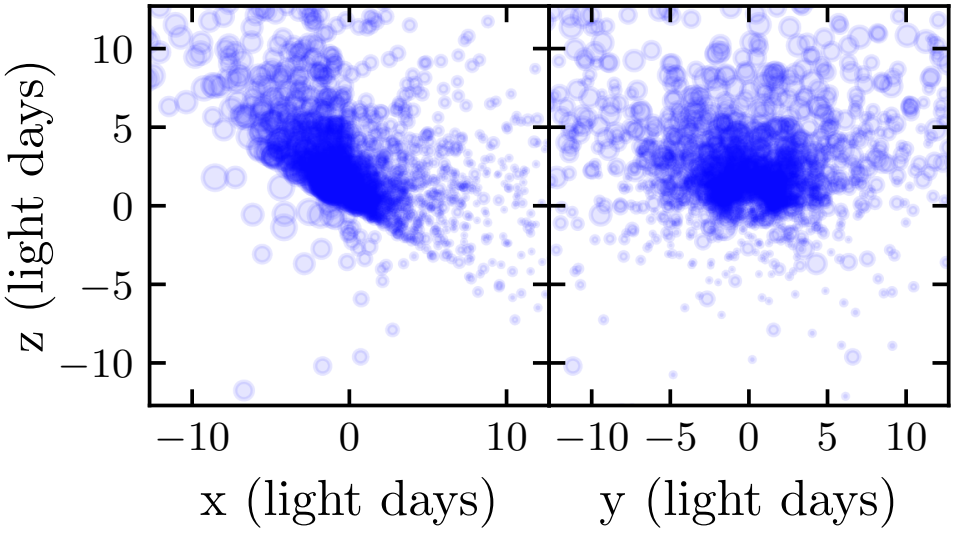

FIGURE 5.22: Geometric model of the broad line region that was used to create the transfer function in Figure 5.21. Each circle represents one of the particles in the model, and the size of the circle is proportional to the relative strength of emission from the particle, as determined by Equation 5.5.6. The observer is situated along the positive x-axis.

Given that the BLR radius is overestimated, we might have expected the black hole mass to be overestimated also (since the virial estimator scales as $M_{\rm BH} \propto v^2 R$). However, the estimate obtained from the MEMECHO reconstruction is $M_{\rm BH} \simeq 10^8$ M$_\odot$, whereas the black hole mass in our (rescaled) model is $M_{\rm BH} \simeq 2 \times 10^8$ M$_\odot$. Based on Figure 5.17, the main reason for this difference appears to be that the MEMECHO estimate is derived from the *outer envelope* of the brightest parts of the 2-D response function. This outer envelope lies at velocities that are higher than typical for the bulk of the line-forming region. This, coupled with the slightly overestimated inclination, biases the MEMECHO black hole mass estimate towards higher values and more than compensates for the effect of the overestimated BLR radius. In any case, agreement to within a factor of $\simeq 2$ is in line with the accuracy expected for this qualitative assessment.

We finally note that neither the MEMECHO velocity-delay map itself, nor its interpretation by an expert, point towards a rotating *outflow* as the source of the variable emission line. As noted above, given that the line formation in our disc wind model takes place primarily within the dense, rotation-dominated base of the outflow, this should not come as a surprise. It is nevertheless important to keep this in mind when interpreting observational data: physically motivated BLR models can have complex geometries and kinematics that may not be easy to discern even from 2-D response functions. Comparisons with toy models – e.g. Hubble inflows/outflows, pure Keplerian discs – may still provide useful insights in these cases. However, it is crucial to remember that we are only studying those parts of the BLR that dominate the responsivity-weighted line emission. Even if the inferred geometry and kinematics for these regions are broadly correct,

they may not reflect the overall geometry and kinematics of the flow that constitutes the BLR.

5.6.4.2 CARAMEL vs ground truth

The primary output of the CARAMEL analysis is the set of parameter distributions shown in Figure 5.20 and discussed in Section 5.6.3. These parameters define the properties of the cloud population used by CARAMEL to fit the simulated data. The overall geometry of this population is shown in Figure 5.22, which can be compared to our raw and responsivity-weighted emissivity maps (Figure 5.10 and 5.11).

Even though a spherical BLR was not completely ruled out by the CARAMEL modelling, the preferred geometry was a strongly flared disc (opening angle $\theta_o = 32^{+36}_{-12}$ degrees viewed at an inclination of $i \simeq 40°$. The inferred inclination is in excellent agreement with the true value, and a flared disc is a reasonable description of the line-forming region in our biconical disc wind model. Indeed, line emission in the CARAMEL models is produced preferentially near the face of the disc, in line with a conical geometry. In the model, the inner part of the wind cone lies at an angle of $90° - \theta_{\rm min} = 20°$ from the disc surface, which is smaller than, but still consistent with, the inferred opening angle.

The velocity-integrated median delay obtained by the CARAMEL analysis is $\tau_{\rm median} = 6.6^{+1.9}_{-1.5}$ days. This agrees well with the actual median delay $\tau_{\rm median} \simeq 6$ day. In line with this, the characteristic scale of the line-forming region is also correctly recovered, $r_{\rm median} \simeq 7$ light days, in good agreement with the approximate radius of the line-emitting annulus in our model (see Figures 5.10 and 5.11). CARAMEL also correctly finds that the line emission comes preferentially from the far side of the BLR, and that the mid-plane of the disc is opaque.

Turning to the kinematics of the BLR, the picture is less clear. CARAMEL correctly finds that a significant part of the BLR material is on near-circular Keplerian orbits and also that an additional velocity field is required. However, it cannot decisively distinguish between inflow and outflow kinematics, even though it does (correctly) favour a net outflow of material. CARAMEL also finds marginal evidence for a significant macro-turbulent velocity, which we suspect is an artefact of its kinematic parameterization being unable to faithfully describe the "true" BLR kinematics. The black hole mass of $M_{\rm BH} \simeq 2 \times 10^8$ $M_\odot$ is correctly recovered by CARAMEL.

Perhaps the most surprising and concerning aspect of the CARAMEL analysis is the 2-D response function constructed from a model drawn at random from the posterior distribution (Figure 5.21). This velocity-delay map looks completely different from both our input response function (Figure 5.6) and the response function recovered by MEMEcho (Figure 5.18). For example, it does not recover the double-peaked nature of the response, i.e. the suppressed response near line centre. It also shows no bright emission from the

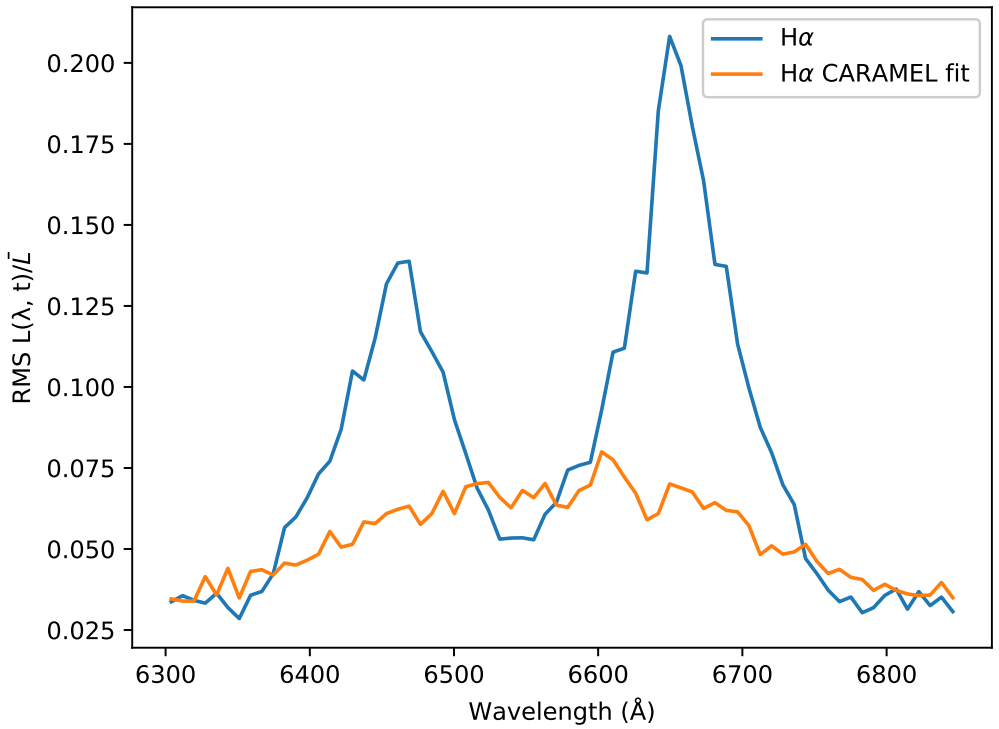

FIGURE 5.23: RMS residuals for the noisy output time series of spectra and CARAMEL fit to it.

virial envelope associated with any particular annulus, just a smooth distribution across the entire width of the envelope at long delays, and a bright, diagonal "line" at short delays (with a blue-leads-red signature).

We have checked whether the particular model shown in Figure 5.21 was just an "unlucky" draw from the posterior distribution, i.e. that it is not representative. We find that other models drawn from the posterior distribution can exhibit (weakly) double-peaked mean line profiles, but the response functions always tend to be quite similar to Figure 5.21 (and hence dissimilar to the input response function).

Given that the 2-D response function is just a by-product of the CARAMEL analysis, it is important to test whether this discrepancy is associated purely with the construction of the response function from the CARAMEL models (rather than the models themselves). What is actually being fit by CARAMEL is the spectroscopic time series itself. We have therefore also constructed the RMS line profile directly from the input time series and also from the CARAMEL model fit to this time-series. These RMS line profiles are shown in Figure 5.23. It is immediately apparent that there does seem to be a fundamental problem with the CARAMEL model fits: the RMS profile constructed from the CARAMEL model has a completely different shape than that constructed from the input data. Most importantly, the CARAMEL RMS profile is single-peaked,

whereas the input disc wind model produces a clearly double-peaked RMS profile (as we would expect, given its rotation-dominated kinematics).

We currently have no simple explanation for this behaviour. It is perplexing that a model that produces a response function and RMS profile that appear to be inconsistent with ground truth should nevertheless be able to match the individual spectra in our time series (as suggested by Figure 5.19). The discrepancy is potentially due to CARAMEL's use of *linear* line response to the continuum, rather than *linearised* response around the mean flux as assumed by MEMEcho .

5.7 Conclusions

We have tested the ability of the two main inversion techniques used in AGN reverberation mapping to recover two physically-motivated response functions from a simulated time-series of spectra. The two reverberation mapping codes we tested were MEMEcho and CARAMEL which represent two different classes of inversion techniques. MEMEcho simply aims to recover the 2-D response function, with the physical interpretation of the results being left to the expert user. CARAMEL carries out forward modelling of the spectroscopic time-series, using a simple, but flexible, description of the BLR as a population of orbiting clouds with known geometric and kinematic properties. All tests were carried out as blind trials, i.e. the MEMEcho and CARAMEL modelling teams were only provided the simulated time series.

The benchmark BLR models used in our test describe a rotating, biconical accretion disc wind. The simulated spectroscopic time series were generated from a self-consistent ionization and radiative transfer simulation that follows the Hα line formation process within the outflow. Two different sets of model parameters were used as input, which were roughly designed to represent Seyfert galaxies and QSOs. In both models, the Hα line-forming region lies primarily in the dense base of the wind, where the kinematics are rotation-dominated.

Neither the maximum-entropy technique of MEMEcho nor Markov-Chain Monte-Carlo forward modelling technique of CARAMEL were able to successfully recover the Seyfert response function, due to the significant negative responsivity in large parts of the velocity-delay space of this model. However, both methods fail "gracefully", in the sense of not generating spurious results.

In the case of the QSO model, the velocity-delay map recovered by MEMEcho was a good match to the input 2-D response function, after accounting for the inevitable smoothing associated with the inversion process. The expert interpretation of the map also correctly captured the annular geometry and rotation-dominated kinematics of the line-forming region. In addition, the estimated observer orientation and black hole mass

were in reasonable agreement with those in the input model. The characteristic size of the BLR was overestimated by roughly 50%, however.

CARAMEL also captured the overall geometry of the line-forming region, describing it as a flared, inclined disc with the correct size and orientation. The importance of rotation to the kinematics was also recovered, but while an additional kinematic component was required by the modelling, CARAMEL was unable to reliably distinguish between inflow and outflow velocity fields for this component. Nevertheless, the black hole mass was correctly estimated by CARAMEL.

The most surprising and concerning result of the CARAMEL analysis is that the velocity-delay map it recovers is strongly inconsistent with the true 2-D response function. In line with this, the RMS profile of the CARAMEL fits to the spectroscopic time series is also inconsistent with that of the input time series. We currently have no explanation for these discrepancies. They are difficult to understand in light of the apparently successful fits CARAMEL achieves to the individual spectra.

Overall, we consider the results of these tests to be quite positive. Even though neither model was able to deal with the Seyfert model, with its net negative response, neither generated misleading results in this case. In the case of the QSO model, both methods broadly recovered the correct geometry of the line-forming region, as well as its dominant kinematics. However, neither method was able to capture that the input model described a disc wind. This should not come as a surprise, given that the rotation dominates the kinematics in the line-forming region. It is nevertheless critical to keep this lesson in mind when interpreting observational data sets: even correctly recovered and interpreted response functions can only tell us about the conditions in the (responsive parts of the) line-forming region. This region can be dominated by rotation, for example, even if this part of the BLR is just the inner part of a larger-scale outflow.

Acknowledgements

Most figures in this paper were prepared using *PGPLOT* (Pearson), *MatPlotLib* (Hunter, 2007) and *Dia Diagram Editor* (Oualline and G., 2018). SWM acknowledges the University of Southampton's Institute for Complex Systems Simulation and the Engineering and Physical Sciences Research Council for the PhD student that funded his research. CK and NSH acknowledge support by the Science and Technology Facilities Council grant ST/M001326/1. JHM is supported by the Science and Technology Facilities Council under grant ST/N000919/1. KH acknowledges support from STFC grant ST/R000824/1.

Chapter 6

Conclusions & future work

The work in this thesis has clear consequences for the field of AGN reverberation mapping. Studies have, to date, found velocity-resolved response maps that correspond to a very broad range of geometries and kinematics, according to previous simple modelling studies (section 1.3.4); Keplerian rotation, inflows (Ulrich and Horne, 1996; Grier, 2013; Bentz et al., 2008, 2010a; Gaskell, 1988; Koratkar and Gaskell, 1989) and outflows (Denney et al., 2009; Du et al., 2016). This raises a vital question of reverberation mapping studies – how do we combine these disparate observations with the otherwise highly successful unification model of AGN (as outlined in section 1.2)?

In chapter 3, we demonstrated how our modifications to the established PYTHON radiative transfer and ionisation code could be used to produce transfer functions that could be matched to those produced by these simple models, by disabling the advanced functionality of the code. We then showed how those simple transfer functions were altered by the consideration of full radiative transfer, and then full ionisation, effects. Each step of the process was consistent with the last, but demonstrated a clear alteration to the transfer function arising from the more detailed physics implemented, and illustrated the need for more advanced models. We then trialled generating transfer functions for a physically-motivated biconical disk wind model (Matthews et al., 2016) and showed that transfer function signatures for rotating biconical disk winds should be a mix of both Keplerian rotation and outflow signatures. However, we also highlighted that the kinematically outflow-dominated parts of the wind may be observationally inaccessible, particularly for Hα and other Balmer series lines, due to the low responses at long delays.

We then further developed this technique in Mangham et al. (2017) as shown in chapter 4, deriving not just transfer functions, but *response functions* that take into account the change in ionisation profile throughout the wind as the continuum fluctuates. This is a vital improvement, as it allows the emission region to shift through the wind geometry as the ionisation fronts move. This allows for the mean lags to change with the continuum, as has been seen in the 'breathing' Hβ emission of NGC5548 (Cackett and Horne, 2006).

This development of the code showed that crucially, even for a model that gives a relatively simple Keplerian disk-like response, the combination of outflow kinematics and direction-dependent line optical depths results in an asymmetry to the disk signature that *could* be interpreted as the redward wing of the line leading the blueward. This feature is conventionally interpreted as a signature of *inflow*. A weak version of the asymmetry effect had been seen in simple models (Chiang and Murray, 1996; Waters et al., 2016), but our analysis shows that it is a very substantial effect in our response functions. Our examples also demonstrate in even more detail the lack of large-scale outflow features. This causes the disk-wind response function to be remarkably similar to that produced by *pure* Keplerian disks in some circumstances. This arises because the Balmer lines in our models are produced mostly in the dense, rotation-dominated wind base. In addition, increases in continuum luminosity tend to over-ionise the low-density extended wind regions, causing them to have a weak or even negative response. Thus the overall line response is weighted strongly towards the disk base, and the mean lag from the response function no longer indicates the mean radius of emission, as is typically assumed. This effect is taken to extremes in our Seyfert model, where the response from the extended wind region *decreases* with increasing luminosity, leading to a net *negative* response. This reproduces effects seen in Cackett and Horne (2006), where the Hβ line flux is anti-correlated with the continuum luminosity. These represent a dramatic break from previous work – producing response functions that can replicate the *full range* of behaviours seen in observation. Equally, they illustrate the difficulties in using reverberation mapping studies to distinguish between disk and disk-wind candidate geometries for the BLR.

Following on from this discovery, we collaborated with the authors of the main codes involved in deconvolving response functions from observational data on a paper in prep Mangham et al. (2018), as shown in chapter 5. In order to fairly test the capability of their codes to recover our physically motivated response functions, we performed *blinded* studies. We provided them with synthetic time-series of line profiles generated using a real observed X-ray continuum and a response function similar to those from Mangham et al. (2017), and tested the accuracy with which they were able to recover the response function used to generate the fake observing campaign. The MEMEcho code described in Horne et al. (1991) performed well in these tests, managing to capture our response functions shape well despite minor smoothing, though this meant it both overestimated mean lags *and* underestimated the SMBH mass of the system. Crucially, though, it captured the asymmetry of the response function arising from angle-dependent escape probability effects, and the roughly annular geometry of the emission region. The CARAMEL code of Pancoast et al. (2011) also captured the emitting geometry, but surprisingly completely failed to capture the inflow/outflow kinematics or reproduce the response function, despite producing a time-series of observations that were a very good fit to the data. This establishes the need for further assessment of the CARAMEL tool's capabilities and limitations. We also established that within the constraints of a

realistic observing campaign, neither code could distinguish between disk and disk-wind models of the BLR. This highlights the need for reverberation mapping studies that encompass not just Hβ but also include a wider range of lines, including those with an origin further out in the wind – for example the C IV line, as seen in chapter 4. We also verified that, as expected neither code could cope with a physically motivated response function with regions of negative response. Fortunately, their failures were relatively graceful, with them simply being unable to fit line light curves to a satisfactory level of error. This suggests that whilst current RM deconvolution work cannot capture negative responses, it has at least not *misinterpreted* them. Still, the failure of currently employed techniques to capture fundamental behaviour represents a clear deficit in the field. This may prompt the re-evaluation of techniques like Regularised Linear Inversion (Krolik and Done, 1995; Skielboe et al., 2015) that have seen less use than their competitors in recent years. The recovery of response functions with regions of negative response thus represents a clear avenue of future development for deconvolution techniques.

To summarise the work in this thesis:

- We have enhanced an existing astrophysical Monte Carlo radiative transfer and ionisation code, PYTHON, to allow it to generate transfer and response functions for AGN (and potentially other systems the code supports).
- These enhancements represent a substantial improvement over previous reverberation mapping models. The response functions produced display real, observed behaviours of AGN that could not be modelled using existing techniques.
- Our response functions raise concerns about the ability of existing reverberation mapping campaigns to differentiate between disk and disk-wind models of the BLR, and have consequences for the design of future observing campaigns.
- They also cast doubt on existing interpretations of red-leads-blue signatures in low-resolution response functions as evidence of inflows.
- We have shown that our physically-motivated response functions can exhibit features that *cannot* be captured by the deconvolution techniques currently in use.
- We have established that full radiative transfer and ionisation modelling of response functions is thus a fundamental necessity for accurate reverberation mapping studies.

As such, this thesis represents a substantial contribution to the field of reverberation mapping of AGN.

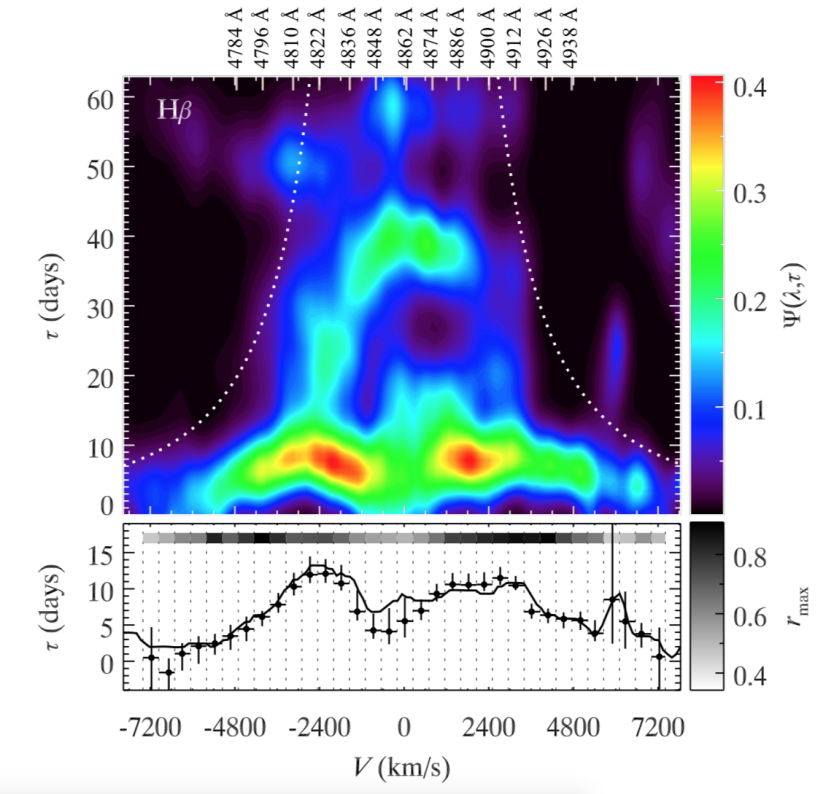

FIGURE 6.1: Hβ velocity-resolved response function from NGC5548 observations reproduced from Xiao et al. (2018b).

6.1 Future work

6.1.1 Forward modelling of NGC5548

As discussed in chapter 4, our models predict centroid delays for Hβ and C IV approximately an order of magnitude lower than would be expected from the observed trends (Peterson et al., 2005; Peterson and Bentz, 2006; Bentz et al., 2013). This indicates the need for further refinements of our models of AGN disk winds. The Seyfert NGC5548 is a popular source for reverberation mapping, and has been the target of multiple observing campaigns over decades (Bon et al., 2016) including AGN-WATCH (Peterson et al., 2002) and most recently AGN-STORM (De Rosa et al., 2015; Edelson et al., 2015; Fausnaugh et al., 2016). Analysis of these observations have put its Hβ lags on the order of $\approx 3-4$ days (Peterson et al., 2005) – an order of magnitude higher than those of our Seyfert model with approximately the same mass. Not only are there robust centroid lag estimates, thanks to the AGN-STORM campaign, a high-quality velocity-resolved transfer function for NGC5548 is now available (Xiao et al. (2018b), figure 6.1).

We have begun preliminary work on fitting our standard Seyfert model to match the lags for NGC5548. As a very first step, we have trialled increasing the radius by factors of 10 and 30×. Thanks to the r^{-2} scaling of both density and ionising flux, this results

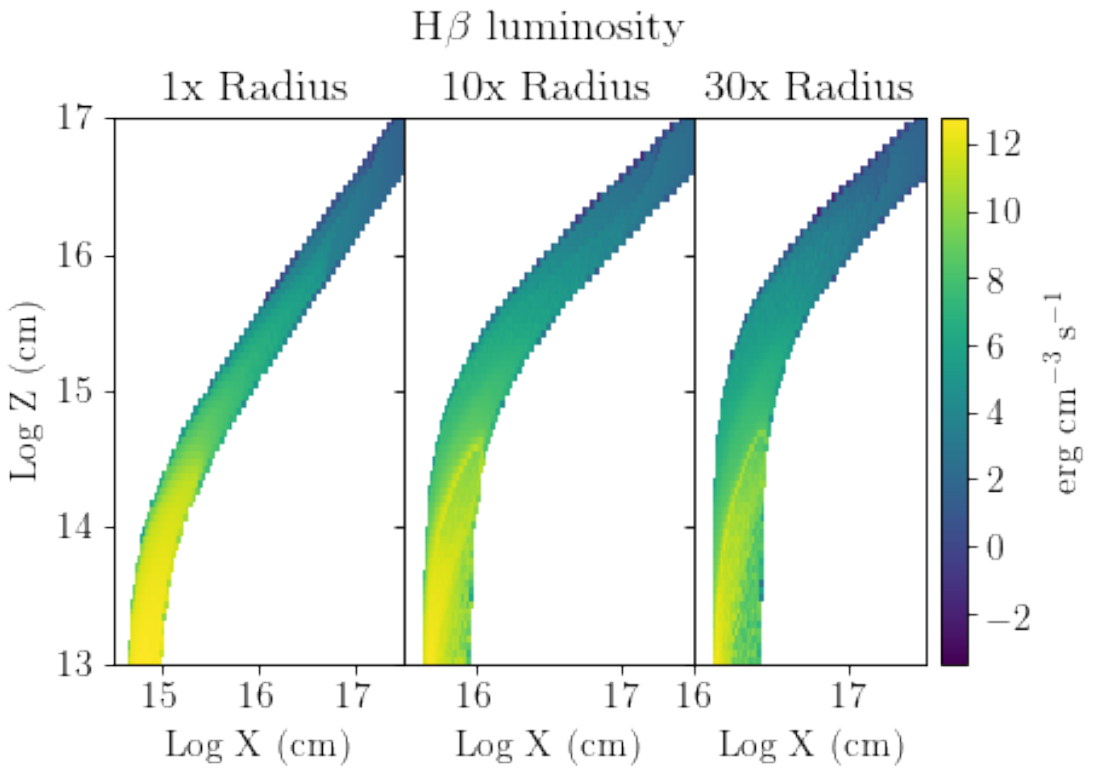

FIGURE 6.2: Hβ line luminosities throughout the wind base for 1×, 10× and 30× models.

in a wind with a broadly similar ionisation state but at a larger radius (Figure 6.2), acting as almost a straight multiplier on the centroid lag (figure 6.3).

Conveniently, this adjustment also results in a substantial increase in the line-to-continuum ration (figure 6.4). One of the major issues with our Seyfert models to date has been their weakness in Hβ, forcing us to use the Hα line in chapters 3 and 4, even though it is less commonly used in reverberation mapping studies. The relative weakness of the lines in our model was one of the major motivations for previous work on PYTHON (Matthews et al., 2016). This single change makes it substantially easier to get sufficient photons out of the simulation for good errors on a reasonable timescale.

Equally, whilst the centroid lags are promising the response function shape shifts and resembles the observed Ψ_R *less* (figure 6.5). This outlines the need for a more comprehensive exploration of our Seyfert models. It is clear a disk wind can reproduce a disk-like signature, but can we reproduce *this* disk-like signature, and match the spectrum, centroid lags and response function simultaneously?

As part of this work, we will explore the dusty wind model of Czerny and Hryniewicz (2011). Czerny proposes that the wind is launched around the dust sublimation radius, rather than around the UV-emitting inner disk as our model assumes. This model predicts the wind launch region should be an order of magnitude further out than an inner-disk wind, and much more closely matches the observed delays.

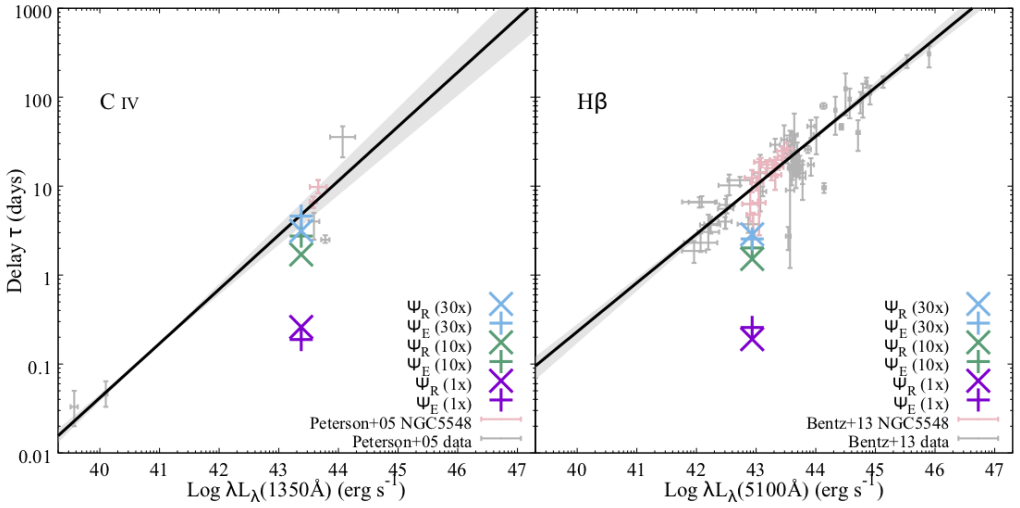

FIGURE 6.3: Luminosity-delay relationship for $H\beta$ and C IV compared to that determined observationally by Bentz et al. (2013) and Peterson et al. (2004). The line and shaded area around it are the fit and error on the fit. The points are the values from Bentz et al. (2013) and Peterson et al. (2004) with errors, with those corresponding to NGC5548 highlighted. Expanded to include 10× and 30× radius models.

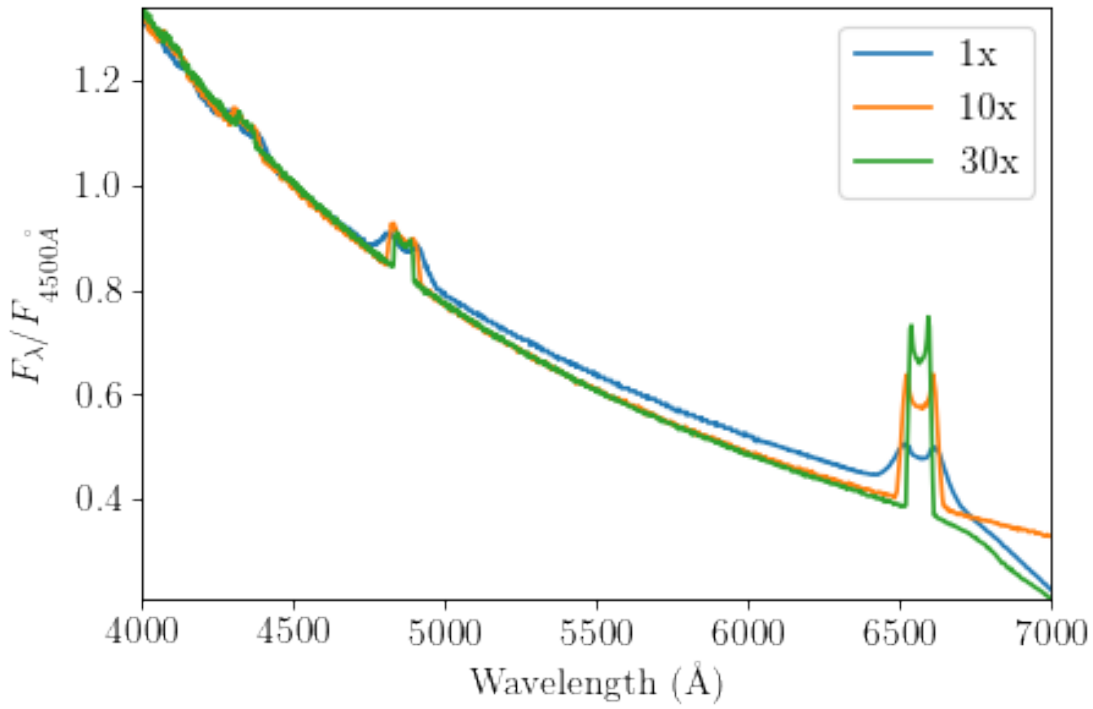

FIGURE 6.4: Spectra for 1×, 10× and 30× models.

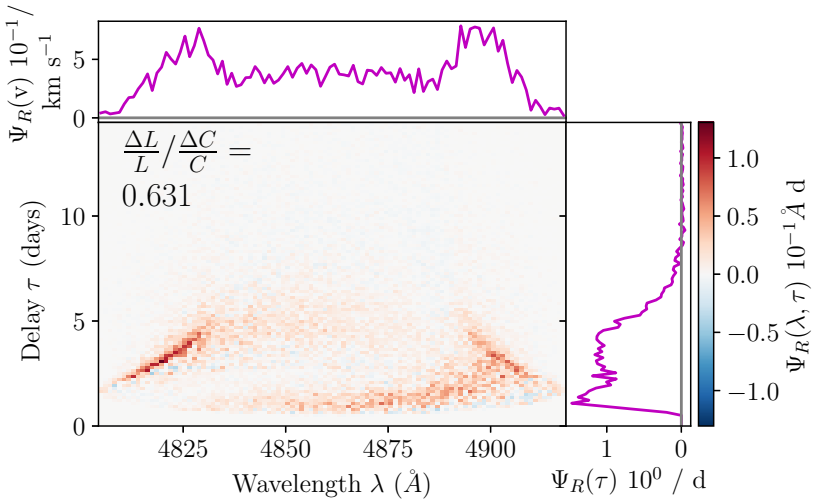

FIGURE 6.5: Hβ velocity-resolved response function for 10× radius Seyfert model.

6.1.2 Time-dependent response functions

The response functions generates in chapter 4 are a substantial advance on those of previous models, but still have substantial limitations. In particular, they assume that the responsivity is linear around a given mean continuum $\bar{L}_{\text{cont}}$. This means assuming that changes in the continuum will only *gradually* change the ionisation state of the wind and thus the luminosity emitted. Whilst this may be a reasonable assumption for $\Delta L_{\text{cont}}/L_{\text{cont}}$ on the order of $\approx 10\%$, realistic light-curves (like the NGC5548 one used in chapter 5) vary by a factor of 2 over the timescales required to recover a response function.

Our technique for generating a response function Ψ_R requires picking two bracketing continuum luminosities with a given L_{cont} and generating transfer functions Ψ for both. The assumption that the resulting response function behaves linearly with ΔL_{cont} cannot reasonably hold beyond the ΔL_{cont} used to generate it. Equally, picking a *large* ΔL_{cont} for generating Ψ_R will result in unphysical behaviour when considering small ΔL_{cont}, as it will not capture the slow movement of an ionisation front through the wind, only its position at the two extremes.

Realistically, then, it is the case that the change in the line profile $\Delta L_{\text{line}}(v, t)$ is generated as

$$\Delta L_{\text{line}}(v, t) = \int_{-\infty}^{\infty} \Delta L_{\text{cont}}(t - \tau)\Psi_R(v, \tau, L_{\text{cont}}(t))d\tau, \tag{6.1}$$

and relies not on a single Ψ_R, but on a *series of continuum-dependent response functions.* This means that in order to properly perform reverberation studies of an AGN with large variability, it would be necessary to generate a time-series of spectra as in chapter 5 from

a set of Ψ_R. At best, this could be performed by generating a grid of Ψ_R across the range of continuum luminosities in the observing campaign. If the timescale of variability is lower than that of the light-crossing time of the BLR, then self-irradiation would have to be considered and a full time-resolved radiative transfer and ionisation calculation would be required to generate the series $\Psi_R(v, \tau, L_{\rm cont}(t))$.

6.1.3 Reverberation mapping of Young Stellar Objects

Disk winds are a ubiquitous feature of accreting objects of all scales, from AGN down. Python has previously been used to model the disk winds of Young Stellar Objects (YSOs) in Sim et al. (2005), young proto-stars that also exhibit accretion disks, outflowing winds, and significant variability in the X-ray and optical (Stelzer, 2015). There have been a series of recent proposals to perform reverberation mapping studies on YSOs, using techniques inspired by AGN reverberation mapping campaigns (Plavchan et al., 2009; Stauffer et al., 2010). Meng et al. (2016) have recently obtained results for a sample of 26 YSOs. Recent high-resolution observations of YSOs have detected spatially resolvable outflows (Ward, 2017). We could therefore build YSO models using these known constraints on the geometry, and compare the resulting model response functions to observationally-derived ones. This would not only help with code validation, but also allow us to more closely probe the physics of YSO disk winds.

6.1.4 Radiation transport in optically thick regions

As discussed in section 2.2.4, we attempted to implement packet splitting/Russian rouletting in Python. Our efforts ran into difficulty with assigning 'importance' to the regions of the problem dynamically. This sort of dynamic assignment is necessary, given the major changes in ionisation profile (and thus opacity) of the wind during the ionisation cycles of a simulation (section 2.2.2.1). It would be possible to further develop our splitting/rouletting techniques to see if they are at all applicable for our wind, as well as exploring other variance reduction techniques like Discrete Diffusion (Gentile, 2001), or Modified Random Walk (Fleck and Canfield, 1984; Min et al., 2009).

6.1.5 Public code release

The Python code is currently hosted on GitHub and technically available to anyone to download and use. However, though great strides have been made in making it easy to install, it is currently not particularly intuitive or accessible to run. Whilst the techniques used in the code are well-documented in papers (Long and Knigge, 2002; Matthews et al., 2016), to make research with Python *truly* reproducible, the code should be available to a wider audience. Whilst the results of any scientific code will always require a

level of expert analysis, if the difficulty of running PYTHON and outputting results for interpretation could be reduced, it would allow other researchers to make use of PYTHON's unique feature-set to test their own models. As a result, we aim to prepare an accessible version of the code for 'public release'. This would involve preparing clearer, more extensive documentation and more comprehensible input formats as outlined in section 2.4, as well as easy-to-follow guidance on how to run and interpret the code. This effort would then enable PYTHON to develop a wider user-base, that would then be capable of fully exploring the capabilities of the code. Further, an expanded user-base could potentially then contribute to the future development of PYTHON in an open-source way. A public release would also allow individual versions of PYTHON to be given a DOI on the software and data citation website Zenodo (Zenodo Team, 2018), making it possible to keep track of the specific code that produced a given set of results.

Bibliography

J. T. Allen, P. C. Hewett, N. Maddox, G. T. Richards, and V. Belokurov. A strong redshift dependence of the broad absorption line quasar fraction. MNRAS, 410:860–884, January 2011.

R. Antonucci. Unified models for active galactic nuclei and quasars. ARA&A, 31: 473–521, 1993.

R. R. J. Antonucci. Optical spectropolarimetry of radio galaxies. ApJ, 278:499–520, March 1984.

R. R. J. Antonucci and J. S. Miller. Spectropolarimetry and the nature of NGC 1068. ApJ, 297:621–632, October 1985.

J. Baldwin, G. Ferland, K. Korista, and D. Verner. Locally Optimally Emitting Clouds and the Origin of Quasar Emission Lines. ApJ, 455:L119, December 1995.

B. Balmaverde, A. Capetti, D. Moisio, Ranieri D. Baldi, and A. Marconi. The HST view of the innermost narrow line region. A&A, 586:A48, February 2016.

M. Begelman, M. de Kool, and M. Sikora. Outflows driven by cosmic-ray pressure in broad absorption line qsos. ApJ, 382:416–432, December 1991.

M. C. Begelman. AGN Feedback Mechanisms. *Coevolution of Black Holes and Galaxies*, page 374, 2004.

M. C. Bentz, K. D. Denney, E. M. Cackett, M. Dietrich, J. K. J. Fogel, H. Ghosh, K. Horne, C. Kuehn, T. Minezaki, C. A. Onken, B. M. Peterson, R. W. Pogge, V. I. Pronik, D. O. Richstone, S. G. Sergeev, M. Vestergaard, M. G. Walker, and Y. Yoshii. A Reverberation-based Mass for the Central Black Hole in NGC 4151. ApJ, 651: 775–781, November 2006.

M. C. Bentz, K. D. Denney, C. J. Grier, A. J. Barth, B. M. Peterson, M. Vestergaard, V. N. Bennert, G. Canalizo, G. De Rosa, A. V. Filippenko, E. L. Gates, J. E. Greene, W. Li, M. A. Malkan, R. W. Pogge, D. Stern, T. Treu, and J.-H. Woo. The Low-luminosity End of the Radius-Luminosity Relationship for Active Galactic Nuclei. ApJ, 767:149, April 2013.

M. C. Bentz, K. Horne, A. J. Barth, V. N. Bennert, G. Canalizo, A. V. Filippenko, E. L. Gates, M. A. Malkan, T. Minezaki, T. Treu, J-H. Woo, and J. L. Walsh. The lick agn monitoring project: Velocity-delay maps from the maximum-entropy method for arp 151. ApJ, 720(1):L46, 2010a.

M. C. Bentz and S. Katz. The AGN Black Hole Mass Database. PASP, 127:67, January 2015.

M. C. Bentz, E. Manne-Nicholas, and B. Ou-Yang. The Black Hole Mass-Bulge Luminosity Relationship for Reverberation- Mapped AGNs in the Near-IR. NOAO Proposal, August 2011.

M. C. Bentz, B. M. Peterson, H. Netzer, R. W. Pogge, and M. Vestergaard. The radius-luminosity relationship for active galactic nuclei: The effect of host-galaxy starlight on luminosity measurements. ii. the full sample of reverberation-mapped agns. ApJ, 697(1):160, 2009a.

M. C. Bentz, J. L. Walsh, A. J. Barth, N. Baliber, N. Bennert, G. Canalizo, A. V. Filippenko, M. Ganeshalingam, E. L. Gates, J. E. Greene, M. G. Hidas, K. D. Hiner, N. Lee, W. Li, M. A. Malkan, T. Minezaki, F. J. D. Serduke, J. H. Shiode, J. M. Silverman, T. N. Steele, D. Stern, R. A. Street, C. E. Thornton, T. Treu, X. Wang, J.-H. Woo, and Y. Yoshii. First Results from the Lick AGN Monitoring Project: The Mass of the Black Hole in Arp 151. ApJ, 689:L21, December 2008.

M. C. Bentz, J. L. Walsh, A. J. Barth, N. Baliber, V. N. Bennert, G. Canalizo, A. V. Filippenko, M. Ganeshalingam, E. L. Gates, J. E. Greene, et al. The lick agn monitoring project: broad-line region radii and black hole masses from reverberation mapping of hβ. ApJ, 705(1):199, 2009b.

M. C. Bentz, J. L. Walsh, A. J. Barth, Y. Yoshii, J.-H. Woo, X. Wang, T. Treu, C. E. Thornton, R. A. Street, T. N. Steele, J. M. Silverman, F. J. D. Serduke, Y. Sakata, T. Minezaki, M. A. Malkan, W. Li, N. Lee, K. D. Hiner, M. G. Hidas, J. E. Greene, E. L. Gates, M. Ganeshalingam, A. V. Filippenko, G. Canalizo, V. N. Bennert, and N. Baliber. The Lick AGN Monitoring Project: Reverberation Mapping of Optical Hydrogen and Helium Recombination Lines. ApJ, 716:993–1011, June 2010b.

P. R. D. Blandford, P. H. Netzer, P. L. Woltjer, T. J. L. Courvoisier, and P. M. Mayor. *Active Galactic Nuclei*. Saas-Fee Advanced Course. Springer Berlin Heidelberg, 2013. ISBN 9783662398166.

R. D. Blandford and C. F. McKee. Reverberation mapping of the emission line regions of Seyfert galaxies and quasars. ApJ, 255:419–439, April 1982.

E. Bon, S. Zucker, H. Netzer, P. Marziani, N. Bon, P. Jovanovic, A. I. Shapovalova, S. Komossa, C. M. Gaskell, L. C. Popovic, S. Britzen, V. H. Chavushyan, A. N. Burenkov, S. Sergeev, G. La Mura, J. R. Valdes, and M. Stalevski. VizieR Online

Data Catalog: NGC 5548 43 year-long monitoring in Hβ (Bon+, 2016). *VizieR Online Data Catalog*, 222, October 2016.

E. W. Bonning, L. Cheng, G. A. Shields, S. Salviander, and K. Gebhardt. Accretion disk temperatures and continuum colors in qsos. *The Astrophysical Journal*, 659(1): 211, 2007.

M. Bottorff, K. T. Korista, I. Shlosman, and R. D. Blandford. Dynamics of Broad Emission-Line Region in NGC 5548: Hydromagnetic Wind Model versus Observations. ApJ, 479:200–221, April 1997a.

M. C. Bottorff, K. T. Korista, I. Shlosman, and R. D. Blandford. Reverberation Modeling of the Broad Emission Line Region in NGC 5548. In D. Maoz, A. Sternberg, and E. M. Leibowitz, editors, *Astronomical Time Series*, volume 218 of *Astrophysics and Space Science Library*, page 247, 1997b.

R. G. Bower, A. J. Benson, R. Malbon, J. C. Helly, C. S. Frenk, C. M. Baugh, S. Cole, and C. G. Lacey. Breaking the hierarchy of galaxy formation. MNRAS, 370:645–655, August 2006.

B. J. Brewer, L. B. Pártay, and G. Csányi. Diffusive Nested Sampling. *Statistics and Computing*, 21(4):649–656, October 2011. Astrophysics Source Code Library.

E. M. Cackett and K. Horne. Photoionized Hβ emission in NGC 5548: it breathes! MNRAS, 365:1180–1190, February 2006.

E. D. Cashwell and C. J. Everett. *A practical manual on the Monte Carlo method for random walk problems*. Internat. Tracts Computat. Sci. Technol. Pergamon, London, 1959.

K. W. Cavagnolo, B. R. McNamara, P. E. J. Nulsen, C. L. Carilli, C. Jones, and L. Bîrzan. A Relationship Between AGN Jet Power and Radio Power. ApJ, 720: 1066–1072, September 2010.

J. Chiang and O. Blaes. Using Multiwavelength Observations to Determine the Black Hole Mass and Accretion Rate in the Type 1 Seyfert Galaxy NGC 5548. ApJ, 586: 97–111, March 2003.

J. Chiang and N. Murray. Reverberation Mapping and the Disk-Wind Model of the Broad-Line Region. ApJ, 466:704, August 1996.

H. Childs, E. Brugger, B. Whitlock, J. Meredith, S. Ahern, D. Pugmire, K. Biagas, M. Miller, C. Harrison, G. H. Weber, H. Krishnan, T. Fogal, A. Sanderson, C. Garth, E. W. Bethel, D. Camp, O. Rübel, M. Durant, J. M. Favre, and P. Navrátil. VisIt: An End-User Tool For Visualizing and Analyzing Very Large Data. In *High Performance Visualization–Enabling Extreme-Scale Scientific Insight*, pages 357–372. Oct 2012.

S. Cielo, R. Bieri, M. Volonteri, A. Y. Wagner, and Y. Dubois. AGN feedback compared: jets versus radiation. MNRAS, 477:1336–1355, June 2018.

CodeDocs Team. Codedocs - document your code. https://codedocs.xyz, 2018.

F. A. Cordova and K. O. Mason. High-velocity winds from a dwarf nova during outburst. ApJ, 260:716–721, 1982.

Darren J. Croton, Volker Springel, Simon D. M. White, G. De Lucia, C. S. Frenk, L. Gao, A. Jenkins, G. Kauffmann, J. F. Navarro, and N. Yoshida. The many lives of active galactic nuclei: cooling flows, black holes and the luminosities and colours of galaxies. MNRAS, 365:11–28, January 2006.

B. Czerny and K. Hryniewicz. The origin of the broad line region in active galactic nuclei. A&A, 525:L8, January 2011.

X. Dai, F. Shankar, and G. R. Sivakoff. 2MASS Reveals a Large Intrinsic Fraction of BALQSOs. ApJ, 672:108–114, January 2008.

Andrew Davis and Andrew Turner. Comparison of global variance reduction techniques for monte carlo radiation transport simulations of iter. *Fusion Engineering and Design*, 86(9):2698 – 2700, 2011. ISSN 0920-3796. Proceedings of the 26th Symposium of Fusion Technology (SOFT-26).

G. De Rosa. Probing AGN Structure on Microarcsecond Scales: The Space Telescope and Optical Reverberation Mapping Program. *IAU General Assembly*, 22:2257825, August 2015.

G. De Rosa, B. M. Peterson, J. Ely, G. A. Kriss, D. M. Crenshaw, K. Horne, K. T. Korista, H. Netzer, R. W. Pogge, P. Arévalo, A. J. Barth, M. C. Bentz, W. N. Brandt, A. A. Breeveld, B. J. Brewer, E. Dalla Bontà, A. De Lorenzo-Cáceres, K. D. Denney, M. Dietrich, R. Edelson, P. A. Evans, M. M. Fausnaugh, N. Gehrels, J. M. Gelbord, M. R. Goad, C. J. Grier, D. Grupe, P. B. Hall, J. Kaastra, B. C. Kelly, J. A. Kennea, C. S. Kochanek, P. Lira, S. Mathur, I. M. McHardy, J. A. Nousek, A. Pancoast, I. Papadakis, L. Pei, J. S. Schimoia, M. Siegel, D. Starkey, T. Treu, P. Uttley, S. Vaughan, M. Vestergaard, C. Villforth, H. Yan, S. Young, and Y. Zu. Space Telescope and Optical Reverberation Mapping Project.I. Ultraviolet Observations of the Seyfert 1 Galaxy NGC 5548 with the Cosmic Origins Spectrograph on Hubble Space Telescope. ApJ, 806:128, June 2015.

K. D. Denney, B. M. Peterson, R. W. Pogge, A. Adair, D. W. Atlee, K. Au-Yong, M. C. Bentz, J. C. Bird, D. J. Brokofsky, E. Chisholm, M. L. Comins, M. Dietrich, V. T. Doroshenko, J. D. Eastman, Y. S. Efimov, S. Ewald, S. Ferbey, C. M. Gaskell, C. H. Hedrick, K. Jackson, S. A. Klimanov, E. S. Klimek, A. K. Kruse, A. Ladéroute, J. B. Lamb, K. Leighly, T. Minezaki, S. V. Nazarov, C. A. Onken, E. A. Petersen, P. Peterson, S. Poindexter, Y. Sakata, K. J. Schlesinger, S. G. Sergeev, N. Skolski,

L. Stieglitz, J. J. Tobin, C. Unterborn, M. Vestergaard, A. E. Watkins, L. C. Watson, and Y. Yoshii. Reverberation Mapping Measurements of Black Hole Masses in Six Local Seyfert Galaxies. ApJ, 721:715–737, September 2010.

K. D. Denney, B. M. Peterson, R. W. Pogge, A. Adair, D. W. Atlee, K. Au-Yong, M. C. Bentz, J. C. Bird, D. J. Brokofsky, E. Chisholm, M. L. Comins, M. Dietrich, V. T. Doroshenko, J. D. Eastman, Y. S. Efimov, S. Ewald, S. Ferbey, C. M. Gaskell, C. H. Hedrick, K. Jackson, S. A. Klimanov, E. S. Klimek, A. K. Kruse, Ladéroute A., J. B. Lamb, K. Leighly, T. Minezaki, Nazarov S. V., C. A. Onken, E. A. Petersen, P. Peterson, Poindexter. S., Y. Sakata, K. J. Schlesinger, S. G. Sergeev, N. Skolski, L. Stieglitz, J. J. Tobin, C. Unterborn, M. Vestergaard, A. E. Watkins, Watson. L. C., and Y. Yoshii. Diverse kinematic signatures from reverberation mapping of the broad-line region in agns. ApJ, 704(2):L80, 2009.

P. Du, C. Hu, K.-X. Lu, F. Wang, J. Qiu, Y.-R. Li, J.-M. Bai, S. Kaspi, H. Netzer, J.-M. Wang, and SEAMBH Collaboration. Supermassive Black Holes with High Accretion Rates in Active Galactic Nuclei. I. First Results from a New Reverberation Mapping Campaign. ApJ, 782:45, February 2014.

P. Du, K.-X. Lu, C. Hu, J. Qiu, Y.-R. Li, Y.-K. Huang, F. Wang, J.-M. Bai, W.-H. Bian, Y.-F. Yuan, L. C. Ho, J.-M. Wang, and SEAMBH Collaboration. Supermassive Black Holes with High Accretion Rates in Active Galactic Nuclei. VI. Velocity-resolved Reverberation Mapping of the Hβ Line. ApJ, 820:27, March 2016.

R. Edelson, J. M. Gelbord, K. Horne, I. M. McHardy, B. M. Peterson, P. Arévalo, A. A. Breeveld, G. De Rosa, P. A. Evans, M. R. Goad, G. A. Kriss, W. N. Brandt, N. Gehrels, D. Grupe, J. A. Kennea, C. S. Kochanek, J. A. Nousek, I. Papadakis, M. Siegel, D. Starkey, P. Uttley, S. Vaughan, S. Young, A. J. Barth, M. C. Bentz, B. J. Brewer, D. M. Crenshaw, E. Dalla Bontà, A. De Lorenzo-Cáceres, K. D. Denney, M. Dietrich, J. Ely, M. M. Fausnaugh, C. J. Grier, P. B. Hall, J. Kaastra, B. C. Kelly, K. T. Korista, P. Lira, S. Mathur, H. Netzer, A. Pancoast, L. Pei, R. W. Pogge, J. S. Schimoia, T. Treu, M. Vestergaard, C. Villforth, H. Yan, and Y. Zu. Space Telescope and Optical Reverberation Mapping Project. II. Swift and HST Reverberation Mapping of the Accretion Disk of NGC 5548. ApJ, 806:129, June 2015.

R. A. Edelson and J. H. Krolik. The Discrete Correlation Function: a New Method for Analyzing Unevenly Sampled Variability Data. In *Active Galactic Nuclei*, volume 134, page 96, January 1989.

M. Elvis. A Structure for Quasars. ApJ, 545:63–76, December 2000.

M. Elvis. Quasar Atmospheres: Toward a 'Low' Theory for Quasars. In G. T. Richards and P. B. Hall, editors, *AGN Physics with the Sloan Digital Sky Survey*, volume 311 of *Astronomical Society of the Pacific Conference Series*, page 109, June 2004.

M. Elvis. Quasar Rain: The Broad Emission Line Region as Condensations in the Warm Accretion Disk Wind. ApJ, 847:56, September 2017.

M. Elvis, B. J. Wilkes, J. C. McDowell, R. F. Green, J. Bechtold, S. P. Willner, M. S. Oey, E. Polomski, and R. Cutri. Atlas of quasar energy distributions. ApJS, 95:1–68, November 1994.

R. T. Emmering, R. D. Blandford, and I. Shlosman. Magnetic acceleration of broad emission-line clouds in active galactic nuclei. ApJ, 385:460–477, February 1992.

D. A. Evans, P. M. Ogle, H. L. Marshall, M. A. Nowak, S. Bianchi, M. Guainazzi, A. L. Longinotti, D. Dewey, N. S. Schulz, M. S. Noble, J. Houck, and C. R. Canizares. Searching for AGN Outflows: Spatially Resolved Chandra HETG Spectroscopy of the NLR Ionization Cone in NGC 1068. In L. Maraschi, G. Ghisellini, R. Della Ceca, and F. Tavecchio, editors, *Accretion and Ejection in AGN: a Global View*, volume 427 of *Astronomical Society of the Pacific Conference Series*, page 97, October 2010.

A. C. Fabian. Observational Constraints on AGN / Active Galactic Nuclei Models. In Wolfgang Brinkmann and Joachim Truemper, editors, *X-ray Emission from Active Galactic Nuclei and the Cosmic X-ray Background*, page 22, March 1992.

A. C. Fabian. Observational Evidence of Active Galactic Nuclei Feedback. ARA&A, 50: 455–489, September 2012.

M. M. Fausnaugh, K. D. Denney, A. J. Barth, M. C. Bentz, M. C. Bottorff, M. T. Carini, K. V. Croxall, G. De Rosa, M. R. Goad, K. Horne, M. D. Joner, S. Kaspi, M. Kim, S. A. Klimanov, C. S. Kochanek, D. C. Leonard, H. Netzer, B. M. Peterson, K. Schnülle, S. G. Sergeev, M. Vestergaard, W.-K. Zheng, Y. Zu, M. D. Anderson, P. Arévalo, C. Bazhaw, G. A. Borman, T. A. Boroson, W. N. Brandt, A. A. Breeveld, B. J. Brewer, E. M. Cackett, D. M. Crenshaw, E. Dalla Bontà, A. De Lorenzo-Cáceres, M. Dietrich, R. Edelson, N. V. Efimova, J. Ely, P. A. Evans, A. V. Filippenko, K. Flatland, N. Gehrels, S. Geier, J. M. Gelbord, L. Gonzalez, V. Gorjian, C. J. Grier, D. Grupe, P. B. Hall, S. Hicks, D. Horenstein, T. Hutchison, M. Im, J. J. Jensen, J. Jones, J. Kaastra, B. C. Kelly, J. A. Kennea, S. C. Kim, K. T. Korista, G. A. Kriss, J. C. Lee, P. Lira, F. MacInnis, E. R. Manne-Nicholas, S. Mathur, I. M. McHardy, C. Montouri, R. Musso, S. V. Nazarov, R. P. Norris, J. A. Nousek, D. N. Okhmat, A. Pancoast, I. Papadakis, J. R. Parks, L. Pei, R. W. Pogge, J.-U. Pott, S. E. Rafter, H.-W. Rix, D. A. Saylor, J. S. Schimoia, M. Siegel, M. Spencer, D. Starkey, H.-I. Sung, K. G. Teems, T. Treu, C. S. Turner, P. Uttley, C. Villforth, Y. Weiss, J.-H. Woo, H. Yan, and S. Young. Space Telescope and Optical Reverberation Mapping Project. III. Optical Continuum Emission and Broadband Time Delays in NGC 5548. ApJ, 821:56, April 2016.

M. M. Fausnaugh, B. M. Peterson, D. A. Starkey, K. Horne, and the AGN STORM Collaboration. Continuum reverberation mapping of agn accretion disks. *Frontiers in Astronomy and Space Sciences*, 4:55, 2017. ISSN 2296-987X.

J. W. Ferguson, K. T. Korista, J. A. Baldwin, and G. J. Ferland. Locally Optimally Emitting Clouds and the Narrow Emission Lines in Seyfert Galaxies. ApJ, 487:122–141, September 1997.

G. J. Ferland, R. L. Porter, P. A. M. van Hoof, R. J. R. Williams, N. P. Abel, M. L. Lykins, G. Shaw, W. J. Henney, and P. C. Stancil. The 2013 Release of Cloudy. Rev. Mexicana Astron. Astrofis., 49:137–163, April 2013.

L. Ferrarese, J. R. Mould, P. B. Stetson, J. L. Tonry, J. P. Blakeslee, and E. A. Ajhar. The Discovery of Cepheids and a Distance to NGC 5128. ApJ, 654:186–218, January 2007.

L. Ferrarese, R. W. Pogge, B. M. Peterson, D. Merritt, A. Wandel, and C. L. Joseph. Supermassive black holes in active galactic nuclei. i. the consistency of black hole masses in quiescent and active galaxies. ApJ, 555(2):L79, 2001.

J.A Fleck and E.H Canfield. A random walk procedure for improving the computational efficiency of the implicit monte carlo method for nonlinear radiation transport. *Journal of Computational Physics*, 54(3):508 – 523, 1984. ISSN 0021-9991.

A. Franceschini, V. Braito, and D. Fadda. Origin of the X-ray background and AGN unification: new perspectives. MNRAS, 335:L51–L56, September 2002.

K. Fukumura, D. Kazanas, I. Contopoulos, and E. Behar. Modeling High-velocity QSO Absorbers with Photoionized Magnetohydrodynamic Disk Winds. ApJ, 723:L228–L232, November 2010.

C. M. Gaskell. Direct evidence for gravitational domination of the motion of gas within one light-week of the central object in NGC 4151 and the determination of the mass of the probable black hole. ApJ, 325:114–118, February 1988.

C. M. Gaskell. What broad emission lines tell us about how active galactic nuclei work. New A Rev., 53(7):140–148, 2009.

C. M. Gaskell and R. W. Goosmann. The case for inflow of the broad-line region of active galactic nuclei. Ap&SS, 361:67, February 2016.

K. Gebhardt, R. Bender, G. Bower, A. Dressler, S. M. Faber, A. V. Filippenko, R. Green, C. Grillmair, L. C. Ho, J. Kormendy, et al. A relationship between nuclear black hole mass and galaxy velocity dispersion. ApJ, 539(1):L13, 2000.

N.A. Gentile. Implicit monte carlo diffusion: An acceleration method for monte carlo time-dependent radiative transfer simulations. *Journal of Computational Physics*, 172 (2):543 – 571, 2001. ISSN 0021-9991.

M. Goad and I. Wanders. The Effect of a Variable Anisotropic Continuum Source upon the Broad Emission Line Profiles and Responses. ApJ, 469:113, September 1996.

M. R. Goad and K. T. Korista. Interpreting broad emission-line variations - I. Factors influencing the emission-line response. MNRAS, 444:43–61, October 2014.

M. R. Goad and K. T. Korista. Interpreting broad emission-line variations - II. Tensions between luminosity, characteristic size, and responsivity. MNRAS, 453:3662–3684, November 2015.

M. R. Goad, P. T. O'Brien, and P. M. Gondhalekar. Response functions as diagnostics of the broad-line region in active galactic nuclei. MNRAS, 263:149–167, July 1993.

A. R. Green, I. M. McHardy, and H. J. Lehto. On the nature of rapid X-ray variability in active galactic nuclei. MNRAS, 265:664–680, December 1993.

C. J. Grier. *Active galactic nuclei: Masses and dynamics*. PhD thesis, The Ohio State University, 2013.

C. J. Grier, P. Martini, L. C. Watson, B. M. Peterson, M. C. Bentz, K. M. Dasyra, M. Dietrich, L. Ferrarese, R. W. Pogge, and Y. Zu. Stellar Velocity Dispersion Measurements in High-luminosity Quasar Hosts and Implications for the AGN Black Hole Mass Scale. ApJ, 773:90, August 2013a.

C. J. Grier, B. M. Peterson, K. Horne, M. C. Bentz, R. W. Pogge, K. D. Denney, G. De Rosa, P. Martini, C. S. Kochanek, Y. Zu, B. Shappee, R. Siverd, T. G. Beatty, S. G. Sergeev, S. Kaspi, C. A. Salvo, J. C. Bird, D. J. Bord, G. A. Borman, X. Che, C. Chen, S. A. Cohen, M. Dietrich, V. T. Doroshenko, Y. S. Efimov, N. Free, I. Ginsburg, C. B. Henderson, A. L. King, K. Mogren, M. Molina, A. M. Mosquera, S. V. Nazarov, D. N. Okhmat, O. Pejcha, S. Rafter, J. C. Shields, J. Skowron, D. M. Szczygiel, M. Valluri, and J. L. van Saders. The structure of the broad-line region in active galactic nuclei. i. reconstructed velocity-delay maps. *The Astrophysical Journal*, 764(1):47, 2013b.

C. J. Grier, B. M. Peterson, R. W. Pogge, K. D. Denney, M. C. Bentz, P. Martini, S. G. Sergeev, S. Kaspi, T. Minezaki, Y. Zu, C. S. Kochanek, R. Siverd, B. Shappee, Stanek K. Z., C. A. Salvo, T. G. Beatty, J. C. Bird, D. J. Bord, G. A. Borman, X. Che, C. Chen, S. A. Cohen, M. Dietrich, V. T. Doroshenko, T. Drake, Y. S. Efimov, N. Free, I. Ginsburg, C. B. Henderson, A. L. King, S. Koshida, K. Mogren, M. Molina, M. Mosquera, S. V. Nazarov, D. N. Okhmat, O. Pejcha, S. Rafter, J. C. Shields, J. Skowron, D. M.. Szczygiel, M. Valluri, and J. L. van Saders. Reverberation mapping results for five seyfert 1 galaxies. ApJ, 755(1):60, 2012a.

C. J. Grier, B. M. Peterson, R. W. Pogge, K. D. Denney, M. C. Bentz, P. Martini, S. G. Sergeev, S. Kaspi, Y. Zu, C. S. Kochanek, B. J. Shappee, K. Z. Stanek, C. A. Salvo, T. G. Beatty, J. C. Bird, D. J. Bord, G. A. Borman, X. Che, C. Chen, S. A. Cohen, M. Dietrich, V. T. Doroshenko, Y. S. Efimov, N. Free, I. Ginsburg, C. B. Henderson,

K. Horne, A. L. King, K. Mogren, M. Molina, S. V. Mosquera, A. M.and Nazarov, D. N. Okhmat, O. Pejcha, S. Rafter, J. C. Shields, J. Skowron, D. M. Szczygiel, M. Valluri, and J. L. van Saders. A reverberation lag for the high-ionization component of the broad-line region in the narrow-line seyfert 1 mrk 335. ApJ, 744(1):L4, 2012b.

W.-R. Hamann and L. Koesterke. Spectrum formation in clumped stellar winds: consequences for the analyses of Wolf-Rayet spectra. A&A, 335:1003–1008, July 1998.

N. Häring and H.-W. Rix. On the Black Hole Mass-Bulge Mass Relation. ApJ, 604: L89–L92, April 2004.

T. J. Harries. Radiation-hydrodynamical simulations of massive star formation using Monte Carlo radiative transfer: I. Algorithms and numerical methods. *ArXiv e-prints*, January 2015.

P. H. Hauschildt and E. Baron. A 3d radiative transfer framework - iii. periodic boundary conditions. *A&A*, 490(2):873–877, 2008.

Kiyoshi Hayashida, Sigenori Miyamoto, Shunji Kitamoto, Hitoshi Negoro, and Hajime Inoue. Central Black Hole Masses in Active Galactic Nuclei Inferred from X-Ray Variability. ApJ, 500:642–659, June 1998.

J. S. Hendricks and T. E. Booth. Mcnp variance reduction overview. In *Monte-Carlo Methods and Applications in Neutronics, Photonics and Statistical Physics*, pages 83–92. Springer, 1985.

P. C. Hewett and C. B. Foltz. The Frequency and Radio Properties of Broad Absorption Line Quasars. AJ, 125:1784–1794, April 2003.

N. Higginbottom, C. Knigge, K. S. Long, S. A. Sim, and J. H. Matthews. A simple disc wind model for broad absorption line quasars. MNRAS, 436(2):1390–1407, DEC 2013. ISSN 0035-8711.

N. Higginbottom, D. Proga, C. Knigge, K. S. Long, J. H. Matthews, and S. A. Sim. Line-driven Disk Winds in Active Galactic Nuclei: The Critical Importance of Ionization and Radiative Transfer. ApJ, 789:19, July 2014.

D. J. Hillier. The effects of electron scattering and wind clumping for early emission line stars. A&A, 247:455–468, July 1991.

L. C. Ho and M. Kim. The Black Hole Mass Scale of Classical and Pseudo Bulges in Active Galaxies. ApJ, 789:17, July 2014.

Y. Homayouni, J. R. Trump, C. J. Grier, Y. Shen, D. A. Starkey, W. N. Brandt, P. B. Hall, K. Horne, K. Kinemuchi, J. I-Hsiu Li, I. McGreer, M. Sun, L. C. Ho, and D. P. Schneider. The Sloan Digital Sky Survey Reverberation Mapping Project: Accretion-Disk Sizes from Continuum Lags. *ArXiv e-prints*, June 2018.

K. Horne. Echo Mapping Problems Maximum Entropy solutions. In P. M. Gondhalekar, K. Horne, and B. M. Peterson, editors, *Reverberation Mapping of the Broad-Line Region in Active Galactic Nuclei*, volume 69 of *Astronomical Society of the Pacific Conference Series*, page 23, 1994.

K. Horne, B. M. Peterson, S. J. Collier, and H. Netzer. Observational Requirements for High-Fidelity Reverberation Mapping. PASP, 116:465–476, May 2004.

K. Horne, W. F. Welsh, and B. M. Peterson. Echo mapping of broad H-beta emission in NGC 5548. ApJ, 367:L5–L8, January 1991.

I. Hubeny and T. Lanz. TLUSTY: Stellar Atmospheres, Accretion Disks, and Spectroscopic Diagnostics. Astrophysics Source Code Library, September 2011.

J. D. Hunter. Matplotlib: A 2d graphics environment. *Computing In Science & Engineering*, 9(3):90–95, 2007.

S. Juneau, M. Dickinson, F. Bournaud, D. M. Alexander, E. Daddi, J. R. Mullaney, B. Magnelli, J. S. Kartaltepe, H. S. Hwang, S. P. Willner, A. L. Coil, D. J. Rosario, J. R. Trump, B. J. Weiner, C. N. A. Willmer, M. C. Cooper, D. Elbaz, S. M. Faber, D. T. Frayer, D. D. Kocevski, E. S. Laird, J. A. Monkiewicz, K. Nandra, J. A. Newman, S. Salim, and M. Symeonidis. Widespread and Hidden Active Galactic Nuclei in Star-forming Galaxies at Redshift ¿0.3. ApJ, 764:176, February 2013.

J. S. Kaastra, Y. Terashima, T. Kallman, Y. Haba, E. Costantini, L. Gallo, Y. Fukazawa, F. Tombesi, N. Anabuki, H. Awaki, G. Brown, L. di Gesu, K. Ebisawa, J. Ebrero, M. Eckart, K. Hagino, K. S. Long, J. Miller, T. Miyazawa, S. Paltani, C. Reynolds, C. Ricci, H. Sameshima, H. Seta, Y. Ueda, M. Urry, and for the ASTRO-H Science Working Group. ASTRO-H White Paper - AGN Winds. *ArXiv e-prints*, December 2014.

A. Kashi, D. Proga, K. Nagamine, J. Greene, and A. J. Barth. On the Virialization of Disk Winds: Implications for the Black Hole Mass Estimates in Active Galactic Nuclei. ApJ, 778:50, November 2013.

S. Kaspi, W. N. Brandt, D. Maoz, H. Netzer, D. P. Schneider, and O. Shemmer. Reverberation mapping of high-luminosity quasars: First results. ApJ, 659(2):997, 2007.

S. Kaspi, D. Maoz, H. Netzer, B. M. Peterson, M. Vestergaard, and B. T. Jannuzi. The relationship between luminosity and broad-line region size in active galactic nuclei. ApJ, 629(1):61, 2005.

S. Kaspi and H. Netzer. Modeling variable emission lines in active galactic nuclei: Method and application to ngc 5548. ApJ, 524(1):71, 1999.

S. Kaspi, P. S. Smith, H. Netzer, D. Maoz, B. T. Jannuzi, and U. Giveon. Reverberation measurements for 17 quasars and the size-mass-luminosity relations in active galactic nuclei. ApJ, 533(2):631, 2000.

T. Kawaguchi, S. Mineshige, M. Umemura, and Edwin L. Turner. Optical Variability in Active Galactic Nuclei: Starbursts or Disk Instabilities? ApJ, 504:671–679, September 1998.

K. I. Kellermann. Radio evidence for AGN activity: relativistic jets as tracers of SMBHs. In Y. Meiron, S. Li, F.-K. Liu, and R. Spurzem, editors, *Star Clusters and Black Holes in Galaxies across Cosmic Time*, volume 312 of *IAU Symposium*, pages 3–12, February 2016.

K. I. Kellermann, R. Sramek, M. Schmidt, D. B. Shaffer, and R. Green. VLA observations of objects in the Palomar Bright Quasar Survey. AJ, 98:1195–1207, October 1989.

A. L. King, P. Martini, T. M. Davis, K. D. Denney, C. S. Kochanek, B. M. Peterson, A. Skielboe, M. Vestergaard, E. Huff, D. Watson, M. Banerji, R. McMahon, R. Sharp, and C. Lidman. Simulations of the ozdes agn reverberation mapping project. *ArXiv e-prints*, April 2015.

A. R. King. The UV delay in dwarf novae. MNRAS, 288:L16–L18, June 1997.

C. Knigge, S. Scaringi, M. R. Goad, and C. E. Cottis. The intrinsic fraction of broad-absorption line quasars. MNRAS, 386(3):1426–1435, 2008.

C. Knigge, J. A. Woods, and J. E. Drew. The application of Monte Carlo methods to the synthesis of spectral line profiles arising from accretion disc winds. MNRAS, 273: 225–248, March 1995.

W. Kollatschny, K. Ulbrich, M. Zetzl, S. Kaspi, and M. Haas. Broad-line region structure and kinematics in the radio galaxy 3c120. A&A, 566:A106, 2014.

W. Kollatschny and M. Zetzl. Accretion disk wind as explanation for the broad-line region structure in NGC 5548. A&A, 551:L6, March 2013.

A. P. Koratkar and C. M. Gaskell. Emission-line variability of Fairall 9 - Determination of the size of the broad-line region and the direction of gas motion. ApJ, 345:637–646, October 1989.

K. Korista and G. Ferland. The ultraviolet-optical albedo of broad emission line clouds. ApJ, 495(2):672, 1998.

K. T. Korista and M. R. Goad. What the Optical Recombination Lines Can Tell Us about the Broad-Line Regions of Active Galactic Nuclei. ApJ, 606:749–762, May 2004.

S. Koshida, T. Minezaki, Y. Yoshii, Y. Kobayashi, Y. Sakata, S. Sugawara, K. Enya, M. Suganuma, H. Tomita, T. Aoki, and B. A. Peterson. Reverberation Measurements of the Inner Radius of the Dust Torus in 17 Seyfert Galaxies. ApJ, 788:159, June 2014.

G. A. Kriss and Agn Storm Team. Space Telescope and Optical Reverberation Mapping Project VI. Variations of the Intrinsic Absorption Lines in NGC 5548. In *American Astronomical Society Meeting Abstracts*, volume 225 of *American Astronomical Society Meeting Abstracts*, page 103.06, January 2015.

J. H. Krolik and C. Done. Reverberation mapping by regularized linear inversion. ApJ, 440:166–180, February 1995.

J. H. Krolik, K. Horne, T. R. Kallman, M. A. Malkan, R. A. Edelson, and G. A. Kriss. Ultraviolet variability of NGC 5548 - Dynamics of the continuum production region and geometry of the broad-line region. ApJ, 371:541–562, April 1991.

J. H. Krolik and G. A. Kriss. Observable Properties of X-Ray–heated Winds in Active Galactic Nuclei: Warm Reflectors and Warm Absorbers. ApJ, 447:512, July 1995.

Y. Krongold, L. Binette, R. Bohlin, L. Bianchi, A. L. Longinotti, S. Mathur, F. Nicastro, A. Gupta, C. A. Negrete, and F. Hernandez-Ibarra. Hubble Space Telescope observations of BALQSO Ton 34 reveal a connection between the broad-line region and the BAL outflow. MNRAS, 468:3607–3614, July 2017.

R. L. Kurucz. Model atmospheres for G, F, A, B, and O stars. ApJS, 40:1–340, May 1979.

C. J. Lada. Cold outflows, energetic winds, and enigmatic jets around young stellar objects. ARA&A, 23:267–317, 1985.

S. M. LaMassa, S. Cales, E. C. Moran, A. D. Myers, G. T. Richards, M. Eracleous, T. M. Heckman, L. Gallo, and C. M. Urry. The Discovery of the First 'Changing Look' Quasar: New Insights Into the Physics and Phenomenology of Active Galactic Nucleus. ApJ, 800:144, February 2015.

A. Laor. What Can We Learn from the Smallest AGN? In L. C. Ho and J.-W. Wang, editors, *The Central Engine of Active Galactic Nuclei*, volume 373 of *Astronomical Society of the Pacific Conference Series*, page 384, October 2007.

K. Leighly. WPVS 007: the little AGN that could. HST Proposal, July 2009.

K. M. Leighly, E. Cooper, D. Grupe, D. M. Terndrup, and S. Komossa. Variable Reddening and Broad Absorption Lines in the Narrow-line Seyfert 1 Galaxy WPVS 007: An Origin in the Torus. ApJ, 809:L13, August 2015.

K. M. Leighly, D. M. Terndrup, S. C. Gallagher, G. T. Richards, and M. Dietrich. The z=0.54 LoBAL Quasar SDSS J085053.12+445122.5: I. Spectral Synthesis Analysis Reveals a Massive Outflow. *ArXiv e-prints*, August 2018.

Yan-Rong Li, Jian-Min Wang, and Jin-Ming Bai. A Non-parametric Approach to Constrain the Transfer Function in Reverberation Mapping. ApJ, 831:206, November 2016.

M. L. Lister, M. H. Cohen, D. C. Homan, M. Kadler, K. I. Kellermann, Y. Y. Kovalev, E. Ros, T. Savolainen, and J. A. Zensus. MOJAVE: Monitoring of Jets in Active Galactic Nuclei with VLBA Experiments. VI. Kinematics Analysis of a Complete Sample of Blazar Jets. AJ, 138:1874–1892, December 2009.

K. S. Long and C. Knigge. Modeling the spectral signatures of accretion disk winds: A new monte carlo approach. ApJ, 579:725–740, 2002.

L. B. Lucy. Monte carlo transition probabilities. A&A, 384(2):725–735, 2002.

L. B. Lucy. Monte carlo transition probabilities. ii. A&A, 403(1):261–275, 2003.

T. J. Maccarone, E. Gallo, and R. Fender. The connection between radio-quiet active galactic nuclei and the high/soft state of X-ray binaries. MNRAS, 345:L19–L24, October 2003.

S. W. Mangham, C. Knigge, J. H. Matthews, K. S. Long, S. A. Sim, and N. Higginbottom. The reverberation signatures of rotating disc winds in active galactic nuclei. *Monthly Notices of the Royal Astronomical Society*, 471(4):4788–4801, 2017.

S.W Mangham, C. Knigge, P. Williams, K. Horne, J. H.and Long K. S. Pancoast, A.and Matthews, S. A. Sim, and N. Higginbottom. Testing reverberation mapping inversion methods. *In prep*, 2018.

F. Marin. Are there reliable methods to estimate the nuclear orientation of Seyfert galaxies? MNRAS, 460:3679–3705, August 2016.

J. H. Matthews, C. Knigge, K. S. Long, S. A. Sim, and N. Higginbottom. The impact of accretion disc winds on the optical spectra of cataclysmic variables. MNRAS, 450: 3331–3344, July 2015.

J. H. Matthews, C. Knigge, K. S. Long, S. A. Sim, N. Higginbottom, and S. W. Mangham. Testing quasar unification: radiative transfer in clumpy winds. MNRAS, 458: 293–305, May 2016.

P. A. Mazzali and L. B. Lucy. The application of monte carlo methods to the synthesis of early-time supernovae spectra. A&A, 279:447–456, November 1993.

R. J. McLure and J. S. Dunlop. On the black hole-bulge mass relation in active and inactive galaxies. MNRAS, 331(3):795–804, 2002.

H. Y. A. Meng, P. Plavchan, G. H. Rieke, A. M. Cody, T. Guth, J. Stauffer, K. Covey, S. Carey, D. Ciardi, M. C. Duran-Rojas, R. A. Gutermuth, M. Morales-Calderon, L. M. Rebull, and A. M. Watson. VizieR Online Data Catalog: Photo-reverberation mapping of 27 YSOs in LDN1688 (Meng+, 2016). *VizieR Online Data Catalog*, 182, August 2016.

D. M. Mihalas. *Stellar atmospheres.* 1982.

M. Min, C. P. Dullemond, C. Dominik, A. de Koter, and J. W. Hovenier. Radiative transfer in very optically thick circumstellar disks. A&A, 497:155–166, April 2009.

T. Misawa, J. C. Charlton, M. Eracleous, R. Ganguly, D. Tytler, D. Kirkman, N. Suzuki, and D. Lubin. A Census of Intrinsic Narrow Absorption Lines in the Spectra of Quasars at z = 2-4. ApJS, 171:1–28, July 2007.

N. Murray and J. Chiang. Wind-dominated optical line emission from accretion disks around luminous cataclysmic variable stars. Nature, 382(6594):789–791, 08 1996.

N. Murray, J. Chiang, S. A. Grossman, and G. M. Voit. Accretion Disk Winds from Active Galactic Nuclei. ApJ, 451:498, October 1995.

R. F. Mushotzky, C. Done, and K. A. Pounds. X-ray spectra and time variability of active galactic nuclei. ARA&A, 31:717–761, 1993. ISSN 0066-4146.

R. Narayan, R. Mahadevan, and E. Quataert. Advection-dominated accretion around black holes. In M. A. Abramowicz, G. Björnsson, and J. E. Pringle, editors, *Theory of Black Hole Accretion Disks*, pages 148–182, 1998.

R. Narayan, I. Yi, and R. Mahadevan. Explaining the spectrum of Sagittarius A* with a model of an accreting black hole. Nature, 374:623–625, April 1995.

H. Netzer. Revisiting the Unified Model of Active Galactic Nuclei. ARA&A, 53:365–408, August 2015.

U. M. Noebauer, K. S. Long, S. A. Sim, and C. Knigge. The geometry and ionization structure of the wind in the eclipsing nova-like variables rw tri and ux uma. ApJ, 719: 1932–1945, August 2010.

P. T. O'Brien, M. R. Goad, and P. M. Gondhalekar. The luminosity-dependent broad-line region in active galactic nuclei. MNRAS, 275:1125–1145, August 1995.

T. E. Oliphant. *Guide to NumPy*. CreateSpace Independent Publishing Platform, USA, 2nd edition, 2015. ISBN 151730007X, 9781517300074.

C. A. Onken, L. Ferrarese, D. Merritt, B. M. Peterson, R. W. Pogge, M. Vestergaard, and A. Wandel. Supermassive black holes in active galactic nuclei. ii. calibration of the black hole mass-velocity dispersion relationship for active galactic nuclei. ApJ, 615(2):645, 2004.

D. E. Osterbrock. The nature and structure of active galactic nuclei. II. Rev. Mexicana Astron. Astrofis., 26:65–72, October 1993.

S. Oualline and Oualline. G. Using dia diagram editor. *Practical Free Alternatives to Commercial Software*, 2018.

P. Padovani. Gamma-Ray Emitting AGN and Unified Schemes. In Y. Giraud-Heraud and J. Tran Thanh van, editors, *Very High Energy Phenomena in the Universe; Moriond Workshop*, page 7, 1997.

P. Padovani et al. Active galactic nuclei: what's in a name? *Astron. Astrophys. Rev.*, 25(1):2, 2017.

T. Page. QSO's, the Brightest Things in the Universe (Quasi-Stellar Objects). *Leaflet of the Astronomical Society of the Pacific*, 9:161, 1964.

A. Pancoast, A. J. Barth, K. Horne, T. Treu, B. J. Brewer, V. N. Bennert, G. Canalizo, E. L. Gates, W. Li, M. A. Malkan, D. Sand, T. Schmidt, S. Valenti, J.-H. Woo, K. I. Clubb, M. C. Cooper, S. M. Crawford, S. F. Hönig, M. D. Joner, M. T. Kandrashoff, M. Lazarova, A. M. Nierenberg, E. Romero-Colmenero, D. Son, E. Tollerud, J. L. Walsh, and H. Winkler. Stability of the Broad-line Region Geometry and Dynamics in Arp 151 Over Seven Years. ApJ, 856:108, April 2018.

A. Pancoast, B. J. Brewer, and T. Treu. Geometric and Dynamical Models of Reverberation Mapping Data. ApJ, 730:139, April 2011.

A. Pancoast, B. J. Brewer, and T. Treu. Modelling reverberation mapping data - I. Improved geometric and dynamical models and comparison with cross-correlation results. MNRAS, 445:3055–3072, December 2014a.

A. Pancoast, B. J. Brewer, T. Treu, A. J. Barth, V. N. Bennert, G. Canalizo, A. V. Filippenko, E. L. Gates, J. E. Greene, W. Li, M. A. Malkan, D. J. Sand, D. Stern, J.-H. Woo, R. J. Assef, H.-J. Bae, T. Buehler, S. B. Cenko, K. I. Clubb, M. C. Cooper, A. M. Diamond-Stanic, K. D. Hiner, S. F. Hönig, M. D. Joner, M. T. Kandrashoff, C. D. Laney, M. S. Lazarova, A. M. Nierenberg, D. Park, J. M. Silverman, D. Son, A. Sonnenfeld, S. J. Thorman, E. J. Tollerud, J. L. Walsh, and R. Walters. The Lick AGN Monitoring Project 2011: Dynamical Modeling of the Broad-line Region in Mrk 50. ApJ, 754:49, July 2012.

A. Pancoast, B. J. Brewer, T. Treu, D. Park, A. J. Barth, M. C. Bentz, and J.-H. Woo. Modelling reverberation mapping data - II. Dynamical modelling of the Lick AGN Monitoring Project 2008 data set. MNRAS, 445:3073–3091, December 2014b.

D. Park, B. C. Kelly, J.-H. Woo, and T. Treu. Recalibration of the Virial Factor and M $_{BH}$-σ_* Relation for Local Active Galaxies. ApJS, 203:6, November 2012.

P. Pavodani. A dust-bound supermassive black hole [artist's impression]. Online, May 2004.

Tim Pearson. PGPLOT graphics subroutine library.

L. Pei, M. M. Fausnaugh, A. J. Barth, B. M. Peterson, M. C. Bentz, G. De Rosa, K. D. Denney, M. R. Goad, C. S. Kochanek, K. T. Korista, G. A. Kriss, R. W. Pogge,

V. N. Bennert, M. Brotherton, K. I. Clubb, E. Dalla Bontà, A. V. Filippenko, J. E. Greene, C. J. Grier, M. Vestergaard, W. Zheng, S. M. Adams, T. G. Beatty, A. Bigley, J. E. Brown, J. S. Brown, G. Canalizo, J. M. Comerford, C. T. Coker, E. M. Corsini, S. Croft, K. V. Croxall, A. J. Deason, M. Eracleous, O. D. Fox, E. L. Gates, C. B. Henderson, E. Holmbeck, T. W.-S. Holoien, J. J. Jensen, C. A. Johnson, P. L. Kelly, S. Kim, A. King, M. W. Lau, M. Li, C. Lochhaas, Z. Ma, E. R. Manne-Nicholas, J. C. Mauerhan, M. A. Malkan, R. McGurk, L. Morelli, A. Mosquera, D. Mudd, F. Muller Sanchez, M. L. Nguyen, P. Ochner, B. Ou-Yang, A. Pancoast, M. T. Penny, A. Pizzella, R. Poleski, J. Runnoe, B. Scott, J. S. Schimoia, B. J. Shappee, I. Shivvers, G. V. Simonian, A. Siviero, G. Somers, D. J. Stevens, M. A. Strauss, J. Tayar, N. Tejos, T. Treu, J. Van Saders, L. Vican, S. Villanueva, Jr., H. Yuk, N. L. Zakamska, W. Zhu, M. D. Anderson, P. Arévalo, C. Bazhaw, S. Bisogni, G. A. Borman, M. C. Bottorff, W. N. Brandt, A. A. Breeveld, E. M. Cackett, M. T. Carini, D. M. Crenshaw, A. De Lorenzo-Cáceres, M. Dietrich, R. Edelson, N. V. Efimova, J. Ely, P. A. Evans, G. J. Ferland, K. Flatland, N. Gehrels, S. Geier, J. M. Gelbord, D. Grupe, A. Gupta, P. B. Hall, S. Hicks, D. Horenstein, K. Horne, T. Hutchison, M. Im, M. D. Joner, J. Jones, J. Kaastra, S. Kaspi, B. C. Kelly, J. A. Kennea, M. Kim, S. C. Kim, S. A. Klimanov, J. C. Lee, D. C. Leonard, P. Lira, F. MacInnis, S. Mathur, I. M. McHardy, C. Montouri, R. Musso, S. V. Nazarov, H. Netzer, R. P. Norris, J. A. Nousek, D. N. Okhmat, I. Papadakis, J. R. Parks, J.-U. Pott, S. E. Rafter, H.-W. Rix, D. A. Saylor, K. Schnülle, S. G. Sergeev, M. Siegel, A. Skielboe, M. Spencer, D. Starkey, H.-I. Sung, K. G. Teems, C. S. Turner, P. Uttley, C. Villforth, Y. Weiss, J.-H. Woo, H. Yan, S. Young, and Y. Zu. Space Telescope and Optical Reverberation Mapping Project. V. Optical Spectroscopic Campaign and Emission-line Analysis for NGC 5548. ApJ, 837:131, March 2017.

Liuyi Pei and AGN STORM Collaboration. Anomalous H-beta Variability in the 2014 NGC 5548 AGN-STORM Monitoring Campaign. In *American Astronomical Society Meeting Abstracts #228*, volume 228, page 314.11, June 2016.

E. Perez, A. Robinson, and L. de La Fuente. The response of the broad emission line region to ionizing continuum variations. III - an atlas of transfer functions. MNRAS, 256:103–110, May 1992.

B. M. Peterson. Reverberation mapping of active galactic nuclei. PASP, 105:247–268, March 1993.

B. M. Peterson. *An introduction to active galactic nuclei.* Cambridge University Press, 1997.

B. M. Peterson. Variability of active galactic nuclei. In I. Aretxaga, D. Kunth, and R. Mújica, editors, *Advanced Lectures on the Starburst-AGN*, page 3, 2001.

B. M. Peterson and M. C. Bentz. Black hole masses from reverberation mapping. New A Rev., 50(910):796 – 799, 2006. ISSN 1387-6473. {QSO} Host Galaxies: Evolution and Environments Workshop on {QSO} Host Galaxies: Evolution and Environments.

B. M. Peterson, M. C. Bentz, L.-B. Desroches, A. V. Filippenko, L. C. Ho, S. Kaspi, A. Laor, D. Maoz, E. C. Moran, R. W. Pogge, and A. C. Quillen. Multiwavelength Monitoring of the Dwarf Seyfert 1 Galaxy NGC 4395. I. A Reverberation-based Measurement of the Black Hole Mass. ApJ, 632:799–808, October 2005.

B. M. Peterson, M. C. Bentz, L.-B. Desroches, A. V. Filippenko, L. C. Ho, S. Kaspi, A. Laor, D. Maoz, E. C. Moran, R. W. Pogge, and A. C. Quillen. Erratum: "Multiwavelength Monitoring of the Dwarf Seyfert 1 Galaxy NGC 4395. I. A Reverberation-based Measurement of the Black Hole Mass" (¡A href="/abs/2005ApJ...632..799P"¿ApJ, 632, 799 [2005]¡/A¿). ApJ, 641:638–639, April 2006.

B. M. Peterson, P. Berlind, R. Bertram, K. Bischoff, N. G. Bochkarev, N. Borisov, A. N. Burenkov, M. Calkins, L. Carrasco, V. H. Chavushyan, R. Chornock, M. Dietrich, V. T. Doroshenko, O. V. Ezhkova, A. V. Filippenko, A. M. Gilbert, J. P. Huchra, W. Kollatschny, D. C. Leonard, W. Li, V. M. Lyuty, Y. F. Malkov, T. Matheson, N. I. Merkulova, V. P. Mikhailov, M. Modjaz, C. A. Onken, R. W. Pogge, V. I. Pronik, B. Qian, P. Romano, S. G. Sergeev, E. A. Sergeeva, A. I. Shapovalova, O. I. Spiridonova, J. Tao, S. Tokarz, J. R. Valdes, V. V. Vlasiuk, R. M. Wagner, and B. J. Wilkes. Steps toward Determination of the Size and Structure of the Broad-Line Region in Active Galactic Nuclei. XVI. A 13 Year Study of Spectral Variability in NGC 5548. ApJ, 581:197–204, December 2002.

B. M. Peterson, L. Ferrarese, K. M. Gilbert, S. Kaspi, M. A. Malkan, D. Maoz, D. Merritt, H. Netzer, C. A. Onken, R. W. Pogge, M. Vestergaard, and A. Wandel. Central masses and broad-line region sizes of active galactic nuclei. ii. a homogeneous analysis of a large reverberation-mapping database. ApJ, 613(2):682, 2004.

B. M. Peterson and K. Horne. Echo mapping of active galactic nuclei. *Astronomische Nachrichten*, 325:248–251, March 2004.

B. M. Peterson and A. Wandel. Keplerian motion of broad-line region gas as evidence for supermassive black holes in active galactic nuclei. ApJ, 521(2):L95, 1999.

F. P. Pijpers and I. Wanders. Reverberation mapping of active galactic nuclei: the SOLA method for time-series inversion. MNRAS, 271:183–196, November 1994.

P. Plavchan, R. Akeson, S. Carey, J. Carpenter, D. Ciardi, K. Covey, R. Gutermuth, P. Ogle, L. Rebull, K. Stapelfeldt, J. Stauffer, and B. Whitney. Measuring YSO inner accretion disk sizes, structure and dynamics with staring mode observations of 14 YSOs in Rho Ophiuchus. Spitzer Proposal, April 2009.

K. A. Pounds. The soft X-ray spectrum of the luminous narrow line Seyfert galaxy PG 1211+143 - evidence for a second high-velocity outflow component. MNRAS, 437: 3221–3227, February 2014.

F. Pozo Nuñez, M. Ramolla, C. Westhues, M. Haas, R. Chini, K. Steenbrugge, A. Barr Domínguez, L. Kaderhandt, M. Hackstein, W. Kollatschny, M. Zetzl, K. W. Hodapp, and M. Murphy. The broad-line region and dust torus size of the Seyfert 1 galaxy PGC 50427. A&A, 576:A73, April 2015.

A. Prieto. Spectral energy distribution template of redshift-zero AGN and the comparison with that of quasars. In *Journal of Physics Conference Series*, volume 372 of *Journal of Physics Conference Series*, page 012012, July 2012.

M. A. Prieto, K. Meisenheimer, O. Marco, J. Reunanen, M. Contini, Y. Clenet, R. I. Davies, D. Gratadour, T. Henning, U. Klaas, J. Kotilainen, C. Leinert, D. Lutz, D. Rouan, and N. Thatte. Unveiling the Central Parsec Region of an Active Galactic Nucleus: The Circinus Nucleus in the Near-Infrared with the Very Large Telescope. ApJ, 614:135–141, October 2004.

D. Proga. How Much X-Ray and UV Radiation Processes Are Coupled in Accretion Disks? The Active Galactic Nucleus Case. ApJ, 630:L9–L12, September 2005.

D. Proga and T. R. Kallman. Dynamics of Line-driven Disk Winds in Active Galactic Nuclei. II. Effects of Disk Radiation. ApJ, 616:688–695, December 2004.

D. Proga, J. M. Stone, and T. R. Kallman. Dynamics of line-driven disk winds in active galactic nuclei. ApJ, 543(2):686, 2000.

ReadTheDocs Team. Read the docs - technical documentation lives here. https://readthedocs.org, 2018.

J. N. Reeves, V. Braito, E. Behar, T. C. Fischer, S. B. Kraemer, A. Lobban, E. Nardini, D. Porquet, and T. J. Turner. High-resolution X-Ray Spectroscopy of the Seyfert 1 Galaxy Mrk 1040. Revealing the Failed Nuclear Wind with Chandra. ApJ, 837:23, March 2017.

J. N. Reeves, V. Braito, E. Nardini, E. Behar, P. T. O'Brien, F. Tombesi, T. J. Turner, and M. T. Costa. Discovery of Broad Soft X-ray Absorption Lines from the Quasar Wind in PDS 456. ApJ, 824:20, June 2016.

T. A. Reichard, G. T. Richards, P. B. Hall, D. P. Schneider, D. E. Vanden Berk, X. Fan, D. G. York, G. R. Knapp, and J. Brinkmann. Continuum and Emission-Line Properties of Broad Absorption Line Quasars. AJ, 126:2594–2607, December 2003.

C. S. Reynolds, A. J. Young, M. C. Begelman, and A. C. Fabian. X-ray iron line reverberation from black hole accretion disks. AJ, 514:164–179, March 1999.

G. T. Richards, M. Lacy, L. J. Storrie-Lombardi, P. B. Hall, S. C. Gallagher, D. C. Hines, X. Fan, C. Papovich, D. E. Vanden Berk, G. B. Trammell, D. P. Schneider, M. Vestergaard, D. G. York, S. Jester, S. F. Anderson, T. Budavári, and A. S. Szalay. Spectral Energy Distributions and Multiwavelength Selection of Type 1 Quasars. ApJS, 166:470–497, October 2006.

G. B. Rybicki and D. G. Hummer. A generalization of the sobolev method for flows with nonlocal radiative coupling. ApJ, 219:654–675, January 1978.

T. Sbarrato, P. Padovani, and G. Ghisellini. The jet-disc connection in AGN. MNRAS, 445:81–92, November 2014.

I. Schlosman and P. Vitello. WINDS FROM ACCRETION DISKS - ULTRAVIOLET LINE FORMATION IN CATACLYSMIC VARIABLES. *ASTROPHYSICAL JOURNAL*, 409(1, 1):372–386, MAY 20 1993. ISSN 0004-637X.

N. I. Shakura and R. A. Sunyaev. Black holes in binary systems. Observational appearance. A&A, 24:337–355, 1973.

M. S. Shaw, R. W. Romani, G. Cotter, S. E. Healey, P. F. Michelson, A. C. S. Readhead, J. L. Richards, W. Max-Moerbeck, O. G. King, and W. J. Potter. Spectroscopy of broad-line blazars from 1lac. *The Astrophysical Journal*, 748(1):49, 2012.

Y. Shen, W. N. Brandt, K. S. Dawson, P. B. Hall, I. D. McGreer, S. F. Anderson, Y. Chen, K. D. Denney, S. Eftekharzadeh, X. Fan, Y. Gao, P. J. Green, J. E. Greene, L. C. Ho, K. Horne, L. Jiang, B. C. Kelly, K. Kinemuchi, C. S. Kochanek, I. Pâris, C. M. Peters, B. M. Peterson, P. Petitjean, K. Ponder, G. T. Richards, D. P. Schneider, A. Seth, R. N. Smith, M. A. Strauss, C. Tao, J. R. Trump, W. M. Wood-Vasey, Y. Zu, D. J. Eisenstein, K. Pan, D. Bizyaev, V. Malanushenko, E. Malanushenko, and D. Oravetz. The Sloan Digital Sky Survey Reverberation Mapping Project: Technical Overview. ApJS, 216:4, January 2015.

Y. Shen and L. C. Ho. The diversity of quasars unified by accretion and orientation. Nature, 513:210–213, September 2014.

Yue Shen, Keith Horne, C. J. Grier, Bradley M. Peterson, Kelly D. Denney, Jonathan R. Trump, Mouyuan Sun, W. N. Brandt, Christopher S. Kochanek, Kyle S. Dawson, Paul J. Green, Jenny E. Greene, Patrick B. Hall, Luis C. Ho, Linhua Jiang, Karen Kinemuchi, Ian D. McGreer, Patrick Petitjean, Gordon T. Richards, Donald P. Schneider, Michael A. Strauss, Charling Tao, W. M. Wood-Vasey, Ying Zu, Kaike Pan, Dmitry Bizyaev, Jian Ge, Daniel Oravetz, and Audrey Simmons. The Sloan Digital Sky Survey Reverberation Mapping Project: First Broad-line Hβ and Mg II Lags at z $\gtrsim$ 0.3 from Six-month Spectroscopy. ApJ, 818:30, Feb 2016.

I. Shlosman and P. Vitello. Winds from accretion disks - Ultraviolet line formation in cataclysmic variables. ApJ, 409:372–386, May 1993.

J. Silk. Unleashing Positive Feedback: Linking the Rates of Star Formation, Supermassive Black Hole Accretion, and Outflows in Distant Galaxies. ApJ, 772:112, August 2013.

S. A. Sim, J. E. Drew, and K. S. Long. Two-dimensional monte carlo simulations of h i line formation in massive young stellar object disc winds. MNRAS, 363(2):615–627, 2005. ISSN 0035-8711. Copyright 2011 Elsevier B.V., All rights reserved.

S. A. Sim, L. Miller, K. S. Long, T. J. Turner, and J. N. Reeves. Multidimensional modelling of X-ray spectra for AGN accretion disc outflows - II. MNRAS, 404:1369–1384, May 2010.

A. Skielboe, A. Pancoast, T. Treu, D. Park, A. J. Barth, and M. C. Bentz. Constraints on the broad line region from regularized linear inversion: velocity-delay maps for five nearby active galactic nuclei. MNRAS, 454:144–160, November 2015.

Sphinx Team. Sphinx - python document generator. http://www.sphinx-doc.org/en/master/index.html, 2018.

John Stauffer, Peter Plavchan, Maria Morales, Luisa Rebull, and Barb Whitney. New Constraints for YSO Inner Accretion Disks with Spitzer and Spartan. NOAO Proposal, February 2010.

B. Stelzer. Variability of young stellar objects: Accretion, disks, outflows, and magnetic activity. *Astronomische Nachrichten*, 336:493, June 2015.

T. Storchi-Bergmann, J. S. Schimoia, B. M. Peterson, M. Elvis, K. D. Denney, M. Eracleous, and R. S. Nemmen. Double-Peaked Profiles: Ubiquitous Signatures of Disks in the Broad Emission Lines of Active Galactic Nuclei. ApJ, 835:236, February 2017.

R. A. Sunyaev and J. Truemper. Hard X-ray spectrum of CYG X-1. Nature, 279: 506–508, June 1979.

The Astropy Collaboration, A. M. Price-Whelan, B. M. Sipőcz, H. M. Günther, P. L. Lim, S. M. Crawford, S. Conseil, D. L. Shupe, M. W. Craig, N. Dencheva, A. Ginsburg, J. T. VanderPlas, L. D. Bradley, D. Pérez-Suárez, M. de Val-Borro, T. L. Aldcroft, K. L. Cruz, T. P. Robitaille, E. J. Tollerud, C. Ardelean, T. Babej, M. Bachetti, A. V. Bakanov, S. P. Bamford, G. Barentsen, P. Barmby, A. Baumbach, K. L. Berry, F. Biscani, M. Boquien, K. A. Bostroem, L. G. Bouma, G. B. Brammer, E. M. Bray, H. Breytenbach, H. Buddelmeijer, D. J. Burke, G. Calderone, J. L. Cano Rodríguez, M. Cara, J. V. M. Cardoso, S. Cheedella, Y. Copin, D. Crichton, D. DÁvella, C. Deil, É. Depagne, J. P. Dietrich, A. Donath, M. Droettboom, N. Earl, T. Erben, S. Fabbro, L. A. Ferreira, T. Finethy, R. T. Fox, L. H. Garrison, S. L. J. Gibbons, D. A. Goldstein, R. Gommers, J. P. Greco, P. Greenfield, A. M. Groener, F. Grollier, A. Hagen, P. Hirst, D. Homeier, A. J. Horton, G. Hosseinzadeh, L. Hu, J. S. Hunkeler, Ž. Ivezić, A. Jain, T. Jenness, G. Kanarek, S. Kendrew, N. S. Kern, W. E. Kerzendorf, A. Khvalko,

J. King, D. Kirkby, A. M. Kulkarni, A. Kumar, A. Lee, D. Lenz, S. P. Littlefair, Z. Ma, D. M. Macleod, M. Mastropietro, C. McCully, S. Montagnac, B. M. Morris, M. Mueller, S. J. Mumford, D. Muna, N. A. Murphy, S. Nelson, G. H. Nguyen, J. P. Ninan, M. Nöthe, S. Ogaz, S. Oh, J. K. Parejko, N. Parley, S. Pascual, R. Patil, A. A. Patil, A. L. Plunkett, J. X. Prochaska, T. Rastogi, V. Reddy Janga, J. Sabater, P. Sakurikar, M. Seifert, L. E. Sherbert, H. Sherwood-Taylor, A. Y. Shih, J. Sick, M. T. Silbiger, S. Singanamalla, L. P. Singer, P. H. Sladen, K. A. Sooley, S. Sornarajah, O. Streicher, P. Teuben, S. W. Thomas, G. R. Tremblay, J. E. H. Turner, V. Terrón, M. H. van Kerkwijk, A. de la Vega, L. L. Watkins, B. A. Weaver, J. B. Whitmore, J. Woillez, and V. Zabalza. The Astropy Project: Building an inclusive, open-science project and status of the v2.0 core package. *ArXiv e-prints*, January 2018.

A. Tolea, J. H. Krolik, and Z. Tsvetanov. Broad Absorption Line Quasars in the Early Data Release from the Sloan Digital Sky Survey. ApJ, 578:L31–L35, October 2002.

F. Tombesi, M. Cappi, J. N. Reeves, and V. Braito. Evidence for ultrafast outflows in radio-quiet AGNs - III. Location and energetics. MNRAS, 422:L1–L5, May 2012.

F. Tombesi, M. Cappi, J. N. Reeves, R. S. Nemmen, V. Braito, M. Gaspari, and C. S. Reynolds. Unification of x-ray winds in seyfert galaxies: from ultra-fast outflows to warm absorbers. MNRAS, 430:1102–1117, April 2013.

F. Tombesi, M. Cappi, J. N. Reeves, G. G. C. Palumbo, T. Yaqoob, V. Braito, and M. Dadina. Evidence for ultra-fast outflows in radio-quiet AGNs. I. Detection and statistical incidence of Fe K-shell absorption lines. A&A, 521:A57, October 2010.

T. J. Turner and L. Miller. X-ray absorption and reflection in active galactic nuclei. A&A Rev., 17(1):47–104, 2009.

M.-H. Ulrich and K. Horne. A month in the life of NGC 4151: velocity-delay maps of the broad-line region. MNRAS, 283:748–758, December 1996.

M. H. Ulrich, L. Maraschi, and C. M. Urry. Variability of active galactic nuclei. ARA&A, 35:445–502, 1997. ISSN 0066-4146.

C. M. Urry and P. Padovani. Unified schemes for radio-loud active galactic nuclei. ApJ, 107:803, September 1995.

S. Valenti, D. J. Sand, A. J. Barth, K. Horne, T. Treu, L. Raganit, T. Boroson, S. Crawford, A. Pancoast, L. Pei, E. Romero-Colmenero, C. Villforth, and H. Winkler. Robotic Reverberation Mapping of Arp 151. ApJ, 813:L36, November 2015.

D. van Heesch. Doxygen - generate documentation from source code. http://www.doxygen.nl, 2018.

M. F. Walker. Studies of extragalactic nebulae. v. motions in the seyfert galaxy ngc 1068. ApJ, 151:71, January 1968.

A. Wandel. The Mass-Luminosity Relationship in AGN. In C. M. Gaskell, W. N. Brandt, M. Dietrich, D. Dultzin-Hacyan, and M. Eracleous, editors, *Structure and Kinematics of Quasar Broad Line Regions*, volume 175 of *Astronomical Society of the Pacific Conference Series*, page 213, 1999.

A. Wandel. Black holes of active and quiescent galaxies. i. the black hole-bulge relation revisited. ApJ, 565(2):762, 2002.

A. Wandel, B. M. Peterson, and M. A. Malkan. Central masses and broad-line region sizes of active galactic nuclei. i. comparing the photoionization and reverberation techniques. ApJ, 526(2):579, 1999.

I. Wanders, M. R. Goad, K. T. Korista, B. M. Peterson, K. Horne, G. J. Ferland, A. P. Koratkar, R. W. Pogge, and J. C. Shields. The Geometry and Kinematics of the Broad-Line Region in NGC 5548 from HST and IUE Observations. ApJ, 453:L87, November 1995.

J. L. Ward. *High-resolution studies of massive young stellar objects in the Magellanic Clouds*. PhD thesis, Keele University, June 2017.

M. J. Ward, C. Done, A. C. Fabian, A. F. Tennant, and R. A. Shafer. X-ray Observations of IRAS-Selected Galaxies and Obscuration of the Broad-Line Region. In *Bulletin of the American Astronomical Society*, volume 19, page 696, March 1987.

T. Waters, A. Kashi, D. Proga, M. Eracleous, A. J. Barth, and J. Greene. Reverberation Mapping of the Broad Line Region: Application to a Hydrodynamical Line-driven Disk Wind Solution. ApJ, 827:53, August 2016.

W. F. Welsh and K. Horne. Echo images of broad-line regions in active galactic nuclei. ApJ, 379(2):586–591, 1991.

R. J. Weymann, S. L. Morris, C. B. Foltz, and P. C. Hewett. Comparisons of the emission-line and continuum properties of broad absorption line and normal quasi-stellar objects. ApJ, 373:23–53, 1991.

R. J. White and B. M. Peterson. Comments on cross-correlation methodology in variability studies of active galactic nuclei. PASP, 106:879–889, August 1994.

J-H. Woo, D. Son, and H-J. Bae. Delayed or No Feedback? Gas Outflows in Type 2 AGNs. III. ApJ, 839:120, April 2017.

J-H. Woo, T. Treu, A. J. Barth, S. A. Wright, J. L Walsh, M. C. Bentz, P. Martini, V. N. Bennert, G. Canalizo, A. V. Filippenko, et al. The lick agn monitoring project: the m bh-σ^* relation for reverberation-mapped active galaxies. ApJ, 716(1):269, 2010.

J.-H. Woo and C. M. Urry. Active Galactic Nucleus Black Hole Masses and Bolometric Luminosities. ApJ, 579:530–544, November 2002.

J. A. Woods. *D. Phil thesis*. PhD thesis, Univ. Oxford, 1991.

M. Xiao, P. Du, K. D. Horne, C. Hu, Y.-R. Li, Y.-K. Huang, K.-X. Lu, J. Qiu, F. Wang, J.-M. Bai, W. Bian, L. C. Ho, Y.-F. Yuan, and J.-M. Wang. Supermassive black holes with high accretion rates in active galactic nuclei. VII. Reconstruction of velocity-delay maps by maximum entropy method. *ArXiv e-prints*, August 2018a.

M. Xiao, P. Du, K.-X. Lu, C. Hu, Y.-R. Li, Z.-X. Zhang, K. Wang, Y.-K. Huang, J. M. Bai, W. Bian, L. C. Ho, Y.-F. Yuan, and J.-M. Wang. A High-Quality velocity-delay map of the broad-line region in NGC 5548. *ArXiv e-prints*, September 2018b.

D. Xu, S. Komossa, H. Zhou, T. Wang, and J. Wei. The narrow-line region of narrow-line and broad-line type 1 active galactic nuclei. i. a zone of avoidance in density. ApJ, 670(1):60, 2007.

S. Y. Yong, R. L. Webster, and A. L. King. Black Hole Mass Estimation: How Good is the Virial Estimate? PASA, 33:e009, March 2016.

S. Young, D. J. Axon, A. Robinson, J. H. Hough, and J. E. Smith. The rotating wind of the quasar PG 1700+518. Nature, 450:74–76, November 2007.

F. Yuan, S. Markoff, and H. Falcke. A Jet-ADAF model for Sgr A*. A&A, 383:854–863, March 2002.

Ft. Yusef-Zadeh, M. Morris, and R. L. White. Bipolar reflection nebulae-monte carlo simulations. ApJ, 278:186–194, 1984. Peeling off.

Zenodo Team. Zenodo. https://zenodo.org, 2018.

Y. Zu, C. S. Kochanek, and B. M. Peterson. An Alternative Approach to Measuring Reverberation Lags in Active Galactic Nuclei. ApJ, 735:80, July 2011.